Ultra-high-Q inverted silica microtoroid resonators monolithically integrated into a silicon photonics platform

Von der Fakultät für Elektrotechnik und Informationstechnik
der Rheinisch-Westfälischen Technischen Hochschule Aachen
zur Erlangung des akademischen Grades eines Doktors der
Ingenieurwissenschaften genehmigte Dissertation

vorgelegt von
Diplom-Physiker
Jens Richter
aus Dresden

Berichter
Univ.-Prof. Dr. Jeremy Witzens
Sr. Lecturer Dr. Maziar Nezhad

Tag der mündlichen Prüfung: 10. Oktober 2018

Diese Dissertation ist auf den Internetseiten der Universitätsbibliothek online verfügbar.

This dissertation is dedicated to my wife Jessi.

Abstract (English)

This work reports on the design, fabrication and the optical characterization of a new singular type of microtoroid high-quality silica resonator, which is monolithically coupled to on-chip silicon nanowire waveguides. In order to enable monolithic waveguide coupling, the microtoroid geometry is inverted such that the resonator is formed by thermal reflow at the circumference of a hole etched in a suspended silica membrane. This configuration is shown to be conducive to integration with a fully functional Silicon Photonics technology platform.

Microresonators shaped by surface tension minimization of a melted silica film (microtoroids) are known for their extraordinarily high-quality factors on the order of a 100 million [1] and above, which enable the generation of frequency combs via nonlinear effects with very low optical power thresholds [2]. In the field of integrated silicon photonics, a high-quality resonator can provide a frequency-comb source. This frequency-comb can be used for telecommunication applications. In this approach, optical comb lines act as individual carriers and are modulated by the help of additional modulators [3–5].

Besides telecommunication applications, high-quality microresonators can be utilized in spectroscopic, sensing applications and many more. Examples are heavy water detection [6], DNA quantification [7], single protein detection [8], single virus detection [9], integrated bio-sensing platforms [10], micro-optic gyroscopes [11], label-free bio-molecular sensing [12, 13], narrow linewidth lasers with external resonant feedback [14, 15], or tunable delay lines used in signal buffering [16], and optical or Radio-Frequency (RF) phase arrays [17].

The first Kerr nonlinearity induced optical parametric oscillation in a microtoroidal structure was reported by Kippenberg in 2004 in a resonator's transition from a stimulated Raman to an optical parametric oscillation regime [18]. This work enabled the generation of a frequency comb by the interaction of a continuous mode source laser ($\lambda = 1550\,\text{nm}$) with the modes of a high-quality microresonator via the Kerr nonlinearity. Repetition rates exceeding 100 GHz and a comb uniformity over a 500 nm wavelength span [19].

During the last years, several materials have been explored for the fabrication of high-quality cavities. Besides silica, for example, CaF_2 [20, 21], TEOS [22], Si [23–25] and SiN [26–28] have been utilized among many others.

The initially proposed silica microtoroids are typically coupled to an external tapered fiber. Existing integration schemes of microtoroid type structures with on-chip waveguides have either relied on silica waveguides [29] or suspended silicon waveguides fabricated in stacked silicon-on-insulator (SOI) device layers with a rather complicated fabrication process [30]. Here we introduce a device geometry allowing straightforward coupling with silicon nanowire-waveguides and integration with existing Silicon Photonics (SiP) technology, monolithically combining microtoroids with devices such as electro-optic modulators, wavelength multiplexers, grating couplers or photodetectors.

For coupling light into a high-Q cavity in principle, three different methods are in use. In the case of a silica microtoroid, most commonly tapered fibers have been used in which a fiber is tapered down to a diameter of several micrometers [1] and approaches the desired cavity until the desired coupling strength is achieved. Previously, for spherical cavities prism-coupling techniques have also been successfully demonstrated [31].

The central concept consists in combining a silicon waveguide fabricated in the device layer of an SOI-chip with an inverted version of a microtoroid fabricated by reflowing the buried oxide (BOX) of the same chip. Even though the inverted geometry results in weakened confinement, simulations indicate that such a structure is able of achieving comparably high Q-factors as conventionally designed microtoroids [32]. A balance has, however, to be found in choosing the thickness of the BOX layer by trading off Si waveguide substrate coupling losses against microtoroid bending losses.

This work shows that the proposed inverted silica-based microtoroid can be coupled monolithically to a silicon waveguide and shows comparatively high-quality factors on the order of a few million. Even though the generation of a frequency comb is not achieved in this work, which is targeted in future work, and the measured quality factor is lower than expected, the proposed device can be seen as a proof of concept for the outlined idea. Also, an optimized in-house fabrication process is established, which can be scaled up for fabricating many inverted microtoroids in parallel, for further testing and improving the proposed device.

Kurzfassung (German)

In der vorliegenden Arbeit wird über das Design, die Herstellung, und die optische Charakterisierung eines neuartigen mikrotoroidalen Siliziumdioxidresonators mit extrem hohen Gütefaktoren (high-Q), welcher monolithisch an einen on-chip-Siliziumwellenleiter gekoppelt wird, berichtet. Um eine monolithische Wellenleiterkopplung zu ermöglichen, wird die herkömmliche toroidale Geometrie invertiert. Ein solcher invertierte Resonator wird durch Schmelzen einer Siliziumdioxidmembrane, unter der Zuhilfenahme eines CO_2-Lasers, gebildet. Diese Membrane verfügt über ein Loch, welches dazu dient diese zusätzlich zu unterätzen. Der eigentliche Schmelzvorgang findet entlang des Lochumfangs statt. Das Ziel dieser Konfiguration ist die Integration eines invertierten Mikrotoroiden mit einer voll funktionsfähigen Silizium-Photonik-Technologie-Plattform.

Mikroresonatoren, welche durch die Minimierung der Oberflächenspannung eines geschmolzenen Siliziumdioxidfilms geformt werden, können einen außergewöhnlich hohen Qualitätsfaktor in der Größenordnung von bis zu 100 Millionen [1] und darüber erreichen. Qualitätsfaktoren in dieser Größenordnung ermöglichen durch nicht lineare Effekte die Erzeugung von Frequenzkämmen mit sehr niedrigen optischen Leistungsschwellen [2]. Im Bereich der integrierten Silizium-Photonik kann ein solcher high-Q Resonator somit als Frequenzkammquelle dienen. Ein solcher Frequenzkamm kann zum Beispiel für Telekommunikationsanwendungen eingesetzt werden. Bei diesem Einsatz werden individuelle optische Kammlinien durch zusätzliche Modulatoren moduliert [3–5] und ein Datensignal aufgeprägt.

Neben Telekommunikationsanwendungen können high-Q Resonatoren auch in spektroskopischen und sensorischen Anwendungen genutzt werden. Beispiele sind die Detektion von schwerem Wasser [6], DNS-Quantifizierung [7], Einzelproteinnachweise [8], Einzelvirusdetektion [9], integrierte Biosensorik-Plattformen [10], mikrooptische Gyroskope [11], markierungsfreie Biomolekularsensoren [12,13], schmalbandige Laser mit externen resonanten Feedback [14, 15], oder abstimmbare Verzögerungsleitungen zur Signalpufferung [16], sowie Phasenarrays [17].

Die erste induzierte optisch-parametrische Schwingung in einer mikrotoroidalen Struktur, basierend auf der Kerr-Nichtlinearität, wurde von Kippenberg im Jahr *2004* in einem Resonator-Übergang von einem stimulierten Raman- zu einem optisch-parametrischen Schwingungsregime gezeigt [18]. Dies ermöglichte die Generierung eines Frequenzkamms durch das Zusammenwirken eines kontinuierlichen Quellenlasers ($\lambda = 1550\,\mathrm{nm}$) mit einem Mikroresonator. Es wurden Wiederholraten, bezogen auf den Abstand der einzelnen Kammlinien, von über 100 GHz und eine Kammuniformität über einen Wellenlängenbereich von 500 nm gezeigt [19]. In den letzten Jahren wurden verschiedene Materialien für die Herstellung von hochwertige Resonatoren verwendet. Neben SiO_2 wurden unter anderem CaF_2 [20, 21], TEOS [22], Si [23–25] und SiN [26–28] eingesetzt.

Die aus der Literatur bekannten herkömmlichen SiO_2-Mikrotoroide werden typischerweise mit einer optischen Faser extern gekoppelt. Eine solche Kopplungsfaser wird dabei auf einen Durchmesser von einigen Mikrometern verjüngt [1] und an den Resonator angenähert, bis die gewünschte Kopplungsstärke erreicht ist. Um im Gegensatz eine monolithische Integration des Resonators mit einem Wellenleiter auf einem Chip zu erreichen, wurden zum Beispiel in anderen Arbeiten Siliziumoxid-Wellenleiter [29] oder freischwebende Silizium-Wellenleiter verwendet. Im letzteren Fall wurde ein aufwendiges Herstellungsverfahren, basierend auf einer gestapelten Silicon-on-Insulator-(SOI) Plattform [30], genutzt.

In dieser Arbeit soll eine Geometrie eingeführt werden, welche es erlaubt einen invertierten Mikrotoroiden mit Silizium-Wellenreitern zu koppeln und eine Integration mit existierender SiP zu erreichen. Dies könnte zum Beispiel die monolithische Kombination und Integration von Mikrotoroiden mit Bauteilen wie elektrooptischen Modulatoren, Wellenlängenmultiplexern, Gitterkopplern und Fotodetektoren sein. Um dies zu erreichen, wird der Wellenleiter in der Siliziumschicht (Device Layer) eines SOI-Chips hergestellt. Der geometrisch invertierte Mikrotoroid wird in der vergrabenen Siliziumdioxidschicht (BOX) desselben Chips fabriziert.

Auch wenn die invertierte Geometrie zwangsläufig zu einem geschwächten optischen Moden-Confinement führt, implizieren optische Simulationen, dass eine solche Geometrie in der Lage ist ähnlich hohe Qualitätsfaktoren, wie herkömmliche Mikrotoroide, zu erreichen [32]. Es ist jedoch entscheidend die optischen Siliziumsubstrat-Kopplungsverluste der Wellenleiter und die zu erwartenden optischen Krümmungsverluste des invertierten Mikrotoroiden, durch die Wahl der verwendeten Dicke der BOX-Schicht, zu optimieren.

Die vorliegende Arbeit zeigt, dass ein invertierter Siliziumdioxid-Mikrotoroid monolithisch an einen Silizium-Wellenleiter gekoppelt werden kann und vergleichsweise hohe Qualitätsfaktoren von einigen Millionen erreichen kann. Die Erzeugung eines Frequenzkamms konnte in dieser Arbeit noch nicht gezeigt werden, ist aber in zukünftigen Arbeiten angestrebt. Die bereits gemessenen Qualitätsfaktoren sind zwar niedriger als erwartet, jedoch kann das erstellte Bauteil als „Proof of Concept“ angesehen werden. Zudem wurde ein dediziertes und optimiertes hauseigenes Herstellungsverfahren entwickelt, bei dem mehrere invertierte Mikrotoroide parallel fabriziert werden können, um weitere systematische Testreihen durchzuführen, um eine stetige Verbesserung des Bauteils in der Zukunft zu erreichen.

Acknowledgments

This dissertation was written during my time as a research assistant at the Institute of Integrated Photonics (IPH) at the RWTH University. Even though I am the person that puts his name under this thesis, the last years in research were a journey, which I shared with my supervisor, colleagues, students, friends, and family. As on every journey, sometimes the weather is sunny, and sometimes it is rainy. Luckily, I can assure you, I had a good time. I guess, without the contribution, help, motivation, and support, no matter in which way, provided by other people, nobody is able to work in a focused, successful and, most importantly, happy way. A fact, which remains true for me. Thanks to all of you!

However, to follow a tradition, I would like to address some of you personally. First, I would like to thank Prof. Dr. Jeremy Witzens, my supervisor during the last years. I still remember your first email after I asked about a position. You were friendly, polite and warm, qualities that never changed over the years. Not only that you secured the funding for my work, but you were also a supervisor to which the words "My door's open" perfectly suits. You gave me the opportunities, motivation, and the full backing a Ph.D. student needs.

Of course, I would like to thank Dr. Maziar Nezhad. You were the first person, that showed me, how a cleanroom looks from inside. Further, you taught me the right spirit for this kind of work, and you showed me that research is fun. Also, Dr. Florian Merget is a person that I want to acknowledge. Honestly, I really miss the time when I just entered your office and started talking about my day-to-day ideas. However, you were always listening to me and gave me valuable advice. Even though that Dr. Alvaro Mártir joined our Institute, later on, I guess nobody can imagine an IPH without him. You were always in a great mood, helped with your expertise and motivated all the people around you. Thank you.

For sure, an Institute has a fundamental base, its administrative staff. In our case, Doro Pawelzick and Anne Schröder. Both of you supported me and helped me throughout my years. I am thankful to work and laughed together with you. Further, I want to address Heijo Ehlen. Talking to you about the world, computers, and programming gave me a restful break in a stressful day.

I want to thank all my other co-workers. Sharing a lab, an office and free time with you gave me the strength I needed. Also, you helped me with the proofread of this dissertation. Thank you: Bin Shen, Saeed Sharif, Bahareh (Farnita) Marzban, Juliana Müller, Ali(reza) Mashayekh, Ibrahim Ghannam, Dr. Sebastián Romero García, Jonas Leuermann, Julio Hernández and finally but not least Johannes Hauck. Thank you for being such great colleagues and friends!

Further, I also want to thank people from other Institutes. First, the Institute of Semiconductor Technology (IHT) was of great help and support, as they shared their equipment and knowledge, making my work possible. As all of you were so friendly and helpful, it is hard to pick names.

However, two persons, I worked with on a daily basis, I would like to acknowledge: Birgit Hadam and Noël Wilck. Both of you treated me as if I was a member of your institute, helping me with my fabrication issues, and made me laugh even though something was not working as expected. For sure, I also want to thank Prof. Dr. Joachim Knoch who is the head of the IHT. Because of you, I was able to work in a fully equipped cleanroom.

Additionally, I would like to thank our neighbors, the Institute of Compound Semiconductor Technology (CST) with their head Prof. Dr. Andrei Vescan. Especially, I want to acknowledge Frank Jessen from the CST. Whenever I asked you for a favor (and I know there were plenty of them), you helped me in your friendly way. It was a pleasure being your neighbor.

Hard to believe but there is a life outside of the university. Not all the support a person needs is of scientific nature. Therefore, I would like to thank my friends and family. I want to acknowledge my close friend Dr. Christoph Santel, who was so kind and read my whole dissertation and gave me so much valuable input. Nonetheless, all my other friends deserve a big "Thank you!". Of course, I want to acknowledge my parents Christa and Frank for supporting me throughout the years. I know, for you, the only thing that ever mattered, is that I am happy with what I am doing. Finally, I want to thank my wife, Jessi. You supported me at every single day in our relationship with your love, your smile, and your care.

Essen, Germany in July of 2018 *Jens Richter*

Contents

List of Figures

List of Tables

Nomenclature

Acronyms and Abbreviations

AlN	Aluminium nitride
AFM	Atomic force microscope
ASK	Amplitude-shift-keying
AWG	Arrayed waveguide grating
BER	Bit error rate
BOX	Buried oxide
BPF	Bandpass filter
C_4F_8	Octafluorocyclobutane
CaF_2	Calcium fluoride
CHF3	Fluoroform
cc	Critical coupling
CCD	Charge-coupled device
CMOS	Complementary metal–oxide–semiconductor
D_2O	Deuterium oxide
DEMUX	Demultiplexer
DFTS	Nondispersive Fourier transform spectroscopy
EBL	Electron lithography
F	Finesse
FDTD	Finite-difference-time-domain

FEM	Finite element method
FEOL	Front-End-Of-Line
FSR	Free spectral range
FTIR	Fourier-transform infrared spectroscopy
FWHM	Full width at half maximum
H_2O	Water
HF	Hydrofluoric acid
HMDS	Hexamethyldisilazane
HSQ	Hydrogen silsesquioxane
ICP	Inductively coupled plasma
IQ	(I)n-phase component; (Q)uadrature component
IVT	Inverted microtoroid
KCl	Potassium chloride
$LiNbO_3$	Lithium niobate
LPCVD	Low Pressure Chemical Vapor Deposition
MgF_2	Magnesium fluoride
MUX	Multiplexer
MZI	Mach–Zehnder interferometer
MZM	Mach-Zehnder-modulator
O_2	Oxygen
oc	Overcoupling
OOK	On-off-keying
OPO	Optical parametric oscillator
PAM	Pulse-amplitude modulation
PEC	Perfect electrical conductor

PECVD	Plasma Enhanced Chemical Vapor Deposition
PIC	Photonic Integrated Circuit
PML	Perfectly matched layer
PMMA	Polymethylmethacrylate
QAM-4	Quadrature amplitude modulation
QCL	Quantum-cascade-laser
QPSK	Quadrature phase-shift keying
RIE	Reactive-ion etching
RMOG	Micro-optical gyroscope
RMS	Root-mean-square
RRM	Resonant ring modulator
SF_6	Sulfur hexafluoride
Si_3N_4	Silicon nitride
SiF_4	Silicon tetrafluoride
SiO_2	Silica, Silicon dioxide
SEM	Scanning electron microscope
Si	Silicon
SiC	Siliciumcarbid
SiP	Silicon Photonics
SNOM	Scanning near-field optical microscope
SOI	Silicon-on-insulator
TE	Transverse electric
TEC	Temperature controller
TEM	Transverse electromagnetic wave
TEOS	Tetraethoxysilicate

TM	Transverse magnetic
TMAH	Tetramethylammonium hydroxide
TPA	Two-Photon Absorption
uc	Undercoupling
VIPA	Virtually imaged phased array
WDM	Wavelength-division-multiplexing
WGM	Whispering-gallery-mode
XeF_2	Xenon difluoride

Chapter 1

Outline

This thesis arose at the Institute of Integrated Photonics (IPH) at the RWTH University supervised by Prof. Dr. Jeremy Witzens.

1.1 Outline of this work

This work is subdivided into six main chapters that are summarized in the following:

Chapter 2 - Prior art - The theory of a waveguide and a coupled ring resonator:

This chapter summarizes and explains the underlying physics and the mathematical description of the proposed monolithically coupled inverted silica microtoroid (IVT). It covers the theory of light propagation in an on-chip waveguide. Furthermore, it deals with the coupling of light from an optical fiber into an on-chip waveguide via an edge-coupler and a grating coupler. Most importantly, it describes the mathematical model of a ring resonator that is coupled to a waveguide. This mechanism will be the fundamental base for analyzing and fitting measurement results and extracting intrinsic quality-factors of the proposed device.

Chapter 3 - Prior art and state of the art - The ultra-high-Q resonator:

In the recent years, several attempts have been carried out to obtain high-quality resonators (high-Q). For obtaining this goal, several material systems have been explored including silica, silicon nitride, and calcium fluoride among many others for the fabrication of high-Q resonators. This chapter summarizes which material system have been explored so far. Further, it describes various applications, which are utilizing a high-Q resonator. In particular, comb generation in high-Q resonators can be triggered, which can be used in the field of optical telecommunications or sensing applications as well.

Finally, this chapter gives a summary about the conventional microtoroid, explains fabrication attempts, and outlines its optical loss channels, which will determine the maximum obtainable intrinsic quality-factor. As the proposed device of this work is based on the concept of a conventional microtoroid, loss channels are of particular interest when designing an inverted microtoroid.

Chapter 4 - Proposed device - The monolithically coupled inverted silica microtoroid:

This chapter illustrates the research idea. For proving the theoretical feasibility of the inverted microtoroid, for example, in terms of the expected quality-factor, various optical simulations are carried out. These simulations include the edge-coupling section (which couples light from an external optical fiber to an on-chip silicon waveguide), the interconnect waveguide section (which is routing the light across the chip), the coupling junction (in which light is coupled from a silicon waveguide to an inverted microtoroidal resonator), and the inverted microtoroid itself. Of particular interest are the bending losses of the proposed device, which are assumed higher, compared to conventional microtoroids.

Chapter 5 - Fabrication - The monolithically coupled inverted silica microtoroid:

A significant part of this work is dedicated to the development and the realization of the fabrication of the inverted microtoroid and is summarized and explained in this chapter. The fabrication of the device is divided into two major parts, the part of the fabrication using cleanroom equipment (including electron lithography, optical lithography, and material-etching processes) and the CO_2-Laser-Reflow, which is forming the actual microtoroidal shape of the silica microtoroid.

Especially the part of the fabrication using cleanroom equipment was explored extensively, using different technologies, including dry- and wet-etching processes and different optical mask designs.

The Laser-Reflow-setup that was built as part of this work is characterized regarding optical output power, beam characteristics and in terms of melting results.

Chapter 6 - Characterization - The monolithically coupled inverted silica microtoroid:

For extracting the optical parameters of the proposed device, including its quality-factors, its coupling regime and its free spectral range among others, a measurement edge-coupling-setup was built. This chapter explains the setup and the procedure for measuring and extracting the parameters of interest from an optical spectrum. For doing so, two coupler designs are investigated and compared. Further, temperature-dependent measurements have been performed. Also, this chapter discusses different parts of the device regarding their optical and mechanical properties and gives an overview, and a discussion of various challenges occurred during the fabrication of the devices and the optical characterization.

Chapter 7 - Conclusion and prospects:

In the last chapter of this work, a conclusion is drawn, separately concluding on the proposed design of the inverted microtoroid device, the fabrication of the device, and the characterization of the device. In addition, the side benefits of this project are discussed.

Finally, a prospect focuses on potential improvements. The potential improvements, which are discussed, involve a potential Front-end and Back-end integration, the improvement of the fabrication flow, the improvement of the device design and the enhancement of the intrinsic quality-factors.

1.2 Collaborators and partners

During the work on the inverted microtoroid project, several collaborators were involved. Especially at the beginning, the fabrication of the IVT was not done in-house. For the first proof of concept fabrication runs, the cleanroom situated at the University of California San Diego (UCSD) and the cleanroom at the FZ-Jülich (FZJ) have been used. Furthermore, for testing a XeF_2 process, the facilities of the Fraunhofer-IPMS in Dresden were used. For further simplifying the fabrication process, for example, for avoiding the necessity of sending chips between different cleanroom facilities, which are equipped with different tools, the Mesa+ cleanroom located at the University of Twente (UT) was used. Finally, the fabrication process was modified to allow for an in-house fabrication, which is carried out in a cleanroom located at the RWTH Aachen University (RWTH). In particular, equipment provided by the Institute of Semiconductor Technology (IHT) and the Institute of Compound Semiconductor Technology (CST) is utilized.

For knowledge transfer and further discussion, we worked closely together with Dr. Maziar Nezhad, who is a former member of our Institute, and now works as a senior lecturer at the School of Electronic Engineering at the University of Bangor.

Chapter 2

Prior art - The theory of a waveguide and a coupled ring resonator

The monolithically coupled inverted silica microtoroid (IVT) is the proposed device of this thesis (Section 4).

This chapter will serve as fundamental theoretical background for the following research work. In a short overview, it will summarize how light is propagated either in free space (or bulk material) (Section 2.1.1) or in a waveguide (Section 2.1.2).

An on-chip waveguide, which is used in this work, is coupled to an external source of light. In this thesis, edge couplers are used for input and output-coupling (Section 2.2.1). Coupling light from a waveguide into a ring resonator (or an inverted silica microtoroid) can be described by a transfer-matrix method. The system of a waveguide and a resonator can be modeled and characterized by different parameters, for example, its quality-factors (Section 2.3.2). In practice, a measurement of this coupled device can be fitted to a theoretical model, and various parameters can be extracted (Section 2.3.4).

Also, different sources of optical loss can occur in such a system. For example, coupler excess losses need to be minimized by dedicated design approach (Section 2.3.5).

2.1 Propagation of light in an on-chip waveguide

One of the requirements when it comes to the design of integrated optical circuits is a way of propagating light across a chip. In this work, this kind of waveguide will be called transition or interconnect waveguide. An on-chip waveguide can be used to route light efficiently, for example, from a coupling device (like an edge or grating coupler) to an on-chip device (like a resonator or a modulator). In the field of silicon photonics (SiP), waveguides are most often monolithically integrated on a chip. Depending on the material and the geometry of a waveguide, different wavelengths can be routed with low loss. In silicon photonics, a single-mode waveguide, which is used for routing light at the optical telecommunication wavelength of 1550 nm is usually made out of silicon. Also, low loss single-mode fibers can be fabricated for the optical telecommunication wavelength [33]

To understand which wavelength can be routed and which electromagnetic field distributions (or also called a mode) can be excited in a waveguide, the propagation of light in bulk media must be understood (Section 2.1.1). Furthermore, the theoretical description of guided light, which is confined in a waveguide can be developed (Section 2.1.2).

2.1.1 Propagation of light in homogeneous bulk media

For describing the propagation of light in media, like solids, bulk materials, gases or in a vacuum, different microscopic concepts need to be taken into account. The underlying fundamental physics of the propagation of light in homogeneous media can be reduced to a macroscopic description. The Maxwell equations in media [34] are describing the interaction of matter and light.

In general, the electrical field **E** and the magnetic field **H** of a transverse plane wave of light, which propagates along the **x**-direction (with **x**-components (x,y,z)), is changing its phase φ as a function of traveled distance and time t. It can be described by the following three equations fulfilling the Helmholtz equation [35, pp. 15]:

$$\begin{aligned} E(\mathbf{x},t) &= E_0 e^{i(\mathbf{kx} \pm \omega t)}, && (2.1)\\ \mathbf{H}(\mathbf{x},t) &= \mathbf{H_0} e^{i(\mathbf{kx} \pm \omega t)}, && (2.2)\\ \varphi &= \boldsymbol{kx} \pm \omega t && (2.3) \end{aligned}$$

where i is the imaginary number, ω is the angular frequency describing the phase-change over time (Eq. 2.4), and $\mathbf{k} = (k_x, k_y, k_z)$ is the wave vector (Eq. 2.5) [35, pp. 15].

$$\begin{aligned} \frac{\partial \varphi}{\partial t} &= \omega && (2.4)\\ \frac{\partial \varphi}{\partial \mathbf{x}} &= \mathbf{k} && (2.5) \end{aligned}$$

Following these equations, it is possible to describe a wave of light in a medium. The angular frequency ω can be defined by the wavelength λ in the medium, the phase speed (or phase velocity) of the light c in the medium and the frequency ν (Eq. 2.6). Furthermore, it is necessary to take the wavelength dependent media specific complex refractive index $N(\omega)$ into account.

As the refractive index N is a complex number, it can be written as $N = n(\omega) + i\kappa(\omega)$. The real part of the refractive index, for simplicity also referred to as refractive index, n plays the role of a factor which is reducing the phase speed c and the wavelength λ of the light relative to its free space speed c_0 and its free space wavelength λ_0 (Eq. 2.7 and Eq. 2.8). Essentially, n is describing the ratio of the speed of light in free space compared to the speed of light in a medium (Eq. 2.9).

In materials, the refractive index is greater or equal to one ($n \geq 1$). An exception occurs in the field of meta-materials, which can show a negative index ($n \leq -1$) [36, pp. 60], as this is not within the scope of this thesis this case will not be further discussed. Consequently, light in media always propagates slower than light in free space (assuming $n = 1$ in free space).

$$\begin{aligned} \omega &= 2\pi\nu = 2\pi\frac{c}{\lambda} = 2\pi\frac{c_0}{\lambda_0} && (2.6)\\ c &= \frac{c_0}{n} && (2.7)\\ \lambda &= \frac{\lambda_0}{n} && (2.8)\\ n &= \frac{c_0}{c} && (2.9) \end{aligned}$$

The direction of the wave vector **k** is the propagation direction (normal to the wavefronts) of the light and the direction of its energy flux. Its absolute value $\mathrm{k} = |\mathbf{k}|$ is referred to the wavenumber which is the spatial frequency of the light wave (Eq. 2.10). This frequency describes the rate at which the phase of the light is changing with $\boldsymbol{x}$. Because the factor n reduces the wavelength and the phase speed of the light in media, the spatial frequency k is increased compared to the spatial frequency k_0 in free space (Eq. 2.11).

$$
\begin{aligned}
k &= \frac{2\pi}{\lambda} \qquad (2.10)\\
k &= nk_0 \qquad (2.11)
\end{aligned}
$$

The field distribution in a medium changes in case electromagnetic boundary conditions need to be taken into account. A waveguide structure, for example, has physical boundaries and therefore its electromagnetic field distribution is affected. In analogy to an infinitely long and wide bulk medium with refractive index n, an effective index $n_{\mathsf{eff}}(\omega)$ can be introduced accounting for the modified field distribution due to electromagnetic boundary conditions. The spatial frequency of a particular field distribution in a medium (or in a device like a waveguide) is referred to as propagation constant β (Eq. 2.12).

$$
\beta = n_{\mathsf{eff}}k_0 = n_{\mathsf{eff}}\frac{2\pi}{\lambda_0} \qquad (2.12)
$$

When light travels through a homogeneous medium, it is attenuated due to absorption and scattering what leads to extinction. In case another medium with a different refractive index is present, reflections at the media's interfaces has to be taken into account. In a homogeneous medium, the initial irradiance or intensity I_0 of the light is exponentially decaying as a function of the traveled optical path length $|\mathbf{x}|$ of the light (Eq. 2.13). The imaginary part of the complex refractive index $\kappa(\omega)$ can be related to the absorption coefficient α of a medium (Eq. 2.13) [37]. A common unit for the attenuation of light a in optical engineering is dB/cm, which can be expressed as a function of κ (Eq. 2.15).

$$
\begin{aligned}
I(|\mathbf{x}|) &= I_o(|\mathbf{x}_0|)e^{-\alpha|\mathbf{x}|} \qquad (2.13)\\
\alpha &= \frac{4\pi\kappa}{\lambda_0} \qquad (2.14)\\
a\left[\frac{\mathrm{dB}}{\mathrm{cm}}\right] &= \frac{10\cdot log_{10}(e)\cdot 4\pi\kappa}{\lambda_0\,[\mathrm{cm}]} \approx \frac{55\kappa}{\lambda_0\,[\mathrm{cm}]} \qquad (2.15)
\end{aligned}
$$

2.1.2 Guided propagation of light

Guiding light or waves via an optical waveguide can be achieved whenever at least two suitable dielectric materials, of a different refractive index, are present and are forming an interface at which light is internally reflected at the boundaries (Total Internal Reflection). The core material of higher refractive index n_1 is embedded into a surrounding material of lower refractive index $n_2 < n_1$ and acts as a light trap [34, pp. 290]. The light can be guided in the inner core without radiating into the surrounding material (cladding and substrate). For example, an on-chip waveguide can be designed in a strip waveguide configuration (Fig. 2.1 (b)). In this work, the silicon-on-insulator (SOI) strip-waveguide will be used. Furthermore, optical fibers are used as interconnects between a tunable laser source and a chip (Fig. 2.1 (c)).

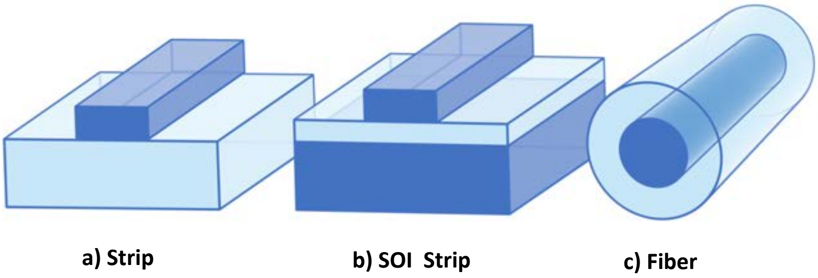

Figure 2.1: This schematic is showing a strip waveguide (**a**), an SOI (Silicon-on-insulator) strip waveguide (**b**) and a fiber (**c**) [34]. A darker shading is related to a higher refractive index.

The field-distribution in SOI-Strip-Waveguides - TE and TM modes

A transverse electromagnetic wave (TEM) is describing a field distribution in which the electrical field vector **E**, the magnetic field vector **H**, and the wave vector **k** are mutually orthogonal.

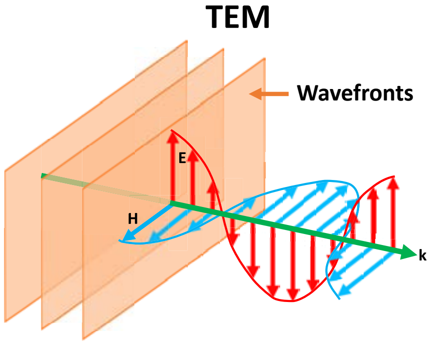

Figure 2.2: This schematic shows the orientation of the field vectors **E**, **H**, and **k** of a plane TEM wave. The field vectors are mutually orthogonal to each other [34, pp. 165]. The wavefronts are surfaces of constant phase.

The wave vector **k** is normal to the wavefronts (surfaces of constant phase) (Fig. 2.2) [34, pp. 165]. A transverse electromagnetic wave can occur in different polarizations [34, pp. 199].When analyzing the electromagnetic field distribution of fields in a waveguide geometry, it is common to distinguish between distributions in which the electric field vector **E** is predominantly parallel to the x-axis (transverse electric (TE)) or predominantly parallel to the y-axis (transverse magnetic (TM)). Where the x and y axes are defined in respect to a device (Fig. 2.3). Therefore, in the case of TM polarization, the **H** field is predominantly parallel to the x-axis. Figure 2.3 shows an example of the orientation of the electromagnetic field vectors for TE and TM polarization in an SOI-Strip waveguide. Also, simulations of the ground modes TE_0 and TM_0 are shown, which were performed with a finite element method (FEM). The software tools, as well as the simulation environment, are described in Section 4.2.1.

In fact, the simulation result for the TM mode shows a non-zero $\mathrm{E_x}$ component (smaller compared to the $\mathrm{E_y}$-component) (Fig. 2.3 (b)). Therefore, the mode is called a quasi-TM mode (and vice versa quasi-TE mode for the TE case). The sum of the integral over the whole field area shows that the total power stored in $\mathrm{E_x}$ is much smaller compared to $\mathrm{E_y}$ and vice versa for TE polarization. Note that pure TE and TM modes are only existing in homogeneously filled metal waveguides. In the following quasi-TE modes and a quasi-TM modes are simply referred to as TE and TM modes.

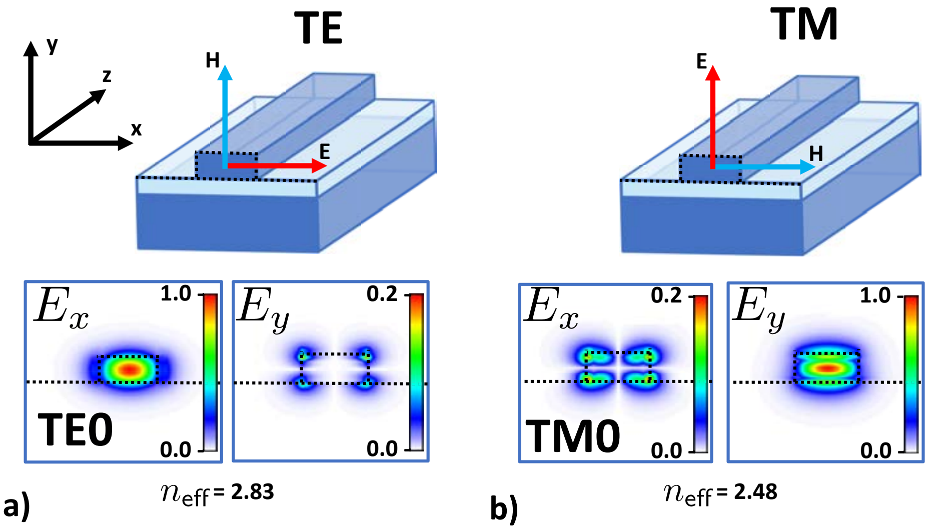

Figure 2.3: This schematic shows the orientation of the field vectors **E** and **H** for TE and TM polarization. The inset (**a**) shows the simulated $\mathrm{E_x}$ field and the $\mathrm{E_y}$ field of TE. The inset (**b**) shows the simulated $\mathrm{E_y}$ field and the $\mathrm{E_x}$ field of TM.

Due to boundary conditions, the field of the wave is mainly confined inside the waveguide core with an exponentially decaying field leaking out of the waveguide. In case of a multi-mode waveguide, there are several possible field distributions for $\mathrm{TE_{mn}}$ and $\mathrm{TM_{mn}}$, which can be excited.

Each field distribution is a function of its surrounding medium, exciting wavelength, and device geometry. The number of zero-field-crossings (in x- and y-direction) of an eigenmode is indicated by indices (or mode-numbers) m and n. Most often, modes in SiP are only described by their mode number m ($\mathrm{TE_m}$ and $\mathrm{TM_m}$) with fixed $\mathrm{n} = 0$. Usually, the high vertical confinement of the light in a thin waveguide does not allow for a mode-number $\mathrm{n} > 0$. Figure 2.4 shows the $\mathrm{TE_0}$ and $\mathrm{TM_0}$ mode of an undercut SOI-Strip waveguide together with its higher order modes $\mathrm{TE_1}$, $\mathrm{TE_2}$, $\mathrm{TM_1}$, and $\mathrm{TM_2}$.

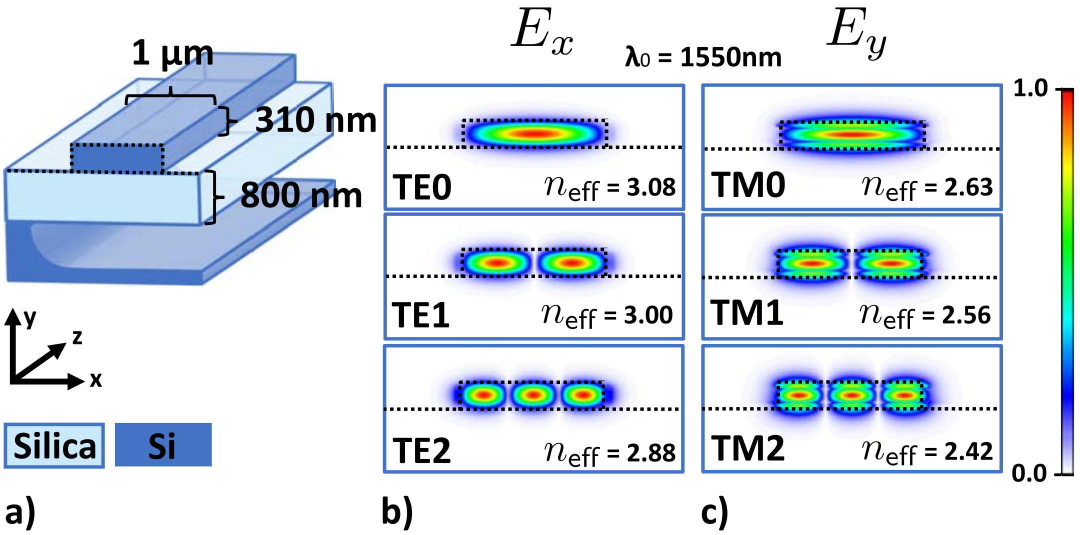

Figure 2.4: The schematic (**a**) shows the geometrical parameters of an undercut multi-mode silicon strip-waveguide on silica. (**b**) shows the higher order TE modes and (**c**) shows the higher order TM modes.

Assuming a waveguide with a silicon core material, the confinement in a waveguide is lower for higher order modes. As a consequence, the field is leaking more into the surrounding material (for example silica or air).

It is convenient to define a complex effective refractive index $N_{\text{eff}} = n_{\text{eff}}(\omega) + i\kappa_{\text{eff}}(\omega)$ where $n_{\text{eff}}(\omega)$ is referred to as *effective index*. The parameter $\kappa_{\text{eff}}(\omega)$ is describing the optical losses of the mode. The surrounding material has a lower refractive index compared to the core material. Therefore, the higher order modes have a lower effective index compared to the ground mode. Also, the guiding of them is weaker. This effect is also wavelength dependent, the higher the wavelength, the higher the leakage of a mode, and the lower its effective index.

As silicon photonics and long-haul telecommunication often are based on single-mode waveguides and fibers [38] (only the propagation of ground modes is possible), it is important to understand under which circumstances higher order modes cannot propagate. Easily spoken, when a waveguide is reduced in its geometrical dimensions (or the exciting wavelength is increased), at some point a mode is not adequately guided anymore.

The wavelength at which no propagation is possible anymore, for a given waveguide geometry, is referred to as *mode-cutoff wavelength* (or frequency). The modes are not fitting into the waveguide anymore. In fact, an imaginary propagation constant is leading to an evanescent field, which is exponentially decaying instead of being propagated in **k**-direction.

Waveguide losses

The imaginary part of the effective index $\kappa_{\mathsf{eff}}(\omega)$ of a waveguide is related to its optical loss. It is describing how much light is lost due to coupling or leakage into the surrounding material (for example, the substrate) and covers the loss of the light in the waveguide. Further, absorption of the light in materials is included. With the help of equation 2.15, it is possible to calculate the optical loss for a given effective index $\kappa_{\mathsf{eff}}(\omega)$ of a waveguide. Figure 2.5 a) shows a scheme of the interconnect-waveguide that is fabricated in this thesis. Figure 2.5 b) shows the TM_0 mode for a waveguide width of 300 nm and 500 nm respectively. For a width of 300 nm, the mode shows lower confinement in the silicon core of the waveguide compared to a width of 500 nm. In the case of lower mode confinement, more light is coupled to the underlying substrate, which is causing an optical substrate leakage loss.

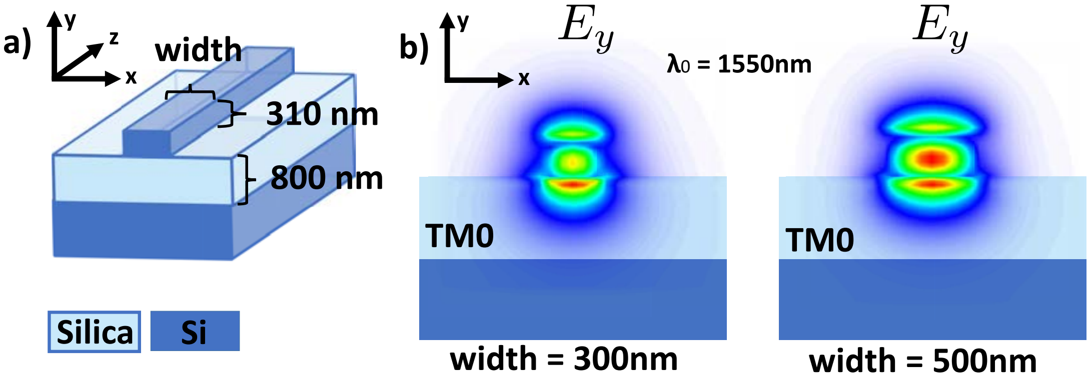

Figure 2.5: Scheme of interconnect-waveguide and simulated field distribution. The schematic (**a**) shows the waveguide structure which is fabricated as interconnect-waveguide in this work. The schematics (**b**) and (**c**) show the simulated E_{y} field of a TM_0 mode for a waveguide width of 300 nm and 500 nm. For a smaller width, the field confinement is lower inside the silicon core of the waveguide.

2.2 Fiber-chip edge coupler

It is possible to distinguish between two leading technologies for coupling light into a waveguide on a chip. In this work, primarily edge couplers will be used for coupling light from an external laser source to on-chip waveguides.

Alternatively, couplers based on grating structures can be used. Both technologies have several advantages and disadvantages when it comes to broadband functionality, TE and TM compatibility, fabrication issues, design and actual on-chip space consumption.

2.2.1 Edge-coupling principle

Edge couplers can be designed as tapered or inversely tapered couplers. Tapering the coupler is essential for matching the emitted light from a fiber with its Gaussian field distribution to the input field distribution of the coupler. For finding matching field distributions, it does not matter if the light is coupled from the fiber to the coupler or vice versa, as this coupling-process is time-reciprocal.

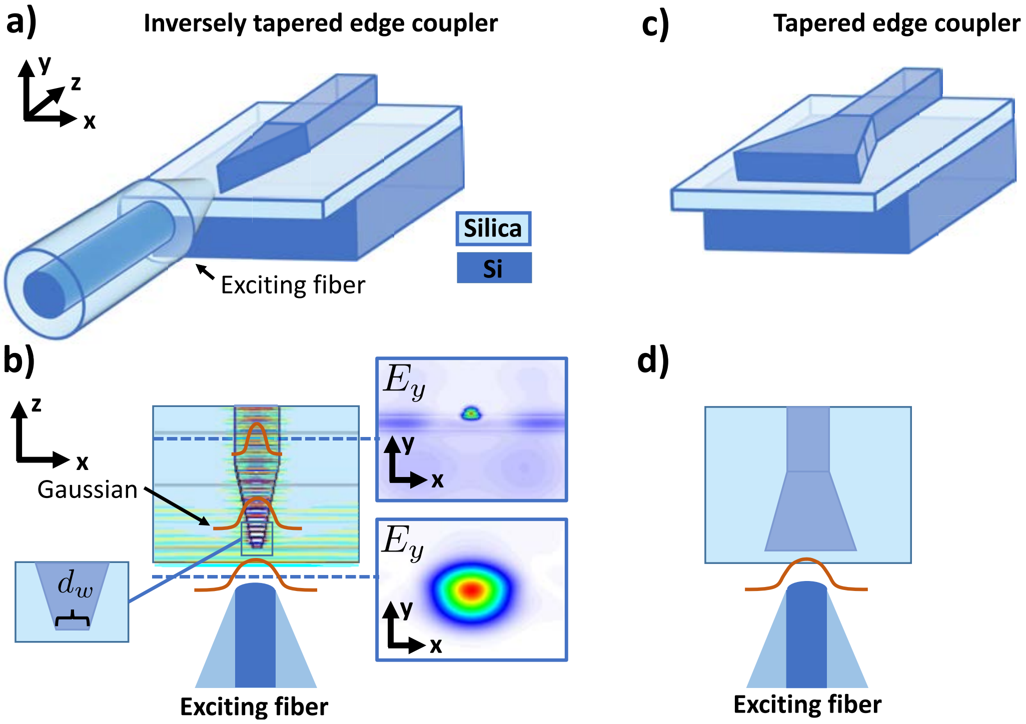

Figure 2.6: Edge coupling mechanism of tapered and inversely tapered edge couplers. (**a**) Schematic of inversely tapered edge coupler and lensed fiber. The inset (**b**) shows the top view of (**a**) and the field distribution before and after coupling the light. The time reversal principle implies that the edge coupler can be used for input and output coupling of the light. (**c**) Tapered edge coupler. Inset (**d**) shows the top view of (**c**).

In fact, when simulating an edge coupler often the field is excited in the waveguide, and the field distribution of the light, which is emitted by the coupler, is analyzed. The length of the tapering area and the width of the tapered coupler define the field distribution at the coupler tip. Figure 2.6 shows a scheme of an inversely tapered and a tapered edge coupler. For coupling light into an edge coupler, a lensed optical fiber can be used.

Throughout this work, inversely tapered edge couplers are used. In simulations, the coupler can be optimized to show a high coupling efficiency by sweeping its tapering width $\mathrm{d_w}$ (Fig. 2.6(b)). For a specific value of $\mathrm{d_w}$, the mode field diameter of the coupler and optical fiber show the highest match and therefore the highest coupling efficiency. With the help of a simulation, the whole coupling mechanism can be simulated in 2D and 3D before fabricating the device.

2.2.2 Comparison of a tapered and an inversely tapered edge coupler

The mode characteristic is different when comparing a tapered and an inversely tapered edge coupler. In the case of an edge coupler, the light is confined in the $y-$ and in $x-$direction (Fig. 2.7). The higher this geometrical confinement is, the more the mode is pressed out of the coupler and is affected by the surrounding medium. The effective mode diameter will change accordingly to the confinement. In case of an inversely tapered edge coupler, the mode confinement in $y-$ and $x-$direction can be tuned to be approximately the same. Therefore, a Gaussian-like emitting characteristic with a high mode quality ($\mathrm{M}^2 \gtrsim 1$) can be achieved. The propagation factor M^2 describes the relation of a real beam compared to an ideal Gaussian beam [39, pp. 424]. The final width of the tapered structure can be designed to match the mode-diameter of a light-collecting optical fiber. This way in principle a high coupling efficiency can be achieved.

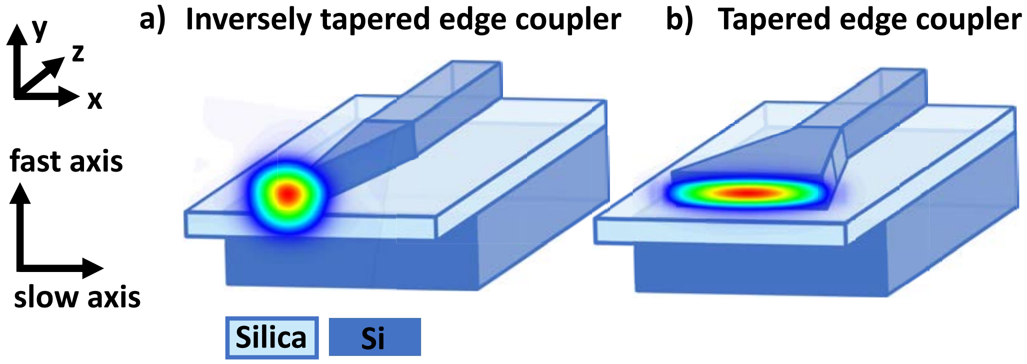

Figure 2.7: Schematic of inversely tapered edge coupler (**a**) and tapered edge coupler (**b**) with intensity field distribution. For a tapered edge coupler, the divergence in $x-$ and $y-$direction is different. One can distinguish between a slow axis ($x-$direction) with low divergence and a fast axis ($y-$direction) with high divergence.

In case of a tapered edge coupler, the confinement of a mode in $x-$and $y-$ direction is different (Fig. 2.7(b)). One can distinguish between a slow axis (in $x-$direction) with low divergence and a fast axis (in $y-$direction) with a high divergence. Coupling such a mode efficiently to an optical fiber mode is harder to achieve as the mode field diameters cannot be matched efficiently in both axes at the same time. In practice, lenses can be used to solve for this issue. Also, back reflection when coupling light into such a coupler is higher compared to an inversely tapered edge coupler as the coupler facet has a larger surface. This effect can be reduced by using an anti-reflection coating [35, 40].

For overcoming these issues, throughout this work, inversely tapered edge couplers are used (Fig. 2.7(a)). Indeed, inversely tapered edge coupler can be hard to align to an external fiber. However, it has been demonstrated that the alignment tolerance in the horizontal direction can be relaxed when using multiple input ports [41]. Alignment tolerance describes how much the position of an optical fiber can be different from an optimal position while still allowing for high coupling efficiencies. In practice, this is expressed as the point where the signal is dropping by 3 dB compared to the optimal signal position.

The fabrication of an inversely tapered edge coupler can be challenging, as the final tapering width can be in the order of 100 nm and below. In this work, this feature size can be fabricated by the use of an electron lithography (EBL) system and an optimized etching process (see Sections 4.2.2 and 6.1).

2.2.3 Advantages and disadvantages of an edge coupler compared to a grating coupler

Another attempt of coupling light into a chip is the use of a grating coupler in which light is coupled under an angle (depending on the design, for example under 10°) [42]. As a grating and an optical fiber have a specific radiation characteristic, they have to be matched to each other as close as possible to achieve efficient coupling. The ideal angle for coupling is a function of the wavelength and grating parameters [40, pp. 293].

The periodicity and the duty cycle of a grating can be adjusted to achieve a sufficient coupling efficiency [43]. By apodizing the grating, even a Gaussian-like radiation characteristic of a grating can be achieved which is further increasing the coupling efficiency [44, 45]. For minimizing the geometrical footprint, a grating can be fabricated as focusing grating [42].

A grating coupler is usually designed to be efficient for TE polarization whereas coupling TM polarized light is harder to achieve. It is reported that in principle it is possible to couple both polarizations to a grating at the same time [46]. However, an inversely tapered edge coupler can intrinsically couple both polarizations with a comparable efficiency [47]. A grating is designed for a specific wavelength so that the 3 dB bandwidth of a grating coupler is approximately 30 nm − 40 nm whereas an edge coupler can be considered to be more or less broadband [42].

Figure 2.8 shows a scanning electron microscope (SEM) image of an edge coupler and a grating coupler in top view fabricated as part of this work. The grating coupler is an apodized fully etched focusing grating coupler.

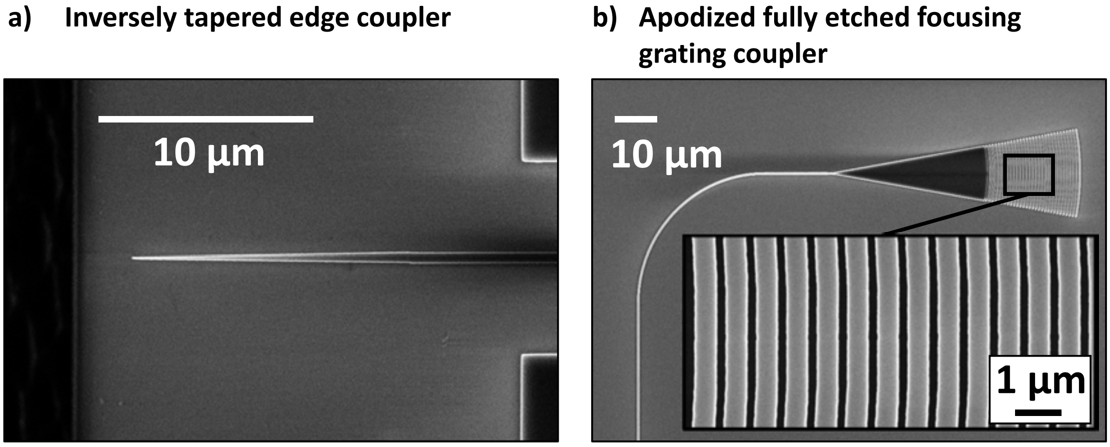

Figure 2.8: SEM image of inversely tapered edge coupler (**a**) and apodized entirely etched focusing grating coupler (**b**) in top view fabricated as part of this work.

For fabricating an efficient silicon grating coupler, shallow etch-processes are used to reduce reflections between adjacent silicon bars, whereas an edge coupler can be fabricated in a single etch process step. The main advantage of a grating coupler is that it can be positioned in proximity to an optical device. Therefore, the need for an extensive routing via interconnect waveguides across a chip is reduced. By using grating couplers, the density of integration of devices on a single chip can be highly increased. Also, as waveguides can be made shorter, the overall optical losses are reduced. Another advantage is the uncomplicated chip handling, as on the contrary, an edge coupler by definition is positioned at a chip edge and can be quickly broken or scratched.

However, in this work, inversely tapered edge couplers are used, as they provide efficient coupling of TE and TM polarized light over a broad wavelength range (here, 1500 nm to 1620 nm).

2.3 Theoretical modeling of a coupled ring resonator

An optical ring resonator can store light for a particular time, depending on its loss coefficient a. The lower the optical loss (for example, caused by scattering, material losses or bending losses) the longer a ring resonator can store the light. This time is called the lifetime τ. In high-quality resonators, this lifetime can reach about 40 ns [1]. The lifetime is proportional to the quality-factor Q of a resonator. The higher the lifetime, the higher the quality-factor, and the smaller the linewidth of an optical resonance.

The light is coupled, for example, with a tapered optical fiber approaching the resonator until the evanescent field of the light in the fiber is overlapping the evanescent field of the resonator. In this work, the coupling step will be done monolithically by fabricating a coupling waveguide in proximity to a resonator (see Section 4.1).

2.3.1 Basic coupling theory of a ring resonator and a waveguide

The normalized complex field amplitudes E_{i1}, E_{i2}, E_{t1} and E_{t2} of a system, in which a ring resonator is coupled to a waveguide, can be described by a matrix equation (Eq. 2.16, Fig. 2.9) [48]. This *2x2*-matrix consists of the coupler parameters t, κ and their complex conjugated values t^* and $-\kappa^*$. These parameters are a function of the distance between the waveguide and the resonator, the wavelength, the material, the mode that is excited, and the ambient temperature.

The passive ring resonator has a time-reversal symmetry. Therefore, the light can be coupled from the waveguide to the ring and vice versa. The related parameter κ is called the cross-coupling coefficient [49]. On the contrary, light can be transmitted through the waveguide (not coupled to the ring) or stays inside the ring (not coupled to the waveguide). The related coefficient t is called the self-coupling coefficient [49]. In other words, as the complex parameter t is describing the part of the light which is transmitted, it is also describing which part is lost due to coupling. For this reason, t can be related to the coupling losses, as no light is disappearing (conservation of energy) (Eq. 2.17). For describing the coupling losses, t can be written as $t = |t|\, e^{i\varphi_t}$ where $|t|$ is the coupling loss, and φ_t is the phase of the coupler.

$$\begin{pmatrix} E_{t1} \\ E_{t2} \end{pmatrix} = e^{i\varphi_t} \begin{pmatrix} |t| & i|\kappa| \\ i|\kappa| & |t| \end{pmatrix} \begin{pmatrix} E_{i1} \\ E_{i2} \end{pmatrix} \tag{2.16}$$

Conservation of energy within system implies:

$$\left|\kappa^2\right| + \left|t^2\right| = 1 \tag{2.17}$$

Figure 2.9 shows a graphical representation of equation 2.16.

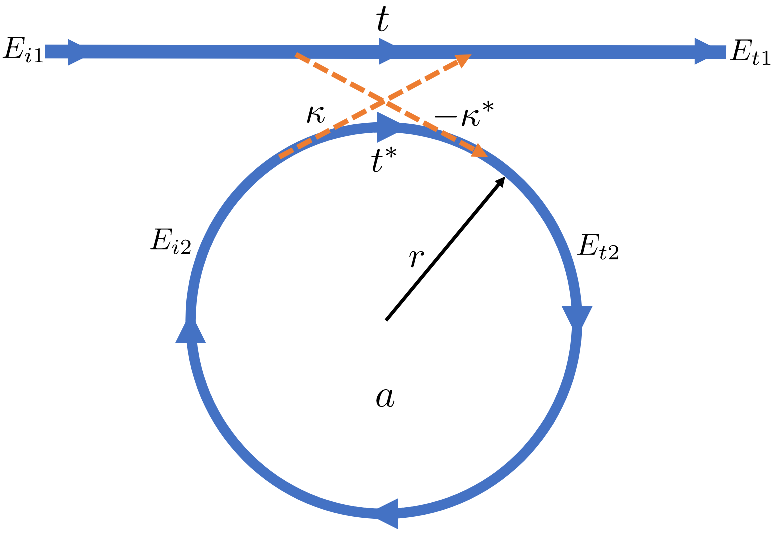

Figure 2.9: A complex electrical field $\mathrm{E_{i1}}$ is partially evanescently coupled from a waveguide to a ring resonator (with radius r) and partially bypassing the resonator. The strength of the coupling from the waveguide to the ring depends on the cross-coupling coefficient $-\kappa^*$. The strength of the bypassing field is dependent on the self-coupling coefficient t where $|\kappa^2| + |\mathrm{t}^2| = 1$. In the same manner, light which is stored inside the resonator ($\mathrm{E_{i2}}$) is partially coupled back to the waveguide (dependent on κ) and is partially staying inside the resonator (dependent on t^*). The output field E_{t1} is the superposition of the directly transmitted field tE_{i1} in the waveguide and the field of the ring which is coupled back to the waveguide κE_{i2} and can be described as $E_{t1} = tE_{i1} + \kappa E_{i2}$. Finally, the field inside the resonator E_{i2} is connected to the transmitted field E_{t2} inside the resonator by $E_{i2} = ae^{i\theta}E_{t2}$ where a is the internal loss coefficient, and θ is the accumulated phase-change of the light when making one round trip. The schematic is adapted from [48].

On average, each photon in the resonator has a lifetime τ. In the wave-picture, each time a wave of light is circulating inside the resonator (performing a round trip) a portion of its energy is lost due to different loss mechanisms. The loss mechanisms will be further discussed in the context of silica resonators in Section 3.3. It is convenient to introduce a combined loss coefficient a (the internal losses) for the ring which is describing the loss accumulated in one round trip. The loss amplitude a can be related to the attenuation coefficient α by the following equation [49]:

$$a^2 = e^{-\alpha L} \tag{2.18}$$

Also, a phase $\theta = \omega \mathrm{L}/c$ is introduced. In a non-active medium, the loss coefficient a follows the relation $0 < a < 1$. The parameters ω and c refer to the angular frequency and the phase velocity of the light in the ring (see Eq. 2.1.1).

$\mathsf{L} = 2\pi r$ is the circumference of the ring resonator and therefore one round trip length. The phase θ can also be expressed by the propagation constant $\beta = k_0 n_{\mathsf{eff}}$ (see Eq. 2.12) by $\theta = \beta\mathsf{L}$. The phase θ describes an accumulated phase change of the light when making one round trip. Assuming $E_{i1} = 1$, the round-trip loss in the ring is given by [48]:

$$E_{i2} = ae^{i\theta}E_{t2} \tag{2.19}$$

The power $P_{t1} = |E_{t1}|^2$ is the power at the waveguide output which can be measured, for example, by a photodetector. Based on reference [48], equations 2.16 and 2.19 lead to:

$$P_{t1} = |E_{t1}|^2 = \frac{a^2 + |t|^2 - 2a\,|t|\cos(\theta + \varphi_t)}{1 + a^2\,|t|^2 - 2a\,|t|\cos(\theta + \varphi_t)}. \tag{2.20}$$

The power stored (circulating) in the ring is given by the Lorentzian shaped function:

$$P_{i2} = |E_{i2}|^2 = \frac{a^2\left(1 - |t|^2\right)}{1 + a^2\,|t|^2 - 2a\,|t|\cos(\theta + \varphi_t)}. \tag{2.21}$$

P_{t1} and P_{t2} are functions of φ_t and θ. As a result, when evaluating the equations 2.20 and 2.21, for periodic values of φ_t and θ, the resonator can be driven into resonance:

$$\theta + \varphi_t = \beta L = 4\pi^2 n_{\mathsf{eff}} \tfrac{r}{\lambda_0} = 2\pi m, \quad m = 1, 2\dots. \tag{2.22}$$

The parameter m is an integer number. Finally, the powers on resonance $\hat{P}_{t1}$ and $\hat{P}_{t2}$ can be described by:

$$\hat{P}_{t1} = \frac{(a - |t|)^2}{(1 - a\,|t|)^2} \tag{2.23}$$

and

$$\hat{P}_{i2} = \frac{a^2\left(1 - |t|^2\right)}{(1 - a\,|t|)^2}. \tag{2.24}$$

In a real measurement, the resonance condition (Eq. 2.22) can be fulfilled, for example, by doing a wavelength sweep (changing λ_0) or changing the temperature (leading to a change of n_{eff}). A local change in temperature, for example, can be triggered by the use of dedicated heating elements [50]. In this work, metal-based modulators are not in use. A temperature change will be done by heating up (or cooling down) the whole chip with the help of a Peltier-element.

2.3.2 Coupling regimes and parameters of a ring resonator

For describing the shape and the extinction of resonances in a waveguide-coupled ring resonator-device (Fig. 2.9) different parameters and concepts have to be taken into account, for example, different coupling configurations (or regimes), dispersion effects and other parameters like the width and the spacing of resonances.

Coupling regimes

Equations 2.20 and 2.21 are describing the power levels at a waveguide output and within a ring-resonator (Fig. 2.9). In the case of resonance (Eq. 2.22), the power values are only dependent on the internal losses a and the coupling losses $|t|$. In general, three cases for the relation between a and $|t|$ can be distinguished [51, pp. 313]:

1. Critical coupling (cc) ($a = |t|$): The coupling losses $|t|$ equal the internal losses a. In this case, the measured power $\hat{P}_{t1}$ at the waveguide output completely vanishes. This can be seen as total destructive interference between the directly transmitted field tE_{i1} in the waveguide and the field of the ring that is coupled back to the waveguide κE_{i2}. Therefore, the output field of the waveguide can be described as a superposition $E_{t1} = tE_{i1} + \kappa E_{i2}$.

2. Undercoupling (uc) ($a < |t|$): The device is on resonance. The light transmitted in the waveguide, and the light coupled back from the ring are showing destructive interference. The amplitude of the light that is coupled back from the ring into the waveguide is not high enough to cancel out the transmitted wave in the waveguide completely. For establishing critical coupling more light needs to be coupled into the ring. For this reason, the light at the output is not entirely vanishing even on resonance.

3. Overcoupling (oc) ($a > |t|$): Like in the case of undercoupling, the device is on resonance, and the wave transmitted in the waveguide, and the light coupled back from the ring are showing destructive interference. As there is too much light coupled into the ring, the light that is coupled back from the ring into the waveguide has a higher amplitude than the light transmitted through the waveguide. For this reason, the light at the output is not entirely vanishing even on resonance.

Figure 2.10 shows an example of a ring-resonance for the three different coupling cases as a function of wavelength. The internal losses α are constant whereas the coupling losses $|t|$ are different. Also, the internal losses a and the coupling losses $|t|$ are functions of the wavelength λ_0. Therefore, critical coupling usually cannot be achieved for every wavelength. In this example, it is assumed that a and $|t|$ are constant in the considered wavelength region.

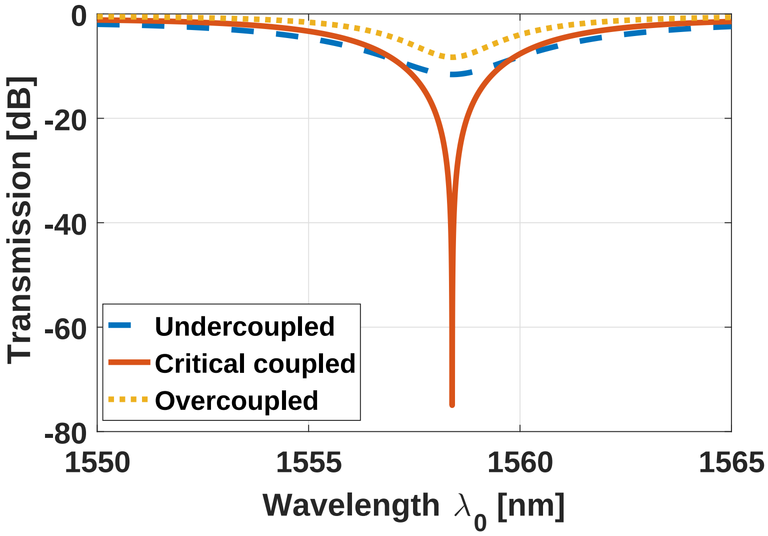

Figure 2.10: Theoretical model of an undercoupled $a < |t|$ (dashed blue), critical $a = |t|$ (solid orange) and overcoupled $a > |t|$ (dotted yellow) resonance of a ring resonator based on equation 2.23.

Phase- and group velocity

For describing the parameters of a ring resonator, it is necessary to investigate what is happening in the underlying material for different wavelengths. The refractive index $n(\omega)$ is a function of the angular frequency ω and for this reason, a function of the wavelength λ_0 (see Eq. 2.1.1). This phenomenon is called material dispersion and is material-specific. Further, a guided mode (for example in a ring resonator) has an effective refractive index $n_{\mathsf{eff}}(\omega)$. The effective index n_{eff} itself can change as a function of λ_0 even if the material is nondispersive. As seen in Section 2.1.2 the effective index is bound to a particular mode. This mode can change its effective index due to geometrical boundary conditions. This type of dispersion is called geometric dispersion. The dispersion relates the change of the angular frequency ω with the wavenumber k (Eq. 2.25). In addition to the phase speed c (or in the following described as v) of light in a medium, a group velocity v_g can be defined. A package of light consists of different wavelengths. The group velocity is describing how fast this package (precisely the envelope) travels. This can be different from the phase speed v of the wave.

In the special case of a nondispersive medium, the dispersion relation is given by $\omega = ck_0$ (with $c = \text{const.}$) which leads to a group velocity of $v_g = c$ which equals the phase velocity v. In addition to the effective index n_{eff}, a group index n_{g} can be defined which is related to the dispersion (Eq. 2.27).

$$v_g(k_0) = \frac{d\omega\,(k_0)}{dk} = \frac{c_0}{n_g\,(k_0)} \tag{2.25}$$

$$v(k_0) = \frac{\omega\,(k_0)}{k} \tag{2.26}$$

Further, the group index n_g can be expressed as a function of n_eff by utilizing equations 2.25 and 2.26 [48]:

$$n_g = n_\mathsf{eff} - \lambda_0 \frac{\partial n_\mathsf{eff}}{\partial \lambda_0} \tag{2.27}$$

In case of a nondispersive bulk medium, the refractive index n is not changing with the wavelength λ_0. In a device in which the material- and the geometric dispersion can be neglected, n_eff approximately equals n_g.

We redefine θ (see Eq. 2.22) (assuming $\varphi_t = \mathit{0}$) the following way:

$$\theta = \beta L = 4\pi^2 n_\mathsf{eff} \tfrac{r}{\lambda_0} = 2\pi m,\ m = 1, 2... \tag{2.28}$$

Free spectral range

An important parameter of a ring resonator is the distance $\Delta\lambda_0$ between two resonance positions. Two neighboring resonances can be identified by their spectral indices (or orders) m and $m - \mathit{1}$. The distance between them is called the free spectral range (FSR) of a resonator. For evaluating an equation for the FSR, it is helpful to investigate the resonance condition from equation 2.22 and calculate the propagation constant β_{m-1} (assuming $\varphi_t = \mathit{0}$), which leads to the following equation for β_{m-1} as a function of β_m:

$$\beta_{m-1} = \frac{2\pi}{L}(m-1) = \beta_m - \frac{2\pi}{L} \tag{2.29}$$

For further simplifying 2.29 this condition, it is evaluated for parameters from a representative resonator of this work. Taking a resonator with r = 125 µm, $\lambda_0 = 1.55\,\mu\mathrm{m}$ and $\mathrm{n}_\mathsf{eff} = 1.4$ the value for m is (assuming $\varphi_t = \mathit{0}$):

$$m = 2\pi \cdot 1.4 \cdot \frac{125\,\mu\mathrm{m}}{1550\,\mathrm{nm}} = 709. \tag{2.30}$$

From 2.30 it can be concluded that the absolute value m is much bigger than the difference in the order of two neighboring resonances. In other words, the absolute spectral order of a resonance m is much higher than one:

$$\Delta m = m - (m-1) = 1 \ll m. \tag{2.31}$$

This result is not surprising, as the wavelength in the material $\lambda_{n_{\text{eff}}=1.4} = 845\,\text{nm}$ fits multiple times into a resonator with a length of L = 785 µm, which leads to a condition for $\Delta\lambda_0$ (taking the definition of β (Eq. 2.28) into account):

$$\mathit{\Delta}\lambda_0 \ll \lambda_{0m}. \tag{2.32}$$

λ_{0m} is the free space wavelength which is fulfilling the resonance condition for m. This result justifies doing a first order Taylor expansion around the m^{th} resonance of equation 2.29, which leads to [52, pp. 199]:

$$\beta_{m-1} \approx \beta_m + \left.\frac{d\beta}{d\lambda_0}\right|_m \Delta\lambda_0. \tag{2.33}$$

This can be further evaluated (using Eq. 2.29), leading to an expression for $\mathit{\Delta}\lambda_0$:

$$\mathit{\Delta}\lambda_0 \approx -\frac{2\pi}{L}\left(\frac{d\beta}{d\lambda_0}\right)^{-1}. \tag{2.34}$$

In the last step the derivative of the propagation constant $\beta = 2\pi/\lambda$ can be calculated (with the help of Eq. 2.27):

$$\frac{d\beta}{d\lambda_0} = -\frac{\beta}{\lambda_0} + k_0\frac{\partial n_{\text{eff}}}{\partial\lambda_0} = -\frac{k_0}{\lambda_0}n_g. \tag{2.35}$$

Finally, the FSR can be defined as a function of n_g, assuming that the FSR is much smaller than the absolute wavelength λ_0:

$$\text{FSR} = \Delta\lambda = \mathit{\Delta}\lambda_0 \approx -\frac{2\pi}{L}\left(-\frac{k_0}{\lambda_0}n_g\right)^{-1} = \frac{\lambda_{\text{res}\,0}^2}{n_g L}. \tag{2.36}$$

Full width at half maximum

In case of a critically coupled ring on resonance, the measurable power at the waveguide output is zero due to destructive interference, whereas there is measurable power in case the ring is not on resonance. The full width at half maximum (FWHM) of a selected resonance is a measure of how narrow this resonance occurs in a wavelength spectrum. It is defined between the two spectral positions of a resonance at which the power dropped by a factor of two (≈ 3 dB) compared to the off-resonance case. The FWHM is related to the inverse lifetime of light inside a resonator. The longer light can propagate inside the resonator (before lost) the narrower the FWHM of a resonance gets.

The power $\hat{P}_{i2}$ in a ring on resonance (at λ_{res}) is twice as high as the power P_{i2} in the ring at $\lambda_{\text{res}} \pm \delta\lambda$. Where $\delta\lambda$ is half of the FWHM leading to the equation:

$$\text{FWHM} = 2\delta\lambda. \tag{2.37}$$

Combining the equations 2.21 (the power in the ring) and 2.24 (the power in the ring on resonance) lead to the following condition:

$$P_{i2}\left(\lambda_{\mathsf{res}} \pm \delta\lambda\right) = \frac{\hat{P}_{i2}}{2}.$$

Which further can be transformed to (assuming $\varphi_t = 0$):

$$1 + a^2 \left|t\right|^2 - 2a\left|t\right| \cos\left(\hat{\theta}\right) = \left(1 - a\left|t\right|\right)^2. \tag{2.38}$$

When assuming a comparatively sharp resonance, the group index n_g is only slightly changing between λ_{res} and $\lambda_{\mathsf{res}} \pm \delta\lambda$. For this reason, the propagation constant β is only slightly changing, and $\hat{\theta}$ can be approximated by [48]:

$$\cos\left(\hat{\theta}\right) \approx 1 - \frac{\hat{\theta}^2}{2}. \tag{2.39}$$

Therefore, $\hat{\theta}$ can be expressed by the following equation (combining equations 2.38 and 2.39):

$$\hat{\theta} = \sqrt{\frac{\left(1 - a\left|t\right|\right)^2}{a\left|t\right|}}. \tag{2.40}$$

As $\hat{\theta}$ is the shift of θ accumulated over $\delta\lambda$, it can be approximated as:

$$\hat{\theta} \approx \left|\frac{d\theta}{d\lambda}\right| \delta\lambda \tag{2.41}$$

Assuming that n_g is constant over $\delta\lambda$ and using equations 2.28, 2.40 and 2.41 $\hat{\theta}$ can be expressed as:

$$\hat{\theta} = \sqrt{\frac{\left(1 - a\left|t\right|\right)^2}{a\left|t\right|}} = \left|\frac{\partial}{\partial\lambda}\left(2\pi n_{\mathsf{g}}\frac{L}{\lambda}\right)\right| \delta\lambda = 2\pi n_{\mathsf{g}}\frac{L}{\lambda_{\mathsf{re}s\,0}^2}\delta\lambda \tag{2.42}$$

therefore:

$$\frac{1 - a\left|t\right|}{\sqrt{a\left|t\right|}} = 2\delta\lambda\frac{\pi n_{\mathsf{g}} L}{\lambda_{\mathsf{re}s\,0}^2}. \tag{2.43}$$

Finally, the FWHM can be defined using equation 2.43 (compare [49]):

$$\mathrm{FWHM} = 2\delta\lambda = \frac{\left(1 - a\left|t\right|\right)\lambda_{\mathsf{res}}^2}{\pi n_g L\sqrt{a\left|t\right|}}. \tag{2.44}$$

Finesse and quality-factors Q_{L}, Q_{u}, and Q_{C}

The finesse F is defined as the ratio of the FSR (Eq. 2.36) and the FWHM (Eq. 2.44) of a resonator:

$$\mathrm{F} \;=\; \frac{\mathrm{FSR}}{\mathrm{FWHM}} = \frac{\Delta\lambda}{2\delta\lambda} = \pi\frac{\sqrt{a\,|t|}}{1-a\,|t|} \tag{2.45}$$

An essential parameter is the quality-factor Q_{L}. The loaded quality-factor is describing the stored energy in a resonator divided by the lost energy within one cycle time. For this reason, it is also a measure of the spectral sharpness of the resonance. The loaded quality-factor is defined as the ratio of the operation vacuum wavelength λ_0 and the FWHM (Eq. 2.46) and takes the coupling to the waveguide into account [49, 53].

$$Q_L \;=\; \frac{\lambda_{\mathsf{res}\,0}}{\mathrm{FWHM}} = \frac{\pi n_g L}{\lambda_{\mathsf{res}\,0}}\cdot\frac{\sqrt{a\,|t|}}{1-a\,|t|} = \frac{n_g L}{\lambda_0}\mathrm{F} \tag{2.46}$$

Furthermore, an unloaded Q_{u} can be defined, which is connected to the uncoupled resonator (neglecting a coupling waveguide). Other intrinsic channels of loss like bending losses, material losses and scattering losses due to sidewall roughness are implicitly covered [53]. Therefore, the unloaded quality-factor is also referred to as the intrinsic quality-factor. In this case, the self-coupling coefficient $|t|$ is set to one [53] as we assume no waveguide ($|\kappa| = 0$) (see Eq. 2.17).

$$Q_u \;=\; \frac{\pi n_g L}{\lambda_{\mathsf{res}\,0}}\cdot\frac{\sqrt{a}}{1-a} \tag{2.47}$$

As the unloaded quality-factor Q_{u} lacks the coupling losses (and excess losses as well), the loaded quality-factor Q_{L} is smaller than the unloaded quality-factor. For convenience, a coupling quality-factor Q_{C} can be defined which is describing how Q_{L} and Q_{u} are related. Therefore, the coupling quality-factor is related to the coupling losses (Eq. 2.48).

$$\frac{1}{Q_{\mathsf{L}}} = \frac{1}{Q_{\mathsf{u}}} + \frac{1}{Q_{\mathsf{C}}} \tag{2.48}$$

It is obvious that without coupling light from a source (a waveguide) to a resonator, there is no light in the resonator. Therefore, the unloaded Q_{u} cannot be measured directly. In case of critical coupling (see Section 2.3.2), Q_{u} equals Q_{c}, and for this reason, the critical coupled $\hat{Q}_{\mathsf{L}}$ can be directly related to Q_{u} by:

$$\hat{Q}_{\mathsf{L}} = \frac{Q_{\mathsf{u}}}{2}.$$

2.3.3 The whispering-gallery mode - Field distribution in the coupled ring resonator

The field distribution within the ring resonator excited by a waveguide or a fiber is referred to as a whispering gallery mode. The term $whispering-gallery-mode$ originates from the field of acoustics.

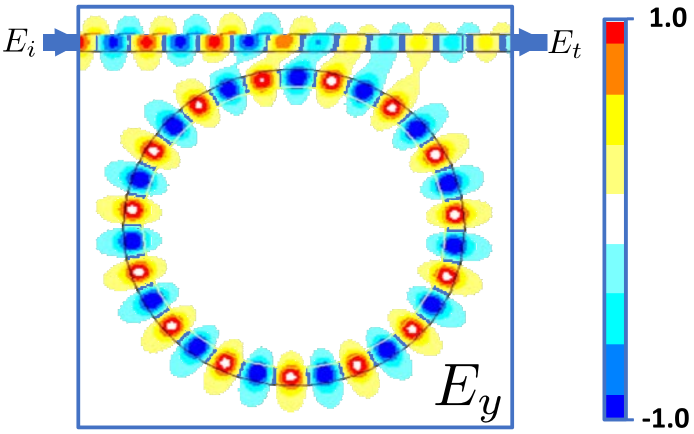

Figure 2.11: The figure shows a simulation of the E_y field of light (E_{i1}) coupled from a waveguide to a ring resonator. The field distribution inside the resonator is referred to as whispering-gallery-mode.

A famous example can be found in the gallery of the St. Paul's Cathedral in London. This gallery itself can act as resonator making it possible to hear somebody whispering on the opposite position within that gallery. Acoustic waves are guided by the gallery, as the walls are stone-faced and smooth, which was first explained by Lord Rayleigh by continuous reflections of the acoustic wave [54]. It has been shown that this acoustic concept can be further transferred to dielectric resonators and therefore to the optical regime. Figure 2.11 shows the field distribution of E_y of a waveguide coupled ring resonator. The wavelength and the geometry are chosen to fulfill the resonance condition (Eq. 2.22).

2.3.4 Fitting the wavelength spectrum of a ring resonator

In a real ring-resonator, the critical coupling condition is not always achieved whether deterministically, due to design issues, or missed fabrication targets. However, it is essential to distinguish between losses arising from the coupling and the intrinsic losses of the ring. This piece of information can be used to redesign a device and optimize the fabrication process to achieve the desired spectral behavior finally.

In this Section, the spectrum of an in-house fabricated silicon ring (Fig. 2.12) is analyzed. In fact, such silicon rings are used as test devices on the chips that are also carrying the inverted silica microtoroids (IVTs). The model, which is used in the following for the extraction of the physical parameters, is used later on for the IVT system, as well (Section 6.3).

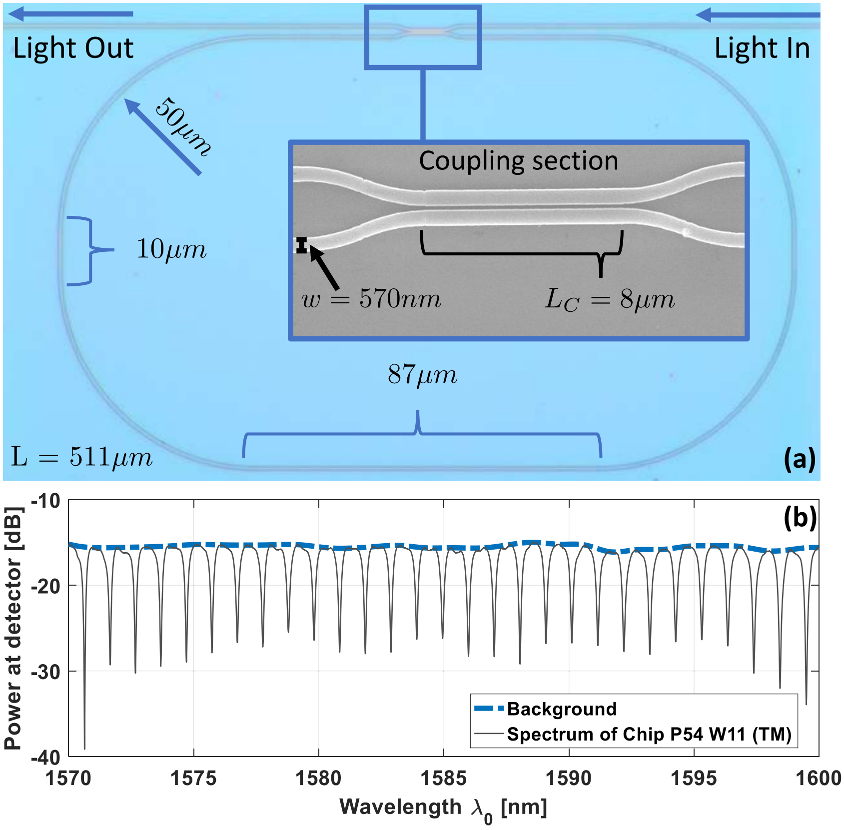

Figure 2.12: (**a**) Microscopic image of an edge-coupled silicon ring resonator. (**b**) Recorded wavelength spectrum (solid line) and extracted background.

Two parameters can be extracted straightforwardly from the spectrum of a resonator, the absolute resonance positions $\lambda_{\mathrm{res}\,m}$ (where m is indexing the resonances) and the FSR. An additional parameter that is known by design is the resonator length L.

Figure 2.12 a) shows a microscope image of the resonator. The resonator has a length of L=511 µm. The inset shows an SEM image of the coupling section. Furthermore, Figure 2.12 b) shows a measured raw data spectrum (solid line) together with the extracted background (dashed line).

The analysis of the spectrum is done by fitting each of the resonance individually with the help of equations 2.20 (assuming $\varphi_t = 0$) and 2.28. The free parameters of the fit are the internal resonator loss a, the coupling loss $|t|$ and the group index n_{g}. The resonance condition 2.28 is linearly dependent on n_{g} and L, that means at least one of these parameters need to be known. Otherwise, n_{g} and L can be mathematically exchanged.

Fitting a single resonance

Figure 2.13 shows the fit (dashed line) of a single background corrected resonance of the spectrum shown in Figure 2.12 b).

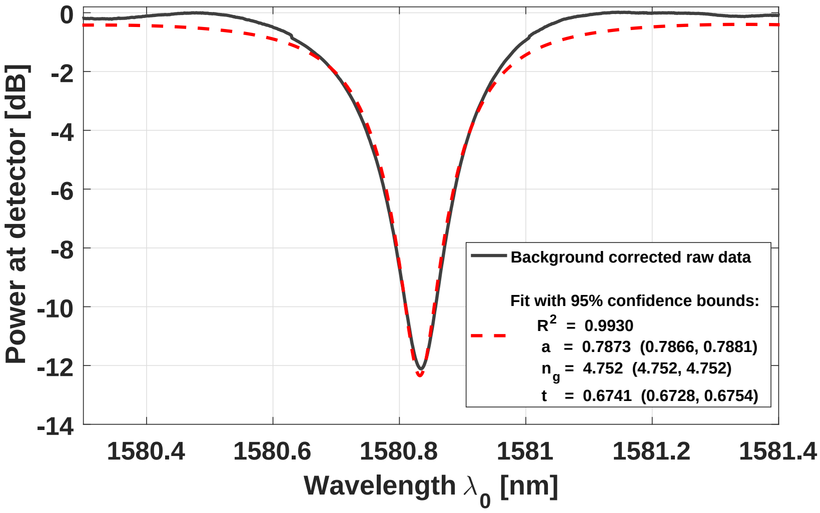

Figure 2.13: Fit of a single resonance of an edge-coupled ring resonator (after background correction) with 95% confidence bounds. The parameters R^2 is the coefficient of determination of the fit. The parameter a is the fitted internal loss of the ring, n_{g} is the fitted group index, and t is the fitted self-coupling coefficient.

The initial start values for the fit were chosen to be $a_{\mathsf{Start}} = 0.76$, $|t_{\mathsf{Start}}| = 0.69$ and $n_{\mathrm{g-Start}} = 4.46$. When multiple resonances are fitted, the initial start values or the extracted values of a previous fit are taken as start values for a new fit. For fitting, the *fminsearch* algorithm provided by the software package Matlab is used.

The chosen resonance ($\lambda_{\mathsf{res}} = 1580.85\,\mathrm{nm}$) is slightly overcoupled ($a > |t|$). The parameters a and $|t|$ are functions of the wavelength. Therefore, in this spectrum, for a wavelength of $\lambda_{\mathsf{res}} = 1570.63\,\mathrm{nm}$ the extinction is about 25 dB and critical coupling is almost achieved ($a_{\lambda=1570.63\,\mathrm{nm}} = 0.732$, $|t_{\lambda=1570.63\,\mathrm{nm}}| = 0.701$).

The resonance position of a specific resonance $\lambda_{\mathsf{res}\,m}$ is defined as the point of highest extinction in a particular fitting window. The distance between two adjacent resonances $\lambda_{\mathsf{res}\,m}$ and $\lambda_{\mathsf{res}\,m\pm1}$ is the FSR (equation 2.36):

$$FSR_{local} = \lambda_{\mathsf{res}\,m} - \lambda_{\mathsf{res}\,m-1}. \tag{2.49}$$

Therefore, it is possible to pairwise calculate a local value for n_{g} by utilizing the equation for the FSR and the fitted values for $\lambda_{\mathsf{res}\,m}$ and the adjacent resonance:

$$n_{g_{local}} = \frac{\lambda^2}{FSR_{local}L}. \tag{2.50}$$

It is assumed that n_g is constant between two neighboring resonances. This way n_g as a function of wavelength λ_0 can be extracted.

Finding an initial average $\overline{\mathrm{FSR}}$

For fitting the resonances of a whole spectrum (Fig. 2.12 b)), an initial start value for the FSR needs to be extracted. By doing a fast Fourier transformation [55, pp. 78] where $\mathrm{Y}(\lambda)$ is the Fourier transformed, an averaged $\overline{\mathrm{FSR}}$ (Fig. 2.14) can be calculated. By using the $\overline{\mathrm{FSR}}$, a window can be defined in which a single resonance lies. This way each resonance can be found and fitted separately. The FSR as a function of λ_0 is based on the absolute resonance positions that were fitted (compare Fig. 2.15(c)).

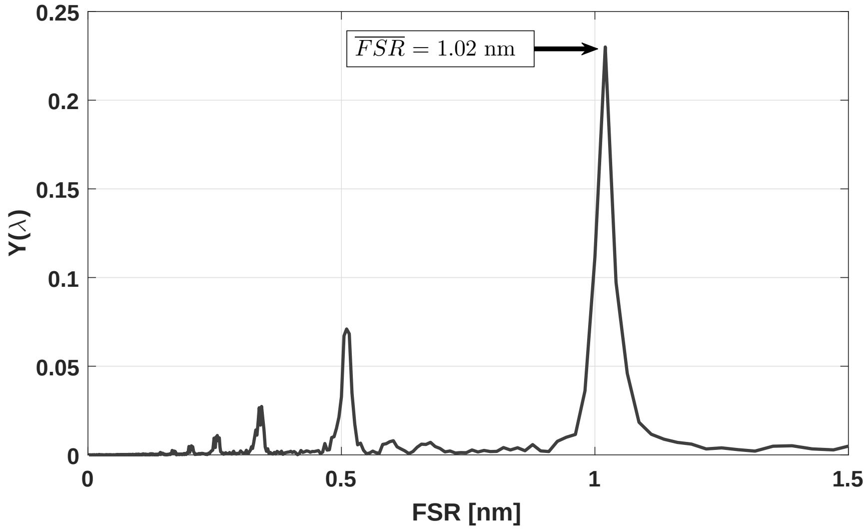

Figure 2.14: Fast Fourier transformation of a wavelength dependent edge-coupled ring resonator spectrum. The point of highest Fourier amplitude $\mathrm{Y}(\lambda)$ is defined as the $\overline{\mathrm{FSR}}$ which is the averaged free spectral range over a whole wavelength spectrum.

Extracting the parameters $a(\lambda_0)$, $|t|\,(\lambda_0)$, $n_\mathrm{g}\,(\lambda_0)$, and $\mathrm{FSR}\,(\lambda_0)$

Figure 2.15 shows the fitted parameters a, $|t|$, n_g and FSR extracted from Figure 2.12 (b).

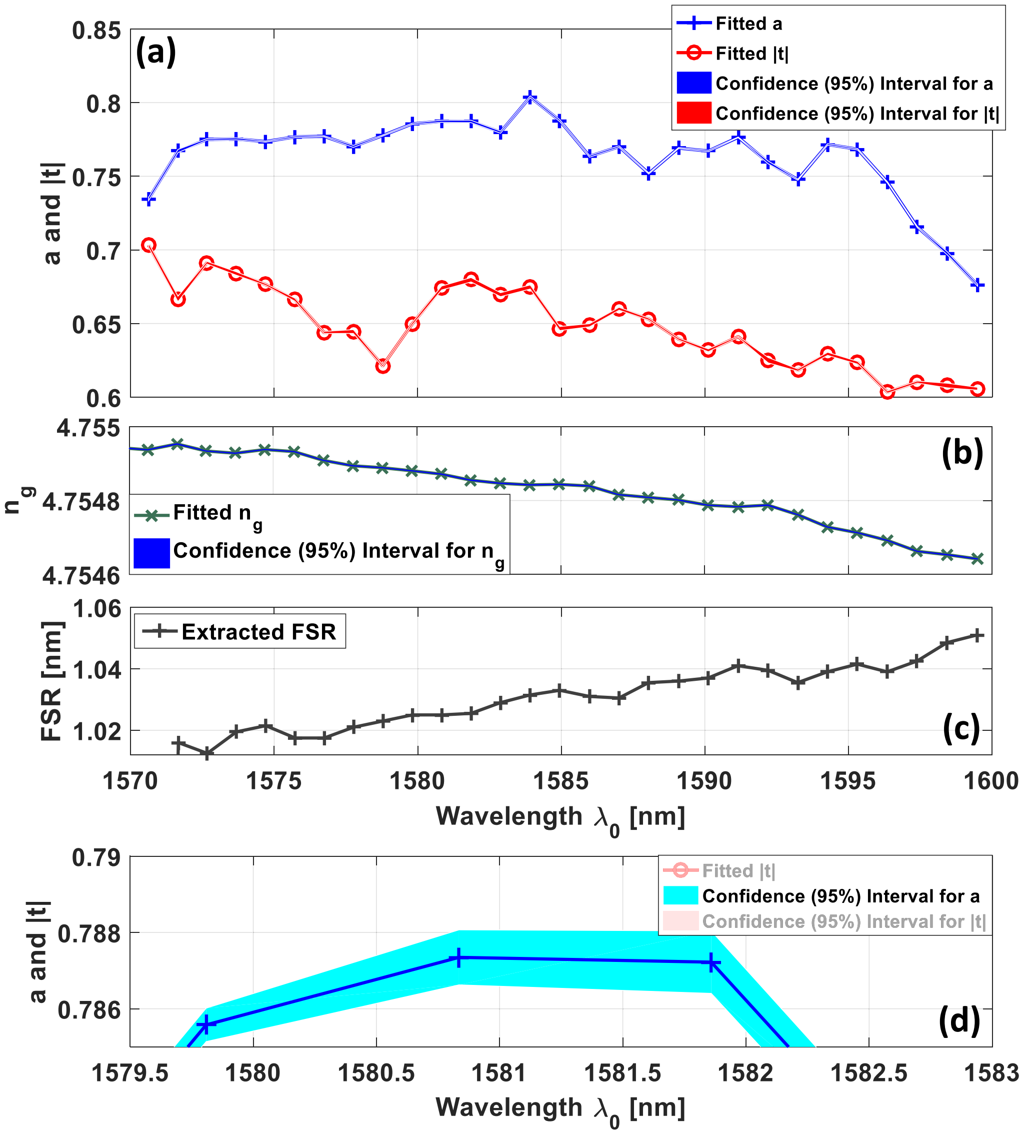

Figure 2.15: Fitted curves of an edge-coupled silicon ring resonator spectrum. (**a**) The parameter a is the fitted internal loss of the ring, and t is the fitted self-coupling coefficient as a function of wavelength λ_0. The confidence intervals are plotted as well, but they are too tight to become visible in the graph. (**b**) The fitted group index n_g as a function of wavelength λ_0 (**c**). The parameter FSR is the derivative of all resonance positions $\lambda_{\mathrm{res}\,m}$ of the analyzed spectrum. (**d**) Zoom of (a) to show the confidence interval for a (compare Fig. 2.13).

As the parameters are fitted for every resonance separately, it is possible to use the resonance positions $\lambda_{\mathsf{res}\,m}$ as grid points for a spline interpolation and generating the functions $a(\lambda_0)$, $|t|\,(\lambda_0)$ and $n_{\mathsf{g}}\,(\lambda_0)$ (Figure 2.15). The extracted $\mathrm{FSR}(\lambda_0)$ is the differential of $\lambda_{\mathsf{res}\,m}$. The confidence in the fitted parameters is high (Figure 2.15(d)). Of course, discrepancies can occur as a background correction is done before processing the raw data (compare Fig. 2.12 (b)). Therefore, the 95 % confidence, relates to the fitted values of the background corrected data.

Based on these results and the help of equations 2.44, 2.46, 2.47 and 2.48 it is possible to calculate the functions $\mathrm{FWHM}\,(\lambda_0)$, $\mathrm{Q}_{\mathsf{L}}\,(\lambda_0)$, $\mathrm{Q}_{\mathsf{U}}\,(\lambda_0)$ and $\mathrm{Q}_{\mathsf{C}}\,(\lambda_0)$ (Fig. 2.16).

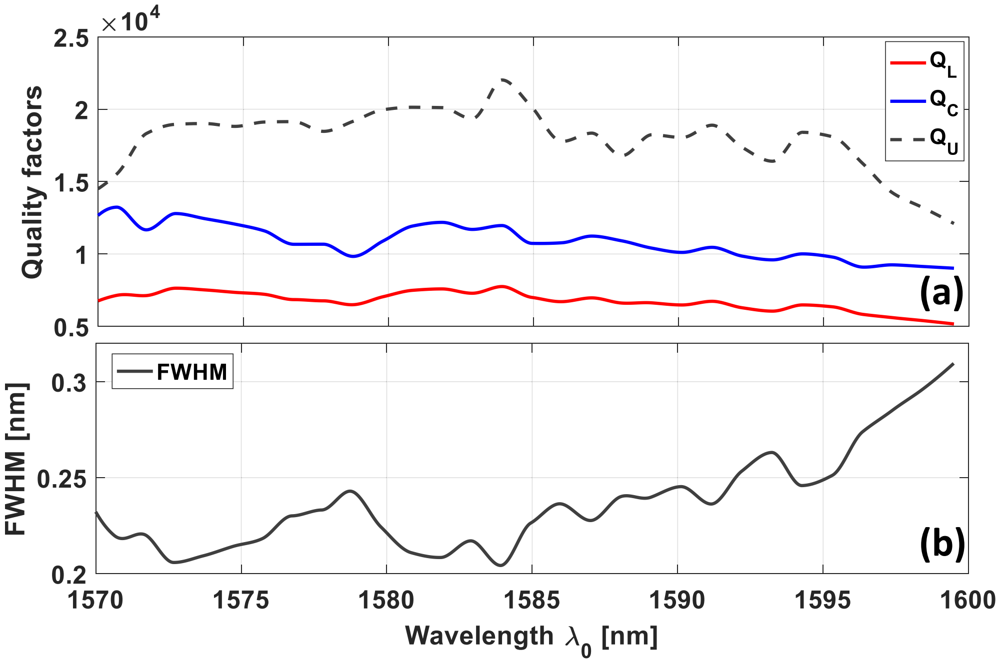

Figure 2.16: Derived quality-factors Q_{L}, Q_{U}, and Q_{C} of an edge-coupled silicon ring resonator spectrum (**a**). Graph (**b**) shows the FWHM as a function of λ_0.

Generated spectrum based on extracted parameters

In the final step, a spectrum will be calculated and is compared to the background corrected raw data spectrum. Figure 2.17 shows the final fitted spectrum together with the background corrected raw data. The residuum is defined as the derivation between the generated, and the original background corrected spectra. The coefficient of determination R^2, in this case, is related to each individual fit of the spectrum.

For evaluating that the fit quality is sufficient to extract the desired parameters, Figure 2.17 shows a residuum plot, defined as the difference between fitted and measured spectrum. The maximal discrepancy is in the order of 1 dB compared to an average resonance extinction of 10 dB.

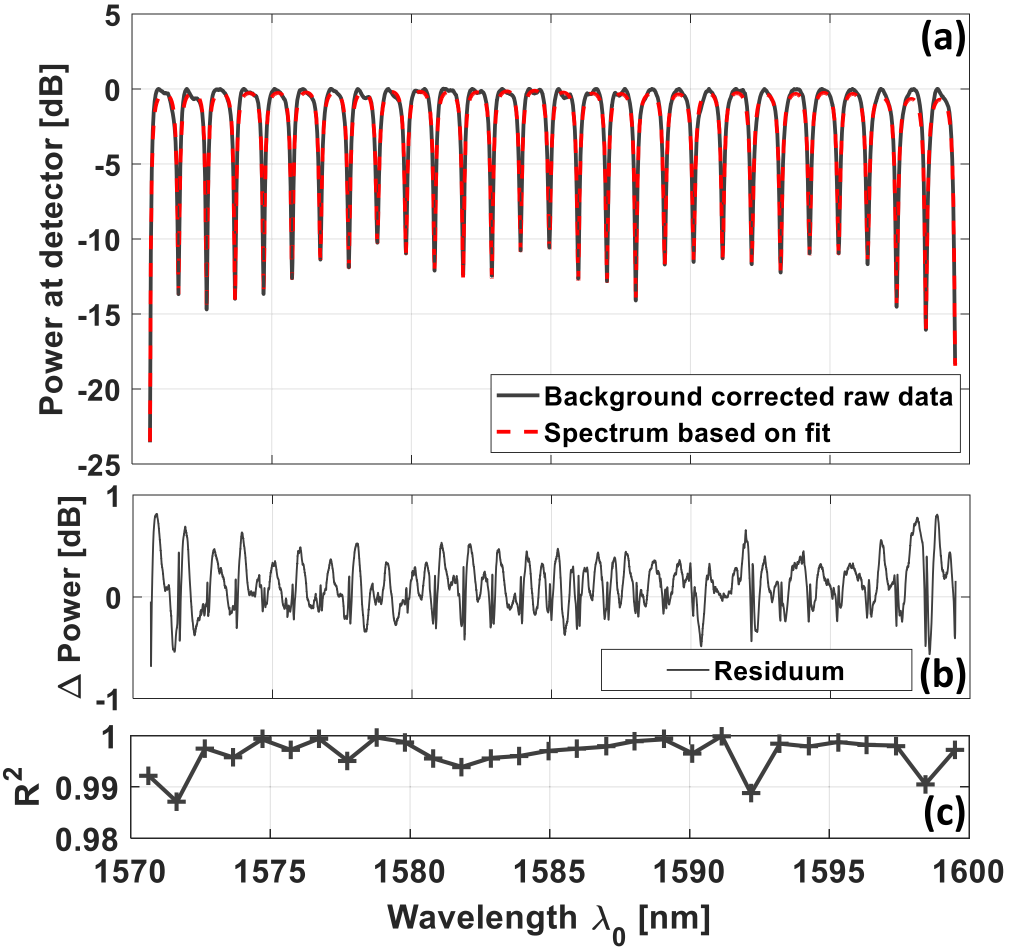

Figure 2.17: The upper graph (a) shows an overlay of the calculated spectrum (based on fits) and the background corrected raw data spectrum. The middle graph (b) shows the residuum of the spectra. The lower graph (c) shows the coefficient of determinations for each underlying resonance fit.

Overview of the fitting algorithm

The proposed method for fitting a spectrum of a resonator can be summarized in the following algorithm:

1. Do a background correction of the raw data spectrum.
2. Find an averaged $\overline{\text{FSR}}$ with the help of Fourier transformation.
3. Find the resonance with the highest overall extinction (globally).
4. Create a fitting window around this resonance based on the averaged $\overline{\text{FSR}}$ and the current resonance position λ_{res}.

5. Recalculate the current n_g and set it as start value based on λ_res.
6. Fit the first resonance with initial values for a, $|t|$ and n_g.
7. For fitting the remaining resonances, repeat steps (a) to (e) until all resonances are fitted.
    (a) Save the fitting result and set values for a, $|t|$ and n_g as start parameters for the next resonance.
    (b) Move to the next resonance and define fitting window based on the $\overline{\mathrm{FSR}}$.
    (c) Find the current exact resonance position λ_res by taking the point of highest extinction (locally) and create a fitting window around it.
    (d) Recalculate the current n_g and set it as start value based on λ_res.
    (e) Do the fit for a, $|t|$ and n_g

For the implementation of this algorithm, the commercially available Matlab software package was used.

2.3.5 Coupler excess losses and coupler-design

The directional coupler excess power losses per pass γ are parasitic losses and are caused by the coupler. This kind of losses can occur due to scattering losses, coupling into unwanted higher order modes, or radiation modes and are limiting the maximal obtainable loaded quality-factor Q_L [27]. In case of low internal optical ring losses, equation 2.46 of the loaded quality-factor Q_L can be rewritten (using Eq. 2.18) and extended [27, 56]:

$$\mathrm{Q}_\mathsf{L} \;=\; \frac{2\pi n_g L}{\lambda_\mathsf{res}} \left(\kappa^2 + \alpha L + \gamma\right)^{-1} \tag{2.51}$$

In the case that the excess losses γ are in the same order compared to the total round trip loss αL of the resonator, the loaded quality-factor Q_L is noticeably worsened. Especially for high-quality resonators, this can become an issue. For minimizing the occurring excess losses, and for avoiding the coupling of light into unwanted higher order modes, the coupler design itself can be optimized. In this work, two different coupler designs are considered, the straight coupler and the weakly tapered gap coupler (Fig. 2.18) [27].

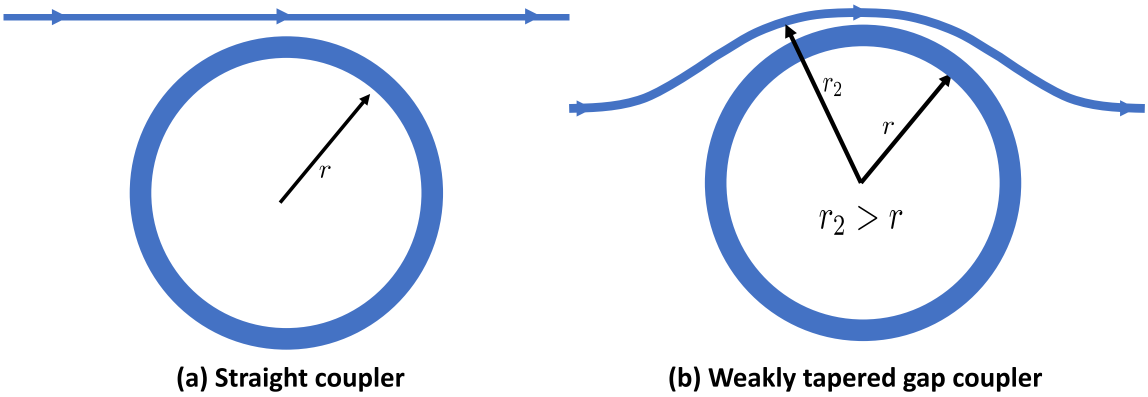

Figure 2.18: In contrast to a straight coupler (**a**) the mode mismatch (difference in the propagation constant β) between the two arms of a weakly tapered gap coupler (**b**) is reduced which leads to a more efficient coupling into the fundamental modes instead of exciting higher order modes. Also, the weakly tapering of the gap yields a more adiabatic transition region from the input waveguide to the coupling section, which potentially lowers the excess losses compared to other coupler designs.

Reference [27] reports that a straight-coupler design has drawbacks. First, a straight coupler shows an excess loss that is associated with the gap between coupler and resonator. Furthermore, the straight coupler shows appreciable coupling to higher order modes, effectively lowering the quality-factor of the resonator due to multiple families of resonances with different free spectral ranges.

The weakly tapered gap coupler is designed to overcome these limitations. The mode mismatch (difference in the propagation constant β) between the two arms of the coupler is reduced which leads to a more efficient coupling into the fundamental modes instead of exciting higher order modes. Also, the weakly tapering of the gap yields a more adiabatic transition region from the input waveguide to the coupling section, which potentially lower the excess losses, compared to other coupler designs.

The intrinsic quality-factor can be expressed, in analogy to equation 2.51, by (assuming $\kappa = 0$) [27, 56]:

$$\mathrm{Q}_U = \frac{2\pi n_g L}{\lambda_{\mathsf{res}}} \left(\alpha L + \gamma\right)^{-1} \tag{2.52}$$

Figure 2.19 shows the altering of the intrinsic quality-factor $\mathrm{Q_U}$, for fixed radii of $\mathrm{r} = 140\,\mu\mathrm{m}$, $200\,\mu\mathrm{m}$ and $400\,\mu\mathrm{m}$, as a function of assumed excess losses γ. Further, it is assumed that the propagation loss α in the resonator is $0.1\,\mathrm{dB/m}$ (which translates into an undisturbed $\mathrm{Q_U}$ of about 60 million), a refractive group index of $\mathrm{n_g} = 1.46$ and a wavelength of $\lambda_{\mathrm{res}} = 1550\,\mathrm{nm}$. The resonator length can be calculated by $\mathrm{L} = 2\pi\mathrm{r}$. In this work, a typical resonator radius is about $140\,\mu\mathrm{m}$.

For example, an excess loss of $\gamma = -30\,\mathrm{dB}$, means that the excess loss is $30\,\mathrm{dB}$ below the transmitted power through the coupling junction. In other words, the excess loss is $0.1\,\%$.

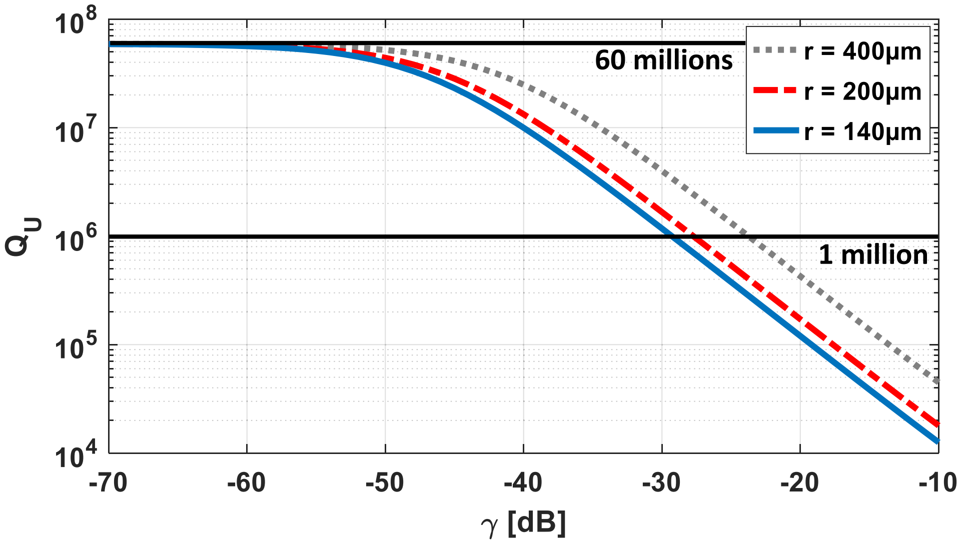

Figure 2.19: Altering of the intrinsic quality-factor Q_U as a function of directional coupler excess losses for fixed resonator radii. The graph shows the theoretically obtainable intrinsic quality-factor as a function of excess losses for fixed resonator's radii of r = 140 µm, 200 µm and 400 µm according to equation 2.52. The propagation loss α is 0.1 dB/m, the refractive group index is $n_g = 1.46$, and the wavelength is $\lambda_{res} = 1550\,\text{nm}$. An excess loss of $\gamma = -30\,\text{dB}$, means that the excess loss is 30 dB below the transmitted power through the coupling junction (excess loss is 0.1 %).

For excess losses smaller than $\gamma = -50\,\text{dB}$ the quality-factor is almost not altered anymore, as the propagation losses are about 10 times higher compared to the excess losses. For a radius of 140 µm, an excess loss of $\gamma = -30\,\text{dB}$ would be sufficient to spoil the quality-factor to ~1 million. For comparison, the graph also shows the trend for longer resonators. Even for a resonator with a radius of 400 µm an excess loss of $\gamma = -30\,\text{dB}$ would be sufficient to spoil the quality-factor to ~4 million. Therefore, a longer resonator helps to decrease the sensitivity to excess losses, but the resonator length is not considered to become a crucial parameter in case the excess losses are high in the first place. Consequently, the excess losses need to be small.

Chapter 3

Prior art and state of the art - The ultra-high-Q resonator

Resonators with high quality-factors have a number of applications in the fields of communication and sensing. Nonlinear wavelength conversion with the help of Four-Wave-Mixing (FWM), for example, can lead to the formation of phase-locked optical combs [19], which can be used as frequency references [57], multi-carrier sources for optical communications [4], or as multi-frequency sources for coherent spectroscopic sensing [58, 59].

Other applications consist, for example, in resonant micro-optic gyroscopes [11], label-free bio-molecular sensing [12,13], narrow linewidth lasers with external resonant feedback [14,15], or tunable delay lines used in signal buffering [16], or optical or Radio-Frequency (RF) phase arrays [17].

For all of these applications, obtaining a high quality-factor is critical, as it reduces the threshold for parametric comb generation, increases the obtainable time delays, increases the sensitivity of refractive index sensing and improves the frequency discrimination that can be obtained from the resonator. As the power-threshold for parametric generation is inversely proportional to the mode volume (scaling as Q^2/V with Q the quality-factor and V the mode volume), smaller resonators are more likely to show a smaller power-threshold. Also, a shorter resonator provides an increased Free Spectral Range (FSR).

This chapter summarize the prior art, as well as current work done by other scientific groups, in the field of high-Q resonators, focusing especially on various potential applications. Therefore, this chapter tries to motivate future work and has the goal of putting the work of this thesis into a bigger scientific context.

3.1 Example applications based on ultra-high-Q resonators and frequency combs

In this Section, various applications of high-Q resonators are presented. Some of the applications rely on frequency comb generation, for example, based on femtosecond laser pulses, but potentially allow for utilizing a comb source based on a high-Q resonator.

3.1.1 Comb generation in high-Q cavities and packaging

Silica microspheres were one of the first devices used as ultra-high-quality resonators with low intrinsic losses [60, 61]. Whispering-gallery-modes (WGM) in spheres can be excited by the use of an external tapered optical fiber and are showing small mode volumes (which leads to high electrical fields) and low losses (long storage time of photons). Previously, this was primarily found in Fabry-Pérot cavities [60].

Emerging from silica spheres an on-chip high-Q resonator has been developed. This so-called microtoroid essentially is a disc of silica that is treated with a reflow process and can be fabricated in an on-chip manner. The melting process is causing an almost atomically smooth surface with a root-mean-square roughness in the order of several nanometers or below and is leading to loaded quality-factors in the order of 100 million [1].

Additionally, it has been shown that silica disks without any reflow process can also be used as high-Q cavities [62–64]

The first Kerr nonlinearity induced optical parametric oscillation in a microtoroidal structure was reported by Kippenberg in *2004* in a resonator's transition from a stimulated Raman to an optical parametric oscillation regime [18]. This work enabled the generation of a frequency comb by the interaction of a continuous mode source laser ($\lambda = 1550\,\mathrm{nm}$) with the modes of a high-Q microresonator via the Kerr nonlinearity. Repetition rates exceeding 100 GHz and a comb uniformity over a 500 nm wavelength span were shown [19].

For using microresonator-based frequency combs as an *optical ruler* in applications like gas sensing, molecular fingerprinting, astronomy and other fields the stabilization of the comb is essential. The two determining parameters are the repetition rate of the comb, which is given by the FSR of the resonator, and the comb mode, which can be directly accessed by the wavelength of a pump laser. The mode spacing can be modified by changing the optical path length, as the effective refractive index of the cavity is power dependent [65]. The optical path length is a function of the resonators diameter, and therefore the desired repetition rate can be targeted by design in the first place.

A significant milestone is the generation of a full octave-spanning frequency comb based on a silica microresonator. It represents a crucial step for $f - 2f$ self-referencing of the optical comb spectra and therefore the precise determination of the absolute frequency of individual comb lines [57]. Recent work targeted this self-referencing issue successfully, and $f - 2f$ self-referencing of a microresonator-based optical frequency comb with a repetition rate of 16.4 GHz was demonstrated [66].

During the last years, several materials have been explored for the fabrication of high-Q cavities. Beside silica, for example, CaF_2 [20,21], MgF_2 [67,68], $LiNbO_3$ [69], AlN [70], Polymer [71,72] ,TEOS [22], Si [23–25] and SiN [26,28,73] have been used.

For coupling light into a high-Q cavity in principle, three different methods are in use. In the case of a silica microtoroid, most commonly tapered fibers have been used, in which a fiber is tapered down to a diameter of several micrometers [1] and is approaching a cavity until the desired coupling strength is achieved. Previously, for spherical cavities prism-coupling techniques have been successfully demonstrated [31].

For real-world commercial applications, of course, a robust packaging is desirable, which is challenging in case of an optical fiber. However, it has been shown that a silica microtoroid together with an optical fiber can be put into a polymer matrix [74]. The monolithic integration of a waveguide (instead of an optical fiber) with a high-Q cavity has multiple advantages. First, the handling itself becomes easier as no movable parts (like the optical fiber for coupling) are necessary. In the case of SiN-cavities, a monolithic integration has been achieved [23]. The challenge when using silicon nitride as the base material is to achieve a smooth cavity surface during etching, as there is no post-melting process involved. The intrinsic quality-factors (in the order of $Q_U = 1 \cdot 10^6$ [2, 28]) of SiN-cavities are currently some orders below the quality-factor of silica- or crystalline fluoride based resonators ($Q_{int} = 1 \cdot 10^7$ to $1 \cdot 10^9$) [2,75,76]. Since the threshold for comb generation (or the initiation for parametric oscillation) is a function of the inverse quality-factor squared [2,28] a higher quality-factor is reducing the initially required optical power level in the exciting waveguide or fiber.

3.1.2 Data transmission in telecommunications

In the field of integrated silicon photonics a high-Q- resonator can provide a frequency-comb source if the resonator is engineered to show, or intrinsically shows anomalous dispersion (as a prerequisite for comb generation) [77, 78]. Such a frequency-comb might be used for telecommunication applications.

In this approach, optical comb lines act as individual carriers. Each line is modulated with the help of additionally integrated modulators. In particular, this might be used in ultrafast chip-to-chip optical data communications. In the field of silicon photonics, the development of coherent optical sources for chip-to-chip communication is challenging as creating lasers in silicon is not trivial due to the indirect band gap of silicon. The hybrid co-integration of already demonstrated III/V based lasers is challenging [3].

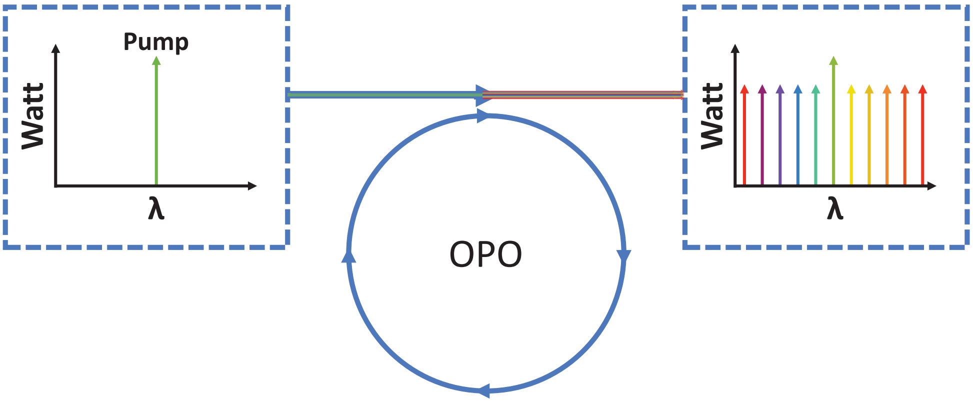

Figure 3.1: A single pump laser with wavelength λ is tuned to the resonance frequency of an optical parametric oscillator (OPO). The light stored in the resonator enables the generation of a narrow linewidth comb-source. The comb-lines are equally spaced. Together they can act as sources for data communication. This can enable the parallel encoding of data streams and therefore increase the communication bandwidth. This figure is adapted from [79].

A typical scheme for enabling high-bandwidth communication (e.g., 40 channels with $10\,\mathrm{Gbit\,s^{-1}}$ each) is wavelength-division-multiplexing (WDM). In this technique, many data channels are transmitted simultaneously on different carrier frequencies but within the same physical channel (e.g., a waveguide or an optical fiber). For providing multiple carriers either multiple lasers or a comb source is required [3]. By reducing the number of optical parts the effort of packaging is reduced.

The monolithic integration also provides a way to use on-chip electronics with integrated feedback channels for the stabilization of the comb source. Figure 3.1 shows a schematic of an optical parametric oscillator (OPO) based on a comb source.

Data communication system

For building an entirely (or partially) integrated chip that is providing data communication functionality several other devices have to be integrated [4] or packaged. Let us assume that a feedback-stabilized comb is used as a source in a hypothetical scenario. This source is based on an OPO that is pumped, for example, by an external III/V laser, and exhibits low phase noise. Furthermore, the pump polarization is already controlled. In this case, several lines (or carriers) of the comb need to be preselected, for example, by the use of a bandpass filter (BPF). Also, it is necessary to clean up the comb spectrum from residual pump light, for example, by the use of a notch filter.

Only one physical channel carries all comb lines. For the modulation of each comb line (individually), two different techniques can be used (Fig. 3.2). The more common technique is splitting the spectrum by the use of a wavelength division demultiplexer (DEMUX) (Fig. 3.2 a)) [4, 50].

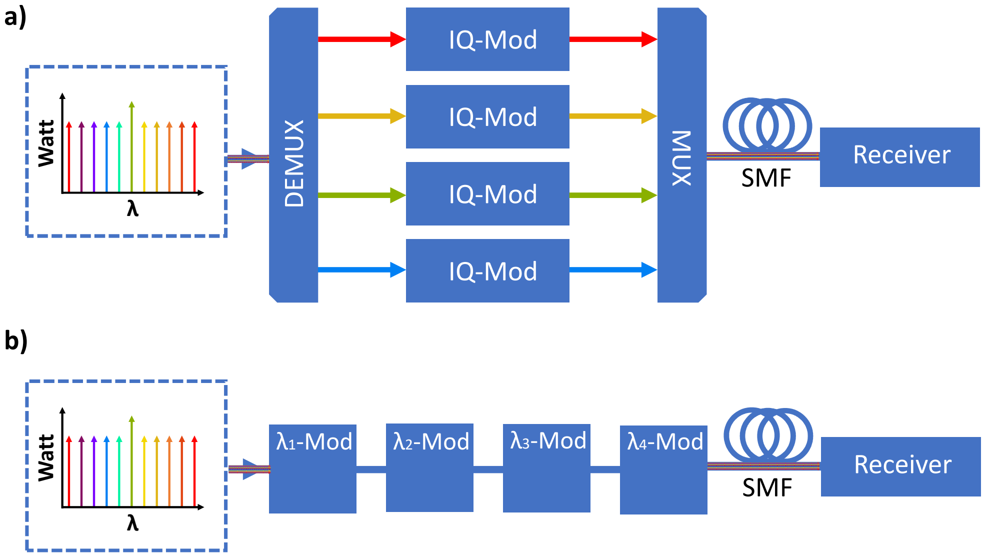

Figure 3.2: Schematics of integrated comb modulation for data communication systems. (**a**) An initial optical comb source is spectrally split by a wavelength division multiplexer (DEMUX). Each comb line is modulated in amplitude and phase (IQ-Modulation). After modulation, all lines are multiplexed again (MUX) and can be transmitted, for example, by a single-mode-fiber to a coherent receiver. (**b**) The full comb is sent through an array of wavelength selective modulators. The different lines of the comb are not spectrally split. Ideally, each selective modulator is modulating one comb line. A wavelength selective modulator, for example, can be a tunable ring resonator modulator (RRM) [80].

For example, an on-chip division multiplexing in silicon can be achieved by using an arrayed waveguide grating (AWG) [81]. The other technique is using a wavelength selective modulation, for example, a tunable resonant ring modulator (RRM) [80]. In this case, the demultiplexing and the multiplexing (MUX) are intrinsically integrated.

Using light for data communication involves the modulation of the amplitude or/and phase of the light. Advanced modulation formats/protocols are using amplitude and phase modulation at the same time. As the phase of light cannot be directly measured, data that is encoded via phase modulation needs a coherent receiver (e.g., using a heterodyne measurement setup). In a heterodyne measurement, a local oscillator interferes with the signal, which enables the extraction of the signal's amplitude and phase information [34, pp. 1112].

The simplest of amplitude-shift-keying (ASK) is on-off-keying (OOK). Essentially, light is turned on and off for representing logical zeros and ones. Each symbol can have two states. All symbols together will create a signal stream. On the transmitter side, a driver is used, which is providing two voltage levels, each representing one logical state. This driver drives the modulator. As this will result in an intensity modulation on the receiver side, no heterodyne measurement is necessary in the case of OOK, and direct detection is possible. Each protocol relates to a particular constellation diagram on the receiver side in which one axis is representing the imaginary and the other axis is representing the real part of a transmitted symbol. The $I-$axis is the in-phase-component, and the $Q-$axis is the quadrature component.

In reference [80], the comb-providing source is a mode-locked laser from which individual comb lines are modulated by individual ring resonators using OOK. Reliable data transmission rates per channel up to $14\,\mathrm{Gbit\,s^{-1}}$ are reported. As RRMs are in use, parasitic phase modulation is present.

Other prominent modulation schemes are quadrature phase-shift keying (QPSK), quadrature amplitude modulation (QAM) and pulse-amplitude modulation (PAM). QPSK and QAM-4 will result in the same constellation diagram but differ in the way the symbols are generated (or the light is modulated). QPSK is based on phase modulation, and QAM-4 is based on phase- and amplitude modulation (IQ-Modulation). QPSK and QAM can be implemented, for example, by the use of linear phase shifters [50]. This kind of phase shifters can be based on the plasma dispersion effect [50, 82, 83] or based on the thermo-optic effect [84]. Technically, for QPSK only one linear phase shifter is necessary, while for the generation of a QAM-4 signal usually interferometers (MZI based IQ modulator) are used.

It also has been shown [85, 86] that RRMs can act as IQ-Modulators. Also, different alternative technologies have been carried out for fabricating high-speed and low voltage electro-optic silicon photonics modulators [82]. This includes organic polymer modulators [87, 88] and strained silicon modulators based on the Pockels-effect [89, 90] among others.

In a push-pull configuration, two Mach-Zehnder-modulators (MZM) are required with one phase shifter in each arm of each MZM to implement QAM-4. Both arms of each MZM have a fixed phase offset of $\pi/2$, this way one arm is preforming the I- and one arm is performing the Q-Modulation. In a push-pull configuration, the two different arms of an MZM are configured to apply an opposing phase shift to an optical signal. Therefore, a signal's average phase is not changing at the output of an MZM. The voltages (modulating each arm) which are necessary to create destructive or constructive interference (between the two arms) are reduced by a factor of two, making a push-pull configuration more efficient regarding power consumption and compatibility to drivers. Also, the additional chirp of the signal is suppressed, as the signal's phase is constant over the applied voltage.

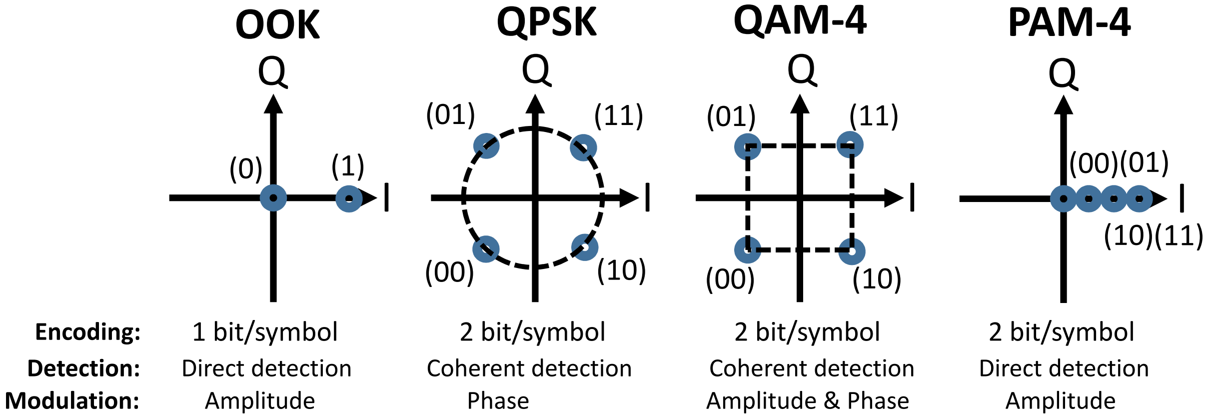

Figure 3.3: Example of IQ-constellation diagrams for different digital modulation protocols. The $I-$axis is the in-phase-component, and the $Q-$axis is the quadrature component. On-off-keying (OOK) is using amplitude modulation and can be directly detected. Quadrature phase-shift keying (QPSK) is based on phase modulation and needs coherent detection. Each symbol on its constellation diagram is located on a circle. The angle of each symbol (in polar coordinates) on this circle is connected to the phase of the symbol. Quadrature amplitude modulation (QAM-4) is based on phase- and amplitude modulation at the same time. Each symbol in its constellation diagram is located in one corner of a rectangle. The position is connected to the phase and amplitude of the symbol. 4-level Pulse-amplitude modulation (PAM-4) is mostly like OOK but uses four amplitude levels to provide a higher data rate.

It is shown that a SiN-OPO comb source system is capable of transmitting data via QPSK and QAM-16. The lowest bit error rate (BER) for QPSK is below $1 \cdot 10^{-9}$ and $7.5 \cdot 10^{-4}$ for QAM-16 providing symbol rates of 14 GBd and 18 GBd respectively. In case of QAM-16, a maximum data rate of 1.44 Tbit s^{-1} is achieved [4].

The described system has one drawback that needs to be addressed in the future. For generating an OPO comb with a SiN ring (with a Q-factor in the order of $1 \cdot 10^6$) a 2.5 W pump laser is used which is too high for a practical telecommunication application. Since the power threshold for comb generation is inversely proportional to the square of the quality-factor, increasing the quality-factor by a factor of 10 (e.g., by further optimizing the fabrication process) will reduce the necessary pump power by a factor of 100. This way the pump source could be replaced by a 20 mW laser diode. It has been demonstrated in reference [19] that silica microtoroids can show comb generation with pump powers as low as 50 µW.

Pumped high-Q-Cavities

By using erbium doping, an OPO can additionally act as a light source. A high-Q cavity is pumped, like a conventional laser system, and is providing a coherent comb source intrinsically. The pumping wavelength is not necessarily a resonance frequency of the OPO. In the example of a silica-based microtoroid, it has been shown that erbium atoms do not diffuse during a laser reflow process. Lasing in silica-based microtoroids at 1552 nm has been shown when being optically pumped at 1440 nm for both groups of pre- and post-implanted microtoroids (before or after reflow) [91].

In [72] a sol-gel process based microtoroid is used to create a Raman microlaser. The threshold for lasing is 660 nW, which is even lower than previously presented work of this group with a threshold in the order of 100 µW and a slope efficiency of 10% [92]. For comparison, a pure silicon Raman laser presented in [93] has a lasing threshold of 9 W with a slope efficiency of 8.5%.

3.1.3 Spectroscopic and sensing applications

For some sensing and spectroscopic applications, high-Q cavities can be used. A high-Q optical cavity shows an exceptionally narrow spectral linewidth, reaching values as low as 0.01 pm on resonance, assuming an intrinsic quality-factor of 100 million. This narrow linewidth is determined by the long average lifetime of photons in a low loss cavity. Slightly changing the absorption of the cavity or the refractive index of the surrounding media will cause a change of the intrinsic quality-factor Q_U and a shift of its resonance wavelength λ_{res}. Furthermore, an OPO comb might be used as a device that provides mesh points for analyzing the absorption of chemical samples at different comb line wavelengths.

Microresonator based detection

Reference [6] reports on heavy water (D_2O) detection at a wavelength of 1320 nm by the use of a silica microtoroid. For different concentrations of heavy water in water (H_2O) the intrinsic quality-factor of the microtoroid is studied.

The microtoroid is put into a solution during a measurement. As the optical absorption of water is higher than the optical absorption of heavy water, the measured intrinsic quality-factor is lower for lower concentrations of D_2O. This way it is possible to detect concentrations of heavy water as low as 0.0001 % (1 part in 10^6 per volume or 1 ppmv).

This concept of either analyzing the decrease or increase of the intrinsic quality-factor of a silica cavity or analyzing the wavelength shift of a cavity resonance is used, for example, in DNA quantification [7], single protein detection [8], single virus detection [9] or integrated bio-sensing platforms [10].

The influence of nanoparticles in the reach of high-Q cavities can cause a considerable mode splitting. A small nanoparticle acts as an imperfection that scatters light from one of the cavity modes (either clockwise or counter-clockwise) into free space and also partially into the opposite mode direction. This mode splitting is dependent on the geometric size of the nanoparticle. The intrinsic quality-factor decreases when the light is scattered out of the cavity by the nanoparticle due to Rayleigh scattering [94]. Considering these two effects, the authors of reference [95] determine the size of different dielectric nanoparticles with diameters between 50 nm to 170 nm (Fig. 3.4). The nanoparticles are sprayed onto the microresonator using a differential mobility analyzer and a nozzle. Other sensing applications, for example, are force sensing [96] and temperature sensing [29].

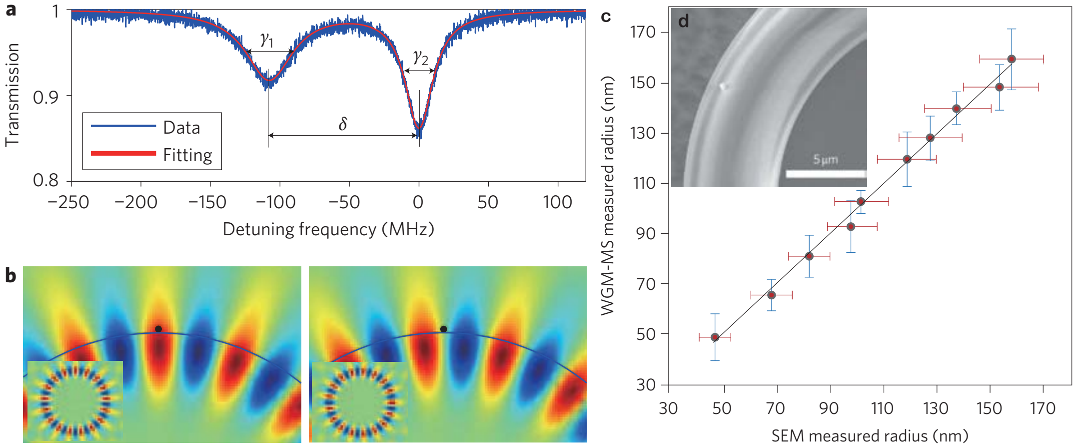

Figure 3.4: Mode splitting of a high-Q silica cavity resonance induced by a nanoparticle. (**a**) Experimentally obtained transmission spectrum (blue) after the deposition of a single nanoparticle and the curve fitting (red). A single nanoparticle is detectable if $\delta > (\gamma_1 + \gamma_2)/2$ is satisfied. (**b**) Field distributions of symmetric modes (left) and asymmetric modes (right) relative to the position of the nanoparticle using a finite-element-method simulation. The insets show the mode along the periphery of the resonator. (**c**) Estimated sizes of particles as a function of their actual sizes are shown for potassium chloride (KCl) particles. (**d**) SEM image of a nanoparticle of radius R = 150 nm deposited on the resonator surface. All figures and descriptions were taken from [95].

Comb based spectroscopy

In the past, numerous applications in the field of spectroscopy and detection rely on optical combs, based on femtosecond lasers or quantum-cascade lasers (QCL) [97].

In the field of spectroscopy, the analysis of known or unknown material compositions is of high interest. Each material, gas or liquid consists of molecules that have unique spectral absorption features. In the far-infrared this is called the fingerprint region and an FTIR-spectrometer (Fourier-transform infrared spectroscopy) equipped with a broadband light source can be used to measure an absorption spectrum. However, dual-comb spectroscopy has shown to have several advantages compared to the use of an FTIR. The frequency accuracy that can be achieved with dual-comb spectroscopy is several orders higher (2-8 orders) compared to an FTIR [58, 59, 98].

The second significant advantage is the compact design of the device, as the resolution is determined by the comb repetition rate instead of the scan distance in the case of an FTIR. Furthermore, no moving parts are involved in dual-comb spectroscopy, which further increases the stability of the setup. On the other hand, dual-comb spectroscopy also suffers from disadvantages. The range of operation of comb-based spectroscopy is much more limited compared to an FTIR (an FTIR covers the terahertz range down to the ultraviolet). Also, the realization of high-frequency accuracy and high-resolution requires stabilized, phase-coherent frequency combs.

One approach of sampling gasses with dual-comb spectroscopy is presented in [58], where two combs, with slightly different repetition rates, are interfered with each other. Figure 3.5 shows a simplified setup of a dual-comb spectrometer.

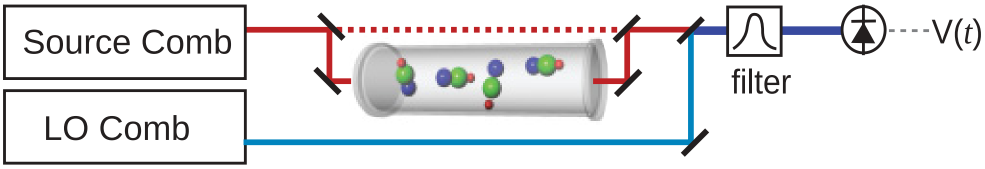

Figure 3.5: The pulse train from a source comb passes through the sample (and is possibly split as well to pass around the sample to yield a time-multiplexed normalization signal). It is then combined with a local oscillator (LO) pulse train. The heterodyne signal between the source and LO is detected and digitized to yield the gas sample's response. In this configuration where the LO bypasses the sample, both the phase and magnitude of the sample response are measured. The Figure and description are taken from [58].

The source comb is providing a pulse passing through a sample (for example a cell filled with gas). This pulse is subsequently combined with a local oscillator comb (LO comb). In contrast to traditional FTIR measurements (which are only providing the intensity absorption spectrum) in dual-comb spectroscopy, both magnitude and phase can be measured. For measuring both simultaneously, the combs should be combined after one of them has passed through the sample (similar as in nondispersive Fourier transform spectroscopy (DFTS)) [58].

A challenging task when doing dual-comb spectroscopy or adaptive real-time dual-comb spectroscopy [99] is the stabilization of combs. A frequency comb is not accurate by itself. A frequency comb needs to be locked or monitored against a pair of absolute references. There are different ways of achieving a frequency accuracy. If an absorption band of a spectrum is known regarding its absolute frequency, it can be used as an absolute reference. However, this method usually provides an accuracy below what can be achieved with stabilized combs. Alternatively, as done in [58] a tooth of a comb can be locked to an underlying continuous-wave-reference laser of known frequency.

It has also been reported that a single comb, provided by a femtosecond laser, can be used to measure the absorption spectrum of iodine vapor in the visible and the near infrared range [100]. A high-resolution virtually imaged phased array (VIPA) disperser is used together with a diffraction grating to spatially resolve a stabilized frequency comb, making it possible to resolve each selected comb line on a 2-D power detector (e.g., a CCD-camera). Each mode/line will be represented by a dot in a 2-D array spaced by the VIPA free spectral range (in one direction) and by the initial combs mode spacing (in the other direction). Therefore, it is possible to extract the intensity spectrum of a sample inserted into the beam path before the VIPA.

3.1.4 High-Q-Resonators as a gyroscope

The Sagnac-effect causes a phase difference between two counter-propagating modes in a resonator with respect to a rotation axis. By rotating a passive resonant micro-optical gyroscope (RMOG), based on an ultra-high Q resonator, an excited clockwise (CW) and counterclockwise (CCW) mode are experiencing an opposite Sagnac frequency shift [11,101]. This shift can be related to the rotation speed of the resonator. References [101, 102] and [103] are using either a tapered fiber or prisms for the excitement and out-coupling of the CW and CCW modes.

A chip-based gyroscope is more immune against shock and vibrations leading to higher stability for applications. In reference [101], a ring resonator is bidirectionally pumped by an external cavity diode laser. An initial first counterclockwise propagating Stokes wave is generated. With the help of Brillouin-scattering and further pumping, in which an optical pump wave is interacting with microwave-rate phonons, a second Brillouin-Stokes wave is excited and further pumped by the first Stokes wave. The second wave is propagating in the opposite direction shifted to a lower frequency (Fig. 3.6 a)) relative to the first wave. This process can even trigger higher and higher order Stokes waves (each propagating in the opposite direction compared to its previously generated pump wave).

The FSR of the resonator is precisely designed to match an integer-fraction of the Brillouin shift so that the excited CW and CCW modes can propagate within the cavity. For the detection of the Sagnac induced frequency shift, the CW and CCW modes are combined on a fast photodetector to generate a microwave beat tone. The beat note is electrically processed and contains the rotation information.

This way a minimum detectable rotation rate of 22 °/h is measurable (Fig. 3.6 b)). The whole setup was mounted in a box (Fig. 3.6 c)).

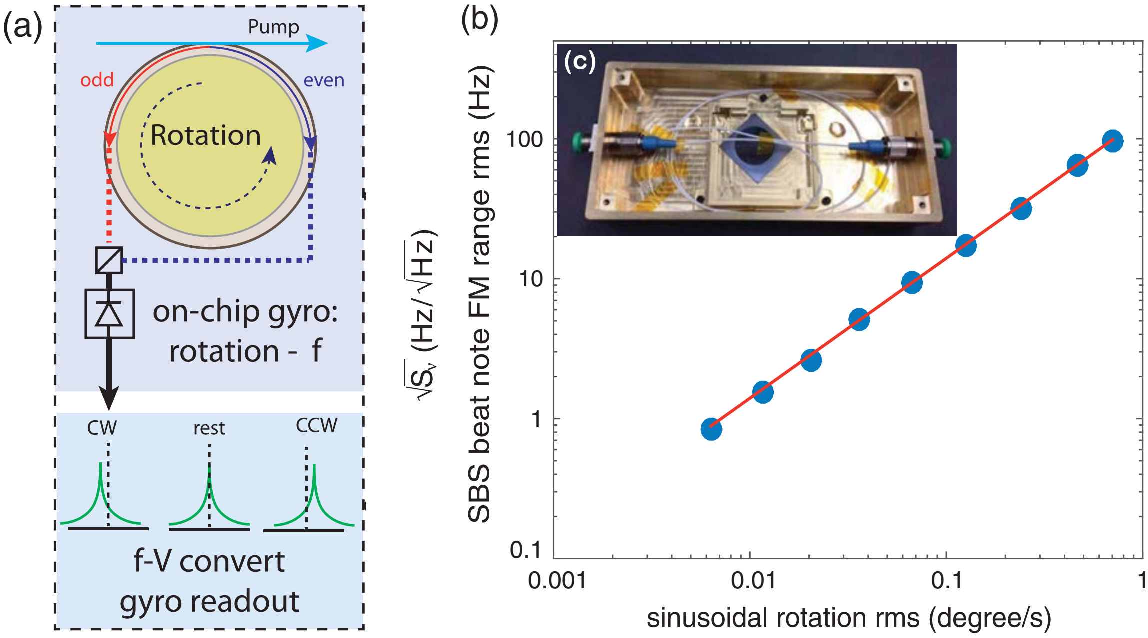

Figure 3.6: (**a**) Simplified schematic illustrating the principle of Brillouin laser gyroscope operation. Optical pumping (clockwise) induces Brillouin laser action, which results in cascaded odd (counter-clockwise, CCW) and even (clockwise, CW) order Stokes lasers. These lasing modes experience opposing Sagnac frequency shifts. Detection of the beat frequency of these co-lasing signals followed by a frequency-to-voltage readout (f-V) provides rotation sensing. Laser action on odd Stokes (red) and even Stokes (blue) lines are shown. CW, resting, and CCW rotation induces beat frequency shifts as indicated. (**b**) The plot of root-mean-square (RMS) Sagnac frequency shift versus RMS angular rotation rate measured. (**c**) A gyro resonator was packaged into a fiber connectorized box for rotation measurement. The lid of the box is removed, and the 18 mm diameter resonator is visible as the gray silicon chip. The figures and descriptions are taken from [101].

3.2 The conventional silica microtoroid

Lately, high quality-factors, on the order of 10^9, have been obtained with discrete resonators formed by macroscopically polishing crystalline materials such as CaF_2 or MgF_2 [104]. However, the highest quality-factors for smaller, chip-scale devices, in excess of 100 million, have been obtained with microtoroids obtained by melting and reflowing a SiO_2 membrane with a CO_2 laser [1]. Since these microtoroids are formed by the minimization of surface tension energy of the molten SiO_2, they feature very little roughness minimizing scattering induced optical losses. A silica microtoroid belongs to the class of whispering-gallery resonators (compare Section 2.3.3) with an exceptional long storage time of light (which is related to an exceptional high-quality-factor, for example, in excess of 100 million). A silica microtoroid consists of a microtoroidal resonator structure made from silica on top of a silicon pillar.

The critical requirement for a long photon lifetime is to reduce optical losses of the resonator as much as possible by primarily reducing its sidewall roughness. Of course, there are also other sources of losses like intrinsic material absorption, scattering due to material induced imperfections, tunneling losses and coupling losses [57, pp. 12]. In this Section, the fabrication of a conventional microtoroid is explained. The second part of this Section deals with the intrinsic and external optical loss channels of a microtoroid.

3.2.1 Initial fabrication steps

When fabricating a conventional silica microtoroid, the base material is silicon (Si) with a silicon dioxide (SiO_2) layer on top. Figure 3.7 shows the three essential fabrication steps of a silica microtoroid. In a first step, a circle is defined in the top silica layer (Fig. 3.7 a)).

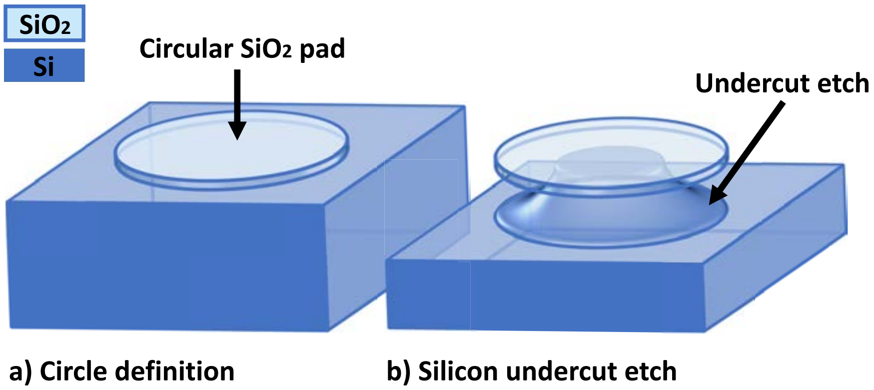

Figure 3.7: (**a**) A circular pad is etched into a SiO_2 layer with the help of a dry- or a wet etch process. (**b**) The silica pad is isotropically underetched with the help of XeF_2 or an other suitable dry etch process (e.g., using SF_6), which is creating a partially free-standing silica disk on top of a silicon pillar.

As the diameter of the ring usually is at least in the order of 100 µm optical mask lithography can be used. This feature size primarily arises from the fact that smaller diameters will cause higher bending losses for the light in the cavity, which will degrade the intrinsic quality-factor. By creating structures with a radius in the order 170 µm, a resonance spacing (FSR) of 200 GHz is achievable. For structures with a radius of 670 µm, a mode spacing of 50 GHz can be achieved. For etching a circular pad, either a wet-etch process [1] or a dry-etch process can be used [105].

In a second step, an isotropic silicon-undercut-etch is performed (Fig. 3.7 b)). It is essential that the etch selectivity between silicon and silica is high enough so that the undercut-etch process is almost not affecting the circular pad. Typically the undercut-etch depth is in the order of $30 - 50$ µm whereas the height of the silica pad is in the order of 2 µm or below. It has been shown, that dry-etch processes can be used for this purpose either by the use of xenon difluoride (XeF_2) [1] or Sulfur hexafluoride (SF_6) [106]. Using XeF_2 for isotropic etching is known to show an extraordinary high selectivity between etching silicon and other materials like SiO_2, SiC and Si_3N_4 [107]. It is possible to optimize a XeF_2-etch to provide a low surface roughness (down to about 175 Å) by lowering the charge pressure, with a selectivity against SiO_2 of about 1:10000 [108].

Using SF_6 as a base for an isotropic undercut in silicon shows a lower selectivity against SiO_2. For example, when using a PlasmaPro 100 Cobra ICP-RIE system, the vendor (Oxford) specifies the selectivity to be bigger than 500:1.

3.2.2 CO_2-laser - reflow process

The last step in the fabrication of a conventional microtoroid is a CO_2-Laser-Reflow to remove residual roughness and create the actual resonator [1]. A CO_2 laser is a gas-based laser that can be designed to be a powerful mid-IR device and was developed by Patel in *1964* [109].

The previously underetched silica disk (Fig. 3.7 b)) is surface-normal-irradiated with a nearly Gaussian distributed focused beam of CO_2 laser light ($\lambda = 10.6$ µm) (Fig. 3.8 a)) leading to power density levels of about $100 - 400\,\mathrm{W/mm^2}$ at the undercut disk. A typical beam radius that will be used for the fabrication in this thesis is about $150 - 400$ µm (Section 5.3.2), depending on the position of the focusing optics. The optical output power of the laser is typically between $10\,\mathrm{W} - 20\,\mathrm{W}$.

Selective absorption of the laser light, thermal isolation of the rim (the part of the disc that is undercut) and surface tension are causing a melting along its periphery into a microtoroidal shape. The optical absorption of fused silica is about 100 times stronger than that of silicon at a wavelength of 10.6 µm [110,111]. Even thin silica disks can absorb light at this wavelength very efficiently [111]. This way the supporting silicon pillar is acting as a heat sink for the silica disc on top. Therefore, the silicon pillar is not melted or physically affected due to its low optical absorption and high thermal conductivity.

As the thermal transmittance of fused silica is significantly reduced with increasing temperature [111], the melting process starts suddenly, due to thermal runaway, whenever a specific laser power level is reached [112], and the silica is heated up above its melting temperature of about 1650 °C [113]. It is reported that evaporation of silica can lead to redeposition, which leads to surface defects. These surface defects can likely alter the quality of the resonator, as they serve as additional sources for scattering [114, pp. 62].

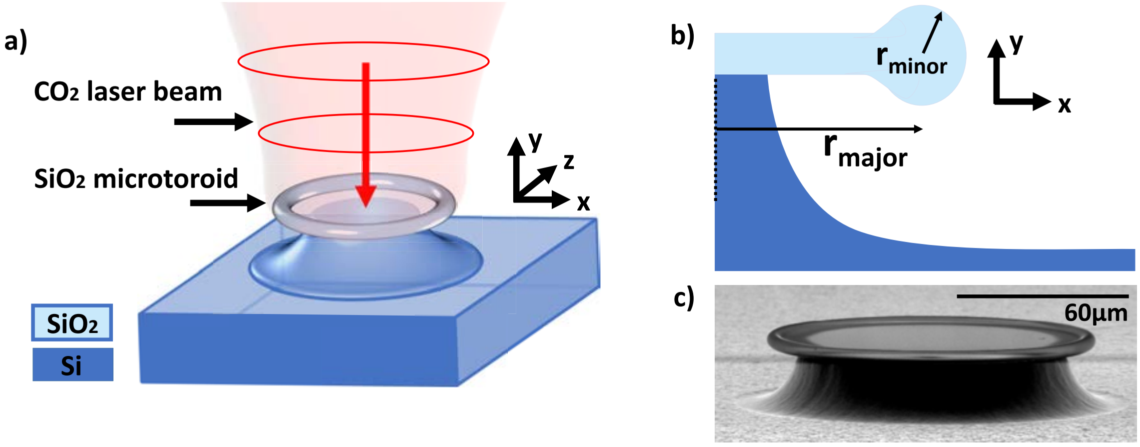

Figure 3.8: Schematic of CO_2-Laser based reflow process for creating conventional silica microtoroids. (**a**) A silica disk is irradiated with CO_2 laser light ($\lambda = 10.6\,\mu m$). Selective absorption of the laser light, thermal isolation of the rim (the part of the disc that is undercut) and surface tension are causing a melting along its periphery into a microtoroidal shape. (**b**) Schematic of the cross-section of a microtoroid after reflow. Two radii can define the microtoroid. The major microtoroid radius r_{major} and the minor microtoroid radius r_{minor}. (**c**) SEM image of conventional silica microtoroid taken from reference [1].

The heat sink effect of the silicon pillar gets more pronounced as the rim approaches the pillar during reflow. This combination of decreasing absorption cross-section and increased heat sinking leads to a self-quenching process. The final microtoroid radius r_{minor} and the radius r_{major} (Fig. 3.8 b)) are primarily determined by the preform diameter and the silica layer thickness. In practice, it is also possible to interrupt this process before this steady state is reached and create microtoroids with smaller r_{minor} and bigger r_{major}.

3.3 Loss mechanisms in a conventional silica microtoroid

In a microtoroidal shaped ring resonator like a conventional silica microtoroid, multiple optical loss channels exist. These losses are arising from intrinsic material absorption, scattering due to material induced imperfections, tunneling losses and coupling losses (to an external coupler) [115, pp.12]. It is possible to distinguish between intrinsic losses and external losses like the coupling losses to an external fiber. It is convenient to relate these loss channels to individual loss rates. The light either stays inside the cavity or is lost due to a loss channel during one resonator round trip. The loaded quality-factor $\mathrm{Q_L}$ describes the ratio of the stored energy (or light) in a resonator divided by the lost energy within one cycle (see Section 2.3.2). Therefore, $\mathrm{Q_L}$ describes the joined ratio of all loss channels and it is possible to define a quality-factor accounting for each loss channel:

$$\frac{1}{Q_{\mathsf{L}}} = \frac{1}{Q_{\mathsf{u}}} + \frac{1}{Q_{\mathsf{c}}} \quad = \quad \left(\frac{1}{Q_{\mathsf{mat}}} + \frac{1}{Q_{\mathsf{surf}}} + \frac{1}{Q_{\mathsf{con}}} + \frac{1}{Q_{\mathsf{rad}}}\right) + \frac{1}{Q_{\mathsf{C}}}. \tag{3.1}$$

In the following, each of the quality-factors $\mathrm{Q}_{\mathsf{mat}}$, $\mathrm{Q}_{\mathsf{surf}}$, $\mathrm{Q}_{\mathsf{con}}$, $\mathrm{Q}_{\mathsf{rad}}$, and Q_{c} are explained [57, 113, 116].

1. Material losses - $\mathrm{Q}_{\mathsf{mat}}$: The material-limited quality factor is given by [113,116, pp.6]:

$$Q_{\mathsf{mat}} \quad = \quad \frac{2\pi n}{\alpha\lambda}. \tag{3.2}$$

Where α is the absorption coefficient including absorption and Rayleigh scattering. For the telecommunication wavelength of $\lambda = 1.55\,\mu\mathrm{m}$, a $\mathrm{Q}_{\mathsf{mat}}$ for microspheres as high as 10^{11} and more is predicted [116] and reported [117].

However, it has been shown that the material losses and intrinsic scattering losses in principle are small, so that they are considered not to be the primary limitation for the intrinsic quality-factor Q_u. Other sources of loss, especially surface contamination loss induced by water, turned out to be more severe for spheres and microtoroids [1, 118].

2. Surface-inhomogeneity losses - Q_surf: The surface quality regarding the roughness of the microtoroidal structure plays a significant role. The reflow process itself is creating an almost atomically smooth surface. However, it is reported that redeposition of evaporated silica can cause surface impurities that can lead to a degradation of Q_surf [114]. The quality-factor Q_surf scales with the wavelength λ, the root-mean-square surface roughness σ and the correlation length B and its dependency can be roughly described by [60, 113, pp.6]:

   $$Q_\mathsf{surf} \quad \propto \quad \frac{\lambda^3}{\sigma^2 B^2}. \tag{3.3}$$

   For melted silica spheres values of $\sigma = 2\,\mathrm{nm}$ and $\mathrm{B} = 5\,\mathrm{nm}$ are reported [60]. In reference [118], loss mechanisms of microtoroids are investigated. This analysis is done with the help of the thermal bistability effect [119], which is describing the partial absorption of light and the subsequent heating that is causing a shift of the resonators resonance frequency due to its temperature dependent refractive index. The arising losses depend on the distribution of the mode, which is guided by the resonator. In particular, the ratio of stored light inside the resonator, and the light that is leaking out of the resonator that is affected by the surface roughness. It is reported that the mode volume for silica microtoroids is comparatively small, enabling scattering loss limited quality-factors in the order of a few hundred million [118].

3. Contamination losses - Q_con: Optical high-quality resonators are often characterized under the ambient environment. The chip temperature, for example, can be controlled by using a temperature controller (TEC) based on a Peltier-element. Chemical water absorption due to ambient humidity by the resonator can cause a severe effect on its quality-factor [60, 116, 118]. The surface of the silica microtoroid is highly hygroscopic leading to water molecules on the surface. Water absorbs light quite efficiently in the near-infrared ($\lambda = 1.55\,\mu\mathrm{m}$), and even a monolayer on the resonator's surface leads to additional losses and is decreasing the quality-factor [113]. The quality-factor is altered to a steady state within about 100 s but can be partially recovered when the resonator is baked out at about 400 °C [116].

4. Radiative losses - Q_{rad}: For conventional microtoroids (Fig. 3.8 c)) the radiative loss due to the bending of the resonator is negligible, in case the major radius is not too small. For example, for a conventional microtoroid with a major radius of $r_{major} = 30\,\mu m$ and a minor radius of $r_{minor} = 2\,\mu m$ the Q_{rad} is reported to be bigger than 10^{11} in the visible and near-infrared range [113, 120, 121]. In this thesis, a novel design for a microtoroidal structure is presented in which radiative losses needs a higher attention compared to conventional microtoroids. In Section 4.2.4 a detailed comparison of the two design attempts is given.

3.4 Discussion

High-quality resonators based on different materials have the potential to be used in different scientific fields, and their use can even be extended to industry-relevant environments and applications (Section 3.1). The relevant fields involve, for example, telecommunication and spectroscopy (Section 3.1.2, 3.1.3). Also, high-quality microresonators might be used in the field of astronomy, waveform generation or optical clock setups [2].

In the field of integrated photonics, significant challenges are arising for high-quality resonators. For example, one major challenge is the integration with other components like couplers and waveguide architectures. Of course, integration with more complex systems, like chip based interferometers is desirable. For achieving the integration ideally high-quality resonators need to be integrated monolithically, or it should be possible to make them a part of a robust package. A monolithic integration scheme would allow for a more cost-efficient design flow, as the high-quality resonator is fabricated along with all other devices. Another benefit would be the avoidable alignment procedure when it comes to the packaging of different photonic chips (each chip containing different devices). In the example of an integrated silica microtoroid, the integration scheme should also allow for back-end integration.

Most non-monolithically integrated resonators are coupled with the help of fibers or prisms. In the case of an optical fiber, the fiber is tapered down by heating up and pulling it to generate an inbuilt coupling section with a diameter in the order of $1\,\mu m$. The tapering causes the light in this section to spread out of the fiber. Fabricating the tapered fiber itself can become challenging and requires specially designed holders and additional equipment.

If a resonator is positioned close to this coupling section, light can be coupled from the fiber to the resonator and vice versa [114, pp. 27]. This procedure involves different movable control stages and suitable holders for the resonator and the fiber and aligning can become challenging. The primary advantage of this procedure is that in principle, all coupling regimes (Section 2.3.2) can be accessed and fine-tuning of the coupling strength by moving the fiber is possible. Furthermore, a broadband comb spectrum can be generated allowing a spectral width of an octave and more [57].

For targeting an entirely integrated version of a high-quality resonator, different approaches have been carried out. For example, packaging a silica microtoroid into a polymer matrix [74]. This Packaging, which is not considered a monolithic integration, allows for more structural resistance in a harsh environment.

In the recent years, promising attempts have been made with silicon nitride resonators [4] that can act as fully monolithically integrated high-quality resonators.

However, their primary drawback up to now is the comparable high threshold for comb generation due to their lower quality-factor compared, for example, to reflown silica-based resonators [19]. In reference [27], silicon nitride resonators have been fabricated that are showing an exceptional high intrinsic quality-factor of 81 million. This quality-factor was achieved by increasing the bend radius of a resonator to 9.65 mm and the use of a custom layer-stack of material. In the case where a smaller footprint of the resonator is desirable, the intrinsic quality-factor is dropping to below 1 million for a bend radius of 1 mm. For applications, in which high confinement, anomalous dispersion (as a prerequisite for comb generation), or large FSRs are not needed, low confinement SiN waveguides might be applicable [27].

Chapter 4

Proposed device - The monolithically coupled inverted silica microtoroid

The targeted device of this work is an integrated, high-quality microtoroidal shaped optical resonator based on silica that is monolithically coupled to an on-chip silicon waveguide. This class of reflown silica microtoroidal resonators in principle can achieve quality-factors in the order of $Q_U > 10^8$ [66].

However, conventional silica-based microtoroid-resonators typically need to be coupled to a free-standing tapered fiber. This results in a complex assembly of optical and mechanical components. Further, it is preventing monolithic chip-scale integration with further photonic devices inside a Photonic Integrated Circuit (PIC). Especially, the monolithic integration of a high-quality-resonator was studied extensively, and several ideas have been outlined for targeting this issue of missing on-chip integration capabilities.

For example, on-chip silica waveguides, which were created by the same reflow process as the microtoroids themselves, facilitate packaging and quality-factors on the order of 4 million were achieved [29]. Even though such a device in principle can be edge-coupled, instead of using a suspended optical fiber next to a resonator, arbitrary waveguide routing, which is required for forming complex on-chip devices is difficult. For example, high-speed modulation capabilities are not achieved.

Also, the use of silicon directly for forming resonators has been studied. For example, annealing of waveguide-coupled micro-disks out of silicon has been shown, but suffers from low quality-factors up to 110,000 [30]. Indeed, quality-factors up to $3{\cdot}10^6$ have been shown with monolithically coupled silicon micro-disks. However, silicon-based resonators suffer from Two-Photon-Absorption (TPA) at higher power levels which makes them unsuitable for cascaded FWM as the basis for frequency comb-generation.

Recently, silicon nitride (SiN) as a promising material candidate has received a lot of attention. On-chip comb generation with SiN waveguides [79] as well as with high index glass waveguides [78] was first shown in *2010* by the use of high-confinement waveguides which were engineered to show anomalous dispersion as a prerequisite for comb generation. Also, it was possible to increase the quality-factors in high confinement SiN platforms up to several millions with the help of various process improvements [122]. For applications, in which high confinement, anomalous dispersion, or large FSRs are not needed, low confinement SiN waveguides with quality-factors in excess of 80 million might be applicable [27]. An approach for combining SiN waveguides with electro-optically enabled Silicon Photonics (SiP) technology is the use of vertically coupled multi-layer stacks [123]. In this case, typically Plasma Enhanced Chemical Vapor Deposition (PECVD), due to constraints related to the thermal budget of the SiP Front-End-Of-Line (FEOL) devices, is used to deposit SiN layer (which are used for SiN waveguides) rather than a Low Pressure Chemical Vapor Deposition (LPCVD) process, typically used in low loss platforms (due to its low hydrogen material content). Thus, the combination of high quality-resonators suitable for parametric comb generation (requiring suppressed TPA) with electro-optic devices in a monolithically integrated SiP chip remains challenging.

Of course, multi-chip assemblies are possible, in which multiple chips are connected, for example, by the use of wire bonds [4].

However, bonding and packaging can become quite costly, and a fully integrated solution like monolithically combining parametric comb generation with a fully functional SiP platform on a single chip might be superior.

For targeting these challenges, Section 4.1 describes the research idea of the monolithically coupled inverted silica microtoroid. For a proof of concept, various optical simulations of the targeted device have been performed which are described in Section 4.2.

4.1 Hypothesis - Research idea

An ultra-high-quality resonator can be used as a base for various applications (Section 3.1). By integrating this device onto a chip monolithically, it can overcome limitations arising from a lab environment and make packaging less complicated and therefore less costly. Furthermore, an optimized fabrication flow can enable the back- or even front-end integration with other photonic on-chip devices.

In this thesis, a novel type of silica-based microtoroid is presented that can be integrated monolithically and is compatible with integration with a fully functional silicon photonics platform. For allowing monolithic integration, the conventional microtoroid geometry is inverted. A thermal reflow step creates the resonator itself at the circumference of a hole etched in a suspended silica membrane [32]. The resulting device is coupled monolithically to a previously created on-chip silicon waveguide. The figure of merit, besides the integration capability, is the resulting intrinsic quality-factor of the device. The quality-factor is dependent on the internal bending losses of the device that play a critical role (4.2.4).

Simulations are indicating that the proposed inverted microtoroid (IVT) theoretically can achieve a higher quality-factor for TM_0 polarized ground modes (instead of TE_0 polarized ground modes). Therefore, the whole design of the device (including waveguides) is adapted for TM polarization. For example, the light from a tunable laser source that will be used is aligned to TM polarization with the help of an external rotatable polarizer before being coupled to the chip holding the IVTs.

For enabling this design scheme, a silicon-on-insulator (SOI) wafer is used for fabrication. The wafer is diced up into chips. The exact fabrication flow is described in Section 5.2 and Section 5.3. The central concept consists in combining a silicon waveguide fabricated in the device layer of the base chip with an inverted version of a microtoroid fabricated by reflowing the buried oxide (BOX) of the same chip [32].

The design flow, besides the reflow process, relies solely on dry etch process and is not including metal or other metallic components directly on the CMOS-chip. The absence of metallic components makes it potentially compatible with standard semiconductor technologies.

Figure 4.1 (a) shows a top view of a fabricated device before reflow, already including a silicon waveguide and a heat spreader.

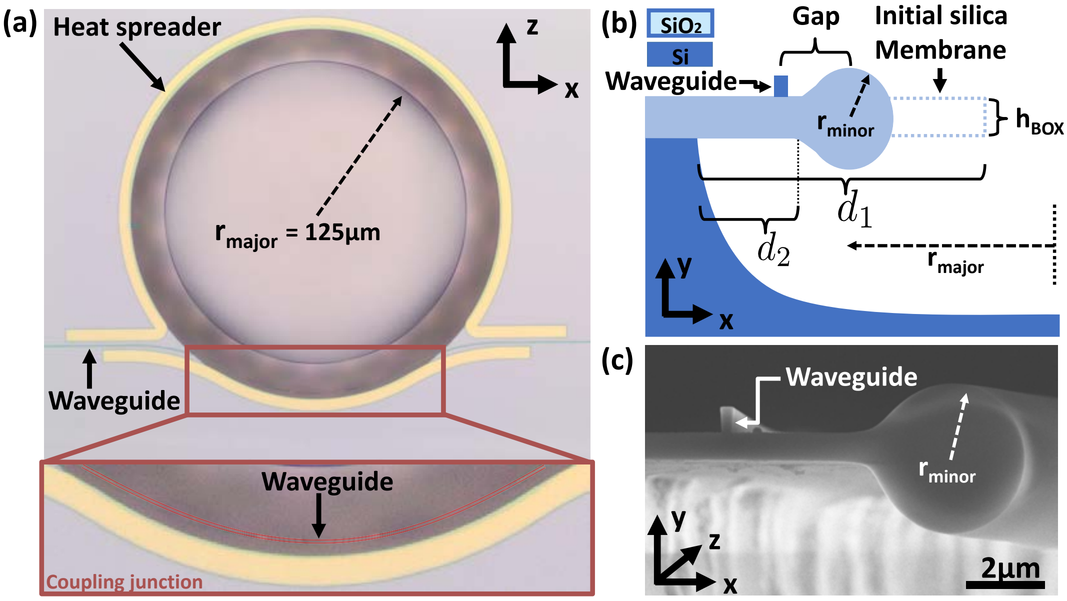

Figure 4.1: Monolithically coupled inverted silica microtoroid before and after melting. (**a**) Top view microscopic image of the fabricated structure before melting. The zoom image shows the waveguide coupling section. The waveguide is shaded in red. (**b**) A schematic of the cross-section of the device after melting. Selective absorption of the laser light by the silica membrane results in melting and reflow of its circumference into a microtoroidal shaped structure with a minor (inner) radius r_{minor} and a major (outer) radius r_{major}. (**c**) SEM image of the melted device in cross-section view.

The heat spreader is an additional silicon frame (fabricated in the silicon device layer of the chip) (Fig. 4.1(a)). It is used to manipulate the melting process of the silica membrane during the thermal reflow process and additionally acts as a mechanical stabilizing frame.

During the reflow, the heat spreader helps to achieve a predictable gap between the center of the microtoroid and the center of the coupling waveguide. The heat spreader and the on-chip silicon waveguides are created during the same etch process. The mask for this etch process is written with the help of electron lithography (EBL). The inset of Figure 4.1(a) shows the position of the waveguide (highlighted in red). Figure 4.1 (b) shows a scheme of the cross-section of the IVT and its geometrical parameters after reflow. The following geometrical parameters are introduced: The major radius r_{major}, the minor radius r_{minor}, the initial undercut depth d_1 and the remaining undercut after reflow d_2, the Buried Oxide (BOX) thickness h_{BOX}, as well as the gap that defines the microtoroid-to-waveguide distance (center to center). Figure 4.1 (c) shows an SEM image of a cleaved IVT after melting.

4.2 Modeling - Simulation of the optimized device

The optical properties of the proposed inverted silica microtoroid (IVT) needs to be simulated before the actual fabrication takes place to verify its theoretical functionality. A functional device is able to couple light from a silicon waveguide to an inverted microtoroid, and the theoretically expected intrinsic quality-factor is comparable to the ones of conventional microtoroids [19].

In fact, up to now, comparable quality-factors in the order of 100 million are not achieved in real measurements. Of course, during the process development, based on literature research, new findings, availability of cleanroom equipment, different new ideas have been developed and alternative attempts were incorporated into the design and fabrication processes of the proposed device. The primary purpose of this Section is to get initial evidence whether the targeted design, regarding the expected quality-factor and the expected coupling parameters, is feasible.

In Section 4.2.1, the simulation environment is explained. Section 4.2.2 deals with the edge-couplers that are used for input and output coupling of light to and from the chip. The transition/interconnect waveguides are explained in Section 4.2.3. Transition waveguides are routing the light from the edge-couplers to the inverted microtoroids. In Section 4.2.4, the inverted microtoroid's intrinsic quality-factor is calculated based on simulation results. The intrinsic quality-factor is limited by the microtoroid's geometric bending. The waveguide that is used for coupling light to the microtoroid is not present in this simulation.

Subsequently, Section 4.2.5 deals with the coupling between the waveguide and the microtoroid. As an additional heat spreader is used, its impact on the expected quality-factor is analyzed in Section 4.2.6. The last Section 4.2.7 presents the full 3D simulation of the coupling mechanism between waveguide and microtoroid.

4.2.1 Simulation methods and simulation environment

For the simulation of the proposed device, different simulation tools are used. For performing optical simulations, the design software RSoft by Synopsys® is used. RSoft is providing different tools for simulating 1D, 2D−, and 3D-structures. All simulations were carried out on different high-performance multi-core computer systems. In this work, the simulations were performed on a computer with four AMD-Opteron 6380-Processors (2500 MHz clock speed with 16 logical cores each) and a random access memory (RAM) of 512 GB.

Cross-section and conformal mapping simulations

In this work, two simulation packages are primarily used. One is a mode solver (FemSIM™) based on the finite element method (FEM). This mode solver can solve the vector wave equation with boundary conditions for an arbitrary structure of an arbitrary anisotropic material. Simulation boundaries, for example, can be defined by perfectly matched layers (PML). A PML is added to the simulation domain boundaries to minimize reflections for all angles of incidence and wavelengths. This way the structure ideally is not affected by the boundaries and can be regarded as being situated in an infinite box. The PML itself is terminated at the domain edge with a perfect electrical conductor (PEC) [124]. The use of finite elements helps to subdivide the structure into different independent parts that can be treated separately to calculate the optical field distribution. The solution of the structure is the sum of all sub-solutions from each finite element. In the end, a matrix eigenvalue equation needs to be solved, leading to the squared complex propagation constants β_m^2 and the corresponding mode field distributions, where m is indicating the m$^{\text{th}}$ eigenvalue. The resulting eigenmodes can be analyzed regarding their spatial distribution and their optical losses. Further information about this method can be found for example in [125, 126] or in the RSoft manual.

An essential feature of FemSIM$^{\text{TM}}$ is the possibility of extending a 2D cross-section simulation to a quasi-3D simulation with the help of conformal mapping. In this method, bending of a structure is emulated. The design of a 2D-cross-section of a structure is sufficient and can be virtually extended to solve for optical modes as if the structure were bent in 3D. When using conformal mapping the material specific µ− and $\epsilon-$ tensor (or the effective refractive index profile) of the underlying material are adjusted in a way that each FEM component is a function of the bending radius. An artificial material is created, that has the desired bent geometry imprinted [127, 128]. This method is valid as long as the segment width that is bent (in the case of this work twice the minor radius $\mathrm{r}_{\mathsf{minor}}$) is much smaller than the bending radius (in the case of this thesis the major radius $\mathrm{r}_{\mathsf{major}}$) (compare Fig. 4.1 c)).

The second software package of RSoft, which is primarily used, is a full-vectorial field simulation tool (FullWAVE$^{\text{TM}}$), which is based on the finite-difference-time-domain method (FDTD). The finite-difference-time-domain method is replacing the Maxwell equations by a set of finite difference equations, which can be solved numerically [129]. An appropriate choice of the underlying field points makes these equations applicable to boundary conditions. FullWAVE$^{\text{TM}}$ is using a Yee mesh [130] for this discretization. The result is a set of six equations, describing the electrical and magnetical fields for each Yee-mesh point.

Simulation issues - Advantages and disadvantages of simulation tools

Most often, simulations are based on numerical calculations that are subdividing a complex problem, which is not solvable analytically, into smaller solvable sub-problems. Therefore, different assumptions have to be made, and usually numerical inaccuracies have to be accepted. The number of sub-problems that need to be solved can be high, leading to high computational requirements for computer systems. The trade-off consists in having a suitable and sufficient resolution of a simulation domain by still finishing a simulation in an acceptable period.

When the resolution (or the number of sub-problems) is getting too low, for example, the resolution is smaller than the smallest feature size of the device, numerical artifacts can appear, like non-physical reflections or inaccurate results. On the other hand, increasing the resolution too much can cause long simulation times. A convergence study can be carried out for picking a suitable resolution (the number of sub-problems). A simulation with a high resolution is compared to a simulation with a lower resolution. If the difference in the results is negligible, using a lower resolution will result in a lower computational effort and therefore in a decreased run time of the simulation.

For further decreasing the computational time most often, adaptive meshing is used. Areas, which are considered bulk areas, have a coarse mesh with a lower resolution than areas that include corners, like small geometrical features. It is vital that the different mesh size areas are transferred to each other as smooth as possible by adding transition areas of adjusted mesh size. Otherwise, reflections can occur at neighboring mesh cells leading to numerical artifacts.

Another effect that needs to be taken into account is the staircasing effect. The staircasing effect becomes pronounced when using a Cartesian mesh for a radial structure. As the resolution is limited, the Cartesian cells are not able to mesh the rim of a radial structure. These corners can be a numerically induced source of optical loss as they scatter light and can act as sharp field enhancement spots. This artificial field enhancement leads to wrong and distorted simulation results. Internally this issue is automatically targeted by RSoft using triangular meshes and non-uniform meshes along with a suitable interface alignment of cells.

4.2.2 Optical simulation of the edge-coupler

Light needs to be coupled from an external laser source to the on-chip inverted microtoroid. As mentioned in Section 2.2, this can be done either by using grating couplers or edge-couplers. In this work, primarily inversely linear tapered edge-couplers without top cladding are used. Due to the underlying fabrication process of the proposed device, the edge-couplers show slight differences compared to conventional edge-couplers regarding their geometry. Furthermore, due to the comparable thin BOX-layer of about 800 nm and the missing top cladding and an accompanied asymmetric refractive index distribution in the y-direction, the performance of the edge-coupler is slightly degraded [131, 132].

Figure 4.2 (a) shows a top view of an edge-coupler that is used for coupling light from and to the chip carrying the inverted microtoroids. The tip of the inverse coupler has a width of about 90 nm (Fig. 4.2 (b)). Figure 4.2 (c) shows a three-dimensional scheme of the edge-coupler. The inverse taper is situated mainly on top of a free-standing silica membrane with a depth of d_1 (Fig. 4.2 (a) and (d)). In order to protect the membrane from breaking, silicon stabilizers are integrated. These stabilizers are situated partially on the undercut and partially on the non-undercut region. The undercut of the edge-coupler is created simultaneously to the undercut of the inverted microtoroids. The distance s from the tip of the edge-coupler to the rim of the membrane is about 2 µm to 3 µm.

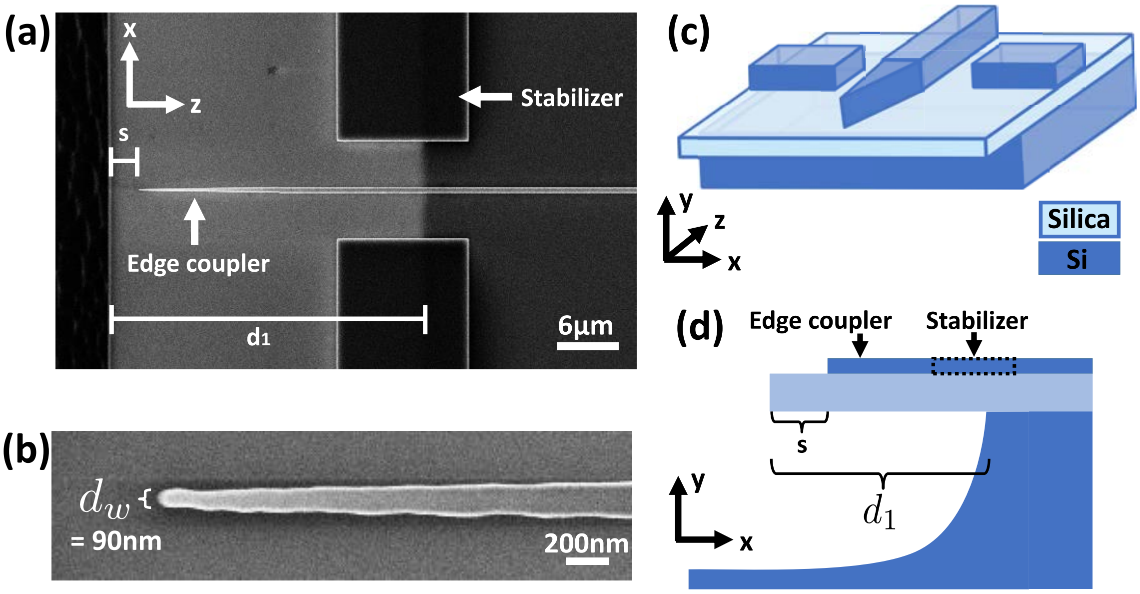

Figure 4.2: Inversely tapered edge-coupler design. (**a**) Top view SEM image of edge-coupler used for the proposed IVT. The edge-coupler tip is positioned on top of a free-standing silica membrane. For avoiding cracks in the membrane, dedicated stabilizers are defined. (**b**) Zoom image of the same edge-coupler tip with a width of about 90 nm. (**c**) 3D-schematic of the edge-coupler. The stabilizers and the edge-coupler are fabricated in the device layer of an SOI chip. (**d**) Schematic of a cross-section of the edge-coupler. The distance s from the tip of the edge-coupler to the rim of the free-standing silica membrane is crucial for its optical coupling efficiency. Usually, s is in the order of about 2 µm to 3 µm.

Initially, the inversely tapered coupler was not planned to be situated on top of a membrane. However, the undercut is advantageous as since otherwise light in the tapered region of the edge coupler can couple to the substrate leading to higher substrate leakage losses. Once the mode is adiabatically converted into a confined waveguide mode the leakage loss through the comparatively thin silica BOX layer of 800 nm is reduced. The waveguide height is 310 nm. A thin layer with a thickness of approximately 20 nm of Hydrogen silsesquioxane (HSQ) is still present. HSQ is used as a resist during electron-beam lithography.

For coupling light into the chip, a lensed fiber is used, which radiates light in a Gaussian ground distribution with a spot diameter of 2.5 µm. The spot diameter is defined by the two points for which the intensity is dropping to $1/e^2$ of the peak intensity.

Figure 4.3 (a) shows the result of a 3D-FDTD simulation in which a Gaussian ground source mode is used for excitement. The light initially has a Gaussian field profile with 2.5 µm spot diameter 1) before being converted into a $\mathrm{TM_0}$-waveguide mode 2). The performance of the coupler can be calculated by solving a full-vectorial overlap integral [133] of the field distribution at 2) with the $\mathrm{TM_0}$-eigenmode calculated with the help of FEM at the same position. The overlap value is normalized with the initial power of the exciting source field of the FDTD simulation.

The taper width $\mathrm{d_w}$ plays a significant role, as this width will define the mode-field-diameter at the input of the taper. The smaller $\mathrm{d_w}$ gets, the bigger the mode-field-diameter gets that is needed for efficient coupling. The distance s is an additional offset between the rim of the chip and the input coupler. This distance is chosen to be 2 µm in the simulation and is causing additional optical loss. During the fabrication process, this distance is needed to guarantee a sufficient mechanical and chemical protection for the input coupler. Throughout the etch-process, an optical resist is protecting the coupler's facets.

For providing an efficient coupling from a lensed fiber mode into the desired $\mathrm{TM_0}$ -waveguide mode the power-coupling efficiency η needs to be as high as possible. The power-coupling efficiency η between two field distributions is a measure of how much power between two modes can be exchanged and is connected to the overlap integral OI which can be defined in its scalar form as [35, pp. 81] [40, pp. 295]:

$$\mathrm{OI} = \frac{\int\int E_1 E_2^* d\mathbf{S}}{\sqrt{\int\int E_1 E_1^* d\mathbf{S} \cdot \int\int E_2 E_2^* d\mathbf{S}}} \tag{4.1}$$

where $\mathrm{E_1}$ and $\mathrm{E_2}$ are the fields to be overlapped, and $\mathrm{d}\mathbf{S}$ is the surface-element. In our case $\mathrm{d}\mathbf{S}$ equals $\mathrm{d}\mathbf{x}\mathrm{d}\mathbf{y}$. For further extracting the power-coupling efficiency η, the following relation holds [40, pp. 295]:

$$\eta = \mathrm{OI}^2. \tag{4.2}$$

The parameter η (Eq. 4.2) has a value between zero and one and describes how much power is coupled from a mode $\mathrm{E_1}$ with power $\mathrm{I_1}$ into a mode $\mathrm{E_2}$ with power $\mathrm{I_2}$.

For the determination of an effective taper tip width $\mathrm{d_w}$ and the optimized spatial position of the Gaussian launch field, the FDTD simulation is done the other way around making use of the reciprocity principle. An eigenmode, which is calculated with FEM, is launched inside the waveguide, and the field that is radiated from the tip of the taper is analyzed and overlapped with a pure Gaussian ground mode at different positions in z and $\mathrm{x, y}$-directions. The Gaussian ground mode is adjusted to show the same caustic as one would expect from a lensed fiber. This way the theoretical optimal $\mathrm{x, y, z}$ position of a lensed fiber as a function of $\mathrm{d_w}$ can be calculated and the global maximum of power transfer between lensed fiber and edge-coupler can be extracted.

Due to the asymmetric refractive index distribution in the y-direction and the offset distance s, the light is partially coupled to the membrane (see Fig. 4.3 (b)) and is then loosely guided before being finally coupled into the taper. Therefore, the undercut itself is helping to improve the coupling efficiency of the coupler as no light can leak into the substrate.

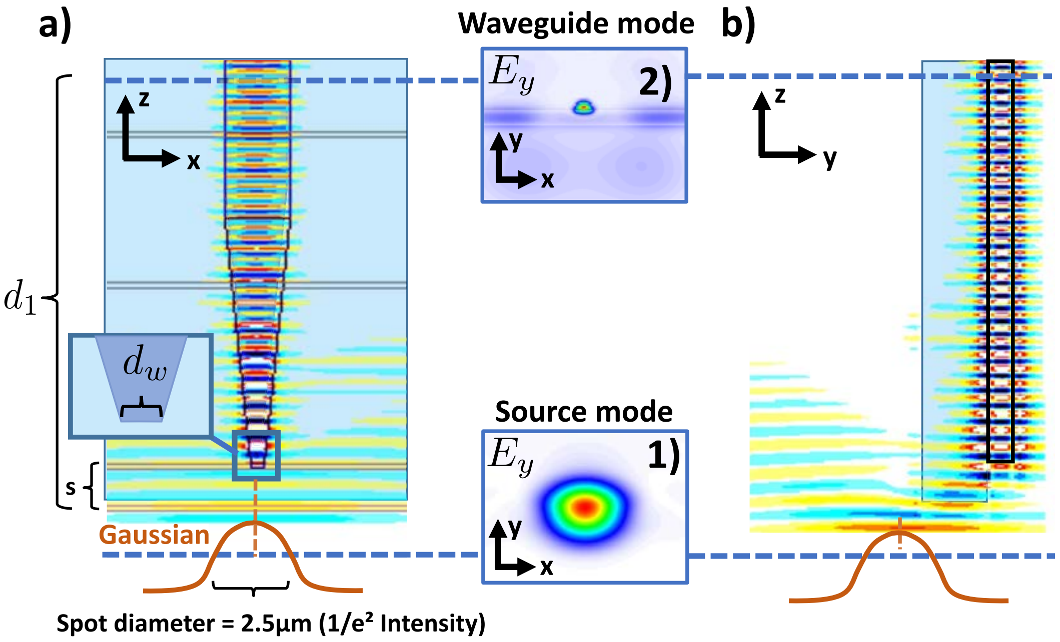

Figure 4.3: Optical 3D FDTD simulation of an undercut edge-coupler. (**a**) Top view of simulation setup for an inversely tapered edge-coupler of length $\mathrm{d_1}$. A Gaussian source mode 1) with a spot diameter of 2.5 µm is launched. The light is coupled partially to the free-standing silica membrane before being coupled into the inversely tapered edge-coupler with a tip width of $\mathrm{d_w}$. The field coupled to the waveguide 2) can be analyzed to calculate the coupling efficiency. For the determination of an effective taper tip width $\mathrm{d_w}$ and the optimized spatial position of the Gaussian launch field, the FDTD simulation is done the other way around making use of the reciprocal principle. An eigenmode that is calculated with FEM is launched inside the waveguide, and the field that is radiated from the tip of the taper is analyzed and overlapped with a pure Gaussian ground mode. (**b**) The side view of the simulation.

The described overlap at position 1) between the field distribution found by FDTD and the original $\mathrm{TM_0}$-eigenmode solution found by FEM can be translated into an expected coupling loss in dB by:

$$\alpha_{\mathsf{Edge-Coupler}}[\mathrm{dB}] = 10 \cdot log_{10}(\eta). \tag{4.3}$$

Finally, the Fig. 4.4 shows the expected optical insertion loss per coupler as a function of the taper tip width $\mathrm{d_w}$. The span for $\mathrm{d_w}$ is chosen to hit a realistic fabrication target.

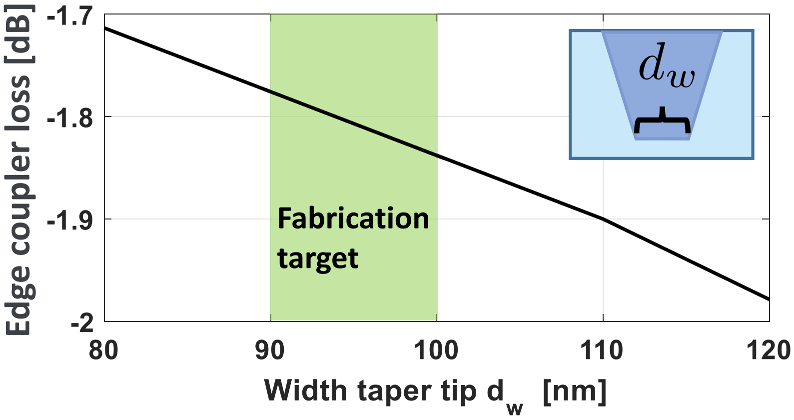

Figure 4.4: Simulated optical coupling insertion loss of one inversely tapered edge-coupler. The span for $\mathrm{d_w}$ is chosen to hit a realistic fabrication target. The final selected fabrication range is resulting in a tip width $\mathrm{d_w}$ of 90 nm to 100 nm and a simulated coupling loss per coupler of about 1.8 dB.

The fabrication target for $\mathrm{d_w}$ is set to be in the region between 90 nm and 100 nm. This region shows an acceptable coupler performance, can be fabricated reproducibly and the aspect ratio of the tip width and height is high enough to show satisfying mechanical stability. For an inversely tapered edge-coupler with a tip width of 90 nm, the optical insertion loss including input and output coupling is expected to be in the order of 3.6 dB as the lower limit.

4.2.3 Optical simulation of the transition/interconnect waveguides

As pointed out in section 2.1.2 the width of a waveguide can have a significant impact on the expected substrate coupling losses.

In order to find the eigenmodes of a transition waveguide, from which the substrate coupling loss can be found, FEM simulations have been performed, and the imaginary part of the effective refractive index $\kappa(\omega)$ is analyzed for $\mathrm{TE_0}$ and $\mathrm{TM_0}$ polarization. Since the goal pursued here is the integration of inverted microtoroids with a fully functional silicon photonics platform, waveguide substrate coupling losses should be low enough to allow efficient waveguide routing over several centimeters.

The SOI that is used for the chip fabrication has a top-Si (device) layer thickness of 310 nm and a BOX thickness of 800 nm. A thin layer with a thickness of approximately 20 nm of hydrogen silsesquioxane (HSQ) is still present. HSQ is used as a resist during electron-beam lithography. The BOX thickness is comparably thin, compared to widely used SOI wafers with a BOX thickness of 2 µm. Therefore, particular attention has to be drawn on potential substrate coupling losses of a waveguide fabricated in the device layer of the chip.

Figure 4.5 shows the simulated losses for TE_0 and TM_0 polarization as a function of waveguide width. For a waveguide width of 500 nm and above, these coupling losses become small even for the TM_0-mode. As primarily TM_0-polarization is of significant interest in this work, the expected optical loss for a transition/interconnect waveguide wider than 500 nm is evaluated, which drops below 1 dB/cm. The inset of figure 4.5 shows the setup of the transition waveguides that will be used in this work.

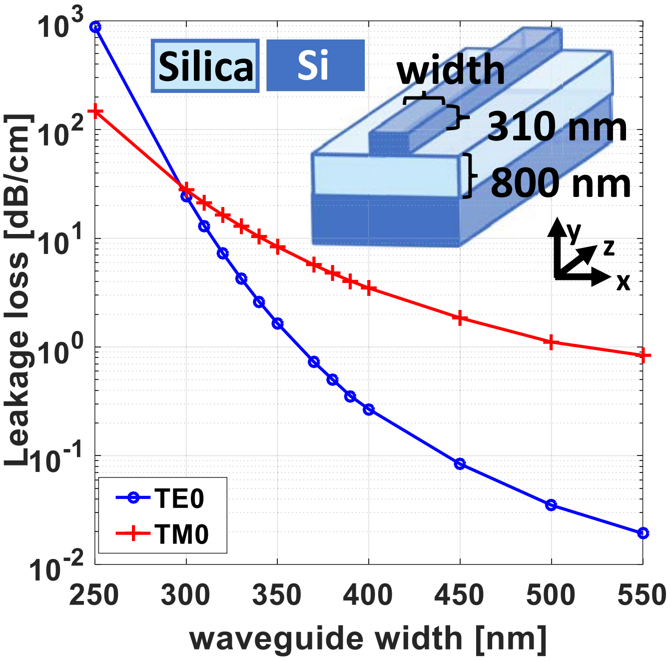

Figure 4.5: Simulated optical leakage losses in dB/cm of a waveguide for TE_0 and TM_0 ground modes as a function of waveguide width. The inset shows a 3D-schematic of the simulated waveguide design.

4.2.4 Optical simulation of the intrinsic inverted microtoroid modes

An inverted microtoroid is created when an initially undercut silica membrane (see Section 5.2.5) is irradiated with CO_2-laser-light. The melting process causes the microtoroidal shape. In order to simulate the optical loss, caused by the bending with a radius r_{major} (see Fig. 4.1 b)), an FEM simulation with conformal mapping was performed. Also, the expected bending loss is connected to the minor radius r_{minor}.

The minor radius of the inverted microtoroid

A simple model can be used for estimating the final minor radius $\mathrm{r}_{\mathrm{minor}}$. It is assumed that during the melting process the volume of the silica, which is melted, is conserved. Figure 4.6 (b) shows a scheme of the microtoroid's cross-section after melting. The initial membrane depth d_1 collapses to a final undercut depth of d_2. This way the core radius can be calculated by the length of the reflown part of the membrane and the thickness of the buried oxide (BOX) $\mathrm{h}_{\mathrm{BOX}}$ with the help of volume conservation by:

$$r_{\mathrm{minor}} = \sqrt{\frac{(d_1 - d_2)\, h_{\mathrm{BOX}}}{\pi}}. \tag{4.4}$$

Figure 4.6 (a) and (c) show an example of a melted microtoroid and the minor radius $\mathrm{r}_{\mathrm{minor}}$ as a function of d_2 for a value of $\mathrm{d}_1 = 30\,\mu\mathrm{m}$ and $\mathrm{h}_{\mathrm{BOX}} = 800\,\mathrm{nm}$.

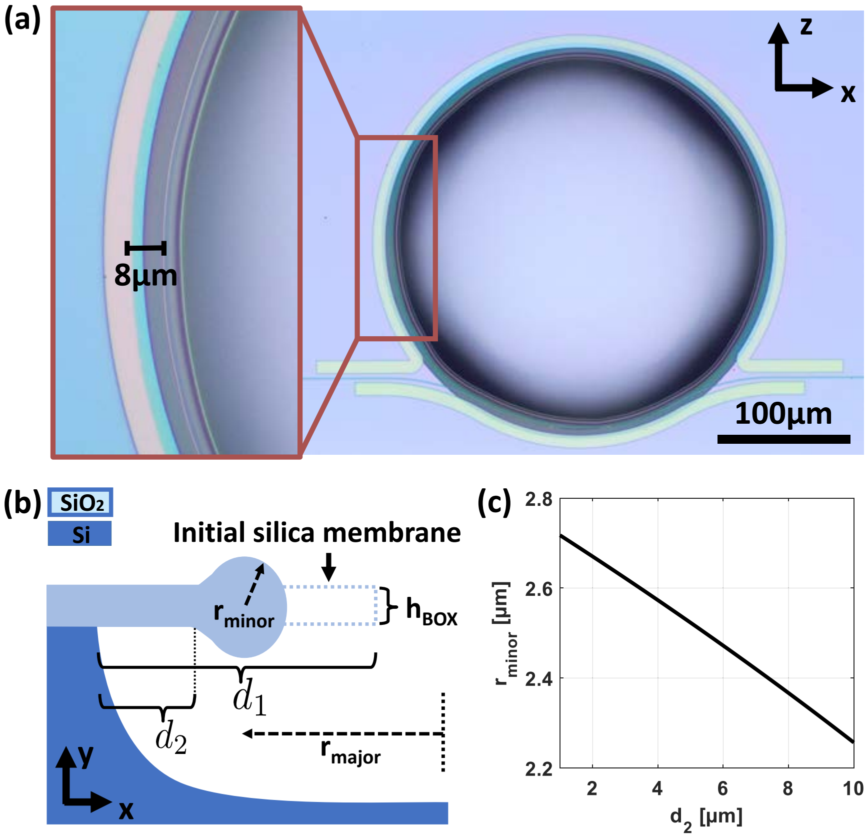

Figure 4.6: Melted inverted microtoroid's minor radius $\mathrm{r}_{\mathrm{minor}}$ as a function of remaining silicon substrate undercut d_2. (**a**) Example of a melted inverted microtoroid with a remaining undercut of $\mathrm{d}_2 = 8\,\mu\mathrm{m}$. (**b**) Schematic cross-section view with geometric parameters. (**c**) Graph of the inverted microtoroid's minor radius $\mathrm{r}_{\mathrm{minor}}$ as a function of silicon remaining substrate undercut d_2 assuming $\mathrm{h}_{\mathrm{BOX}} = 800\,\mathrm{nm}$ and $\mathrm{d}_1 = 30\,\mu\mathrm{m}$.

The minor radius r_{minor} is only changing slightly with the remaining undercut d_2, which is caused by the square root dependency of r_{minor} with d_2. As the remaining undercut is dependent on the process parameters during the reflow process, it can only be adjusted to a particular amount, until a heat sinking effect, and a screening effect due to increasing r_{minor} becomes so pronounced that even further irradiation with CO_2-laser-light is not changing the inverted microtoroid's minor radius anymore [112]. In most of the experiments in this work, the final radius r_{minor} is assumed to be between 2.2 µm – 2.6 µm. Indeed, it is challenging to cleave a device in a way to measure its minor radius, for example, by means of an SEM. However, Figure 4.1 (c) shows a cleaved microtoroid, whose r_{minor} is in accordance with equation 4.4.

Bending losses of an inverted microtoroid

A primary difference between conventional microtoroids (Section 3.2) and inverted microtoroids are the expected optical bending losses. The mode confinement towards the outer region of the microtoroid's circumference is weaker in the case of an inverted microtoroid compared to a conventional microtoroid. In a conventional microtoroid, the mode is pressed towards the outer rim of the core located opposite to the suspended silica membrane. This region shows a high dielectric index contrast between the silica and the surrounding air. On the contrary, in the case of an inverted microtoroid, the mode is pressed into the opposite direction, which can lead to higher bending losses, due to leakage into membrane modes, which have a higher effective index than the refractive index of air [32].

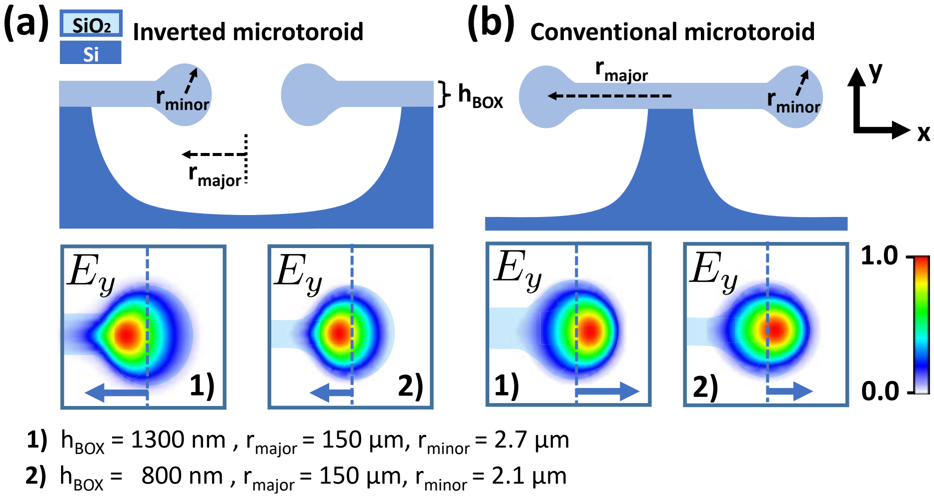

1) h_{BOX} = 1300 nm , r_{major} = 150 µm, r_{minor} = 2.7 µm
2) h_{BOX} = 800 nm , r_{major} = 150 µm, r_{minor} = 2.1 µm

Figure 4.7: Comparison of TM_0 ground-modes between (**a**) an inverted microtoroid and (**b**) a conventional microtoroid (from optical FEM mode-solves using rigorous conformal mapping). The mode confinement towards the outer region of the inverted microtoroid's circumference is weaker since the mode is pressed towards the suspended silica membrane. This effect becomes even more pronounced for thicker BOX layers, compare cases **1**) versus **2**).

Figure 4.7 (a) and (b) are showing a qualitative comparison of how a TM_0 mode appears in the case of an inverted microtoroid and a conventional microtoroid. The lower the BOX thickness h_{BOX} gets, **1**) versus **2**), the less the mode is pressed into the direction of the non-suspended BOX (in the case of an inverted microtoroid). Nevertheless, the smaller the major radius r_{major} gets, the higher the bending losses get.

In order for the bending losses not to become the limiting factor for the microtoroid's quality-factor, without requiring excessively large bending radii, the BOX thickness needs to be thin enough, as a reduction of its thickness reduces the effective index of the slab modes and thus also suppresses optical leakage into the slab. On the other hand, reduction of the BOX thickness also increases substrate leakage losses of silicon waveguides fabricated elsewhere on the chip [134]. Therefore, a trade-off exists between reducing the bending losses of the microtoroid and reducing the waveguide substrate leakage losses.

Figure 4.8 shows the simulated loaded quality-factor Q_{Bend} limited by bending losses, assuming critical coupling to the coupling waveguide, as a function of the BOX thickness for two major radii r_{major} of 125 µm and 150 µm and for both the TE_0 and the TM_0 ground modes.

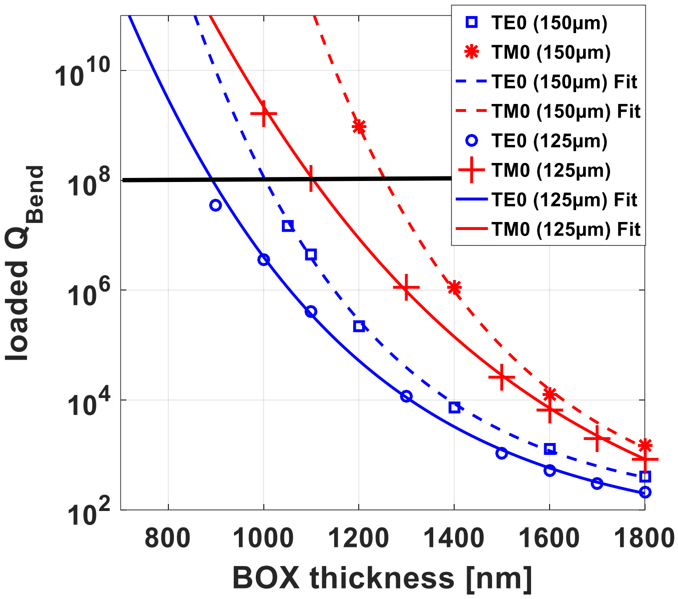

Figure 4.8: Simulated bending loss limited loaded quality-factor for an inverted microtoroid for TE_0 (blue) and TM_0 (red) modes as a function of the BOX thickness h_{BOX}. The core radius r_{minor} is implicitly varied according to equation 4.4. The parameter d_1 is assumed 22 µm, and d_2 is assumed 5 µm and therefore, $d_1 - d_2 = 17\,\mu m$. The BOX thickness is assumed to be $h_{BOX} = 800\,nm$. The solid lines correspond to a major radius of $r_{\mathsf{major}} = 125$ µm and dashed lines to a major radius of $r_{\mathsf{major}} = 150$ µm.

A Q_{Bend} of more than a 100 million is ideally targeted since this is on the order of the highest quality-factors measured with conventional microtoroids and can be considered as the limit constrained by material properties such as impurities, residual roughness, SiO_2 redeposition or water adsorption.

From Fig. 4.8 it can be concluded that the BOX thickness h_{BOX} needs to be smaller than 0.9 µm (1.0 µm for r_{major} = 150 µm) for the transverse electric ground mode (TE_0) and smaller than 1.1 µm (1.3 µm for r_{major} = 150 µm) for the transverse magnetic (TM_0) ground mode. The core radius r_{minor} is implicitly varied according to equation 4.4. The parameter d_1 is assumed 22 µm, and d_2 is assumed 5 µm. For example, an 800 nm BOX thickness h_{BOX} is resulting in a r_{minor} of 2.1 µm. The actual layer thicknesses of our SOI chips are also constrained by our vendor's offerings so that I decided on using a 310 nm Si device layer thickness and an 800 nm BOX layer thickness. Since 800 nm is substantially thinner compared to the 2 µm BOX SOI wafers, which are more commonly used in silicon photonics, particular attention has to be given to potential substrate coupling losses of silicon transition/interconnect waveguides fabricated in the device layer of the chip, which are used to route the light over several millimeters in total.

4.2.5 Optical simulation of the coupling section between the waveguide and inverted microtoroid

A fundamental part of the proposed IVT system is the waveguide-to-microtoroid coupling section. This junction needs to be analyzed regarding its expected optical loss and under which circumstances index matching between a mode of the waveguide and a mode of the microtoroid can be achieved. The coupling mechanism is dependent on the wavelength and the geometric parameters of the waveguide and the microtoroid.

Total expected optical losses of the coupling section

Since the coupling section is located on top of the undercut silica membrane (Fig. 4.9 (a) inset), coupling to the silicon wafer substrate is not an issue (even though the silicon-waveguide is tapered down in the coupling region). However, since the waveguide width in the coupling section is chosen to verify phase matching with the microtoroid mode, and the waveguide's effective index is thus close to the refractive index of SiO_2, a coupling of the waveguide mode into the underlying silica membrane can occur. Figure 4.9 (a) shows the simulated effective index of a silicon waveguide situated on top of a freestanding silica membrane as a function of its width. For a width above ≈150 nm, the effective index rises above the refractive index of silica. While critical coupling is then no longer maintained, a sufficient coupling strength can still be obtained (as will be shown later on in Fig. 4.13) for a 160 nm wide waveguide. In the fabricated devices, the waveguides are tapered down to approximately 120-150 nm. At this point, the effective index of the silicon waveguide is already slightly below the bulk refractive index of silica. However, the waveguide losses in the coupling region remained small and did not present a problem for the experimental characterization (they are simulated as being below a few tens of a dB).

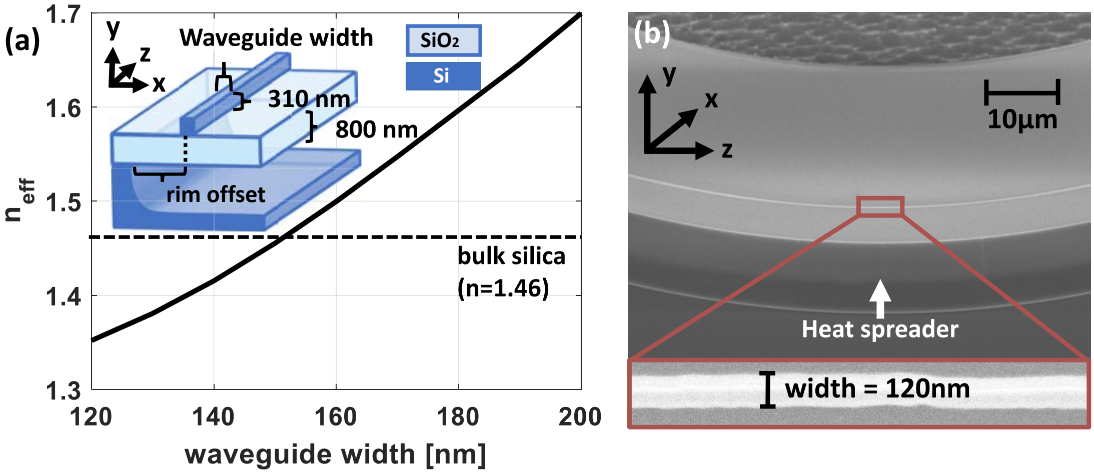

Figure 4.9: (**a**) Effective index n_{eff} of the coupling section waveguide as a function of its width. The inset shows a 3D schematic of coupling section waveguide. (**b**) SEM image of a coupling section of an inverted microtoroid-to-waveguide before melting with an inversely tapered gap coupler. The inset shows the coupling waveguide with its minimal width of about 120 nm. In this thesis, the width of the coupling section is between 120 nm and 160 nm.

Figure 4.9 (b) shows an SEM image of the coupling junction (before reflow) with a width of 120 nm and a heat spreader (see Section 5.2.3). The heat spreader is situated at least several microns apart from the coupling section. Therefore, no additional loss for the coupling junction is expected from simulations. The total length of the coupling section is approximately 180 µm where 60 µm of the length is dedicated to the smallest waveguide width.

Refractive index, phase matching, and power transfer

To maximize the optical power build-up inside the microtoroid, for example, to minimize the threshold for parametric wavelength conversion, it is crucial to reach a coupling point at, or close to critical coupling [114]. For conventional microtoroids, this can be achieved by adjusting the gap between a suspended tapered fiber and a conventional microtoroid. In an integrated solution, the gap is fixed and needs to be well targeted by design and fabricated on the spot.

The coupling strength can be corrected to some extent by tuning the wavelength or the temperature in an inverted microtoroid. The silicon waveguide and silica microtoroid are made out of different materials. Silicon has a substantial thermo-optic coefficient compared to silica. Therefore, thermal tuning can be used for fine-tuning the coupling strength by moving in and out of the phase matching condition. Moreover, due to the high geometric dispersion of the tapered silicon waveguide, changing the wavelength can also serve to tune the coupling strength [32].

As the coupling system out of waveguide and microtoroid is sensitive to wavelength and temperature changes, an initial design wavelength has to be formulated.

The designs described in the following are targeted to reach critical coupling at a wavelength of 1550 nm and room temperature, with further wavelength, and temperature tuning applied experimentally to correct for deviations.

In case the effective refractive indices of the tapered waveguide section and the inverted microtoroid are almost equal ($\mathrm{n_w} \approx \mathrm{n_T}$) the light is traveling in both at quasi-identical speeds. In this system, the tapered coupling section is bent with approximately the same curvature as the microtoroid. In fact, the coupling section's bending is slightly lower (compare to Fig. 2.18). Therefore, the propagation constants ($\beta_\mathsf{w} \approx \beta_\mathsf{T}$) are quasi-matching, and the phase speeds of light in the waveguide and in the microtoroid are nearly the same. When choosing the right wavelength, temperature, and curvature, the system will accumulate almost no phase difference during the coupling process. In other words, the system is phase-matched. When changing the wavelength or temperature, this phase-match condition might not be fulfilled anymore.

For comparison, we assume a system of two coupled non-identical waveguides $\mathrm{W_1}$ and $\mathrm{W_2}$ in Mach-Zehnder geometry. Further, the waveguides have independent non-coupled propagation constants β_1 and β_2 and are exchanging power along $z-$direction. In case of small coupling (the cross-coupling coefficientκ is much smaller than one), it can be shown [135, pp. 192] that the power transfer function for power $\mathrm{P_1}$ and $\mathrm{P_2}$ can be formulated with the help of perturbation theory as:

$$\frac{P_2(z)}{P_1(0)} = \frac{|\kappa|^2}{K^2}\sin^2(Kz) = \frac{\sin^2(Kz)}{1+\left(\frac{\varDelta\beta}{|\kappa|}\right)^2} \leq 1 \tag{4.5}$$

where:

$$K = \sqrt{(\varDelta\beta)^2 + |\kappa|^2} \tag{4.6}$$

and:

$$\varDelta\beta = \frac{\beta_1 - \beta_2}{2}. \tag{4.7}$$

Only in the case of $\beta_1 = \beta_2$, a full power transfer between two waveguides is possible. Additionally, the power stored in each waveguide is oscillating as a function of the distance z. After a coupling length of $L_C = \pi/2|\kappa|$ the power is completely transferred from one waveguide to the other waveguide in case of symmetric waveguides. A widely used optical device is a 3 dB-splitter that splits the power equally between two coupled waveguides. This device would have a coupling length of $L_{3dB} = L_C/2$.

Further, the coupling leads to a symmetric solution with propagation constant β_+ and an asymmetric solution with propagation constant β_- as eigensolutions. The splitting of the two propagation constants can be related to the fundamental non-coupled propagation constants by:

$$\beta_\pm = \frac{\beta_1 + \beta_2}{2} \pm K. \tag{4.8}$$

Figure 4.10(b) shows the simulated effective indices (FEM using rigorous conformal mapping in cylindrical coordinates) of an uncoupled waveguide mode and an uncoupled microtoroid mode as a function of wavelength, obtained by either removing the silicon waveguide from the simulation setup or by extending the silica film. Following geometrical parameters are assumed: $\mathrm{r}_{\mathrm{major}} = 145\,\mu\mathrm{m}$, $\mathrm{r}_{\mathrm{minor}} = 2.3\,\mu\mathrm{m}$, gap = 3.2 µm (with a gap defined as the center-to-center distance, see Fig. 4.10(a), for experimental reasons as this quantity could be more precisely determined from microscopic images). The width of the waveguide in the coupling section is 140 nm. The very strong geometric dispersion of the silicon waveguide is visible. Phase matching is predicted to occur at 1572 nm for the given geometrical parameters.

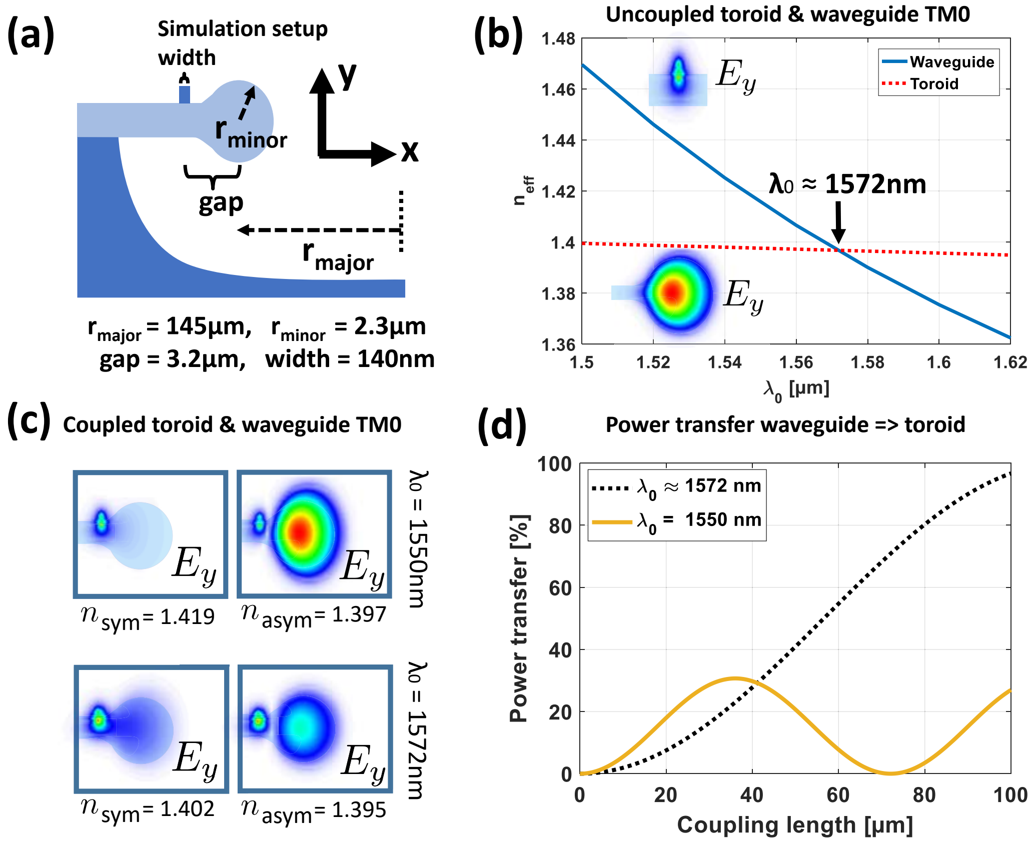

Figure 4.10: Simulated optical power transfer between the silicon waveguide and inverted microtoroid as a function of the coupling length and wavelength based on super-mode modeling with the help of FEM using conformal mapping. (**a**) Schematic of the simulation setup. (**b**) The effective index of the uncoupled silicon waveguide's (solid blue) and microtoroid's (dashed red) TM_0 ground modes. The effective indices are crossing at a wavelength of $\lambda \approx 1572$ nm. (**c**) Coupled symmetric and antisymmetric TM_0 super-modes for two different wavelengths of $\lambda_1 = 1550$ nm and $\lambda_2 = 1572$ nm. (**d**) Maximum possible power transfer as a function of the coupling length between waveguide and microtoroid for the two selected wavelengths.

Figure 4.10(c) shows the field distributions for the symmetric and the antisymmetric super-modes of a silicon waveguide coupled to a microtoroid at two selected wavelengths of λ_0 =1550 nm and 1572 nm. The theoretical maximum power transfer is between 35 % for λ_0 = 1550 nm and reaches up to 100 % for λ_0 =1572 nm (Fig. 4.10(d)).

Therefore, even for a lithographically defined waveguide-to-microtoroid distance, phase matching can be achieved by tuning the wavelength if the gap is sufficiently close to the target. Also, the desired coupling point can be accessed in case the coupling length is long enough. In this work, the coupling length is about 60 µm for a weakly tapered junction (see Section 2.3.5)).

These 2D-simulation results act as a proof of concept study for the proposed inverted microtoroid. The gap between the waveguide and the inverted microtoroid is fixed by design and can only be slightly adjusted by changing the power level or spot size during laser reflow. Therefore, a significant result of this 2D-simulation is the dependency of the coupling efficiency on the wavelength, due to the different dispersion of the silica microtoroid and the silicon waveguide (Fig. 4.10 (b)). In case of a conventional microtoroid, the gap can be almost freely adjusted and therefore the coupling strength. In case of an inverted microtoroid, the wavelength tunability primarily takes over this role.

4.2.6 Optical simulation of a silicon heat spreader

Another potential issue that needed to be validated by simulations is whether the heat spreader out of silicon can spoil the resonator's quality-factor due to the nearby presence of a high refractive index structure. A series of simulations, using conformal mapping, were performed, assessing the quality-factor of a microtoroid with a major radius of 145 µm and a minor radius of 2.3 µm as a function of the distance (d_3) between the center of the inverted microtoroid and the edge of the heat spreader. The offset to the rim of the suspended silica membrane is fixed to be 8 µm. Figure 4.11 (a) shows a schematic cross-section view of the simulated structure. In Figure 4.11 (b), the simulated loaded bending limited quality-factor is shown as a function of d_3.

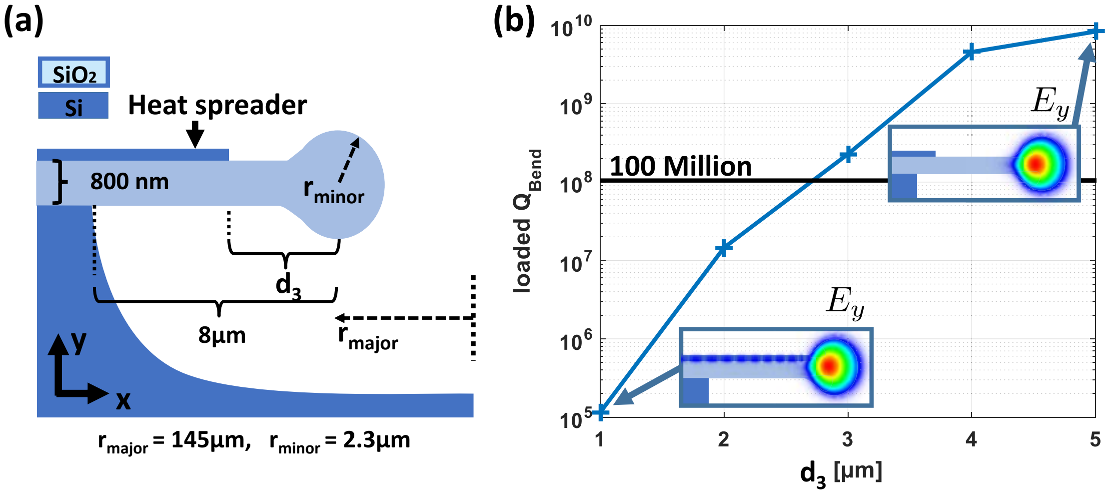

Figure 4.11: FEM simulations of the loaded quality-factor as limited by bending losses and evanescent losses to the heat spreader as a function of the distance d_3 between the microtoroid center and the edge of the heat spreader. (**a**) Schematic of the simulation setup. (**b**) Graph of the loaded quality-factor as a function of the distance to the heat spreader. Simulations are indicating that a distance above 3 µm is sufficient to provide a loaded quality-factor of about 100 million so that the simulated loss channels should then become negligible compared to excess coupler losses and fabrication related losses.

The presence of the heat spreader is expected not to spoil the expected quality-factors if d_3 is larger than 3 µm since the loaded quality-factor as limited by evanescent coupling to the heat spreader then stays above 100 million. Since in the fabricated devices d_3 is always larger than 5 µm, direct evanescent coupling to the heat spreader should not play a determining role in the recorded quality-factors.

4.2.7 Optical simulation of the final device

The final intrinsic quality-factor of an inverted microtoroid is not known apriori. Also, the simulation tools in use are not taking any surface roughness, structural inhomogeneities, like a melting-induced varying r_{minor} into account. However, in order to simulate the 3D-geometry of the coupling section, several 3D-FDTD simulations are performed, assuming a weakly tapered silicon waveguide (see Section 2.3.5) located at different gaps from an inverted microtoroid. The microtoroid in the simulation has a major radius r_{major} = 145 µm and a minor radius r_{minor} = 2.3 µm. Inside the coupling section, the weakly tapered waveguide has a curvature 1.2 times larger than the major radius of the microtoroid. As a full 3D-Simulation of the whole device would take too long only the coupling part together with a section of the ring is simulated. The simulation area has a size of 200 µm times 48 µm. Simulating this reduced area still takes approximately five days on a high-performance computer, even when using adaptive meshing.

Figure 4.12 shows the setup of the 3D-FDTD simulation. A power-normalized TM_0 mode, which was previously calculated with FEM, is used as a source mode. The light is propagated through the waveguide (from the left). The waveguide is tapered down while approaching the rim of the microtoroid. A gap (defined as the center-to-center distance) between the microtoroid and the waveguide is causing a particular coupling κ of the light from the waveguide into the microtoroid.

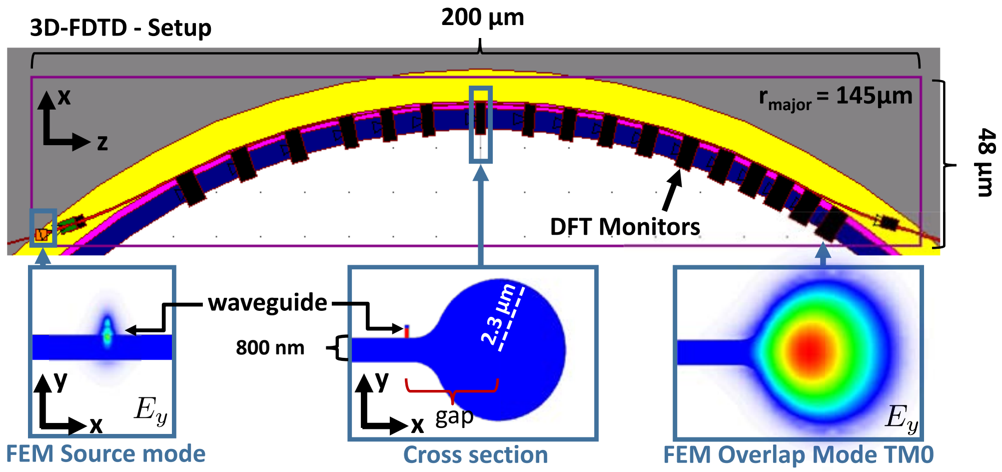

Figure 4.12: Simulation setup of a 3D-FDTD simulation of a monolithically coupled inverted silica microtoroid using a weakly tapered silicon waveguide as a coupler. A previously simulated TM_0 waveguide source mode is launched inside a weakly tapered gap coupler (from the left) and is coupled to an inverted microtoroid. The gap is defined as the smallest distance from the microtoroid center to the waveguide center. Due to the high computational effort, it is not possible to simulate the full structure. Therefore, only a segment of the structure is simulated (200 µm times 48 µm). At the end of the simulation time, the resulting fields inside the microtoroid are full-vectorial overlapped with a previously simulated TM_0 mode.

This way it is possible to calculate how much of the light from the source mode is ending up in the microtoroid's TM_0 mode. The gap required to obtain critical coupling for a given loaded quality-factor Q_L, assuming no excess losses, can be extracted from the simulated coupling strengths κ (for example, assuming Q_L to be half the intrinsic quality-factor).

Figure 4.13 shows the theoretical loaded quality-factor Q_L for TM_0 that is related to the simulated coupling strength κ (assuming critical coupling) as a function of the gap for different wavelengths and waveguide widths on a logarithmic scale.

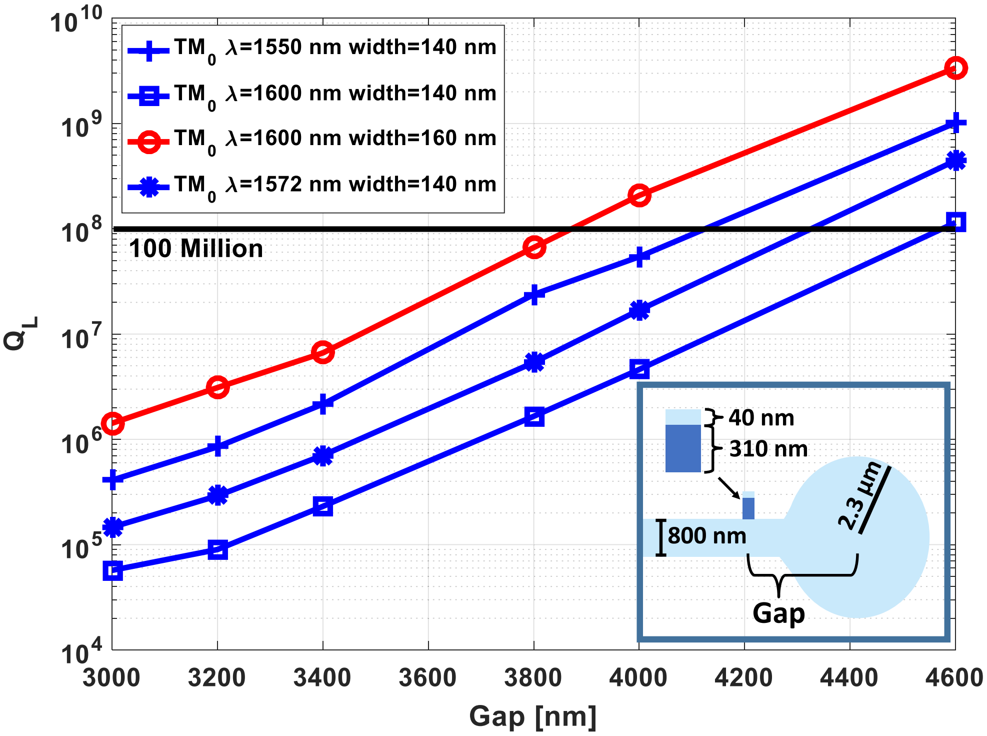

Figure 4.13: Graph showing the waveguide-to-microtoroid gap required to obtain critical coupling as a function of the expected microtoroid quality-factor. Q_L is the resulting loaded quality-factor, for example, half the assumed intrinsic quality-factor, assuming no excess coupling losses. Simulations were done with 3D- FDTD. The inset shows a schematic of the microtoroid and waveguide cross-section in the plane where the waveguide is closest to the microtoroid.

For a fixed gap, a longer wavelength means a lower potential quality-factor, as the light is less confined inside the waveguide and is causing a stronger coupling into the microtoroid. As evanescent power transfer causes the coupling, a wider gap causes an exponentially decaying coupling strength κ with increasing gap. Also, by comparing different tapered silicon waveguide widths in the coupling section, it is apparent that for wider waveguides the light is more confined, therefore resulting in lower coupling strength. By changing the wavelength within a range of 50 nm, the coupling strength can be adjusted for quality-factors that differ by one order of magnitude, which is an essential feature as the intrinsic quality-factor, as limited by fabrication related non-idealities, is not possible to be predicted apriori. For example, a microtoroid with a fixed gap of 3400 nm to the center of a waveguide with a width of 140 nm can be critically coupled with real quality-factors between $2 \cdot 10^5$ and $2 \cdot 10^6$ by changing the wavelength from $\lambda = 1550\,\text{nm}$ to $\lambda = 1600\,\text{nm}$.

However, as simulations might not be perfectly accurate since they rely on Perfectly Matched Layers (PML) acting as absorbing boundary conditions, which can be problematic when extremely small losses are being modeled, the results of these simulations are understood to help to formulate initial fabrication goals.

4.3 Discussion

Several attempts can be carried out to improve the proposed IVT. First, the initial input coupling efficiency from a lensed fiber to the inversely tapered waveguide can be improved by adding an oxide cladding. This way the symmetry in $y-$direction is improved which can lead to a higher coupling efficiency. Also, an oxide cladding would improve the handling stability and cleanliness of the waveguides (including interconnect-transition waveguide) in general as they are not exposed to the environment directly anymore. Cleanliness here is meant that foreign particles cannot directly deposit onto a waveguide. Even though this seems quite manageable, the current fabrication flow and the environment do not allow this step to be done straightforwardly.

The transmission waveguides themselves are situated on top of a comparably thin buried oxide layer, which can cause substrate leakage when their width gets too small (Fig. 4.5). The oxide layer needs to have a minimal thickness avoiding this leakage. In principle, a thinner BOX would allow for a higher bending radius of the microtoroid by not affecting its intrinsic quality-factor. Therefore, a thinner BOX layer from the perspective of the microtoroid would be desirable. As an undercut-etch in the silicon substrate is done anyway, an attempt would be to define small circles placed in parallel to the waveguides as opening holes in the BOX. These opening holes will cause the waveguide to be undercut, which would allow for thinner BOX thickness as the substrate leakage is reduced. This attempt will be further discussed in the prospect Section 7.2.3 of this work.

A fundamental parameter that is used for adjusting the coupling strength between microtoroid and waveguide is the wavelength, which can change the coupling strength by approximately one order of magnitude (Fig. 4.13). In return, this means that the bandwidth (the span in which resonances of the microtoroid have an acceptable extinction as a function of wavelength) is smaller compared to a conventional microtoroid. Of course, this implies that the proposed IVT can become unemployable for applications that need a broader bandwidth than the device can support.

Up to now, only TM-polarization is under consideration as this theoretically leads to higher intrinsic quality-factors for the inverted microtoroid. However, most devices in SiP rely on TE-polarization due to the usage of grating couplers. In principle, it would be purposeful to test the proposed device with the common TE-polarization, avoiding the necessity of integrated polarization converters when coupling to other devices on the same chip. Also, grating couplers are usually more suitable for TE-polarization allowing for a denser integration of the microtoroid as no extensive routing of waveguides to the chip edges is required.

Combining a grating coupler with an oxide cladding and a local undercut, the coupling efficiency can be high. In the current setup entirely etched TE grating couplers showed a coupling loss per coupler in the order of 8 dB at a wavelength of $\lambda = 1590\,\mathrm{nm}$. This high coupling loss is likely caused by the relative thin BOX.

Chapter 5

Fabrication - The monolithically coupled inverted silica microtoroid

A significant part of this thesis is dedicated to the development and the realization of the fabrication steps of the proposed inverted silica microtoroid described in Section 4.1. Each fabrication step needs to be optimized, tested and designed to create the device in the desired monolithic way. The following chapter deals with the two fabrication parts. The first part (Section 5.2) is entirely done in a cleanroom environment, whereas the second part is done in a lab environment (Section 5.3). Section 5.1 gives a detailed outlook of the two fabrication parts. The subsequent Sections explain the different fabrication steps in further detail.

5.1 Fabrication outlook

As a fabrication platform, a high-grade, industry compatible 8-inch silicon-on-insulator (SOI) wafer is used. It is desirable to use SOI wafers that can be bought out of stock, avoiding costly contracted work. Furthermore, the integration with other devices would be more straightforward, in case the design of the microtoroid is in accordance with standard wafer specification. The SOI system, provided by Soitec with the part number $G8P-208-01$, has a nominal silicon device-layer thickness of 310 nm with a 10 nm 3σ deviation. The crystal orientation of the silicon is specified to be in (100) direction. In-house SEM measurements showed excellent conformity. The BOX layer is specified to have a target thickness of 800 nm with a 6 nm 3σ deviation. The handle silicon wafer has a thickness of 725 µm and crystal orientation in (100) direction.

The first part of the fabrication flow can be subdivided into four process modules carried out entirely in a cleanroom environment: The waveguide definition, the circular opening definition, the silicon undercut, and the final dicing and cleaning step. The second part of the fabrication consists of the CO_2-laser reflow carried out on a dedicated setup. Figure 4.1 (a) shows the targeted device after performing the first part of the fabrication process, whereas Figure 4.1 (c) shows an SEM image of the melted device in cross-section view after additionally performing the second part of the fabrication process.

In the following, the two fabrication parts with their submodules are summarized:

1. Part 1 - Fabrication of the device (Section 5.2):
   (a) Preparation and electron-beam lithography (EBL): An 8” SOI-wafer is diced up into 20 by 20 mm chips. After a standard cleaning procedure (Appendix B), the chips are further processed by writing a waveguide mask into HSQ resist using EBL. Also, heat spreaders, stabilization bridges, and other parts are defined in this step.

   (b) Device layer fabrication: Subsequently the silicon-structures are etched, by a mixed gases dry-etch process using SF_6 and C_4F_8, into the silicon device layer of a chip at a processing temperature close to room temperature.

   (c) Circle definition: A chip is spin-coated with optical resist (Appendix C). By using optical lithography, holes are defined that are subsequently etched into the BOX by a dry-etch process, using CHF_3 plasma and Argon. For improving the anisotropy of the etch process, the inert argon is added [136].
   (d) Undercut of the BOX: Undercut into the substrate-silicon below the BOX-layer of about 30 µm in the lateral direction by a dry-etch process using SF_6. Due to the use of zero acceleration voltage, the dry-etch process becomes dominated by isotropic chemical etching. Also, no oxygen is involved in the etch process, as it would attack the photolithography resist used to protect the silicon structures.
   (e) Dicing and cleaning: Each chip is protected (Appendix C) and diced along the input and output edge-coupling sections.
   (f) Cleaning the chip: A wet-cleaning process is performed, and subsequently an oxygen plasma is applied. This cleaning step removes the resist layers accumulated during the previous fabrication steps which would disturb the subsequent reflow step.

2. Part 2 - Melting of the microtoroid (Section 5.3):
   (a) CO_2 laser reflow: The undercut circular silica-membrane is melted to form the inverted microtoroid silica-resonator in close proximity to the previously defined silicon-structures.

5.2 Part One - Fabrication of the device

The first part of the fabrication takes place in a dedicated cleanroom environment. Each sub-flow of the first fabrication part is studied and optimized separately before assembling the process steps for fabricating the final device.

Special care was taken when developing the process for fabricating the waveguides. Roughness, geometrical offsets (like missed fabrication targets) can lead to waveguides with increased optical loss. In the coupling section between the waveguide and microtoroid, the tapering is optimized in a way that the desired width is met. Furthermore, the transition sections in which an interconnect waveguide was tapered down was optimized to be as smooth as possible, providing adiabatic mode coupling between the different sections of the waveguide.

In particular, the undercut-etch process was studied as surface-roughness induced by the etching plays a significant role, as any roughness will affect the shape of the final microtoroid.

For all the etching processes of the first fabrication part, an Oxford PlasmaPro 100 ICP system with an ICP source diameter of 300 mm was used.

A silicon wafer was used as a carrier for the chips, potentially allowing scaling up of the process from chip to wafer level without changing process biases, as the underlying silicon carrier wafer was etched simultaneously resulting in the same loading effects during critical silicon etches. In fact, up to four chips were processed in parallel without noticeable process bias. Fomblin oil was used for establishing a thermal coupling between the chips and the carrier wafer, cooling them down, and keeping them at a constant temperature of 15 °C to 20 °C.

5.2.1 Preparation and Electron-beam lithography

First, a wafer (see Section 5.1 specifications) is protected with resist and diced into chips with a size of 20 by 20 mm each. After a standard cleaning method (Appendix B), to remove contaminations, the chips are prepared for further processing.

Electron-beam lithography

Electron-beam lithography (EBL) is widely used for creating features down to the nanometer scale. Initially, EBL systems were developed based on SEM systems [137]. Throughout this work, a RAITH 150 TWO - EBL system is used for fabrication. In an EBL system, a beam of focused accelerated electrons is used to interact with photoactive resist like polymethylmethacrylate (PMMA) (positive) or like HSQ (negative). In the case of positive resist electron irradiation breaks polymer bonds in the resist that is causing a lower molecular weight, which can be selectively washed away by a developer, leaving a resist pattern with a positive tone. In case of a negative resist, irradiated areas are cross-linked. A suitable developer is only removing the non-cross-linked areas, leaving a negative resist pattern [137]. As EBL is a sequential writing process, the downside of this technology is the long writing time. It would take too long to write all parts of the proposed IVT system with the help of an EBL system.

For the proposed device of this thesis, a chip is coated with a layer of negative HSQ resist (Dow Corning XR-1541) with a thickness between 20 nm to 100 nm. For electron exposure, an acceleration voltage of 10 KV, a beam current of 198 pA and a base dosage of 185µC/cm^2 are used. The resist is developed subsequently in tetramethylammonium hydroxide (TMAH) developer (concentration 25%) for 75 seconds. Afterward, the chip is cleaned in high purity water (DI-water).

Figure 5.1 shows a top view of an extract of a standard EBL-pattern used for the proposed device and a zoom of the different parts, including the output section with an inversely tapered edge coupler and the microtoroid section that consist of the heat spreader and the coupling section with its weakly tapered gap coupler. The waveguide is defined to possess a left turn which ensures that the input- and output- coupling sections are not situated on a straight line, which reduces direct light illumination from the input to the output and therefore suppresses direct stray light when coupled later on to an external laser source.

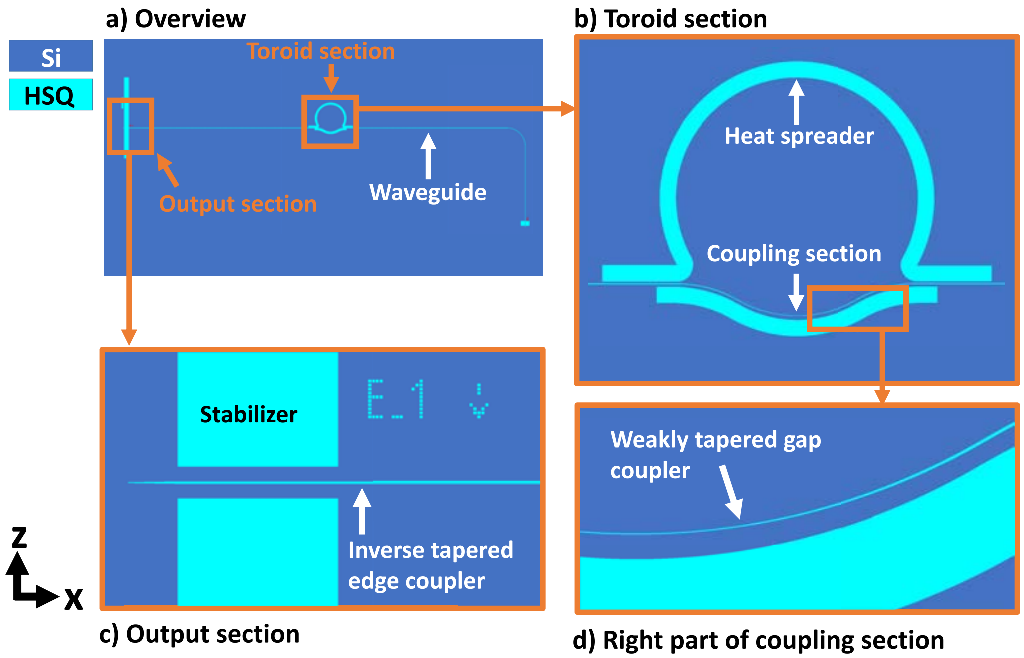

Figure 5.1: (**a**) Top view of an extract of a standard EBL-pattern used for the proposed IVT. The EBL-pattern consists of the input and output section, the microtoroid section, and the transition waveguides. The pattern in the input and output section defines the inversely tapered edge-coupler and stabilizers (**c**) that are protecting the coupler from breaking off. This protection is necessary as the coupler, later on, sits on an undercut membrane (see Section 6.1.2). The microtoroid section (**b**) contains the weakly tapered gap coupler (**d**) and the heat spreader.

For hitting the desired fabrication target, regarding the waveguide width in each section, the dosage used during EBL needs to be adjusted and tested. Special care has to be taken in the tapered sections of the waveguide and its connection points to the regular transition/interconnect waveguides. The dosage is gradually adjusted from the base dosage of $185\mu C/cm^2$, depending on the desired feature size. Figure 5.2 shows a comparison of an optimized writing process and an unoptimized writing process of the coupling section (see also Fig. 5.1(d)). In the unoptimized case, the point between thinnest waveguide width and tapering region is not matched (labeled as Defect in Fig. 5.1(a)). Therefore, the connection area acts as a non-adiabatic transition area, which induces optical loss. This can be crucial in the coupling section as the mode is only loosely guided and is affected by the waveguide sidewalls.

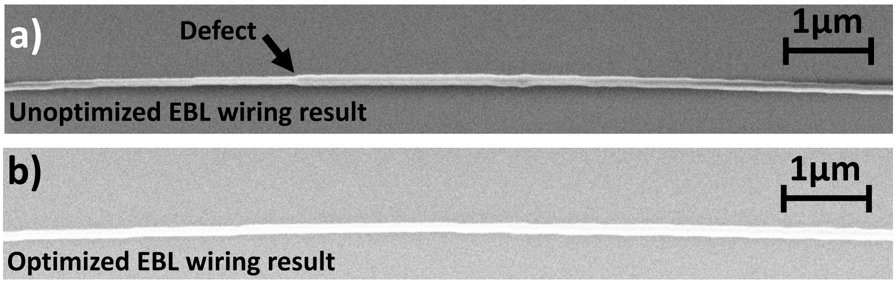

Figure 5.2: Comparison of coupling section waveguides after silicon-etching for two different EBL-dosages. (**a**) SEM-image that shows slight defects origin by an unoptimized EBL writing process versus (**b**) SEM-image of the optimized result.

The dosage needs to be further adjusted to guarantee smooth edges when the structures are subsequently developed. Rough edges in the resist cause the structures to take up the roughness during etching, which can lead to a substantial optical loss.

Figure 5.3 compares a resist test pattern (for transition/interconnect waveguides) for an unoptimized dosage versus an optimized dosage for EBL exposure. An optimized dosage leads to a structure with the targeted width while additionally having smooth edges. For finding the optimal dosage as a function of the structure's geometric parameters, several dosage tests for various structure sizes have been done and analyzed.

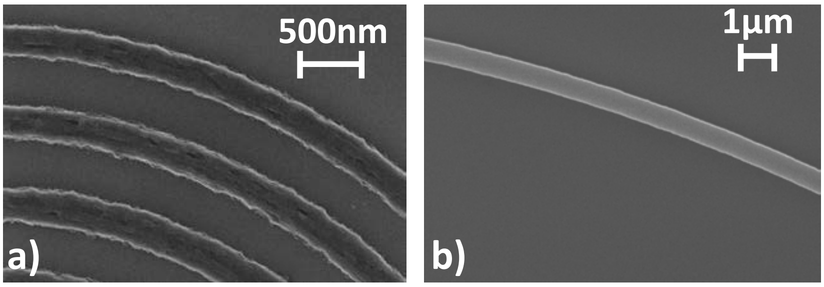

Figure 5.3: An example of EBL-dosage optimization for two different transition waveguide test structures before silicon etching. (**a**) Unoptimized rough pattern after development due to unoptimized dosage during EBL writing. (**b**) The dosage, which is used during EBL-exposure and the development process is optimized and shows smooth edges.

Furthermore, the time the chip is developed in TMAH has a crucial impact on the geometric properties of the structures. If the developing-time is too long, the structures can get overdeveloped. Overdevelopment can lead to undercutting the resist among other problems. On the other hand, in case the structures are not developed long enough, residual resist can remain on the chip in the region where it should have been normally removed, acting as parasitic micro-masks.

5.2.2 Waveguide fabrication

In the following, the fabrication process of the silicon waveguides is described.

Etching process

For etching the waveguide based on the written EBL resist pattern (see Section 5.2.1), different processes can be used alternatively. In this work, two dry-etch processes for silicon etching were investigated. Both dry-etch processes rely on reactive-ion etching with inductively coupled plasma (ICP-RIE) technology.

One dry-etch process which was investigated is a cryogenic process at a temperature of $-130\,°\mathrm{C}$. The process is based on sulfur hexafluoride (SF_6) and oxygen O_2. In a cryogenic etch process, SF_6 is used to provide fluorine radicals that have the capability of etching silicon in the form of silicon tetrafluoride (SiF_4) gas. During cryogenic etching, a blocking layer of oxide and fluoride with a thickness of 10 nm to 20 nm is formed on the sidewalls. Due to the low temperature, the attack of fluorine radicals on this layer is inhibited, leading to sufficient sidewall protection, which is enabling vertical etch profiles, as desirable in the case of a waveguide. Usually, the etch rate of mask material is reduced drastically leading to a higher etch selectivity between mask material (for example photoresist or SiO_2) and silicon [138]. Table 5.1 is showing typical process parameters for a cryogenic ICP-RIE silicon-etch used in this work. As long cooling time and process stability was an issue in this process, later on, it was not further used and investigated.

Temp.	SF_6	O_2	Chamber Pressure	ICP Power	RIE Power	DC Bias	Duration
-130 °C	37 sccm	9 sccm	6 mTorr	700 W	100 W	70 V	30 s

Table 5.1: ICP-RIE process parameters for cryogenic anisotropic silicon dry-etch.

The second dry-etch process that has been investigated is a mixed gases process using SF_6 and octafluorocyclobutane (C_4F_8) close to room temperature. The SF_6 is used to provide fluorine radicals for etching silicon. The sidewall and mask protection is provided by fluorocarbon polymer originating from the interaction of C_4F_8 and the inductively coupled plasma (ICP) [138]. Table 5.2 shows the typical optimized process parameters that were used for etching waveguides in this work.

Temp.	SF_6	C_4F_8	Chamber Pressure	ICP Power	RIE Power	DC Bias	Duration
15 °C	25 sccm	50 sccm	20 mTorr	1200 W	30 W	240 V	75 s

Table 5.2: Optimized ICP-RIE process parameters for mixed gases silicon dry-etch. This table shows the optimized process parameters for the silicon-etch used in this work. During this process step, edge couplers and their stabilizers, transition waveguides, coupling section waveguides and heat spreaders of the IVT system are fabricated.

As the mixed gases process has the advantage that it can be done at room temperature, no time-consuming cooling-step of the process chamber needs to be done. Furthermore, even small temperature deviation of a few kelvins can lead to a change in the sidewall angle when doing a cryogenic etch. The mixed gases process showed to be much more tolerant of temperature deviations. Therefore, the mixed gases process is primarily used in this work.

Sidewall roughness and optical waveguide losses

As a figure of merit for the waveguide fabrication, the sidewall roughness and the steepness of the sidewalls need to be investigated and optimized. Any significant roughness can act as scattering points for the guided light and therefore can cause optical losses. Steepness is related to the angle of the sidewall of the waveguide. The sidewall ideally needs to be perpendicular to the surface of the chip.

It should be noted that during the etching process, two other defects could occur. One is caused by a lateral attack of the mask (lateral mask erosion) during etching, which can induce roughness that later on is taken up by the waveguides sidewalls. In Bosch or cryogenic-like processes, the vertical etching relies on a sidewall protection mechanism during etching. If this sidewall protection mechanism locally breaks down, so-called notching can occur. Notching is a lateral undercut of the waveguide at the point between underlying BOX and waveguide bottom. It can be caused by the partial charging of the underlying BOX, which pushes ions into the corner of the etched waveguide and therefore can remove the sidewall protection of the waveguide in the bottom region.

Figure 5.4 (a) shows a part of the heat spreader together with a fabricated waveguide. The sidewall angle is found to be perpendicular to the chip surface.

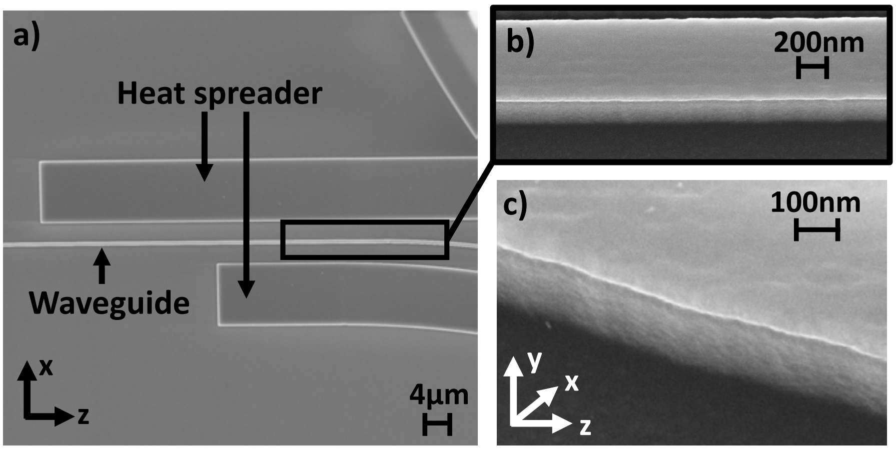

Figure 5.4: SEM images of optimized transition waveguides after fabrication. (**a**) Top view SEM image that shows a part of the heat spreader together with a fabricated waveguide. (**b**) Slightly tilted top view zoom SEM image of the fabricated waveguide shown in (**a**). (**c**) Further tilted SEM image of the same waveguide.

The sidewall roughness was not further investigated once no defects or etching induced roughness was noticeable. Figure 5.4 (b) shows a zoom image of the waveguide and (c) shows an image of the same waveguide taken under an angle.

5.2.3 Silicon heat spreader

Supporting silicon frames (or heat spreaders) are introduced in the silicon device layer (like any interconnect waveguide elsewhere on the chip) with the dual function of acting as a heat spreader for fine-tuning of the silica membrane melting process as well as to provide substantial mechanical stabilization of the free-standing membranes (compare also Fig. 4.1). In the same manner, the input and output edge-coupling regions at the chip edges are stabilized by silicon stabilizers (compare Fig. 4.2.2 (a)), which will be further discussed in Section 6.2.1.

Suppression of wobbling

The region in which the silica membrane merges with the non-undercut silicon substrate is subjected to high local strain, which can lead to a deformation of the membrane (wobbling) (see Figures 5.5(a) and (b)).

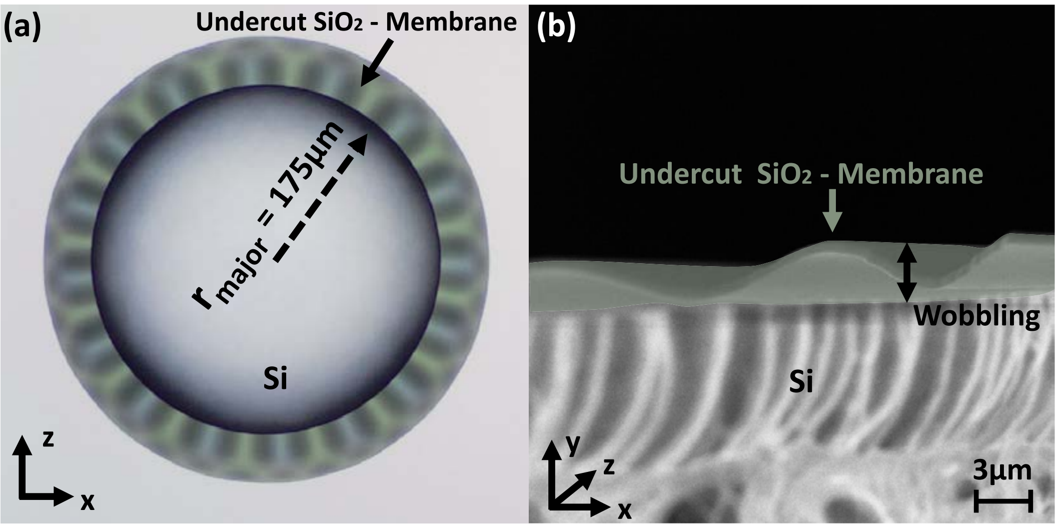

Figure 5.5: Wobbling of the undercut silica membrane in the absence of a heat spreader. (**a**) The Top view is taken with an optical microscope and (**b**) side view SEM image revealing wobbling of the membrane (green shaded) with a wobbling-amplitude of several µm.

Even in top view, the wobbling is visible. Wobbling of the membrane, after undercut due to built-in strain in the thermally grown BOX, has been observed in all fabrication runs. Even though this wobbling typically was suppressed after reflow, it leads to concerns, as residual wobbling might lead to a reduction of the resonator's quality-factor.

In addition to the wobbling, broken membranes have been observed in extreme cases. As the severity of the wobbles increases with the depth of the undercut, this can restrict the addressable design space. For these reasons, it was concluded that it would be highly advantageous to have a mechanically stabilizing structure in the form of a frame etched into the silicon device layer and straddling both the undercut and non-undercut regions of the silica film.

An annularly shaped silicon heat spreader, etched into the silicon device layer at the same time as the waveguide, surrounding the microtoroid and the silicon waveguide carries out two functions, the desired stabilization effect and the heat spreading effect for fine-tuning of the silica membrane melting process (see Figs. 5.6(a)). The heat spreader is partially situated on top of the undercut region and partially on top of the non-undercut region. This overlay is resulting in a more mechanically stable membrane. Figures 5.6 (a) and (b) show a top view of the heat spreader and the undercut membrane with an overlay of 3 µm. It is apparent that the wobbling of the free-standing silica membrane is suppressed, which greatly increased the reliability of the fabrication process.

As the heat spreader is written in the same step as the waveguide by EBL, the relative position between the heat spreader and the silicon waveguide is only limited by the precision of the electron lithography machine (in the order of nanometers) (see Fig. 5.6(b)). The opening hole in the silica layer is defined, later on, by optical contact lithography. The relative position of the waveguide to the center of this hole has a precision in the order of 1 µm, limited by the precision of the mask aligner.

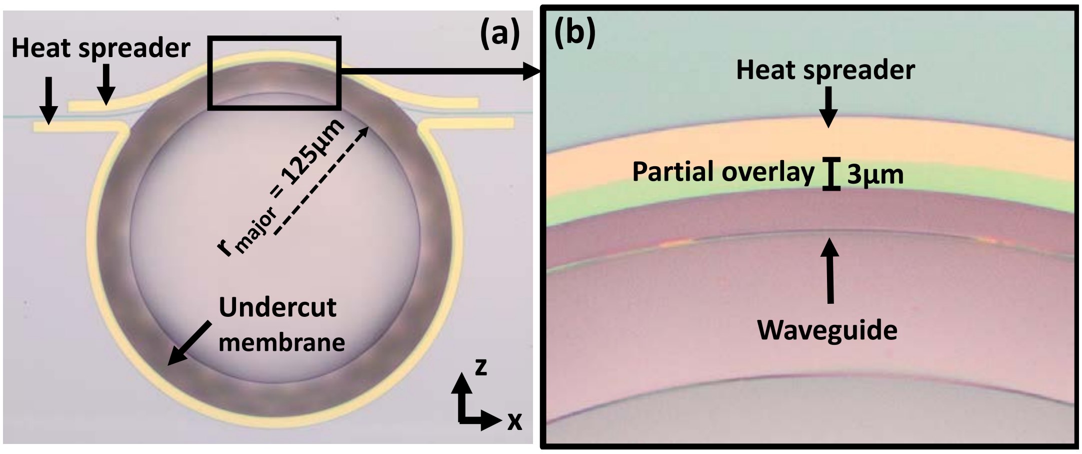

Figure 5.6: Mechanical stabilization of the undercut membrane by means of a heat spreader. (**a**) An intact membrane with much-reduced wobbling by means of a heat spreader. (**b**) Detailed view showing the heat spreader reaching 3 µm into the undercut region of the silica film (blue: non-undercut region with no heat spreader, yellow: non-undercut region with heat spreader, green: undercut region with heat spreader (partial overlay), light mauve: undercut region without heat spreader, deep mauve: etched away silica film).

The introduced stabilizing heat spreader also reduces the thermal resistance to the substrate once the microtoroid approaches its vicinity and stops the reflow process. Since it is defined at the same time as the waveguide, it dramatically improves the overlay accuracy between the waveguide and reflown microtoroid. Moreover, since the anisotropic dry etch used for waveguide definition has nanometric roughness, the latter is also greatly improved.

Thermal simulation of heat spreading performance

For validating the heat spreading functionality of the silicon frame (the heat spreader), a 3D thermal simulation was done, corresponding to the modeling in cylindrical coordinates of the device cross-section shown in the inset of Figure 5.7 with FEM using the commercially available COMSOL package.

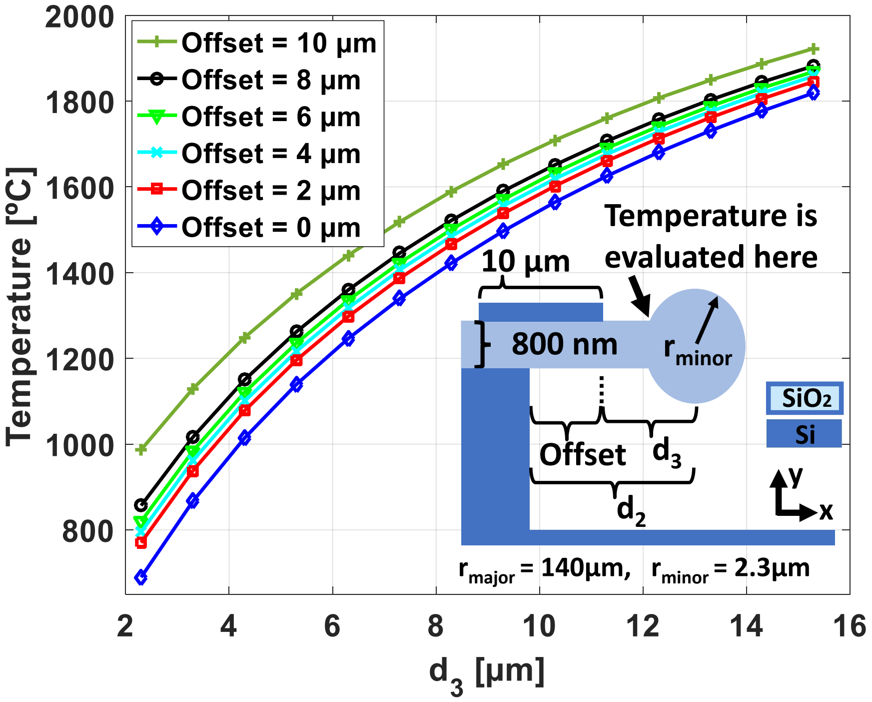

Figure 5.7: Simulation of the effect of the heat spreader on heat sinking during microtoroid reflow. The cross-section shown in the inset is simulated in cylindrical coordinates. In the simulation setup, the microtoroid itself is designed as a heat source calibrated to result in the typical temperatures for high-purity silica reflow (~1650 °C). The distance d_3 between the heat spreader and the microtoroid is varied and the simulation repeated for different values of the parameter “Offset” that would in practice result from fabrication tolerances (overlay between lithography steps and depth of undercut). It is apparent that even though a large span of Offsets is considered, the curves remain clustered, pointing to the distance to the heat spreader d_3 as the primary determining factor.

In the simulation setup, the microtoroid core is heated by a constant heat source, calibrated to lead to a maximum temperature of approximately 1650 °C at the microtoroid's surface when the heat spreader is not present, and the distance d_2 between the edge of the microtoroid and the edge of the undercut is 8 µm. The simulation is done for different microtoroid to heat spreader distances d_3 in order to monitor the effectiveness of the silicon frame as a heat spreader (see Fig. 5.7) for a constant, typical heat spreader width of 10 µm.

The heat spreader overlays with the undercut region by an amount labeled as "Offset". For example, when offset equals 0 µm, the heat spreader is located entirely in the non-undercut region, and when the offset equals 10 µm, the heat spreader is located entirely in the undercut region.

As the offset is varied from 2 µm to 8 µm, the distance d_3 resulting in a 1650 °C microtoroid temperature sustaining melting of the silica varies by less than 1 µm (with an average value around ~10.7 µm). It is apparent that even though a large span of Offsets is considered, the curves remain clustered, pointing to the distance to the heat spreader d_3 as the primary determining factor for the reflown microtoroid radius.

5.2.4 Circle definition and silica-etching

Subsequent to the fabrication of the waveguide and the heat spreader, in the next step, a circle definition is performed. A chip is coated with hexamethyldisilazane (HMDS), which is an adhesion promoter for optical resist. The optical resist in use is AZ 5214E by MicroChemicals in its positive form with a final thickness of about 1.5 µm.

For defining the circles, optical contact lithography is used. As the circles have at least a radius of 125 µm, EBL would be too time-consuming for their definition. With the help of markers, an optical mask is aligned to the previously created waveguides and heat spreaders with a precision of approximately 1 µm and better. For optical contact lithography, a SÜSS MicroTec MA6BA6 mask aligner is used. Figure 5.8 (a) shows a scheme of the device after circle definition and resist development in top view. Also, the markers ((b) and (c)) for performing the mask alignment (after fabrication) are shown. In this case, the alignment precision in $z-$and $x-$direction was about 500 nm.

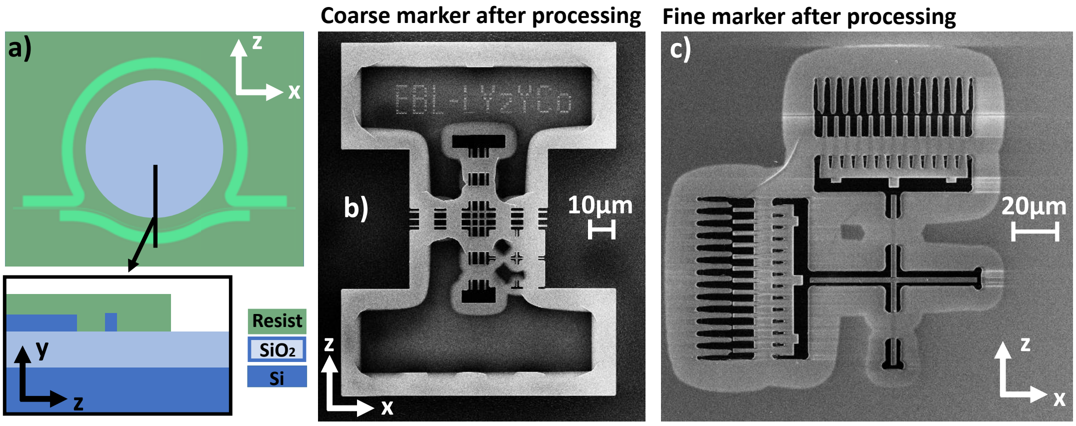

Figure 5.8: Setup and markers for optical contact lithography for circle definition in silica. (**a**) Top view schematic of a circle after optical lithography and resist development. The circle (light blue) is defined using optical lithography and needs to be aligned. (**b**) Coarse alignment marker after fabrication. The coarse-marker is aligned with crosses previously defined via EBL. Three coarse-markers with an inter-chip-distance of about 10 mm are available. By aligning two coarse-markers simultaneously, also a chip rotation can be balanced out. (**c**) Image of the fine-marker after fabrication. For further increasing the precision of the alignment during optical lithography, two fine-markers are available. The fine-markers consist of a center cross and two Vernier structures. This way a final alignment precision of better than 1 µm is possible.

After optical lithography, the opening holes are developed with AZ 726 MIF. For etching the circles, the same Oxford PlasmaPro 100 is used as for etching the waveguides (see Section 5.2.2). The dry etching of silica in the RIE is done with fluoroform (CHF_3) gas. This gas provides the fluorine radicals and leads to a primarily isotropic chemical etch, whereas the additionally added inert Argon gas causes inert ion bombardment (ion milling) of the surface and therefore gives rise to an anisotropic etch profile [136].

The ratio of CHF_3 and Argon mainly determines the etch profile. The available ICP-RIE system is a shared system for silicon and silica-etching. For maintaining the Si process stability, a silica-etch is only allowed without using the ICP mode. Figure 5.9 a) and b) show the etching result. The sidewall angle is approximately 70°. As the sidewall part will be reflown, the sidewall angle was not further optimized but might be the subject of future investigations.

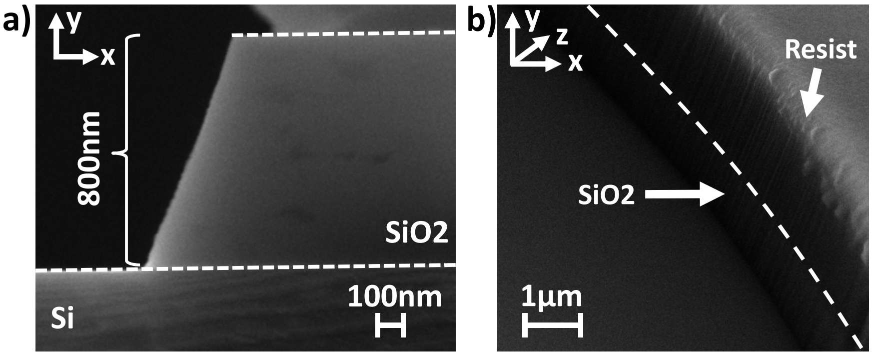

Figure 5.9: Steepness and roughness of SiO_2 circle etching result. (**a**) SEM side view image of etched SiO_2. The sidewall angle is approximately 70°. (**b**) Tilted SEM side view image of etched SiO_2. The optical resist mask used during etching is still present.

By adding additional Argon gas into the RIE-chamber, the sidewall angle may be improved to become more vertical since the ratio between CHF_3 and Argon is mainly determining the etch profile. An additional resist reflow before etching may lead to a smoother resist and therefore a smoother sidewall profile. However, as this part will be reflown, it is not considered the primary limiting factor, but can be the subject of future investigations. Table 5.3 gives an overview of the parameter set that is used for the SiO_2-etching.

Temp.	CHF_3	Argon	Chamber Pressure	ICP Power	RIE Power	DC Bias	Duration
15 °C	50 sccm	50 sccm	30 mTorr	0 W	100 W	430 V	50 min

Table 5.3: Optimized RIE process parameters for anisotropic mixed gases silica dry-etch. This table shows the optimized process parameters for the silica-etch used in this work. During this process step, the circles in the BOX-layer of the chip are opened. Later on, these circles will be undercut leading to free-standing membranes, which will be reflown, creating the inverted microtoroid.

Since the subsequent undercut-etch is highly selective between Si and SiO_2 (Section 5.2.5), it is essential that the circle is entirely etched through the BOX down to the substrate. The optical resist is not removed after this step.

Moreover, it serves as protection for the silicon structures (waveguide, heat spreader, stabilization bridges, and couplers) during the subsequent undercut.

Later on, these circular opening holes in the BOX layer of the chip will be undercut, leading to a formation of a free-standing membrane.

5.2.5 Undercut-etching in silicon

For performing an isotropic etch in silicon, two technologies are investigated. Xenon difluoride (XeF_2) has primarily been used for creating the undercut of conventional microtoroids [1]. In some cases also etches based on Sulfur Hexafluoride (SF_6) have been done [106]. XeF_2 is a solid (crystalline powder under ambient conditions) which can be sublimated with a vacuum pump. The chemical reaction of XeF_2 and Si leads to silicon fluoride SiF_4 [107, 108]. Since the existence of water in the etching chamber would lead to the formation of hydrofluoric acid (HF) (which attacks SiO_2), the chamber is purged with nitrogen before the etch step [57]. An unoptimized XeF_2-etch can lead to surface roughness. By adjusting the ratio between XeF_2 and nitrogen, the etch roughness can be minimized. Furthermore, using cycles of etching and purging of the chamber also influences the etch roughness. Figure 5.10 shows a comparison of an unoptimized and optimized XeF_2-etch (100 minutes etch time with 1:20 mass ratio of XeF_2:N_2).

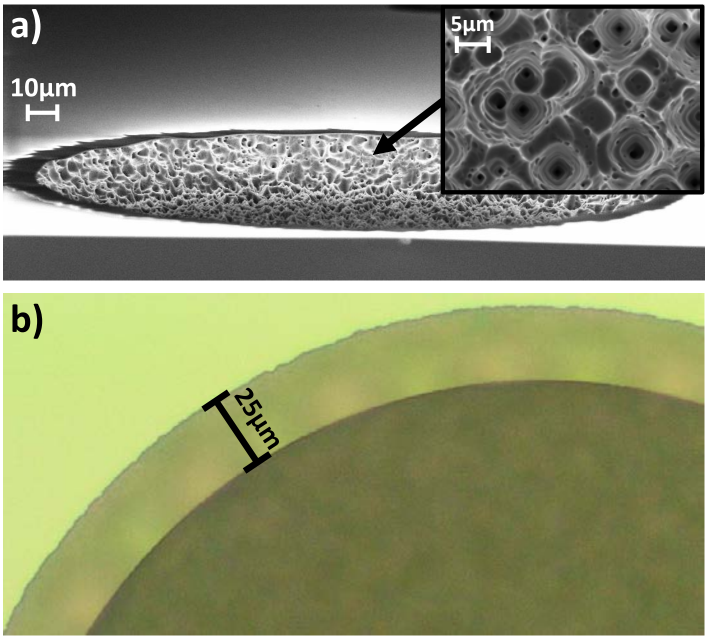

Figure 5.10: Comparison of an unoptimized XeF_2-etch versus an optimized XeF_2-etch. (**a**) A tilted SEM image shows one of the first XeF_2 undercut tests performed in the scope of this work. The inset shows a zoom of the same image. (**b**) Optical image of optimized XeF_2-etched inverted microtoroid with adjusted process parameters (100 minutes etch time with 1:20 ratio of XeF_2:N_2).

However, even the optimized XeF_2-etch shows considerable roughness, which will manifest in the melted resonator and will cause defects like micro-bendings which can lead to non-adiabatic mode transitions and therefore to a degradation of the intrinsic quality-factor. Also, the XeF_2 process is time-consuming, is not directly available in the cleanroom, and needs to be done by a collaborator.

As an alternative, a pure SF_6 dry-etch ICP-RIE process has been investigated for creating an isotropic undercut in the silicon substrate. SF_6 plasma lacks a native passivation mechanism at room temperatures. Therefore, pure SF_6 can be the base for an almost isotropic silicon-etch [139]. The SF_6 is used to provide fluorine radicals that have the capability of etching silicon in the form of Silicon tetrafluoride (SiF_4) gas [138]. By turning off the plate HF-power of an RIE and leaving the ICP power turned on, a high-density plasma can be generated with a low individual kinetic ion energy. The mechanism is considered to be radicals dominated instead of ion dominated [140]. This way the etch-process becomes isotropic.

Figure 5.11 (a) shows an optical image of an undercut silica membrane together with a zoomed image (Fig. 5.11 (b)). The roughness of the optimized SF_6-etch is lower than the roughness of the optimized XeF_2-etch. The SF_6-undercut-etch rate of approximately 6 µm/min is much higher compared to a XeF_2-etch rate of 250 nm/min. The SF_6 turned out to have several other advantages. Prolonged treatment with XeF_2 can make it very hard to remove an optical resist layer later on. Shorter treatment with SF_6 turns out to make the resist removal easier. However, the removal of the resist can be still challenging after a considerable processing time inside an ICP-RIE system. Another advantage is that the SF_6 etch can be done on the same machine as the other etch steps.

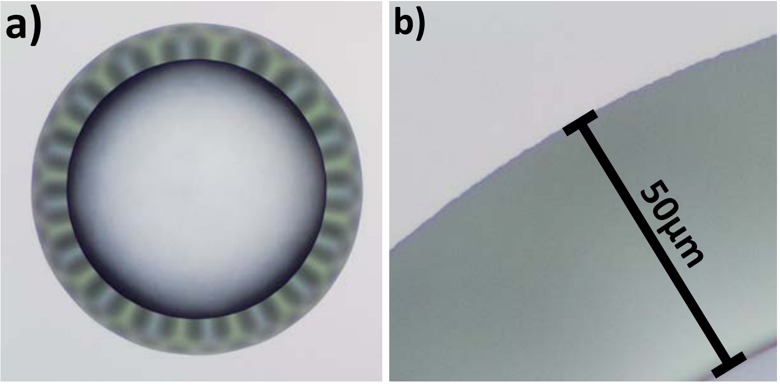

Figure 5.11: SF_6 based dry-etch process for etching an undercut in silicon. (**a**) Optical top view image of the inverted microtoroid. The undercut was etched using SF_6. (**b**) Zoom image of (**a**). The undercut is about 50 µm deep. The roughness of the etch-process is less compared to an optimized XeF_2-etch (see Fig. 5.10 (b)).

Table 5.4 gives an overview of the etch parameters used for the SF_6 undercut to achieve an undercut of about 30 µm. There is no oxygen involved in the etching, as this can attack the optical resist, which is used to protect the silicon structures.

The manufacturer Oxford is specifying the selectivity between Si and SiO_2 of a comparable process using a PlasmaPro 100 Cobra ICP-RIE system to be bigger than 500 : 1. The lower selectivity compared to XeF_2 (10000:1 [108]) turned out not to be a limiting factor.

Temp.	SF_6	O_2	Chamber Pressure	ICP Power	RIE Power	DC Bias	Duration
20 °C	50 sccm	0 sccm	30 mTorr	2000 W	0 W	-	290 s

Table 5.4: Optimized ICP-RIE process parameters for isotropic silicon-etch used for fabricating a silicon undercut.

Figure 5.12 (a) and (b) shows a comparison of how the undercut-etch-roughness of the two different etching processes manifests later on after reflow. The melting process with an SF_6 based undercut leads to a smoother microtoroid (Fig. 5.12 (b)). The heat spreader is even supporting this desired behavior.

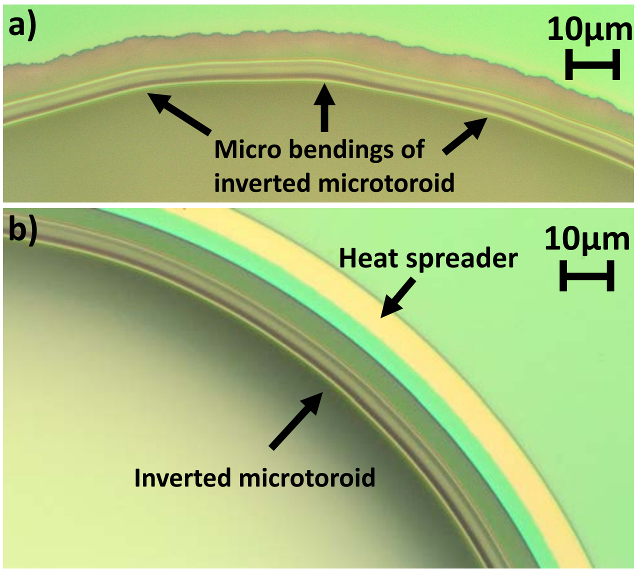

Figure 5.12: Comparison of the heat spreader and undercut-etch technology influence on the reflow homogeneity of an inverted microtoroid. (**a**) The roughness of the XeF_2-etching process manifests later on after reflow. The roughness is averaged out to a certain extent during the melting process of the microtoroid but still leads to undesired micro-bendings. (**b**) The melting process with an SF_6 based undercut has a more homogeneous melting rim. The heat spreader is even supporting this desired behavior.

5.2.6 Dicing and cleaning

A challenge for the proposed device is the dicing and cleaning procedure. As edge couplers are used later on for coupling light in and out, an optical fiber needs to be brought close for this purpose. For doing so, the chip is diced along the input and output edge-coupling-sections. Before dicing the chip, it is coated with a protective resist (AZ 520D by MicroChemicals) and baked out at approximately 110 °C for 5 minutes. The optical resist from the previous coating step is not removed, which makes the additional resist coating challenging.

For the dicing procedure, an ADT 7100 series dicer with an MCT R46 54130 blade is used. The cut has a width of about 30 µm. A dicing-blade can be aligned in the horizontal direction with a precision of about 5 µm to 10 µm. Importantly, the BOX layer dry-etch and the silicon undercut are also applied to the dicing lanes, which are forming the trenches, so that edge couplers used to couple in and out of the waveguides are also undercut. Nonetheless, edge couplers were able to systematically withstand dicing and cleaning without breakage, after design improvements were introduced to increase their mechanical stability (compare Fig. 4.2.2(a)). In the current chip-design (Fig. 5.13 (a)), a trench is located in front of the edge coupler section (Figures 5.13 (b) and (c)).

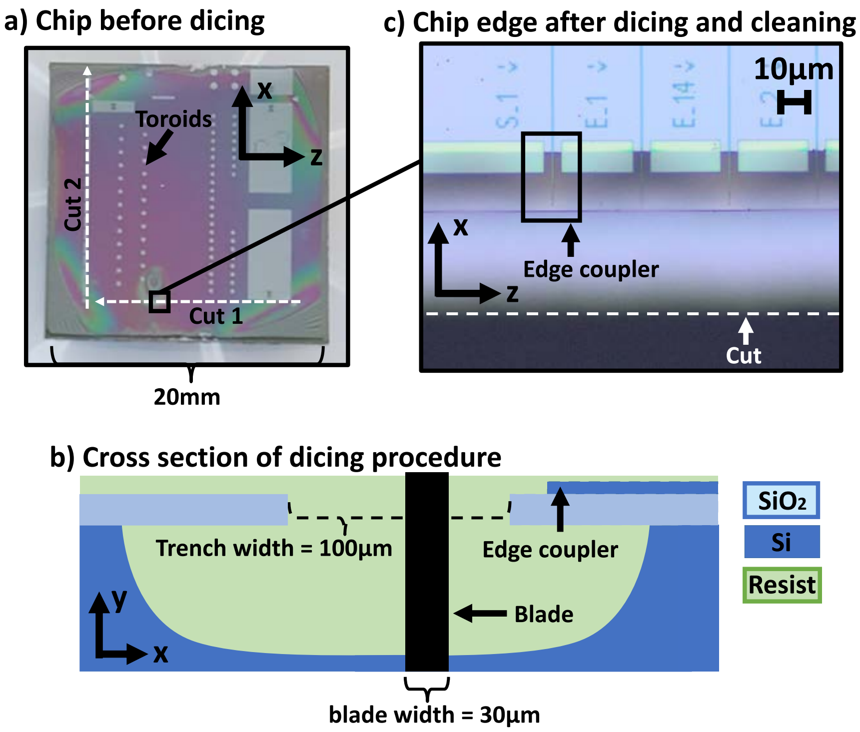

Figure 5.13: Dicing procedure to make inverted microtoroid's edge-couplers available for coupling light by an external fiber. (**a**) Optical top view image of the chip carrying multiple inverted microtoroids and test structures before protective resist coating and dicing. Two cuts (cut 1 and cut 2) are performed after the chip is coated with a protective resist. For each step, the blade is positioned in an edge-coupler trench. (**b**) Schematic side view of the edge-coupler trench. Usually, the blade is intentionally slightly misaligned to be closer to the edge coupler region. (**c**) Optical top view image of the edge-coupling region of a diced chip. After cutting and cleaning the chip, the edge-couplers are accessible to be coupled with external fibers.

The trench is fabricated during the silica-etching process (Section 5.2.4) and is therefore undercut during the final silicon-etch step (Section 5.2.5). The trench rim has a distance of about 2 µm to the tips of the edge couplers and has a width of 100 µm. During the dicing step, it is sufficient to hit this trench with the dicing blade (Fig. 5.13 (b)) and additional accuracy is not required. It is essential that the protective resist had enough time to flow into this trench before dicing. Otherwise, the undercut edge-couplers may break off during dicing. Using these trenches effectively relaxes the necessity of horizontal dicing precision. Also, no polishing of the of the edge couplers' facets is necessary as they are defined in the previous etch-steps. Further, the blade is not dicing through the edge-couplers.

Figure 5.13 (a) shows a top view image of the chip after undercutting but before protective resist coating and dicing (the optical resist from previous etch-steps is visible). After performing a protective resist coating, two dicing steps are performed (cut 1 and cut 2). For each step, the blade is positioned in the edge-coupler trench. Usually, the blade is intentionally slightly misaligned to be closer to the edge coupler region (Fig. 5.13 (b)). After cutting and cleaning the chip, the edge-couplers are accessible to be coupled with external fibers.

The final cleaning procedure itself can be quite challenging. First, after several bakings and dry-etching steps resist removal is challenging. The free-standing membranes can be quite sensitive to any mechanical shock such as using an ultrasonic bath. In the end, the following cleaning procedure was assessed to be adequate for avoiding residual resist on the chip and avoiding cracked membranes:

1. As a pre-cleaning step, the chip is put into TechniStrip P1316 by MicroChemicals for about 5 minutes to remove the majority of the resist. The chip is moved slightly (paddling) for supporting the resist removal. TechniStrip is a TMAH based stripper for optical resist.

2. In the next cleaning step, another beaker of TechniStrip is heated up to about 90 °C, and the chip is left in it for 50 minutes.

3. Subsequently, a short high-purity water dip is done to remove residual TechniStrip from the chip. Subsequent the chip is put into Isopropanol for about 5 minutes. Acetone is not in use, as it turned out that prior treatment with acetone leads to non-removable resist crumbs.

4. In the last step, an oxygen plasma (300 W for one hour) is used to remove last resist residuals.

5.2.7 Summary of fabrication flow (part one)

In Figure 5.14, the fabrication flow of the previous sections is summarized.

Top view and cross-section view	Description
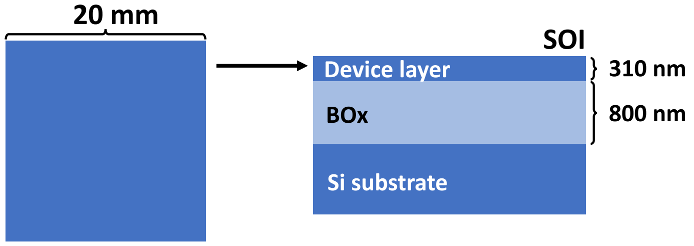	An 8-inch SOI wafer is diced into 20x20 mm chips.
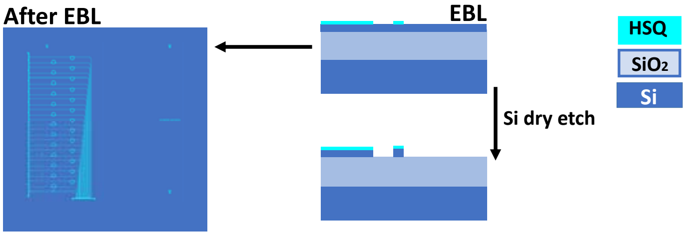	The chip is coated with HSQ resist and is patterned with EBL. Subsequently the pattern is transferred into the underlying silicon layer by dry-etching.
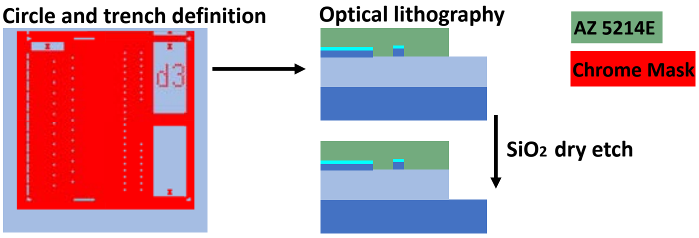	The chip is spin coated with AZ 5124E resist, and optical lithography is used to define circles and trenches. Subsequently the pattern is transferred into the BOX by dry-etching.
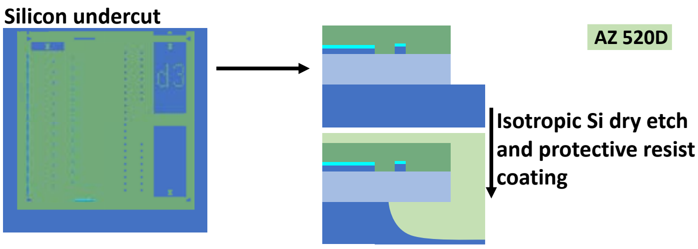	The previously defined trenches and circles are undercut by dry-etching of the underlying silicon substrate. For further processing, subsequently the chip is protected with AZ 520D resist.
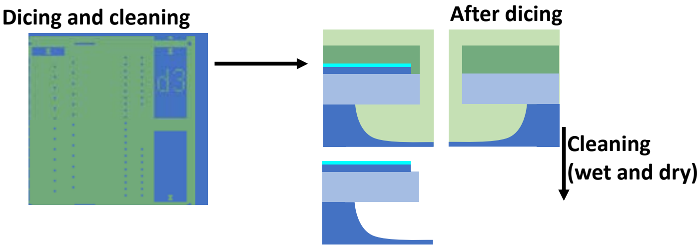	Finally, the chip is diced along its edge-couplers. In the last step, the chip is cleaned.

Figure 5.14: Summarized fabrication flow for creating an inverted microtoroid. The final laser reflow step is not shown.

5.3 Part Two - CO_2-Reflow of the device

For performing a laser reflow, as already described in Section 3.2.2, a Laser-Reflow-setup has been built and characterized. The optical absorption of fused silica is about 100 times stronger than that of silicon at a wavelength of 10.6 µm [110, 111]. A circular free-standing membrane of silica can be melted in the lateral direction into a microtoroidal shape until its supporting silicon substrate's heat sinking effect gets high enough to cool down the membrane below its melting temperature of 1650 °C [113]. Since laser-induced heating is confined to the immediate vicinity of the microtoroid, it is in principle compatible with PICs that are more complex. This comprises electro-optic or heterogeneously integrated active devices as well.

5.3.1 Setup

Figure 5.15 shows an overview of the nitrogen-purged reflow setup that is used for creating inverted microtoroids (see also Fig. A.1).

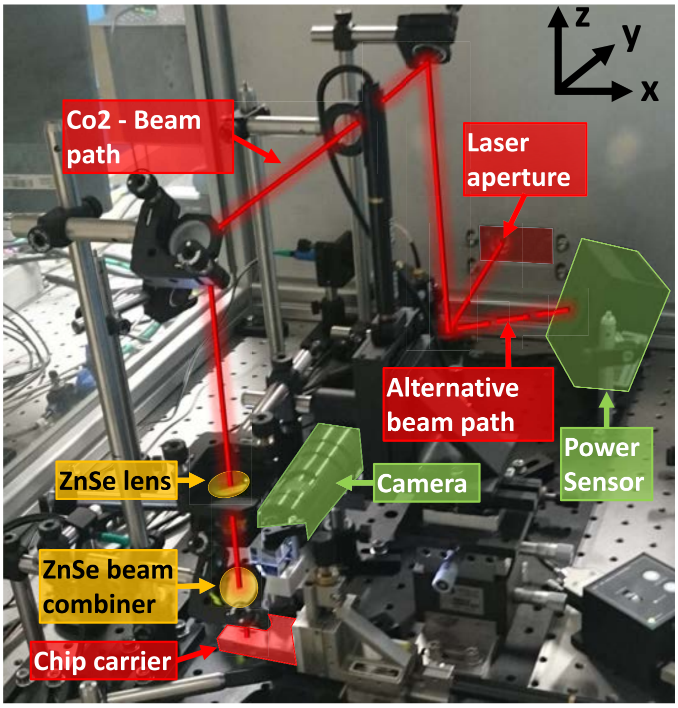

Figure 5.15: Overview image of the nitrogen-purged reflow setup used to reflow inverted microtoroids. The laser beam is routed with the help of a flip mirror to hit a thermal power sensor directly or to enter the setup. When entering the setup, the beam is focused by the use of a ZnSe Bi-Convex lens with a focal length of 100 mm. Before the focused beam hits a chip to be processed located on a chip carrier, a ZnSe-beam combiner is used to overlay a camera system, which makes it possible to get a live view camera image of the melting process.

The free space setup uses an air-cooled Coherent DIAMOND C-20A CO_2 laser with a maximal optical output power of around 20 W with a mode quality of $M^2 < 1.2$ and an aperture beam size of 1.8 mm. Therefore, the laser beam can be considered to lase in the Gaussian ground mode. The laser beam can be routed with the help of a flip-mirror to hit a thermal power sensor (Thorlabs S314C) directly (alternative beam path) or to enter the actual setup. When entering the actual setup, the beam is focused by means of a ZnSe Bi-Convex lens with a focal length of 100 mm (Thorlabs LB7638-F). Before the focused beam hits a chip, located on a chip carrier, a ZnSe-beam combiner (Acal BFi BCZ-1.03-3) is used to overlay a camera system, which makes it possible to have a live view camera image of the melting process.

Figure 5.16 shows the front part of the reflow setup.

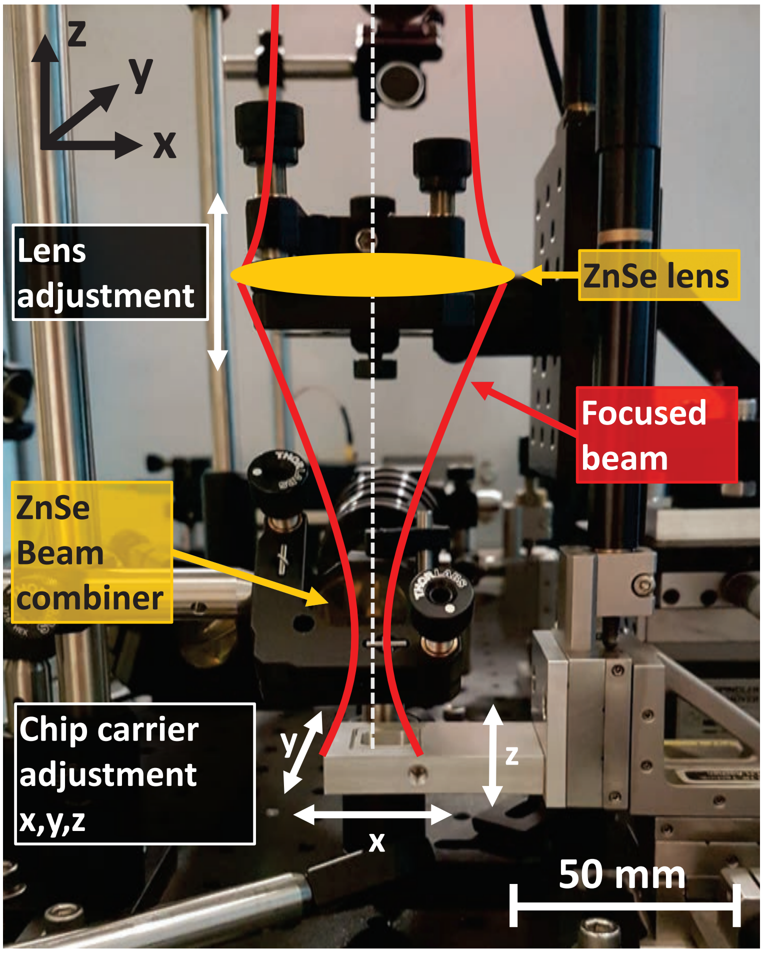

Figure 5.16: Front part picture of the nitrogen-purged reflow setup used to reflow inverted microtoroids. The chip carrier itself can be moved computer-controlled in x, y, z -directions. The x, y -directions are used for selecting the desired area to be illuminated by the CO_2-laser beam, whereas the z-direction of the carrier is used for hitting the working distance of the camera system to generate a sharp live view image.

The laser beam's absolute focus position depends on the position of the ZnSe lens. By a computer controlled movement of the lens (in $z-$direction), it is possible to either put a chip into the beam waist or to use another desired beam radius for processing. This way different spot sizes and different beam power densities can be used for processing.

The motion of the chip carrier itself can be computer-controlled in x, y, z-directions. The x, y-directions are used for selecting the desired area to be irradiated by the beam, whereas the z-direction of the carrier is used for hitting the working distance of the camera system to generate a sharp live view image.

The setup also records the transmitted power of the laser through a sample, as the chip carrier has a rectangular hole in the center and the laser light is routed subsequently to the thermal power sensor. Indeed, this is helpful to guarantee that the chip is positioned in the right way, covering the center of the rectangular hole, as only then the light is transmitted instead of being reflected at the underlying metal-sample-holder.

5.3.2 Beam characterization

By using the knife-edge method (see for example, [141]), it is possible to characterize the caustic of a beam (the beam radius as a function of z). The knife-edge method is used to measure the beam radii w_p in $x-$ and $y-$ directions separately (Fig. 5.16). For the final fit of the caustic function, both series of measurements were taken into account, as it turned out, that the differences for the caustics in $x-$ and $y-$ directions are negligible (as expected from the mode quality of $\mathrm{M}^2 < 1.2$). For fitting the caustic, the following model for the beam radius w_p as a function of z is used:

$$w_p\left(z\right) \quad = \quad w_0\sqrt{1+\frac{\left(z-f_T\right)^2}{z_R}}\,. \tag{5.1}$$

Where $\mathrm{w_0}$ is the beam waist radius (defined by a power drop to $1/\mathrm{e}^2$ of the peak power), $\mathrm{z_R}$ is the Rayleigh length and $\mathrm{f_t}$ is the focal position in $z-$direction in table coordinates. Figure 5.17 shows the result of this fit. The beam waist radius is $\mathrm{w_0} = 137\,\mu\mathrm{m}$, the Rayleigh length is $\mathrm{z_R} = 3.13\,\mathrm{mm}$, and the focus position in table coordinates is at $\mathrm{f_t} = 18.1\,\mathrm{mm}$.

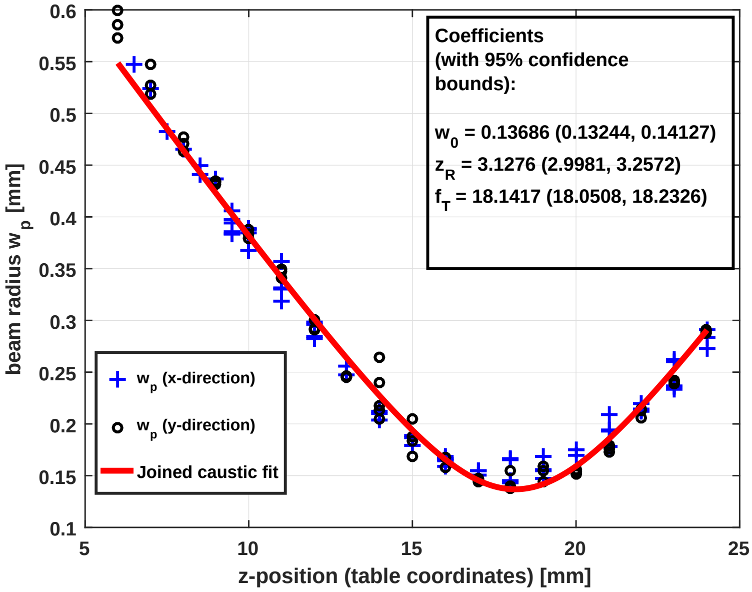

Figure 5.17: Measured and fitted caustic parameters of $\mathrm{CO_2}$ reflow laser. The knife-edge method has been used to measure the beam radii w_p in $x-$ and $y-$ direction separately. The fitted beam wait radius is $\mathrm{w_0} = 137\,\mu\mathrm{m}$, the fitted Rayleigh length is $\mathrm{z_R} = 3.13\,\mathrm{mm}$, and the fitted focus position in table coordinates is at $\mathrm{f_t} = 18.1\,\mathrm{mm}$.

5.3.3 Reflow process

The reflow process is done by first positioning a sample on the chip carrier. Initially, the laser beam is routed directly onto a power sensor. By moving the chip in $x-$ and $y-$directions, a targeted device can be selected. A LabVIEW graphical user interface (GUI) is used for controlling the whole melting process. The laser spot position on the chip is fixed in $x-$ and $y-$directions, during processing, and a crosshair is indicating its position. By flipping a mirror, the laser beam is routed to the chip, which triggers the melting process.

Melting a microtoroid in two different ways is feasible. Either doing a single-shot melting in which the laser spot is positioned in the microtoroids center throughout the whole melting process. Another way is to use a spiral movement. The chip is moved so that the laser beam is approaching the rim of the microtoroid in a circular movement with increasing radius. In most of the cases in this work, the single-shot approach has been used. The benefit of the second method is that large microtoroid radii can be handled, but the control of the spiral-movement can be challenging.

Finding a suitable parameter set for laser power and laser spot size is done experimentally. As an example, the result for two different parameter sets used on the same chip is shown in Figure 5.18. The left microtoroid shows fractures due to a too high initial laser power of 13 W. The right microtoroid shows an almost ideal result regarding circularity and rim offset. The left microtoroid is melted partially too far, even though the spot size is slightly smaller compared to the right microtoroid. Both microtoroids were irradiated for the same time span.

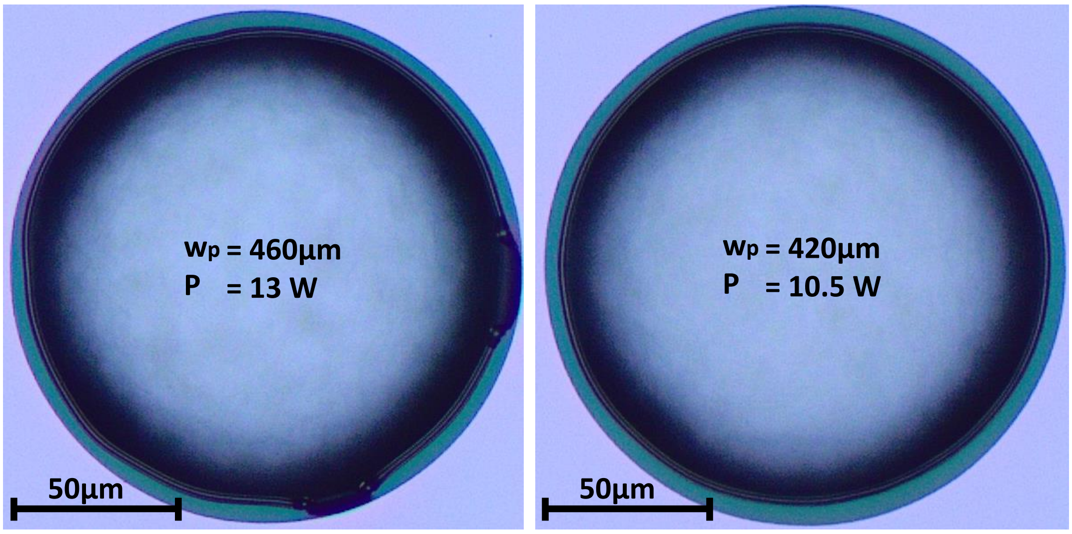

Figure 5.18: Comparison of reflown microtoroids for two different sets of melting parameters. The left microtoroid shows fractures due to a too high initial laser power of 13 W. The right microtoroid shows and almost ideal result regarding circularity and rim offset.

From chip to chip, slight variations regarding ideal melting-parameters have been observed. For initial melting tests, several test rings are fabricated, which can be used for adjusting the laser power and examine the integrity of the reflow setup regarding its target-accuracy. At first a laser power level of 10 W to 11 W with a spot size with a radius of $w_0 = 420\,\mu m$, for a major microtoroid's radius of $r_{major} = 125\,\mu m$, and an initial undercut of 30 µm, is used and further optimized. For increasing undercut sizes or increasing microtoroid radii, this set of parameters has to be adapted.

A significant challenge is the alignment of the microtoroid and the coupling waveguide. The optical resolution of the camera system is not high enough to visualize the gap between microtoroid and a waveguide during the melting process. However, the melting process usually takes about a few seconds, therefore a precise manual control would be challenging anyway.

A possible approach to overcome this issue is a local remelting step of the microtoroid in the coupling section. By locally performing a second melting step with reduced power, it is possible to melt the microtoroid further into the direction of the waveguide. This way a small correction in the order of 1 µm is possible. The same way it is also possible to correct the shape of the microtoroid, in case of the melting process not flawlessly worked out locally.

Figure 5.19 shows an example of a remelted coupling section. By locally remelting, the gap was decreased from 7 µm down to 5 µm.

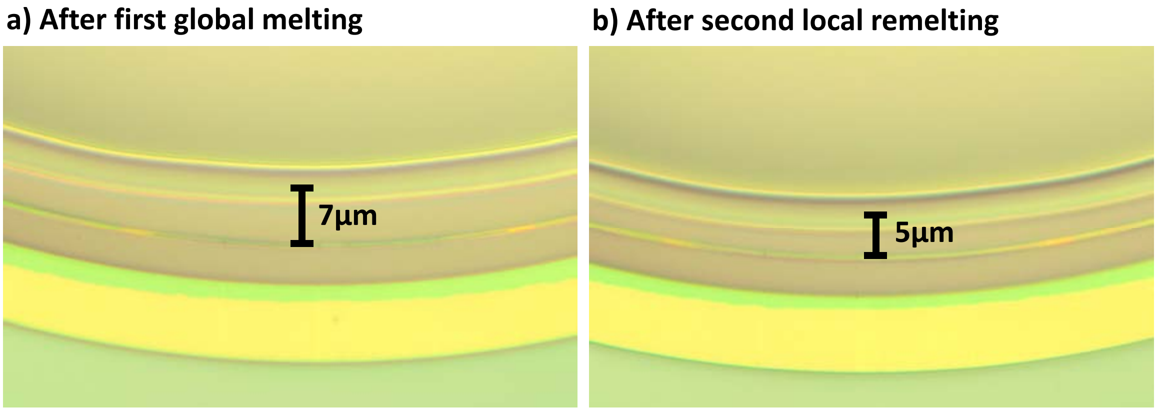

Figure 5.19: Example of second local remelt of an inverted microtoroid in the waveguide coupling section for adjusting the coupling strength. By locally performing a second melting step with reduced power, it is possible to melt the microtoroid further into the direction of the waveguide. This way a small correction in the order of 1 µm is possible. (**a**) Inverted microtoroid's coupling section after the first reflow. The center-to-center gap between microtoroid and waveguide is about 7 µm. (**b**) The same inverted microtoroid after a second local reflow. The gap is reduced to 5 µm.

5.4 Discussion

There are some points that need to be improved in future fabrication runs. First, the silica-circle-etch (Section 5.2.4) can be improved regarding steepness and smoothness. The steepness might be improved by doing further experiments on the right ratio between CHF_3 and Argon. Alternatively, another fabrication process might be explored. As the silica-etch is quite time-consuming (about 50 minutes), using an etch involving an ICP may be a beneficial alternative. The smoothness may be improved by using an additional resist reflow step.

It is not ideal to perform the dicing and cleaning step after the undercut is etched (Section 5.2.6). First, there is the danger that the free-standing membranes are breaking off during the dicing or the previous protective resist coating step. Even though the stability of the membranes is higher than one might first expect, residual resist or any other source of dirt could severely decrease the quality-factor of a microtoroid. In the current fabrication flow, this process order is necessary for two reasons.

First, during the silicon-undercut, the waveguides (out of silicon) need to be protected. Otherwise, they would be etched away. There are two possible solutions for protecting the waveguides from being etched away. Either, depositing an additional layer of oxide before doing the circle-etch (keeping the restrictions regarding maximum BOX thickness (Fig. 4.8)), or performing an oxidation step of the waveguides. The oxidation step, for example, can be done in a dry oxidation oven. As a test of this approach, a bare SOI chip was oxidized for 17 min at 1050 °C, which resulted in an oxide layer of about 40 nm. In fact, early fabrication attempts intended an oxidation step.

Second, it is critical to dice up the chips before the silica-etch is done. The edge-couplers need to be located as close as possible on the chip edges. Otherwise, no efficient light coupling is possible. In EBL, it is not possible to write a structure close to the chip edge. Therefore, a dicing step is unavoidable. Cutting through the waveguide edge-couplers is critical, as they can easily break off if no top cladding is present. Indeed, this was observed in earlier fabrication runs. Furthermore, this would involve a facet-polishing step, as a dicing edge can be rough. Even if this can be achieved, the facets need to be protected during a subsequent silicon-undercut-etch as the blank silicon-facets of the edge coupler would act as entrance opening. In fact, in early-stage experiments, even a capillarity effect was observed, meaning the waveguide edge couplers are entirely etched away, leaving a hollow core of silica, which is indeed an interesting way of fabricating such structures but is not helpful at all in this work. As an alternative, there is also the possibility of using multiple optical lithography steps. An alternative to the edge couplers would be grating couplers. Grating couplers would be more suitable for TE polarization instead of TM polarization. However, designing an efficient grating coupler could be challenging as the desired high-quality-factor of the microtoroid is causing limitations on the BOX and device layer thicknesses of the used SOI. In fact in this work, grating couplers were fabricated with about 8 dB insertion loss each, for TE polarization.

Chapter 6

Characterization - The monolithically coupled inverted silica microtoroid

For coupling light into the proposed monolithically coupled inverted silica microtoroids (IVT) (Section 4.1), it is necessary to couple light from an external laser source. For this purpose, an edge-coupling setup was designed and built (Section 6.1). The edge-coupling setup was used to measure the spectral response of chips carrying the IVT devices. Each chip consists of multiple devices and additional test structures. One test structure, a silicon ring resonator, which is coupled to a waveguide, is used for measuring the waveguide losses. Other test structures serve as melting test targets to adjust the reflow process before melting a waveguide-coupled IVT.

An entirely fabricated and melted microtoroid needs to be characterized regarding various aspects. The central figure of merit is the quality-factor of the proposed IVT-system. Cleanliness plays a crucial role in the proposed devices as any contaminations can degrade the quality-factor of the device (compare Section 3.3). Therefore, parasitic residuals like optical resist, inhomogeneous melting areas or other defects like a microtoroid, which was melted too far to the rim of the undercut (Section 6.2), need particular attention. Also, the roughness of the microtoroid itself is of importance, as any roughness leads to a degradation of the intrinsic quality-factor of a device (Section 3.3) as well. The roughness is evaluated by using an atomic force microscope (AFM) (Section 6.2.3).

Finally, the optical properties of the proposed device need to be measured and characterized (Section 6.3).

6.1 Edge-coupling setup and fiber alignment

The edge coupling setup is the essential tool for measuring the optical properties of the proposed IVT. By sweeping the wavelength of the external laser light, the spectral response of the inverted microtoroid can be measured. By extracting a spectrum as a function of wavelength, parameters like the full width at half maximum (FWHM), the free spectral range (FSR) and the extinction of occurring resonances can be measured and evaluated. Furthermore, by changing the temperature and keeping the wavelength, the thermal effects can be measured as well.

6.1.1 Setup

Figure 6.1 shows an overview image of the edge coupling setup. A chip (red) is mounted on a y, z -stage equipped with a chip holder. The chip-holder uses a Peltier-element for setting a desired chip temperature via a temperature controller (TEC). Furthermore, the chip-holder uses vacuum to ensure that the chip is not moving during the measurement. Two lensed fibers (from OZOptics with a spot diameter of 2.5 µm and a working distance of 14 µm) are used as input and output to connect the chip (green) optically. Each lensed fiber is positioned on an x, y, z -stage. One stage serves as the input coupling stage, and the other stage serves as the output coupling stage. The lensed fibers are coupled to the chip by moving the stages to a suitable position.

Furthermore, each stage can be slightly rotated in the transverse and in the axial direction to compensate for undesired angular misalignment. Generally, in this work, the input fiber is aligned to TM polarization. A top mounted computer-controlled IR-Camera (Xenics X-XEVA-Large HS) helps to find the $x - y - z$ position at which the laser light is efficiently coupled into the input-coupler, as the waveguide starts to light up on a camera image. Precisely, the light that is collected by the IR-camera is the portion of light that is lost and not guided by the waveguide structures.

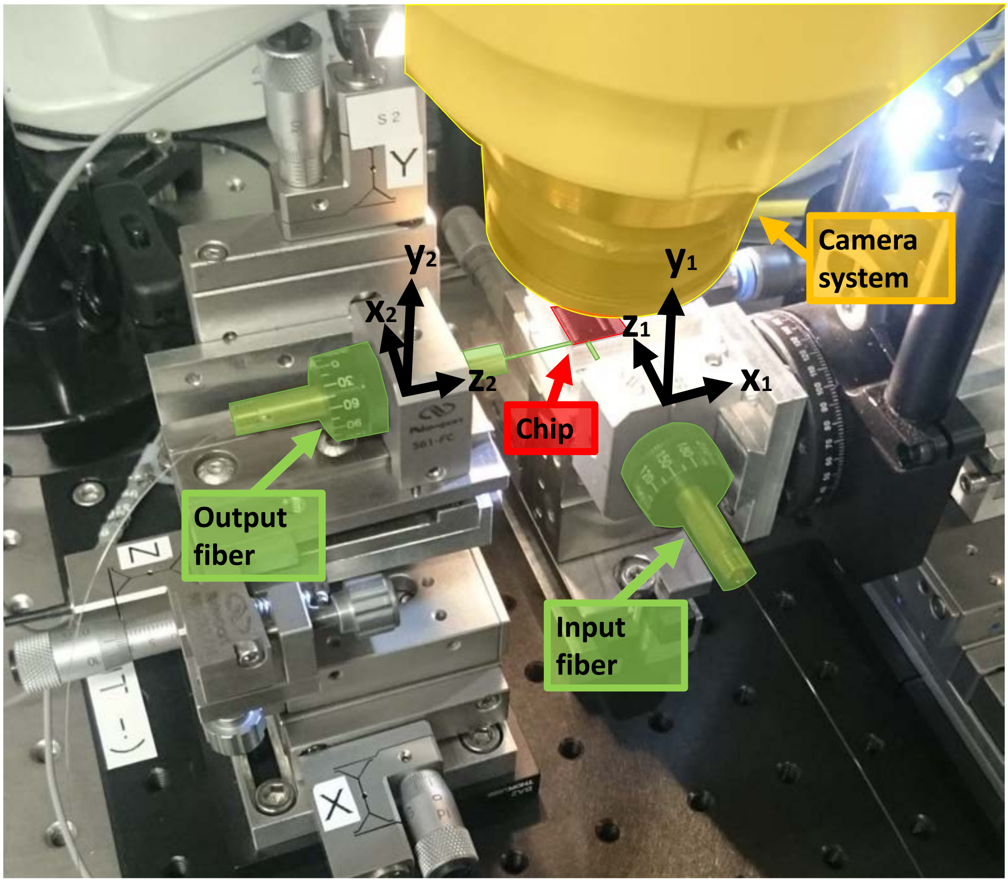

Figure 6.1: Overview picture of the edge coupling setup with a mounted chip. The edge coupling setup uses two x, y, z -stages. Furthermore, each stage can be slightly rotated in the transverse and in the axial direction to compensate for undesired angular misalignment. On each stage, a TM aligned lensed fiber (from OZOptics with a spot diameter of 2.5 µm and a working distance of 14 µm) is mounted. One stage serves as the input coupling stage, and one stage serves as the output coupling stage. A top mounted computer attached IR-Camera (Xenics X-XEVA-Large HS) helps to find the $x - y - z$ position at which light is efficiently coupled into the input coupler, as the waveguide starts to light up on the camera image. Precisely, the light that is collected by the IR-camera is the portion of light that is lost and not guided by the waveguide structures.

Various tunable laser systems are available as a source for the edge-coupling setup. Primarily, an Agilent 81600B laser source with a typical linewidth of 100 kHz and an Agilent 81634B power sensor is used for the measurements. Both modules are plugged into an Agilent 8164B chassis that is controlling the sweeping of the wavelength and the communication of the modules. This laser source has a tunable wavelength range from 1490 nm to 1620 nm with a resolution of 0.1 pm and a maximal output power of 6 dBm. The scan speed of a wavelength sweep depends on the resolution, but a wavelength sweep covering the full range at highest resolution takes approximately one hour.

In practice, for doing a test measurement to examine the quality of a spectrum, regarding artifacts and low signal levels, a lower resolution is sufficient. Such an overview sweep at a resolution of 10 pm can be accomplished in less than one minute.

The lensed fibers are connected to an external laser source by polarization maintaining optical fibers. An additional polarization validation is performed by using an external detector equipped with a rotatable polarizer for aligning the output of the lensed fiber to TM-polarization in table coordinates (and therefore, in chip coordinates). Typically, the measurements are performed using TM-polarization, as this polarization, theoretically, leads to a higher intrinsic quality-factor for the proposed IVT-system (see Section 4.1).The edge couplers of the chip can couple TE and TM polarized laser light with similar efficiency.

6.1.2 Optimization of the edge-coupler's input and the output signal

Inversely tapered edge-couplers are used for coupling light into the chip and out of the chip (see Section 4.2.2). Their coupling efficiency leads to an offset for the overall detectable power signal at the output. When recording a spectrum as a function of input wavelength, a pronounced signal level helps to distinguish between a real effect (like a resonance) and noise.

Due to the developed fabrication process, each edge-coupler is situated on top of an undercut SiO_2-membrane. For stabilizing this membrane, silicon-stabilizers are fabricated (Section 4.2.2). Due to the asymmetric refractive index distribution in the y-direction and an offset distance s (between the rim of the undercut and the tip of the edge-coupler), the light is first partially coupled into the membrane and is loosely guided before being coupled into the edge-coupler. Therefore, the undercut itself helps to improve the coupling efficiency of the coupler, as no light can be lost due to substrate leakage in the first place. Figure 6.2 shows an image of a typical edge coupling section with membrane-stabilizers out of silicon.

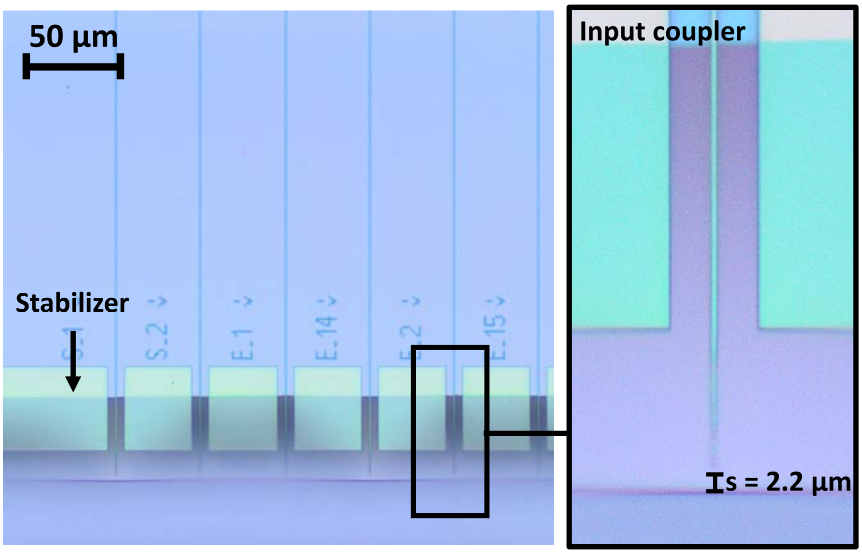

Figure 6.2: Optical top view image of a typical edge coupling section with inversely tapered edge couplers and silicon-stabilizers sitting on an undercut silica membrane after fabrication. The offset distance s (between the rim of the undercut and the tip of the edge-coupler) is usually in the order of $2 - 3\,\mu\mathrm{m}$.

For coupling light into an edge-coupler, the input and output coupling stages are manually coarse-aligned in a way, that the tips of the mounted fibers are facing the input- and output-couplers. A top mounted computer attached IR-Camera (Xenics X-XEVA-Large HS) helps to find the $x - y - z$ position at which light is coupled into the input-coupler as the waveguide starts to light up on the camera image. Figure 6.3 shows an IR-image of the coupled waveguide with its input and output section together with a coupled microtoroid. The waveguide is lighting up, which is of considerable help during the initial fiber alignment. Also, the output is lighting up which is an indication that the waveguide's or the microtoroid's coupling section are not broken or partially damaged. As the waveguide is tapered down in the coupling section (to form a weakly tapered gap coupler) to the microtoroid, the light is less guided. Therefore, the coupling section is also lighting up. Likewise, the IR-Camera can be used as debugging tool for finding broken waveguides, as a broken section is usually accompanied by a bright spot on the IR-Camera image since the light is lost due to scattering.

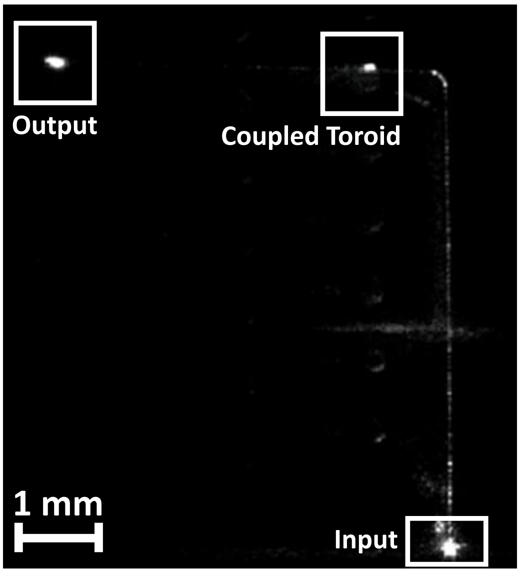

Figure 6.3: IR-image of the coupled waveguide with its input and output sections together with a coupled microtoroid. TM_0 polarized light from an external lensed fiber is coupled to an input edge-coupler. The light is routed to an inverted microtoroid before coupled out again by an output edge-coupler. The IR-mode of the camera makes it possible to see the scattered light on the IR-Camera image.

After light propagates in the waveguide and an initial power signal at the output-fiber is found, the stages can be fine-aligned. Each stage has a piezo motor built in with a traveling range of about 30 µm. The fine-alignment is done for each stage separately by sweeping the position of the fiber with the piezo motor, controlled by a computer. This sweep is done in the form of a spiral-like movement in the $x-$ and $y-$ directions. By tracking the signal, it is possible to find the "sweet spot" with the highest power signal. By doing this multiple times between input and output stages, the best coupling point is usually found after a few cycles. This whole procedure takes about 1 minute.

Figure 6.4 shows a schematic of the spiral algorithm.

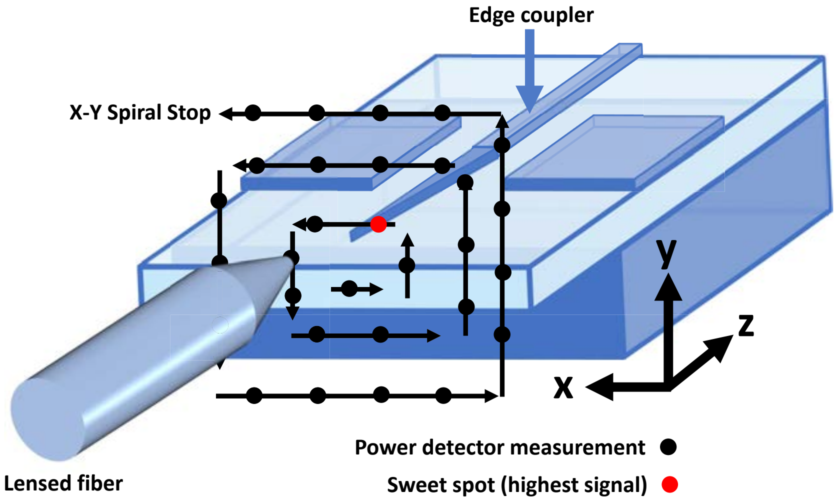

Figure 6.4: Schematic of an automatized spiral algorithm for optimizing the signal strength of a coupled IVT. Two lensed fibers (only one is shown in the schematic) are brought close to an input and an output edge-coupler. After an initial coarse-alignment, which is done manually, the lensed fibers are performing spirals in the $x-$ and $y-$direction, one after each other. For each position, the measured signal strength is recorded, and finally, the lensed fibers are moved to their “sweet spots” of highest signal strength. By repeating this process in quick succession for each fiber respectively, the signal strength can be optimized.

Alternatively, a simplex search method can be used. This method is provided as *fminsearch* by Matlab. Since this method searches for the minimal value the measured signal is digitally inverted (the highest signal value becomes the most negative value).

6.1.3 Waveguide losses and insertion loss caused by the edge-coupler

The chip waveguides are optimized to propagate the coupled light with a low optical loss (Section 5.2.2). For extracting the upper limit for the expected optical losses, a waveguide is critically coupled to an on-chip silicon ring resonator (length $L = 511\,\mu m$) (see Fig. 6.5). The silicon ring resonator has the same width as the attached waveguide of $w = 570\,nm$. In the current setup, based on optical simulations, a waveguide with a width of $w = 570\,nm$ acts as a single-mode waveguide, which is only able to guide the TE_0 and TM_0 polarized modes efficiently.

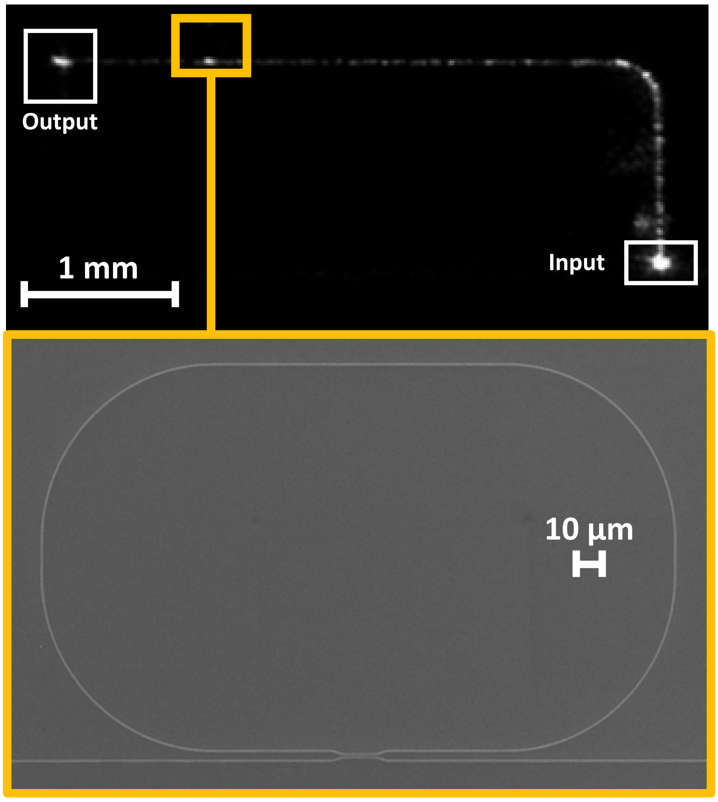

Figure 6.5: IR-Camera image of an edge coupled silicon ring resonator. The inset shows an SEM image of a silicon ring resonator. For extracting the upper limit for the optical waveguide losses, a waveguide is critically coupled to an on-chip silicon ring resonator (length $L = 511\,\mu m$). The silicon ring resonator has the same waveguide width as the width of the coupling waveguide ($w = 570\,nm$). By measuring the loaded quality-factor Q_L, and calculating the intrinsic quality-factor Q_U, the loss in dB/cm of the resonator can be calculated to be approximately 38 dB/cm for $\lambda = 1575\,nm$ for TM_0 input polarization.

By measuring the loaded quality-factor Q_L and extracting the intrinsic quality-factor Q_U (Fig. 2.16 b)), the optical loss in dB/cm of the resonator can be calculated.

This optical loss value is assumed to be the upper limit for the expected waveguide losses and is found to be approximately 38 dB/cm for $\lambda = 1575\,\mathrm{nm}$ for TM_0 input polarization. Figure 6.5 shows an overview IR-Camera image of the waveguide with its input and output coupling sections together with an SEM image of the silicon ring resonator.

Alternatively, cutback structures can be used to extract the optical loss of waveguides. In this method, multiple waveguides of different lengths are fabricated. Each waveguide shows a particular optical loss as a function of its geometric length. Therefore, the optical loss of a waveguide can be extracted by considering all measurements. This method assumes that the coupling efficiency of all waveguides is approximately equal. Furthermore, a considerable space is taken up on the chip.

The extracted and calculated optical loss of 38 dB/cm is high compared to the simulated loss (compare Fig. 4.5). However, this loss value is considered the upper limit for the expected waveguide losses. In fact, the measured total loss (including the input and output coupling losses arising from the edge coupling) of a waveguide (which is attached to a silicon ring resonator) with a length of approximately 6 mm is in the order of 15 dB or below (compare Fig. 2.12 b))

The high optical losses of the silicon ring resonator are most likely a result of the EBL-writing process as SEM images revealed mechanical defects, like gaps within the waveguides, that can act as severe sources of optical loss.

6.2 Structural characterization of the proposed device

The structural properties of the proposed device are profoundly affecting the possibility of achieving its desired functionality. In particular, the circular shape of the microtoroid is analyzed regarding its homogeneity. Furthermore, the surface roughness is analyzed with the help of an atomic force microscope (AFM) (as a part of a scanning near-field optical microscope (SNOM)).

During the development of the fabrication flow, different problems arose that impaired the structural quality of the proposed IVT system. In an early stage of this project, the SOI quality of the wafer was not sufficient regarding layer thickness homogeneity and layer-to-layer adhesion. An inhomogeneous device layer thickness makes it almost impossible to simulate the properties of the proposed IVT.

Especially, the missing adhesion between BOX- and device-layer was leading to delaminated waveguides in the coupling section between waveguide and microtoroid, caused by induced mechanical stress during fabrication. The SOI was later on exchanged by a higher quality industrial grade material, which solved these issues. As an example, Figure 6.6 shows an SEM image of delaminated coupling section waveguides.

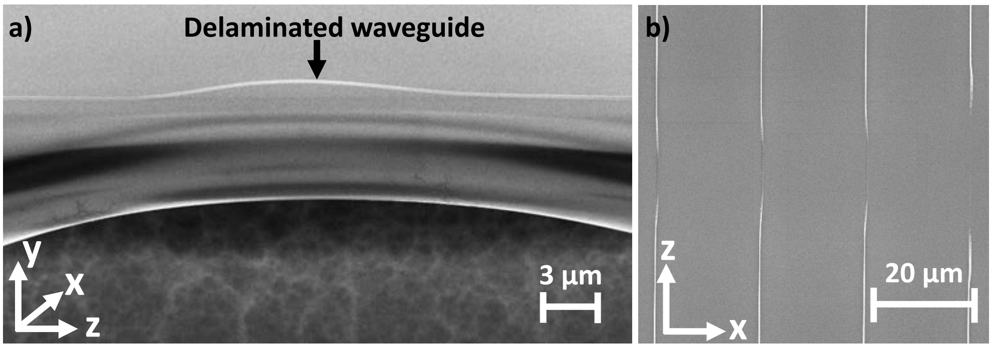

Figure 6.6: Delaminated waveguide due to mechanical stress because of insufficient adhesion between BOX and device-layer in the coupling-section to the inverted microtoroid. (**a**) SEM-Image of a delaminated coupling-section waveguide taken under an angle. (**b**) SEM-Image of an EBL waveguide writing test after processing and etching. All waveguides are tapered down. The delamination effect gets more pronounced the thinner a waveguide gets.

Another crucial parameter is the quality of the silica undercut before reflow. A rough undercut is leading to micro-bendings. These micro-bendings are affecting the quality of the melted microtoroid (Section 5.2.5). The newly introduced heat spreader (Section 6.2.1) solved various problems. First, the fabrication tolerance for the gap between waveguide and microtoroid was reduced. Furthermore, the microtoroid's shape became much more circular and homogeneous leading to lower bending losses and fewer micro-bendings.

The additional stabilization of the underlying membrane also makes the undercut more resistant to mechanical damage and suppresses a wobbling of the membrane, due to built-in strain (Section 5.2.3).

The fully processed chip needs a final dicing step (Section 5.2.6). Therefore, the input and output coupling sections can break off quickly if they are not sufficiently protected. The stabilizers are providing this stability.

6.2.1 Heat spreader and stabilizers for the prevention of broken silica membranes

Besides their original planned heat spreading capability during reflow, the heat spreaders are also providing a substantial stabilization effect for an underlying membrane. In parallel, the input and output coupling regions are stabilized in the same way by stabilizing silicon bridges. Figure 6.7 (a) shows an extreme case in which a membrane of an unprotected IVT shows multiple cracks. Usually, an initial crack occurs at the intersection (rim) between the membrane and underlying silicon substrate. Cracks seem to occur more likely for deeper undercuts and most probably originate from a lever in case the membrane is pressed down due to external handling forces. Furthermore, lacking mechanical rigidity (wobbling) of the membrane, due to built-in strain, amplifies this effect. Figure 6.7 (b) shows an IVT with a heat spreader. The wobbling and the cracking of the free-standing silica membrane are suppressed.

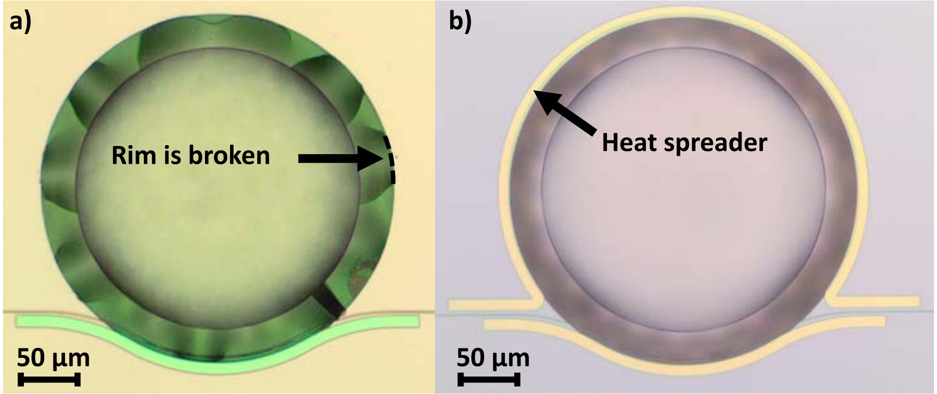

Figure 6.7: Stabilization effect of a silicon heat spreader on an inverted microtoroid. (**a**) An extreme case of a cracked membrane of an inverted microtoroid before reflow without a full stabilizing heat spreader. (**b**) Intact inverted microtoroid that is protected by a heat spreader. Furthermore, a wobbling or cracking of the membrane, due to built-in strain is suppressed.

A broken microtoroid membrane is a severe problem as a subsequent successful reflow process is not possible anymore. In fact, a broken microtoroid membrane is not a usual fabrication result, but for some chips (without heat spreaders), nearly every device showed at least some cracks.

As the undercut, in general, was increased during the process development, this phenomenon became more and more of a substantial problem and led, among other reasons, to the use of heat spreaders.

A similar problem occurred for the input and output edge-coupler sections. As the inversely tapered edge couplers are also situated on top of an undercut membrane, a levering effect can break them off. Especially, during the dicing step, this could happen. Figure 6.8 (a) shows an input coupling section after dicing without stabilizers. The membrane is partially broken, which makes a coupling of light into the on-chip waveguide impossible. Figure 6.8 (b) shows a coupling section after dicing with stabilizing bridges. Even though cracks sometimes can occur, most often the coupling sections stay at least partially intact as further cracking is blocked between neighboring stabilizing bridges.

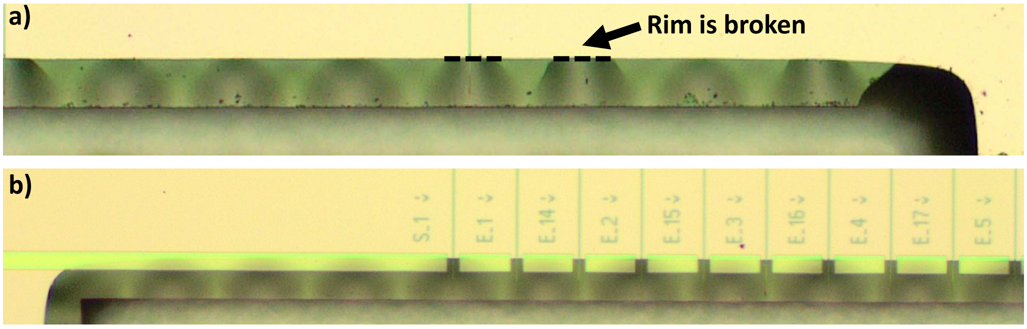

Figure 6.8: Stabilization effect of silicon-stabilizers on the input coupling section of edge-couplers. (**a**) Cracked membranes are causing the inversely tapered edge-coupler to lose their functionality. (**b**) Intact input coupling sections, which are protected from cracking by silicon-stabilizers.

6.2.2 The shape of the inverted microtoroid after CO_2-Reflow

The circular shape of the microtoroid is of importance. In case of micro-bendings (see Section 5.2.5) the intrinsic quality-factor may be reduced notably, as micro-bendings can act as scattering points, areas of non-adiabatic mode transition and areas of high bending losses. After the implementation of the heat spreader, an homogeneous melting of the microtoroids is more consistently achieved and the control over the microtoroid-to-waveguide distance improved. One remaining difficulty remains however with handling the two corner regions where the waveguide is routed away from the microtoroid (Fig. 6.9(a)). Since the heat spreader has to be interrupted in that region, it can locally make things even worse by introducing a sharp discontinuity in the thermal environment resulting in a deformation of the sectional microtoroid shape (notch with a locally decreased bending radius at its tip). In the worst case, the reflow can even break the waveguide (inset of Fig.6.9(a)). In order to alleviate this, the heat spreaders were extended along both sides of the departing waveguide, locally increasing its effectiveness, in an effort to partially compensate for the reduced heat sinking in the middle of the gap.

This approach relies on sufficient averaging in the thermal environment to smooth out these micron-scale variations. It did, however, prove necessary to carefully dial-in the reflow parameters (CO_2-laser beam diameter and optical output power) to obtain notch free results (Fig. 6.9 (b)).

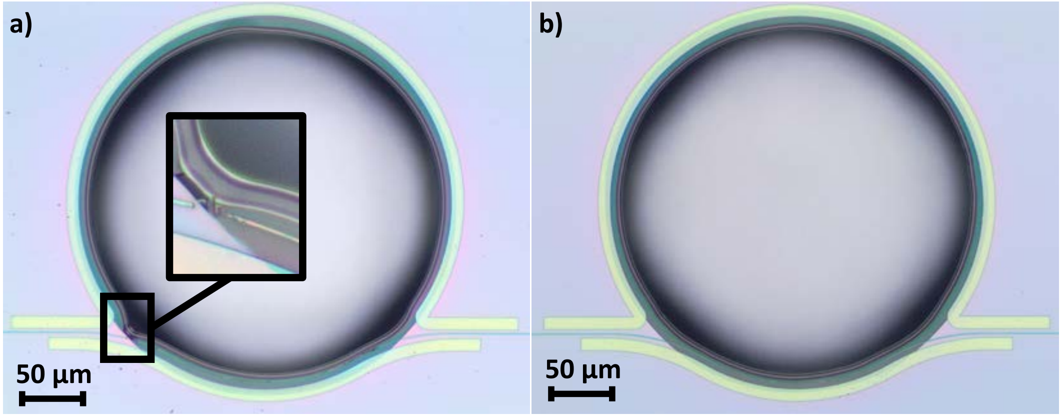

Figure 6.9: Examples of the influence of different CO_2-laser beam sizes during the reflow process of inverted microtoroids with silicon heat spreaders. One remaining difficulty remains in handling the two corner regions where the waveguide is routed away from the microtoroid (**a**) Broken silicon waveguide entry section at the heat spreader as a result of unoptimized CO_2-laser beam size.(**b**) Optimized reflow process parameters with increased beam spot size of the CO_2-laser beam and optical laser output-power.

On average the microtoroids with heat spreaders have a smoother and more homogeneous melting result, and the targeted gap between microtoroid and waveguide can be met more precisely (see also Section 5.2.3). Figures 6.10 (a) through (c) show the melting result for three selected microtoroid designs.

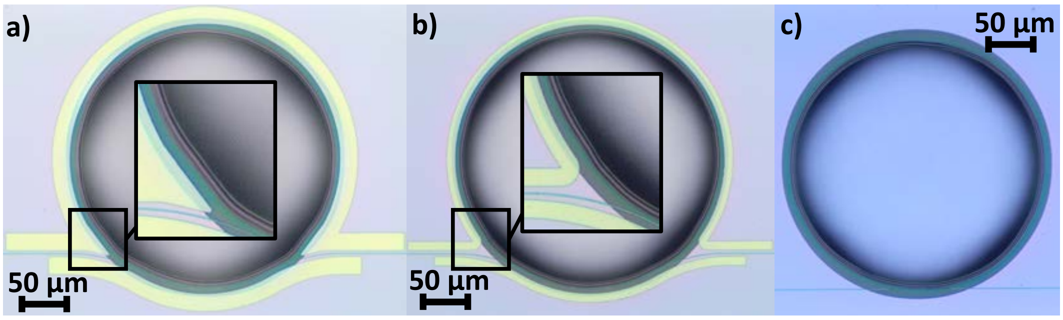

Figure 6.10: Comparison of reflow results of three inverted microtoroid designs. (**a**) An inverted microtoroid with additional spreader extensions to avoid an inhomogeneous melting result in the waveguide entry section of the heat spreader. (**b**) An inverted microtoroid with a smooth melting result in the waveguide entry section by adjusting the CO_2-laser beam spot size and power. (**c**) An homogeneous melted inverted microtoroid without heat spreader, which is showing a slightly varying distance to the rim of the undercut.

Figures 6.10 (a) and (b) show two designs with heat spreaders and a weakly tapered silicon waveguide-to-microtoroid coupling junction. In Figure 6.10 (a), additional spreader extensions are used to avoid an inhomogeneous melting result in the waveguide entry sections of the heat spreader. Unfortunately, this attempt showed to have only a minor or even worsening impact. Figure 6.10 (b) shows a design, including a heat spreader, which is providing the best achieved melting result so far and Figure 6.10 (c) shows a design attempt without heat spreaders and a straight waveguide-to-microtoroid coupling junction.

Reducing the micro-bending in the heat spreader's entry section for the silicon waveguide (see inset of Fig. 6.10 (b)) is of vital importance. The bending radius of such a micro-bending is usually on the order of about 50 µm and way below. A microtoroid with a major radius of $\mathrm{r}_{\mathrm{major}} = 50\,\mu\mathrm{m}$ would have a bending limited quality-factor of about 8 to 9 million. Therefore, it is assumed that micro-bendings can have a degrading influence on the expected intrinsic quality-factor of inverted microtoroids. For full integration with other components on the same chip, the reproducibility of the melting result is essential. Using a heat spreader leads to melting results with lower variability and therefore to better integration capabilities.

6.2.3 Surface roughness of the inverted microtoroid after CO_2-Reflow

Another critical parameter of the microtoroid is its surface roughness after CO_2-reflow (see Section 5.3). Any major or minor surface roughness of the microtoroid can lead to a degradation of the intrinsic quality-factor (Section 3.3). In principle, the reflow process generates an atomically smooth surface. However, it is reported that evaporation of silica can lead to redeposition that leads to surface defects. These surface defects alter the quality of the resonator, as they serve as additional sources for light scattering [114, pp. 62].

For analyzing the surface roughness of a melted microtoroid, a scattering near-field optical microscope (SNOM) in AFM-mode is used to extract its topology after reflow. Figure 6.11 (a) shows an initial test-version of a double microtoroidal structure that was already melted with the current reflow setup. The topological measurement shows a low roughness root mean square (RMS) of $R_{\mathrm{RMS}} = 0.45\,\mathrm{nm}$ in the region that is affected by the reflow process (Fig. 6.11 (c)). The area that is unaffected by the melting process is showing a higher roughness in the order of nanometers.

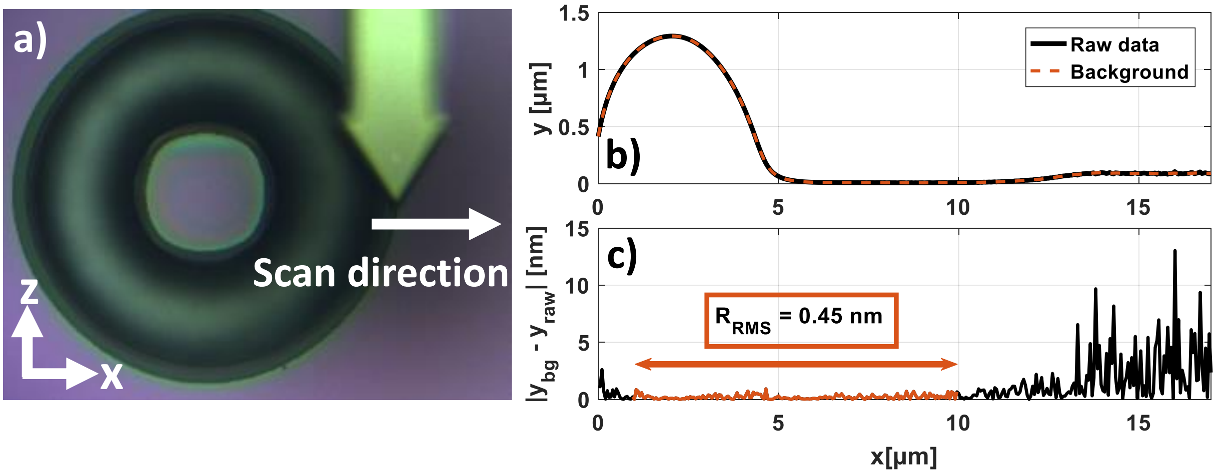

Figure 6.11: Surface roughness of an inverted microtoroid measured with a SNOM in AFM mode. (**a**) Optical top view image of the inverted microtoroid and the measurement needle. The scan direction of the needle is indicated. (**b**) Raw data measurement of y position of the tip as a function of scan distance in micrometers. A background (perfectly smooth) is fitted to the raw data spectrum. (**c**) Extracted surface roughness defined as the residuum of raw data measurement and background. The topological measurement shows a roughness-RMS of $R_{\mathrm{RMS}} = 0.45\,\mathrm{nm}$ in the region that is affected by the reflow process between $x_1 > 0\,\mu\mathrm{m}$ and $x_2 = 10\,\mu\mathrm{m}$.

6.3 Experimental characterization of the Waveguide Coupled Microtoroids

The primary goal of this research is to couple light from a monolithic on-chip silicon waveguide to an inverted silica microtoroid. Ideally, the average lifetime of light coupled to the microtoroid is exceptionally high, originating from a high intrinsic quality-factor Q_u.

Coupling light from a monolithic on-chip silicon-waveguide to an inverted silica microtoroid is more challenging than one might expect. Various challenges had to be faced regarding the development of a working and reproducible fabrication flow (Section 5.2.7).

6.3.1 Spectral resolution of the measurement setup and implications for the microtoroid's quality-factor

The edge coupling setup that is used for measuring the spectral response of the inverted microtoroids is connected to a tunable laser source with a maximum resolution of 0.1 pm between two adjacent measurement points at a maximum output power of 6 dBm. The linewidth of the laser is specified as 100 kHz. On site, it and was measured to be about 90 kHz. Especially, when doing a fast sweep measurement, this linewidth is an adequate value.

Assuming, for example, a loaded quality-factor Q_L in the order of 50 Million with a resonance at $\lambda = 1550\,\text{nm}$ implies a FWHM of about 0.03 pm (see Eq. 2.46). The measured linewidth of the microtoroid is a convolution of the actual linewidth and the linewidth of the laser. Therefore, the linewidth of the used laser is limiting the measurable loaded quality-factor to less than $1 \cdot 10^9$ [142]. More severe is the step size of the laser measurement itself, which is about three times more than a FWHM of 0.03 pm. For overcoming this issue, the laser can be externally frequency-modulated and scanned over a preselected frequency range [1].

For measuring the quality-factor, either the FWHM of a resonance can be measured, or a cavity ring-down measurement can be done. A ring-down measurement is more precise for determining the intrinsic quality-factor Q_U (by measuring the loaded quality-factor Q_L) as it is unaffected by thermal distortion of the microtoroid's linewidth and the laser's linewidth [142]. A ring-down measurement is done by scanning a laser into an ideally critically coupled resonance of a microtoroid. At some point in the elapsed time, a stabilized power transfer is attained. By turning the laser off (for example by the use of a high-speed external modulator), the microtoroid starts discharging [1]. This discharge can be measured as power over discharging time. As the microtoroid is necessarily coupled to a waveguide during this measurement, the ring-down measurement can extract the loaded quality-factor Q_L of a microtoroid [1, 142].

To calculate the intrinsic quality-factor Q_U loading effects of the coupler and the excitation of the counter-propagating mode due to scattering centers in the resonator should be accounted for [1, 142].

Nonetheless, the present tunable laser source (Section 6.1.1) is capable of acquiring a full spectrum at highest resolution in considerable short time. As the inverted microtoroid design has a fixed gap to its coupling waveguide, it is essential to have a procedure in place to distinguish between microtoroids that show resonances of considerable extinction and microtoroids that have are defective.

For evaluating that even for high loaded quality-factors this decision can be made based on the current setup, different computer-generated resonance spectra (assuming almost critical coupling) of varying loaded quality-factors ($Q_L = 5 \cdot 10^6,\ 10 \cdot 10^6, 25 \cdot 10^6$ and $50 \cdot 10^6$) are sampled with a resolution of 0.1 pm (Fig. 6.12).

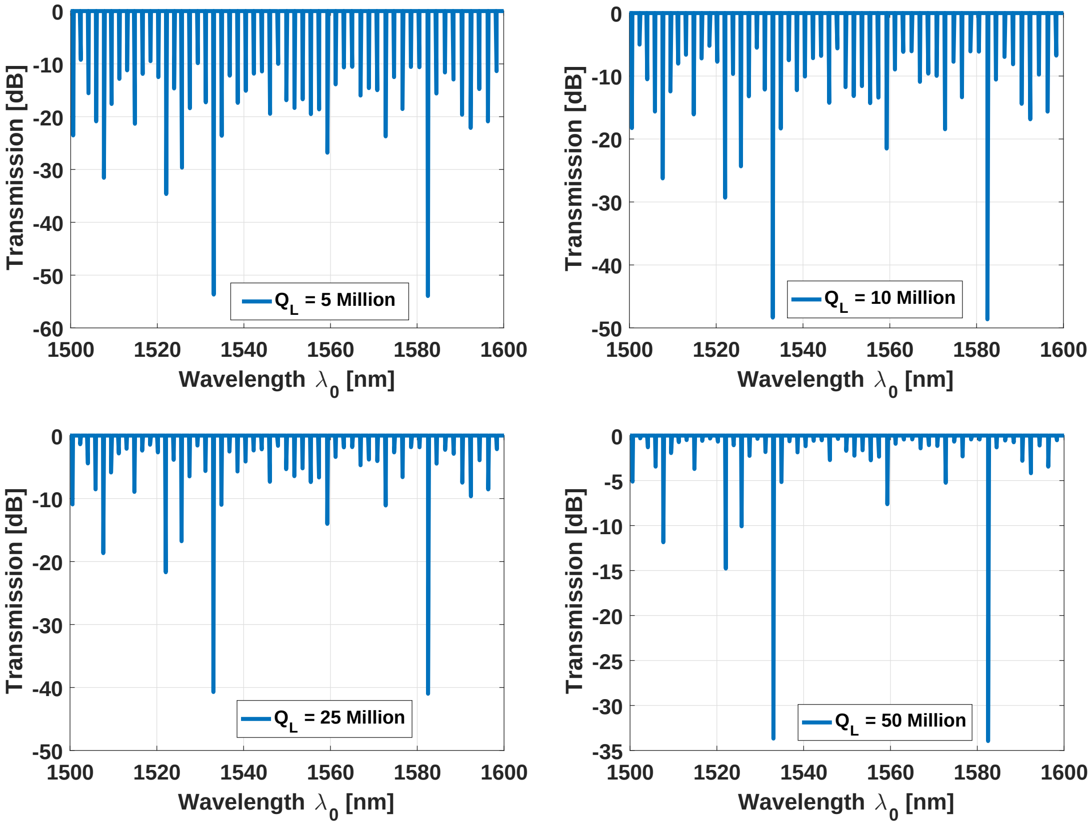

Figure 6.12: Computer-generated resonance spectra (assuming quasi-critical coupling) of varying loaded quality-factors ($Q_L = 5 \cdot 10^6,\ 10 \cdot 10^6, 25 \cdot 10^6$ and $50 \cdot 10^6$) sampled with a resolution of 0.1 pm. Even though the FWHM for a loaded quality-factor Q_L of 50 Million is only about 0.03 pm, the resonances are still recognizable. For the determination of the quality-factor, an external frequency modulation of the laser can be used (for scanning over the desired resonance), or a cavity ring-down measurement can be done.

Even though the FWHM for a loaded quality-factor Q_L of 50 Million is only about 0.03 pm, the resonances are still recognizable when sampling at 0.1 pm (Fig. 6.12). Of course, in case a loaded quality-factor is that high, this can only be seen as an indication that a resonance exists. For evaluating the quality-factor, laser modulation or a ring down measurement needs to be done.

6.3.2 Coupling light to a microtoroid with a straight coupler

The initial design of the proposed device was based on a straight coupler design without a heat spreader. Figure 6.13 shows such a device, which is optically characterized in the following. This microtoroid has a major radius $r_{\mathrm{major}} = 147\,\mu\mathrm{m}$, a minor radius $r_{\mathrm{minor}} = 2.2\,\mu\mathrm{m}$ (calculated based on Eq. 4.4), and a waveguide-to-microtoroid gap of approximately 2.4 µm (± 300 nm) which was measured with the help of an optical microscope. The width of the tapered waveguide in the coupling section is 120 nm.

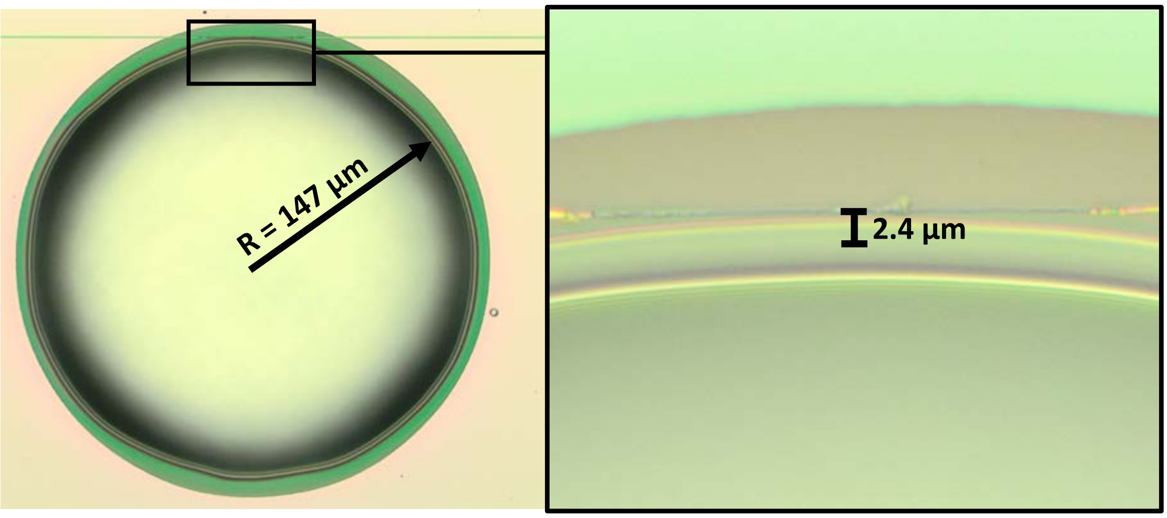

Figure 6.13: Optical image of a monolithically straight overcoupled inverted silica microtoroid with a major radius of 147 µm. The microtoroid shows some micro-bendings and inhomogeneities. The coupling section has approximately a gap of 2.4 µm (± 300 nm) (inset). This gap is comparatively small and is explaining the low resonance extinction (≈ 1 dB), assuming an overcoupling of the microtoroid.

Figure 6.14(a) shows the raw data transmission spectrum of this straight TM-coupled microtoroid without a heat spreader at a temperature setpoint of 25 °C. The spectrum after background removal and the fitted resonances are shown in Fig. 6.14(b). As the gap is comparatively small, the low resonance extinction (≈ 1 dB), assuming an overcoupling of the microtoroid, can be explained.

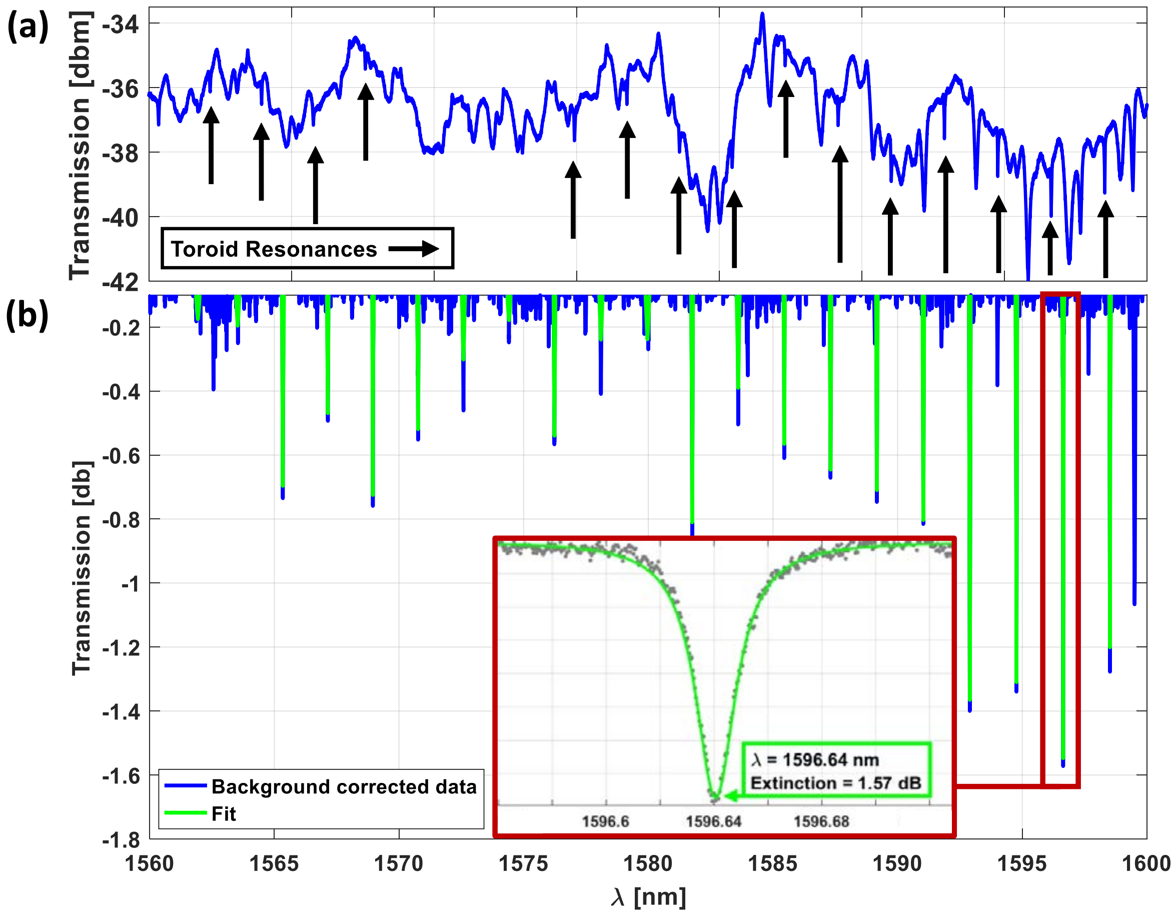

Figure 6.14: Transmission spectrum of an inverted silica microtoroid without heat spreader coupled to a straight Si waveguide at a temperature setpoint of 25 °C. (**a**) Raw data transmission spectrum (blue) as a function of wavelength λ. The black arrows are indicating the positions of the high-Q resonances. (**b**) Background corrected spectrum (blue) and fitted resonances (green). The inset shows a detailed view of a representative resonance.

The free spectral range of the resonances can be directly extracted from the spectrum (FSR $\approx 1.84\,\text{nm}$) (Fig. 6.14). The confidence (95%) interval and the coefficient of determination R^2 are tracked to evaluate the fit quality. For all fits shown in this work, the confidence on the extracted values for the internal resonator loss a, the coupling loss $|t|$ and the group index n_g are high, in case the extinction of a resonance is sufficient (about 1 dB). Therefore, they are not shown as separate confidence interval plots anymore (compare Fig. 2.15 (b)). For example, the confidence interval (95%) for a at $\lambda \approx 1596.64\,\text{nm}$ is between $a_{95\%\,\text{Lower}} = 0.9585$ and $a_{95\%\,\text{Upper}} = 0.9596$ for a fitted value of $a = 0.9590$ for the fitted data shown in the inset of Figure 6.14 (b).

While Q_U and Q_C can both be extracted from a fit (by fitting the resonator loss a and the coupling loss $|t|$) they are interchangeable and cannot generally be distinguished from each other unless it is known whether the resonator is under- or overcoupled.

6.3.3 Temperature dependent straight-coupled microtoroid parameters

In order to verify that the recorded resonances (Fig. 6.14) are indeed from the microtoroid, further measurements were performed at different temperatures, and the shifts of resonances as a function of temperature were recorded.

Figure 6.15 (a) shows three recorded spectra (of the same microtoroid) after background removal at different temperatures (25 °C, 45 °C, and 55 °C) in the wavelength range between 1560 nm – 1600 nm. Figure 6.15 (b) shows different families of resonances. Each family corresponds to the same resonance only shifted by applying a different temperature.

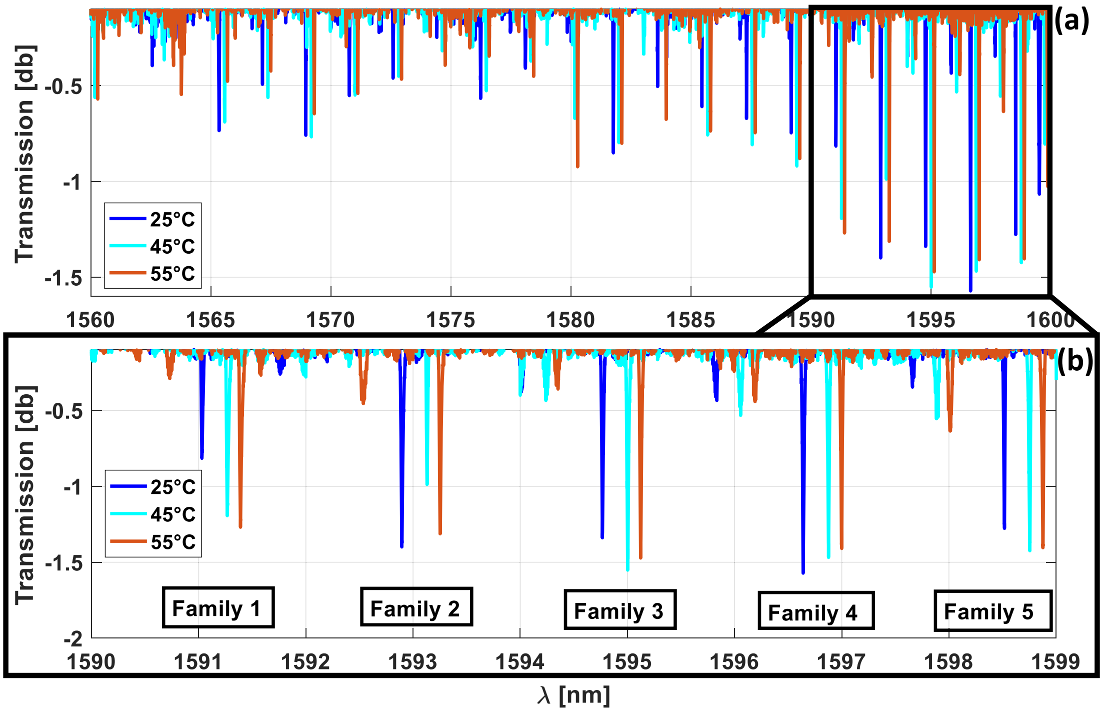

Figure 6.15: (**a**) Background corrected transmission spectra of a single monolithically straight coupled inverted silica microtoroid as a function of wavelength λ at different temperatures (25 °C, 45 °C, and 55 °C). Each resonance is experiencing a spectral shift to higher wavelengths with increasing temperature in the order of $d\lambda/dT = 0.012\,\mathrm{nm/K}$. (**b**) Each family corresponds to the same resonance only shifted by applying a different temperature level.

The group indices n_g were extracted from the FSR. Figure 6.16(a) shows the FSR and (b) the extracted group index n_g at three different temperatures (25 °C, 45 °C, and 55 °C) and Figure 6.16(c) shows the dependency of n_g on the temperature, in the wavelength range between 1565 nm to 1600 nm. Both, the group index and the thermo-optic coefficient confirm that the resonances correspond to light circulating in silica.

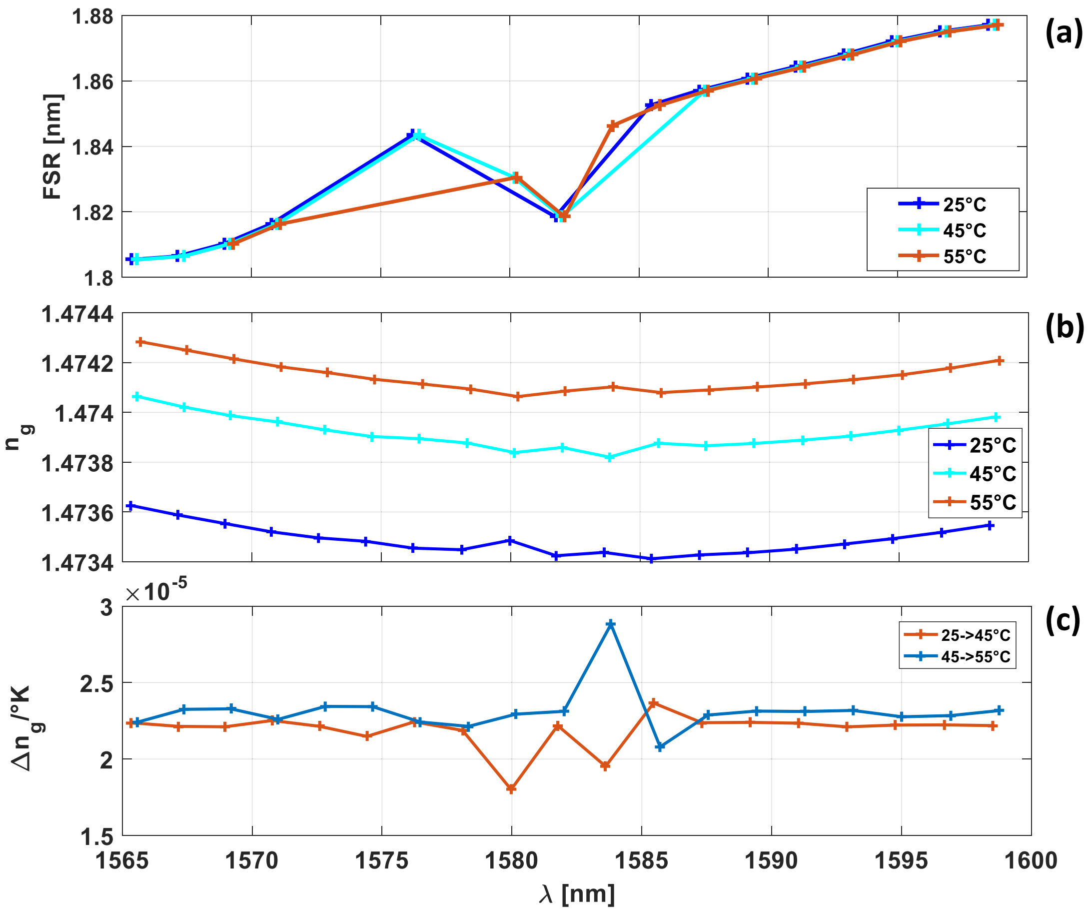

Figure 6.16: Measured FSR and group index of a monolithically straight-coupled inverted silica microtoroid for different temperatures as a function of wavelength λ ($1560\,\mathrm{nm} - 1600\,\mathrm{nm}$). (**a**) The FSR as a function of wavelength and temperature. In the region between $1575 - 1585\,\mathrm{nm}$, the graphs show some slight deviations. These artifacts origin from the fitting algorithm as the extinction of the resonances in this spectral region is comparably small. (**b**) Group index n_g as a function of wavelength and temperature. The free spectral range and the group index meet the theoretical expectation (see Eq. 2.36). (**c**) The shift of group indices n_g as a function of wavelength and temperature.

The thermo-optic coefficient is reported to be about $\mathrm{dn}_{\text{bulk silicon}}/\mathrm{dT} = 1.87\mathrm{E}^{-4}\,1/\mathrm{K}$ for silicon and about $\mathrm{dn}_{\text{bulk silica}}/\mathrm{dT} = 8.57\mathrm{E}^{-6}\,1/\mathrm{K}$ for silica (at $\mathrm{T} = 295\,°\mathrm{C}$ and $\lambda = 1550\,\mathrm{nm}$) [143]. While the extracted thermo-optic coefficient of $\mathrm{dn}/\mathrm{dT} = 2.20\mathrm{E}^{-5}\,1/\mathrm{K}$ is about a factor 2 above the textbook value for silica [143], confinement effects and mechanical deformation might play a role. Moreover, it is a full order of magnitude too low to correspond to high confinement silicon interconnect waveguides, as present elsewhere on the chip.

Further, the intrinsic quality-factor $\mathrm{Q_U}$ and the coupling quality-factor $\mathrm{Q_C}$ can be extracted by analyzing the measured transmission spectrum by extracting the FWHM of each resonance and fitting the internal resonator loss a, the coupling loss $|t|$ and the group index n_g (see Section 2.3.4). The loaded quality-factor Q_L is directly connected to the FWHM (Eq. 2.46) of a resonance and therefore is directly accessible. Q_U corresponds to the Q-factor as limited only by internal losses and excess coupler losses (the internal Q-factor in the absence of excess coupler losses), while Q_C corresponds to the Q-factor as limited only by the coupling losses at the junction. Figures 6.17(a) and (b) are showing the quality-factors as a function of wavelength λ and temperature.

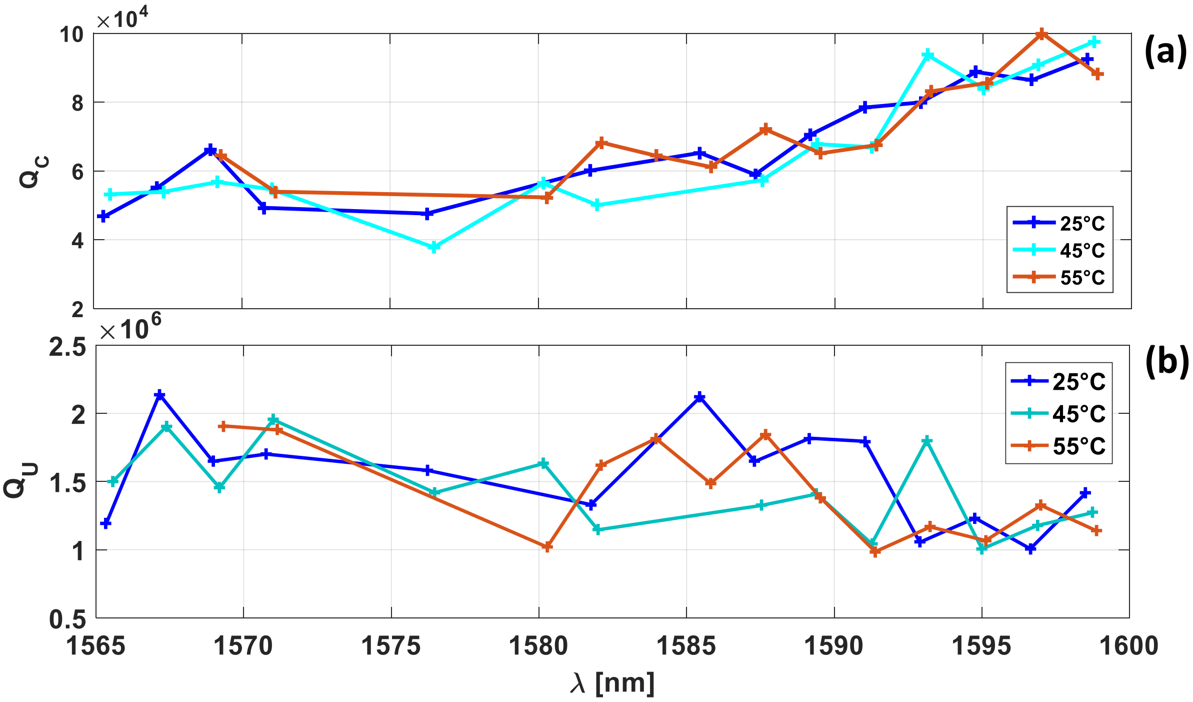

Figure 6.17: Measured quality-factors of a monolithically straight coupled inverted silica microtoroid for different temperatures (25 °C,45 °C and 55 °C) as a function of wavelength λ. (**a**) The fitted coupling quality-factor Q_C as a function of wavelength and temperature. (**b**) The fitted intrinsic quality-factor Q_U as a function of wavelength and temperature. The intrinsic quality-factor Q_U is found to be in the order of up to 2 million. As the coupling section of the microtoroid consists of two different materials (the waveguide is out of silicon and the microtoroid is out of silica), it is expected that the coupling quality-factor Q_C shows an explicit wavelength dependency whereas the intrinsic quality-factor Q_U has only a negligible dependency on the wavelength.

While Q_U and Q_C can both be extracted from a fit of the spectra, they are interchangeable in the fits and cannot generally be distinguished from each other unless it is known whether the resonator is under- or overcoupled. It can be seen in Fig. 6.17 that the Q-factor identified as Q_U has a low sensitivity on the wavelength, as is expected from the intrinsic Q-factor, while the Q-factor identified as Q_C, is highly dependent on wavelength, as is also expected from the coupling strength.

Interestingly, the coupling strength goes down (as Q_C goes up) as the wavelength increases. While this may appear contra-intuitive at first, as longer evanescent fields at longer wavelengths are usually expected to lead to higher coupling strengths in phase matched directional couplers, here the coupling strength is expected to be limited by phase mismatch, with phase matching improving at shorter wavelengths (since the device was designed to feature phase matching at 1550 nm). The extracted coupling Q-factor Q_C is fifteen to thirty times lower than the intrinsic quality-factor Q_U. Thus, the microtoroid is highly overcoupled. The intrinsic quality-factor Q_U is found to be on the order of up to 2 million.

6.3.4 Coupling light to a microtoroid with a weakly tapered gap coupler

During this process, the silica membrane melts until the microtoroid moves sufficiently close to the rim of the undercut region, at which point improved heat sinking slows down and eventually almost stops the reflow process. This also means that any non-uniformity in the thermal environment is transferred to the shape of the microtoroid. One such disturbance that is systematically present by design in case of a straight silicon waveguide junction is the silicon waveguide itself, which locally increases heat sinking (Fig. 6.18(a)). Adiabatically tapering the distance between the microtoroid and a curved waveguide already improves this (Fig. 6.18(b)). A weakly tapered gap coupler, on the other hand, fits well with the natural shape of the microtoroid and results in a weakly tapered (adiabatic) deformation.

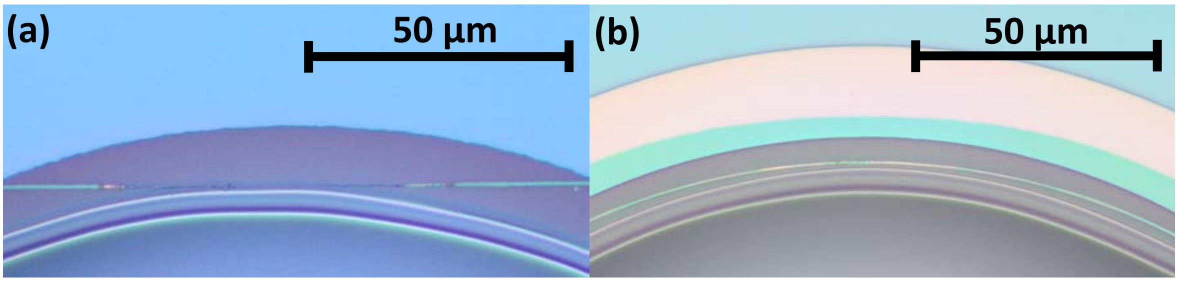

Figure 6.18: Reflow results for waveguide coupled inverted silica microtoroids with (**a**) a straight coupler and (**b**) a weakly tapered gap coupler. In case of a straight coupler (**a**), the coupling section itself acts as a disturbance to the melting process and locally deforms the microtoroid. A weakly tapered gap coupler (**b**), on the other hand, fits well with the natural shape of the microtoroid and results in a weakly tapered (adiabatic) deformation.

Moreover, this adiabatic tapering also reduces the excitation of higher order modes inside the microtoroid and thus the excess losses of the junction (Section 2.3.5), which can have a substantial effect on the quality-factor of ultra-high-Q resonators [27]. The mode mismatch (difference in the propagation constant β) between the two arms of the coupler is reduced in the case of a weakly tapered gap coupler, which leads to a more efficient coupling into the fundamental modes instead of exciting higher order modes.

In the following, another microtoroid is characterized (Fig. 6.19). In contrast to the previously characterized microtoroid (Fig. 6.13), this microtoroid has a weakly tapered gap junction design, and a heat spreader is added. The microtoroid has a major radius $r_{\mathrm{major}} = 140\,\mu\mathrm{m}$, a minor radius $r_{\mathrm{minor}} = 2.3\,\mu\mathrm{m}$ (calculated based on Eq. 4.4), and a waveguide-to-microtoroid gap (center to center) between 3.0 and 3.4 µm. This value was measured with the help of an optical microscope. The width of the tapered waveguide in the coupling section was targeted to be 140 nm, and the distance from the waveguide to the edge of the heat spreader is 4.8 µm. For providing the weak tapering of the coupling junction, the bend radius of the coupling section is 1.2 times the targeted major microtoroid's radius. The heat spreader has a width of 10 µm and has an overlap with the undercut region of 2 µm.

After an initial reflow step, the microtoroid has an intrinsic quality-factor Q_U on the order of 400,000 (Fig 6.20(a)). This value for the intrinsic quality-factor is smaller compared to the microtoroid with a straight-coupler and without a heat spreader (compare Fig. 6.17 (b)). However, optical simulations are indicating (Fig. 4.11 (b)) that the heat spreader is too far away from the microtoroid's resonator to affect the quality-factor due to evanescent coupling losses directly. Indirectly, process related interactions might be responsible for this degradation. Proximity effects during the Si device layer patterning may result in increased surface roughness that likely is transferred to the silica film at the bottom. Furthermore, etching reactants might (re)deposit during processing itself or in the final cleaning step. Additionally, the defects in the microtoroid formation associated with the opening of the heat spreader (see Figs. 6.10 (a) and (b)) remained sufficiently large to spoil the quality-factor. It is also possible that the simulations which are shown in Fig. 4.13 are not entirely accurate, as very small losses are difficult to model.

After initial characterization of the device, a second reflow step is applied. The reason for this is to distinguish the intrinsic and coupling quality-factors from each other. A part of the microtoroid about 200 µm away from the coupling section is locally reflown a second time without affecting the coupling section. The CO_2 laser's beam size and the optical power are decreased for that purpose.

Figure 6.19 shows this microtoroid with a heat spreader, which is coupled via a weakly tapered gap junction. The image shows the microtoroid after the second local reflow that was causing the microtoroid to approach the heat spreader (the remaining distance is about 2 µm to 3 µm). The coupling gap of about 3.0 µm to 3.4 µm was not affected during the second local reflow.

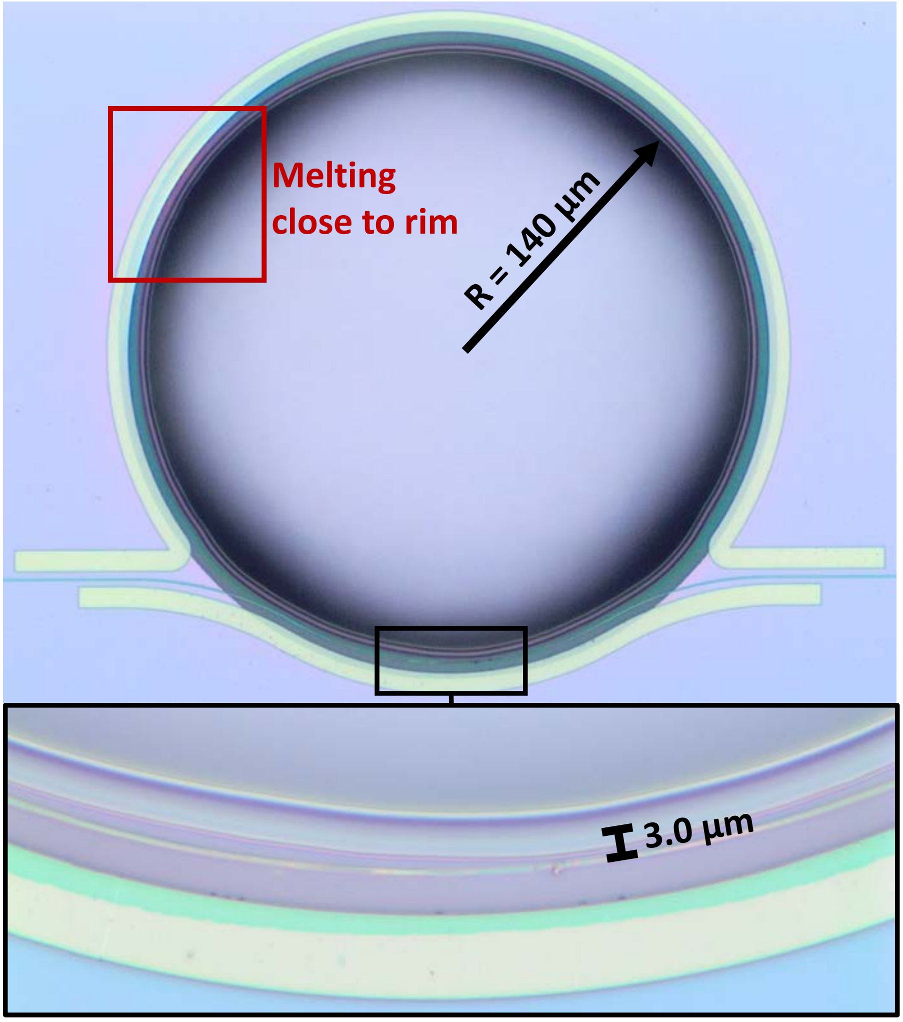

Figure 6.19: Optical image of a monolithically inverted silica microtoroid with a weakly tapered gap junction and a heat spreader. The image shows the microtoroid after a second local reflow that was causing the microtoroid to approach the heat spreader (the remaining distance is about 2 µm to 3 µm). The coupling gap of about 3 µm was not affected during the second reflow (inset).

Figures 6.20 (a) and (b) show the transmission spectra after the first reflow step and the second local reflow step. The sharp resonances are occurring together with broader resonances whose origin is not completely clear yet. The broad resonances' free spectral range is slightly smaller than the sharp resonance spacing, which might be evidence for a higher-order mode of the microtoroid with a slightly higher group index.

Figure 6.20 (c) shows a comparison of the transmission spectra before and after the second reflow step exemplary for an individual resonance. The spectral resonance position is shifted by 0.12 nm as a consequence of the deformation. Further, the extinction of the resonance is also significantly increased, indicating a coupling regime closer to critical coupling.

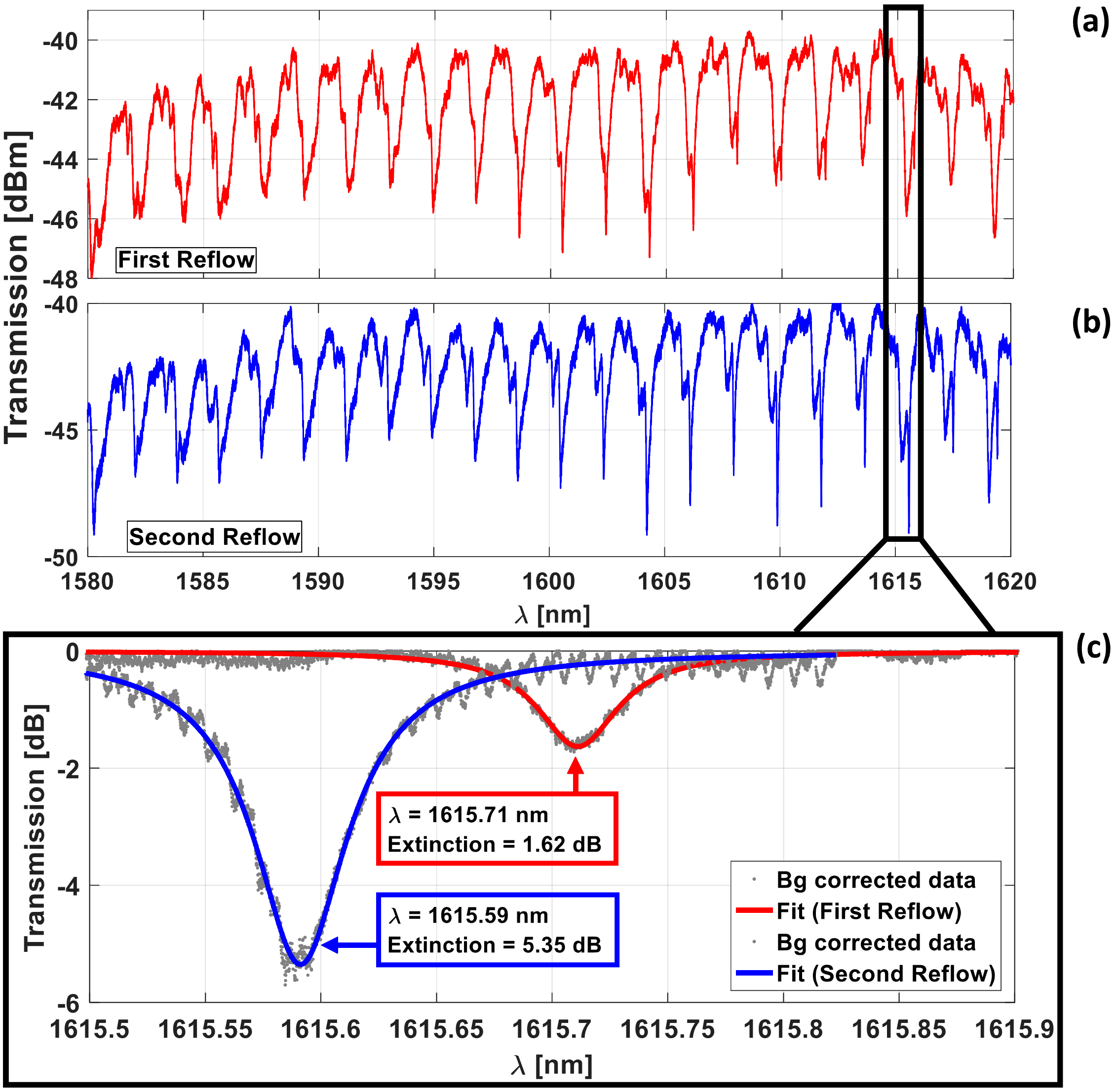

Figure 6.20: Transmission spectrum of an inverted silica microtoroid with weakly tapered gap coupler and heat spreader after a first (**a**) and a second (**b**) local reflow. (**c**) Direct comparison of a selected resonance before and after the second local reflow. The background corrected data after the first reflow is fitted with a resonance at $\lambda_{\mathrm{res}} = 1615.71\,\mathrm{nm}$ with an extinction of 1.62 dB (solid red). The background corrected data after the second local reflow is fitted with a resonance at $\lambda_{\mathrm{res}} = 1615.59\,\mathrm{nm}$ with an extinction of 5.35 dB (solid blue).

Figures 6.21(a) and 6.21(b) show $\mathrm{Q_C}$ and $\mathrm{Q_U}$ as extracted from the transmission spectra before and after the second reflow. It is assumed that the coupling quality-factor $\mathrm{Q_C}$ is not impacted by the second local reflow step, as it was not applied in the vicinity of the coupling junction. Apparently, the second reflow step reduced the intrinsic quality-factor to 100,000 – 200,000. This reduction is expected as this highly localized reflow step locally deformed the microtoroid.

Given the microtoroid-to-waveguide gap is on the order of 3.0 µm to 3.4 µm, the expected coupling quality-factor Q_C would be in the range of 100,000 to 460,000 ($\lambda = 1600\,\text{nm}$) (see Fig. 4.13). Therefore, the Q_C of 40,000 that is extracted from the experimental data is significantly lower than the expected coupling quality-factor.

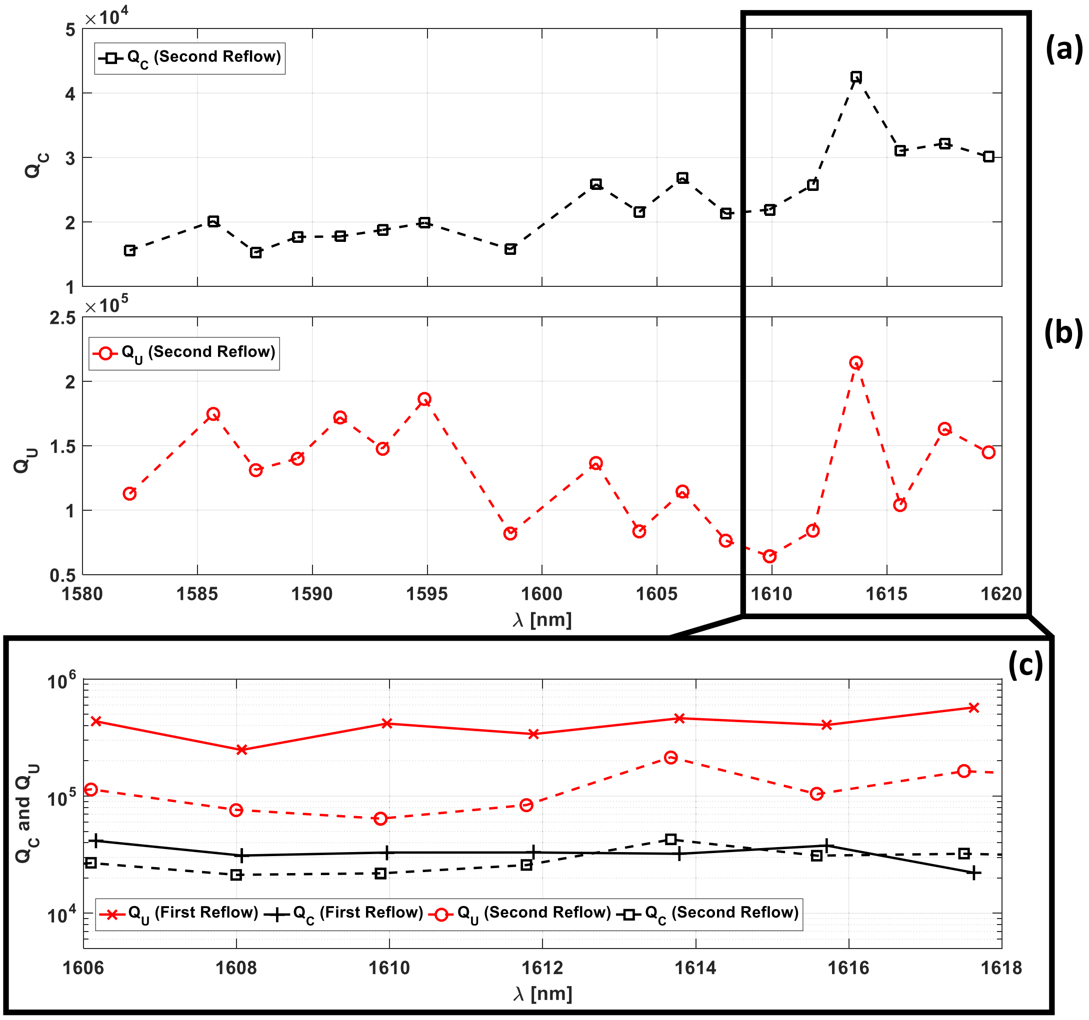

Figure 6.21: Semi-logarithmic plot of the intrinsic and coupling quality-factors Q_U and Q_C of the inverted silica microtoroid with a weakly tapered gap coupler and a heat spreader after a first and a second local reflow as a function of wavelength λ. The coupling quality-factor Q_C (**a**) and the intrinsic quality-factor Q_U (**b**) extracted after the second reflow. (**c**) Comparison of the extracted quality-factors after the first reflow and after the second local reflow step in a limited wavelength range. The quality-factors could not be extracted over the entire wavelength range after the first reflow step as the extinction of the individual resonances are not high enough in that region for a reliable fitting.

In fact, the obtained intrinsic quality-factor Q_U, especially after the second reflow is way below state of the art integrated Si_3N_4 resonators [26, 28, 73]. However, this test structure serves primarily as confirmation that a distinction between the roles of the intrinsic and the coupling quality-factor Q_U and Q_C can be made. Furthermore, it proves that in the current state of the development the inverted microtoroids are generally found to be in the overcoupled regime.

6.4 Discussion

The initial simulation results of the inverted microtoroid (see Section 4.2.4) are indicating a higher intrinsic quality-factor for TM polarization compared to TE polarization for the proposed inverted microtoroid. The whole process flow and design flow, therefore, is adapted to work in TM polarization. In principle, the latest simulation showed that a high intrinsic quality-factor is also achievable with TE polarization (Fig. 4.8) which would enable the use of efficient grating couplers instead of edge couplers. As efficient grating couplers are most often based on a shallow-etch fabrication process, this would lead to a revised fabrication flow. The benefit would be that no final dicing step is necessary. A drawback would be the reduced spectral bandwidth of the edge-coupler compared to a grating coupler. However, the present bandwidth of the proposed device is comparatively small compared to conventional microtoroids. The reason for this reduced bandwidth is the asymmetric coupling between a silicon waveguide and a silica microtoroid. Both materials have a different dispersion relation, and therefore mode matching and effective coupling length are a function of wavelength. In the case of TE polarization, the width of the weakly tapered gap coupler needs to be increased from about 140 nm to about 240 nm to achieve mode matching as the TE_0 mode has a lower confinement in the waveguide compared to the TM_0 mode. The increase in width can potentially also solve another issue. For very thin waveguides, the losses in the coupling section seem to be higher than expected after reflow. A wider waveguide is thermally and mechanically more resistant during the melting-process and can even further act as a heat sink, protecting itself from being melted away.

The edge coupling setup itself can be further optimized. First, using a controlled cleanroom environment would help to stabilize the temperature and the relative humidity during measurements. Additionally, a nitrogen-purged box around the edge coupling setup can help to reduce the problem of the altering of the intrinsic quality-factor due to water deposition (see Section 3.3). This cover box can also help to reduce the problem of vibrations at the fiber tips, which can be caused by air movements.

The obtained quality-factors of the two inverted microtoroid systems (Section 6.3.2 and Section 6.3.4) are not as high as theoretically expected. In fact, the obtained intrinsic quality-factor Q_U of the second device, which is a weakly tapered gap coupled microtoroid (Fig. 6.19), especially after a second reflow, is way below state of the art integrated Si_3N_4 resonators [26, 28, 73].

However, this second test structure serves primarily as confirmation that a distinction between the roles of the intrinsic and the coupling quality-factor Q_U and Q_C can be made. Furthermore, it proves that in the current state of the development the inverted microtoroids are generally in the overcoupled regime. Regarding the coupling quality-factor, it appears as if a simulation or process bias has caused a significant higher coupling strength than initially targeted.

Several explanations can be carried out to evaluate why the obtained quality-factors are significantly lower compared to conventional microtoroids, which are not waveguide-coupled nor inverted [1].

The mode inside an inverted microtoroid is pushed into the direction of the non- or only partially reflown area of the silica film (compare Fig. 4.7), which might be rougher and therefore leads to residual scattering loss. Furthermore, the rather complicated fabrication process of the device, caused by the necessity of defining transition waveguides and couplers, might result in (re)deposition of unwanted residuals, like particles or resist, which are not sufficiently removed during processing and therefore leading to unwanted sources of optical loss. For encountering this contamination issue, the cleaning time in TechniStrip (see Section 5.2.6) was partially increased to above 2 hours. This extended cleaning step seemed to be beneficial regarding the reduction of occurring contaminations.

Also, excess coupling losses (see Section 2.3.5), which cannot be independently extracted from the experimental data, might play a role. For example, assuming an inverted microtoroid with a $r_{major} = 140\,\mathrm{nm}$, excess junction losses of $0.1\,\%$ (meaning the junction excess loss is $30\,\mathrm{dB}$ below what is transmitted through the junction) would be sufficient to limit the quality-factor to about one million (see also Fig. 2.19).

The primary difference between the two presented devices is the geometry of the coupling junction and the heat spreader. Excess losses can explain the limitation of the straight-coupled microtoroid's quality-factor and might be even higher for the weakly tapered gap coupled microtoroid. However, the second local reflow of the gap-coupled microtoroid caused a significant reduction of the intrinsic quality-factor even though the coupling junction was not affected. Therefore, the excess coupling losses might play a significant role for the overall-limitation of the quality-factor after the first reflow, but cannot be made responsible for the further reduction of the intrinsic quality-factor after the second reflow. This reduction of the quality-factor after first and second reflow seems to imply that the quality-factor has an additional processing dependent factor. Before performing a second local reflow, the chip is exposed to ambient environment. Indeed, this is also an issue before performing the first reflow step.

However, after a first reflow, the chip is analyzed under a microscope and optically characterized with an edge-coupling setup. During this characterization, the chip likely collects particles or water deposits on its surface. When doing a second reflow, these contaminations can be integrated into the resonator, severely degrading the intrinsic quality-factor. Furthermore, water deposition cannot be avoided which has been shown to trigger a severe degradation of the intrinsic quality-factor [1, 118].

Geometrical defects occurring during the microtoroid formation associated with the openings of the heat spreader (see Figs. 6.10 (a) and (b)), and defects like micro-bendings might spoil the quality-factor. Reducing the micro-bending (notches) in the heat spreader's entry section for the waveguide (see inset of Fig. 6.10 b)) is targeted. The bending radius of such a micro-bending is about 50 µm and way below. A microtoroid with a major radius of $r_{\mathrm{major}} = 50\,\mu\mathrm{m}$ would have a bending limited quality-factor of about 8 Million.

It is not clear in which way the resonator reacts when locally melted again. The already melted and solidified part of the microtoroid is locally melted again and formed to a new part of the resonator, whereas the rest of the resonator stays unaffected. This is comparable to the situation in which a microtoroid is formed by moving a CO_2-laser beam around the circumference of the initial silica-membrane. During this circular movement, the microtoroid is only partially fabricated, whereas the rest of the membrane stays mostly unaffected. The major difference is the remelting of an already fabricated part of the resonator in this work. In [144] it is reported that using a moving CO_2-laser beam for the fabrication still can lead to extremely high intrinsic quality-factors for conventional microtoroids. Therefore, it is expected that the remelting or a partial fabrication is not a limiting factor, as long as the chip's surface is contamination free.

Since the inverted microtoroid is highly overcoupled (up to 30 times), it is possible to see a substantial improvement of the excess coupling losses if the microtoroid-to-waveguide gap is increased to yield the required coupling strength and might also substantially increase the quality-factor of the device. While we have so far only shown the integration of the microtoroid resonator with a silicon interconnect waveguide, the device, and process flow was conceived to be in principle compatible with monolithic integration with electro-optic devices.

Chapter 7

Conclusion and prospects

The following chapter summarizes the achievements of this work. Furthermore, a prospect is outlined as help for future work.

7.1 Retrospective

In conclusion, a new type of reflown microtoroidal silica resonator with an inverted topology that is monolithically coupled to a silicon waveguide, as part of a monolithic silicon PIC, was demonstrated. Intrinsic quality-factors of up to 2 million have been achieved and may be improved by further process development.

The most challenging part of this work was establishing a working and reproducible fabrication flow for the proposed silicon photonics IVT system. For developing this fabrication scheme, several fabrication techniques were engineered, and various fabrication attempts were tested with the support of multiple international collaborators. Finally, all fabrication steps were successfully moved to an in-house facility, making it possible to create new samples comparatively fast and straightforward. In particular, the time (excluding EBL writing) spent for fabricating up to 4 chips in parallel (each carrying 26 microtoroids) takes approximately two working days and might be further reduced in the future.

The systems built and used for the fabrication and characterization can be used in a variety of other projects. Notably, the CO_2 laser-reflow setup turned out to be useful is other scientific fields including micro-machining of nanocrystalline diamond films [145] as well as the edge-coupling setup and the designed isotropic silicon undercut process [146].

The initial goal of creating a monolithically integrated microtoroid based on silica with a CO_2 laser-reflow process was fulfilled. The target intrinsic quality-factor of 100 million was not achieved so far. The highest observed quality-factor, so far, is in the order of 2 million. In principle, there is confidence that the targeted intrinsic quality-factor is feasible as simulation results are indicating, but further development and process stabilization are necessary. Substantially, the measurement environment can be further improved by using a vacuum measurement setup and a controlled cleanroom working atmosphere for the optical characterization. Also, the coupling between the waveguide and the microtoroid needs to be further optimized, as the microtoroid in its current state is highly overcoupled.

Future work will also involve combining this device with electro-optic components. For enabling this monolithic integration, a process-flow for a local deprocess of the Back-End-Of-Line (BEOL) prior to microtoroid fabrication, needs to be developed.

7.1.1 Design of the IVT system

Originally, the IVT was designed as TM and TE polarization compatible integrated photonic device for the field of optical telecommunication. Existing integration schemes of microtoroid-like structures with on-chip waveguides have relied either on silica waveguides or on suspended silicon waveguides, fabricated in stacked silicon-on-insulator device-layers with a rather complicated fabrication process, which makes integration with standard silicon photonics devices, like electro-optic modulators, wavelength multiplexers, grating couplers or germanium photodetectors challenging. In the presented approach, for providing the full integration capability, a silicon waveguide is monolithically coupled to a melted inverted microtoroid. As the base material, a standard silicon-on-insulator wafer is used, making integration with other photonic devices more feasible.

The primary issue in the design of an IVT is its bending loss limited intrinsic quality-factor. In contrast to conventional microtoroids, the proposed design attempt is suffering more from bending losses, caused by its inverted design (Section 4.1). However, it is possible to define requirements for the base-wafer specification and the inverted microtoroid itself with the help of optical simulations. For example, the BOX thickness has to be smaller than 1.3 µm for an inverted microtoroid with a major radius of 150 µm in case of TM polarization. Following this requirement, an intrinsic quality-factor of 100 Million, not limited by the bending losses, is theoretically achievable.

In contrast to a conventional microtoroid, in an IVT system, waveguide interconnect-sections and coupling-sections have to be designed. The design trade-off consists of reducing optical waveguide losses by still not degrading the potential intrinsic quality-factor of an IVT. For example, a standard SOI wafer with a BOX thickness of 2 µm and a silicon device layer-thickness of 220 nm cannot be used as a base for an IVT system. The BOX thickness is violating the previously defined condition of a maximum BOX thickness. Furthermore, by using SOI with a thinner BOX layer the substrate leakage losses of a waveguide (fabricated in the device layer) become high. Therefore, a device layer thickness of about 300 nm is necessary to allow for an efficient guiding of TE_0 and TM_0 waveguide modes.

The coupling of light to an on-chip device was more challenging than initially expected. For an efficient coupling of light from an external laser source to an on-chip device, either an edge-coupler design or a grating-based attempt is feasible. Based on simulation results, at the beginning of this project, it was decided to base the IVT on TM polarization as the TM_0 mode of an IVT shows the highest bending limited intrinsic quality-factors.

Therefore, edge-couplers are chosen as coupling devices as they provide similar efficiency for TE and TM polarization. The edge-coupler design for an IVT is challenging. First, in the current design, there is no top cladding (for example, SiO_2) for the edge-couplers. In case of a top cladding, the mode would show a symmetric refractive index distribution, as the underlying material (the BOX) is out of silica. The missing top cladding is causing substrate leakage losses, as the used BOX is comparatively thin. Furthermore, the final undercut-etch of the BOX layer requires sufficient protection of the edge-coupler, which was done by using photoresist. A fundamental problem was the control of the distance of the edge-coupler to the chip-edge. Any dicing (through the edge-couplers) before undercutting the BOX caused the edge-coupler to be etched away as its facet was not protected anymore during the undercut. Furthermore, an edge-polishing of the edge-coupler's facets would cause severe damage to the undercut membranes.

For overcoming this issue, it was decided to make use of the undercut itself. By designing trenches close to the edge-coupler tips in the BOX layer, the edge-couplers were undercut themselves. First, this solved another fundamental issue, as the inversely tapered edge-coupler has no silicon substrate underneath, the substrate leakage losses are not playing a role anymore. In particular, the light is even loosely coupled into the underlying BOX before being coupled into the edge-coupler. Furthermore, the dicing blade, in this case, has only to be positioned in the trench. Therefore, cutting through the edge-couplers is not necessary, which leaves their facets unaffected. The distance from the tips of the edge-couplers to the rim of the undercut coupling section membrane is only defined by the initial trench position relative to the edge-coupler tip. Therefore, this final distance is about 2 µm, which is better than the precision of conventional dicing systems. Finally, the edge of the trench does not need to be polished since it is defined during the silica dry-etch in an earlier fabrication step.

In a conventional microtoroid, the coupling distance between an existing fiber and a microtoroidal structure itself can be more or less freely defined with the help of mechanical stages. Therefore, the coupling strength in a conventional microtoroid can be adjusted by moving in and out the coupling-fiber.

In the current design, this gap is fixed by design. In case of an inverted microtoroid, therefore, the wavelength tunability is used primarily to adjust the coupling strength between bus-waveguide and microtoroid.

Furthermore, the coupling-section waveguide and the inverted microtoroid are defined by two different lithographic processes. The coupling section waveguide is defined by EBL and the hole, as the basis for the microtoroid, is defined later on by optical lithography. Since an alignment deviation of about 1 µm during optical lithography is present usually, the relative position of the coupling section waveguide and the hole is also showing this deviation. The deviation is critical, as the underlying silicon substrate will act as a heatsink during the subsequent reflow process. For example, assuming a deviation of 1 µm will lead to an offset for this heat sink, leading to an undetermined heat sinking during reflow. Moreover, the subsequent melting process, which forms the microtoroid, is a function of laser power, especially the stability of the power level, and the laser focus size, leading to another source of deviation for the gap. The deviation is a fundamental issue of the proposed device, as a reproducible gap, in this design, from one device to the other (on different chips) is hard to achieve.

The melting process can be controlled to some extent, but an over-melting of the microtoroid can happen which, in the worst case, can burn and, therefore, destroy the coupling junction. Writing the holes with EBL is not an option as this is too time-consuming due to their geometric size. For overcoming this issue, heat spreaders were designed. The prerequisite for using a heat spreader as effective device is that it is positioned with high precision relative to the coupling-section waveguide. This way, it can manipulate the melting process in a predetermined way relative to the waveguide. Logically, the heat-spreader needs to be located in the device layer of the chip patterned together with the waveguide.

Therefore, the relative position of the heat-spreader and the coupling section waveguide can be well controlled, only limited by the precision of the EBL-system itself. These silicon heat-spreaders are used to manipulate the melting process of the undercut membrane. Once the microtoroid is approaching the waveguide and the heat-spreader, the heat-spreader acts as a heat sink, which can stop the reflow process. Therefore, the effect of the deviation accumulated during the optical lithography step is reduced, leading to a more reproducible gap (Section 5.2.3). As a consequence, the whole reflow process becomes more stable, and it is even possible to correct the gap in a second reflow step, as the melting process is slowed down when approaching the heat spreader (Section 5.3.3).

Furthermore, the heat spreader shows a stabilization effect on the undercut membranes during fabrication. Accordingly, the idea of a heat spreader was extended to be used as stabilization bridges for the undercut edge-coupling membranes (Section 6.2.1).

7.1.2 Fabrication of the IVT system

Developing a working and reproducible fabrication flow for the proposed IVT system was the most challenging part of this work.

In contrast to conventional microtoroids, which can be fabricated comparatively straightforwardly and do not need expensive SOI material as a base, inverted microtoroids require SOI and a sophisticated fabrication process.

Initially, the usage of XeF_2 for developing the undercut process with collaborators in Twente (MESA+) and Dresden (Fraunhofer IPMS) was used, but the smoothness of the undercut was not sufficient. Furthermore, undercut-etch recipes developed with a standard silicon wafer which was oxidized did not show the same etching roughness as the final high-grade SOI wafers.

Due to the extensive fabrication time, up to several weeks, as samples needed to be fabricated in serial at different cleanroom locations, the fabrication process was redeveloped to allow for a complete in-house fabrication. As XeF_2 was not available, a dry-etch SF_6 process was introduced. This way the time spent for creating up to 4 chips in parallel (each carrying 26 microtoroids) is two working days, excluding EBL writing time of several hours, and can be further reduced.

For fabricating an IVT system, two masks are used. One mask is an EBL written pattern. This pattern, transferred vial EBL-lithography, is used to define all structures in the device layer of an SOI chip. Another optical mask is used later on to define all structures in the BOX layer of the chip. For aligning the device-layer structures to the structures of the BOX-layer, particular markers are used. The precision of this alignment process is about 1 µm. By the use of dedicated heat spreaders this unforeseeable alignment deviation can be balanced out leading to a reproducible gap between coupling section waveguide and microtoroid during reflow. Small additional corrections on the gap can be done by using a second reflow step (section 5.3.3).

7.1.3 Characterization of the IVT system

This work shows that an IVT system can be designed and fabricated in a way to allow for monolithic coupling. Furthermore, it is shown that a reproducible and comparatively fast fabrication flow can be established (Section 5.2 and 5.3). The final chosen coupling section design fits well with the natural shape of the IVT, which further promotes a smooth melting result (Section 6.2.2).

The reason for the discrepancy of the current intrinsic quality-factor of up to 2 million and the targeted quality-factor of 100 millions might be a result of contaminating residuals (like resist), the redeposition of water on the microtoroid's surface, micro-bendings (section 3.3) or high coupler excess losses (section 2.3.5), as in the current state the microtoroids are highly overcoupled (compare Figures 6.17 and 6.21).

The microtoroids spectral response is measured in a lab environment. It would be beneficial to move the whole setup for reflow and optical measurement into a cleanroom to reduce any external contamination.

Additionally, the entrance section for the silicon coupling waveguide within the heat-spreader (Section 6.2.2) needs to be optimized to avoid undesired micro-bendings, which can degrade the intrinsic quality-factor due to their high local bending losses caused by their small bending radius.

A crucial step in the current fabrication flow is the final dicing step. First, a chip carrying the fabricated devices needs to be coated with a protective resist. Since the undercut is already performed during an earlier etch process, the protective resist coating can lead to damage. By systematically testing the structural integrity, when being coated with resist, it turned out that the undercut membranes are more stable than expected. More critical is the presence of the resist itself, as the removal becomes hard and residual resist can stick in the undercut area and on the surface. This residual resist can negatively influence the intrinsic quality-factor of the final device. The dicing step itself is the most dangerous step when it comes to the structural integrity of the device. In case the resist had not enough time to entirely flow into the undercut areas severe damage during the dicing was observed.

7.1.4 Side benefits of the IVT project for other work

During the work on the IVT-project, multiple techniques were developed, and various systems were built. It turned out that these results are useful in other scientific work. In the following, these side benefits are collected, and the potential benefits for other work is outlined.

1. CO_2 Laser-reflow setup: The melting setup is a high precision tool for illuminating a desired sample with a focused beam of light at a wavelength of 10.6 µm. Due to the comparable high optical power level of up to 20 W this setup shows micro-machining capabilities. In fact, diamond was structured on top of a doped silicon substrate [145].

Additionally, this tool has the capability of measuring the transmission of a sample (on the fly) during processing, making the acquisition of absorption measurements possible. Furthermore, user-defined arbitrary patterns can be adapted. This way, for example, gratings and dot matrices can be written. By adjusting the spot size, the reflow process can be conducted at various power densities on the sample. This tool might also act as a tool for cutting samples with a glass substrate.

2. Establishing of the Knife-Edge-Method: For the determination of the caustic of a CO_2 -Laser beam the knife-edge-method is used. In principle, the setup can be equipped with another laser source. When replacing the ZnSe-optics with suitable optical components, laser sources of other wavelengths can be characterized. Depending on the wavelength, possibly the thermal detector has to be replaced for this purpose as well. Of course, in the case of a CO_2 -Laser beam this method is particularly precise as the wavelength is comparably long compared to near-infrared or visible light sources.

3. Edge-Coupling-Setup: The edge coupling setup is semi-automatic and can be used to connect an external laser source to measure the optical spectrum of on-chip devices. Two stages are present, each is carrying one lensed optical fiber, which is suitable for near-infrared light, but in principle, it could be exchanged by any other fiber. The coarse alignment of the fibers needs to be done manually, whereas fine-alignment, to achieve high coupling efficiency, is done automatically (Section 6.1.2). Furthermore, each stage can be slightly rotated in the transverse and in the axial direction to compensate for undesired angular misalignment. An optical microscope and an infrared camera help to align the fibers to a chip. With the help of a Peltier-element, it is possible to heat or cool the chip to a desired temperature (up to about 50° C). A computer program (written in Matlab) helps to control the setup and an external laser source as well. In fact, this setup was shared as a lab-tool as the setup is flexible enough to reassemble the present stages in the desired way to account for various chip layouts, chip sizes, and desired wavelengths.

4. Undercut process: Among other developed fabrication processes, the highly-selective silicon undercut-etch is worthwhile for the use in other projects. For example, it is possible to undercut waveguide structures locally with the help of this process. By under-etching a waveguide, fabricated on top of a BOX layer of a SOI chip, substrate leakage losses can be reduced. Since the effective index of an optical waveguide-mode is a function of its environment (and therefore possibly of the substrate), a local undercut can also manipulate the effective index of a mode. In principle, this process can also be used to undercut thermal tuners (as is already done) to enforce a stronger and more efficient tuning capability as no heat is dissipated due to a thermally conductive substrate directly.

7.2 Prospect

The presented IVT system can be further improved. First, the intrinsic quality-factor needs to be increased to allow for efficient frequency comb generation. Consequently, a front- or/and back-end integration flow needs to be developed to allow the integration with other on-chip devices. In the following various ideas and possible attempts are collected to target several potential improvements regarding the integration with other optical components, the reproducibility and general enhancement of the workflow and the enhancement of the intrinsic quality-factor.

7.2.1 Front- and Back-End integration

It is desirable to fabricate an IVT device to be part of a system of other optical components, which would be superior to a hybrid integration since no additional fiber connections and alignment procedures are necessary. Depending on the fabrication process of the other components, a front- or back-end integration would be desirable.

In case of a front-end integration, an IVT system can be tested regarding its optical and mechanical properties and a potential adaption of other optical components can be triggered accounting for the IVT's optical properties.

A potential back-end integration can be desirable in case the fabrication process of other components is restricted regarding cleanliness issues. While so far only integration of the microtoroid resonator with a silicon interconnect waveguide was shown, the device and process flow were conceived to be in principle compatible with monolithic integration with on-chip electro-optic devices. One remaining issue would then be the deprocessing of the Back-End-Of-Line (BEOL) dielectric layers in the immediate vicinity of the microtoroid, prior to microtoroid fabrication out of high-quality BOX oxide. The sides of a silicon rib-waveguide could, for example, form an etch stop for local BEOL removal, after which the silicon-slabs on the sides of the waveguide could be locally removed. Details of the envisioned process flows can also be found in [147].

Figure 7.1 shows a potential back-end integration scheme for the proposed IVT adapting the ideas from [147]. In the described back-end integration scheme for an inverted microtoroid, it is assumed that an already existing silicon layer is beneath a dielectric silica layer. This silicon layer carries a waveguide structure that later on is used for coupling light to an inverted microtoroid. Therefore, the rib-waveguide already needs to be connected to different optical devices/components. Underneath this silicon, a layer of silica is present (most likely the BOX). This additional buried silica layer is required for fabricating the inverted microtoroid later on.

In the first step, a working area is opened up, in which the inverted microtoroid is going to be fabricated, or more precisely, all other areas of the chip need to be protected (Step 1). All other devices, carried by the chip, are masked by a cladding that is sufficiently protecting the devices from a subsequent silica-etch that uses the silicon layer as an etch-stopping layer (the side of a rib-waveguide) (Step 2).

Subsequently, the waveguide area itself is locally protected by resist (Step 3), and a silicon-etch is performed (Step 4). Afterward, an oxidation step (Step 5) ensures that the exposed waveguide gets a protecting oxidation layer for an undercut step that is performed later on. For defining a hole for the actual microtoroid, another resist coating step is necessary before performing a silica-etch step down to the underlying silicon (most likely the substrate of the chip) (Step 6). After assigning a cleaning procedure, an undercut, either by using XeF_2 or another isotropic silicon-etch, is created (compare Section 5.2.5) (Step 7). The oxide cover of the waveguide (resulting from the oxidation) acts as protection during the undercut step. In the last step, the microtoroid is created by thermal CO_2-Laser-reflow (Step 8).

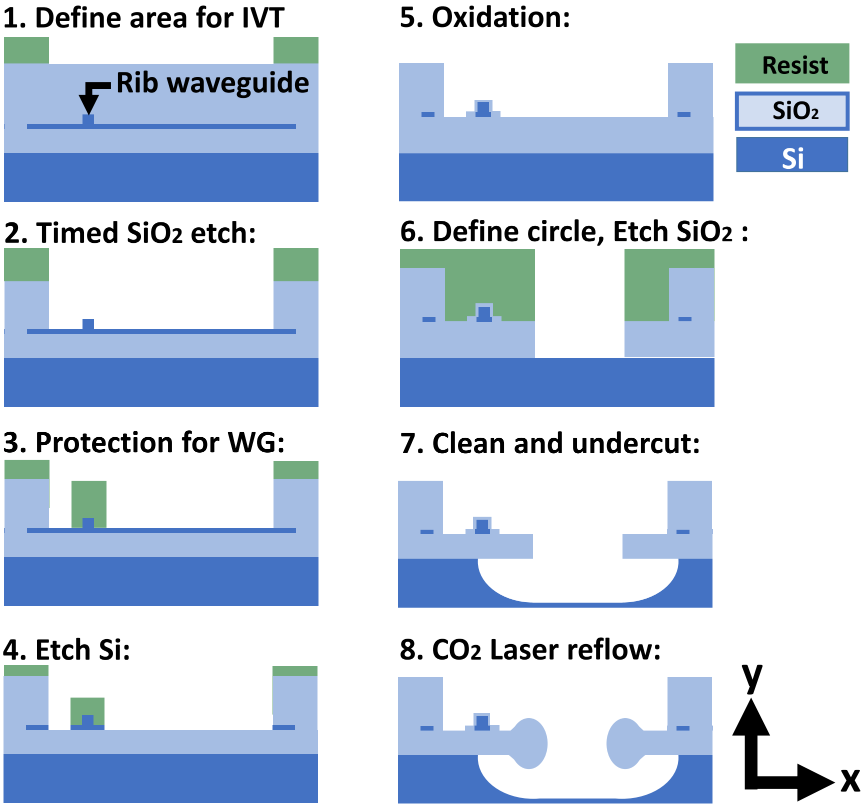

Figure 7.1: Back-end fabrication flow for an inverted microtoroid with different devices (not shown). (**1**) A chip is protected by resist except for an IVT working area. The rib-waveguide, within that area, is buried under an oxide layer. (**2**) A dry-etch removes the silica layer and is using the buried silicon layer as etch-stop. (**3**) The waveguide is protected by the resist. (**4**) A silicon-etch is exposing the rib-waveguide structure. (**5**) An oxidation step ensures that the exposed waveguide gets a protecting oxidation layer for an undercut step that is performed later on. (**6**) A circle as a base for the microtoroid is defined and is exposed by a silica-etch. (**7**) The chips are cleaned and subsequently undercut. (**8**) A thermal CO_2-laser-reflow step is creating the final inverted integrated microtoroid.

In contrast, to the present fabrication flow from Section 5.2.7, an oxidation step is used in the described back-end fabrication scheme (Fig. 7.1). This way the cleaning of the chip can be done before performing an undercut, as the waveguide is protected by an oxide layer. In fact, the cleaning procedure is challenging once the undercut is performed, as the free-standing silica membranes can become fragile and can break. Performing the cleaning step before the undercut may lead to better control on mechanical damage and parasitic resist residuals.

7.2.2 Improvement of the CO_2 -reflow setup

The CO_2-reflow setup (Section 5.3) in its current state is capable of creating the desired microtoroidal shaped microtoroids. In the following various ideas are outlined to improve the current reflow system further, regarding reliability, melting precision, and melting quality.

Camera System

During the melting progress, a camera system acquires a live image of this process. A significant drawback of the current system is the limited resolution and magnification of the acquired image. A higher image resolution would help to analyze the melting result before removing the sample from the setup.

However, as the duration of the melting process is usually on the order of seconds, a higher resolution image cannot help to improve the precision of the melting in the first place. Especially the gap between microtoroid and waveguide is too small to be precisely measured with an optical camera system. However, when performing a second local reflow on the same waveguide-coupled microtoroid a higher resolution image (or increased magnification) could help to improve the precision as a second local reflow usually takes much longer as the heat sinking effect becomes strong. This way the gap between waveguide and gap could be targeted with higher precision. In the current state, the camera image shows approximately an area of $1\,\mathrm{mm}^2$.

Laser power level

A laser that lases in the Gaussian ground mode shows the highest energy density in its center position, due to the Gaussian power distribution. Therefore, the power level is dropping exponentially in the radial direction. Comparing an inverted microtoroid and a conventional microtoroid, regarding the power level during reflow the melt “sees”, two significant differences are arising which are leading to a higher necessary laser power level for melting an inverted microtoroid compared to a conventional microtoroid.

First, in case of a conventional microtoroid, the center consists of a silicon pillar with a silica disc on top (compare Fig. 3.8). The silica disc can only be melted in the area, which is not directly lying on top of the silicon pillar that acts as a direct heat sink.

In case of an inverted microtoroid, the heat sink is not situated in the center of the microtoroid, caused by its inverted shape. Therefore, in the center of an inverted microtoroid the silicon is directly exposed during the undercut and the laser light, in that area, is not affecting the melting behavior of the microtoroid. In fact, the light is directly passing through without heating up the chip. Therefore, a higher laser power level for melting is needed comparing a conventional and an inverted microtoroid.

Second, in case of a conventional microtoroid, during the reflow, the melt is approaching the central pillar. Therefore, the melt “sees” an increasing power level while melting and stops when the heat sinking effect, induced by the pillar, becomes too strong to keep the temperature above the melting temperature of 1650 °C. Additionally, the microtoroid itself has an intrinsic termination behavior, as the minor radius of the microtoroid (see Fig. 3.8 (b)) increases during melting and therefore is shielding the microtoroid itself more and more from being further melted as its volume increases. In the case of an inverted microtoroid, the melt is approaching the outer rim of the microtoroid. Therefore, the melt is moving out of the focal position of the laser and sees a decreasing power level during reflow.

In the current setup, the laser can be utilized to fabricate inverted microtoroids in a single-shot (see Section 5.3.3). In the current state, for fabricating microtoroids with a major radius of $r_{\text{major}} = 250\,\mu\text{m}$, the necessary optical power is already close to the maximum accessible power level of the laser system of around 20 W of optical output power.

The alternative to the single-shot attempt is a spiral movement, in which the laser beam is approaching the rim of the microtoroid in a circular movement with increasing radius by moving the chip. In the current state, the chip is positioned on an $x - y$ stage. Therefore, the circular movement needs to be mimicked by controlled x- and y-movements. A badly behaving movement can lead to a staircasing effect, which can degrade the quality-factor of the resulting resonator. Ideally, a rotation stage is integrated to provide a stable and precise circular movement, either of the chip or the laser beam. Further, a laser with a higher maximum optical output power might be beneficial. As an increased total optical output power of a laser is often accompanied by lower power stability, maybe using a donut-mode (TEM_{01*}) would be superior, as it fits better with the shape of the microtoroid, and therefore does not require an extensively increased power level. Alternatively, an axicon lens might be used, which could replace the current bi-convex ZnSe lens. Of course, this would imply to run multiple optical simulations to decide which system is most suited.

Contamination issues

The reflow setup, as well as the measurement setup for the optical characterization, are currently located in a standard lab environment without precisely controlled temperature and humidity. The possibility cannot be excluded that contaminations, for example originating from an air condition, are dropping onto a microtoroidal device. These parasitic contaminations can lead to defects during the reflow or manifests as an unwanted component after melting inside the resonator. Therefore, the CO_2 setup should be moved into a cleanroom atmosphere and the microtoroids should be boxed before being exposed to the ambient environment.

7.2.3 Device design improvements

In the following different attempts are collected to improve the current design of the inverted microtoroid.

Relaxing BOX thickness requirements

The interconnect waveguide of the inverted microtoroid device is situated on top of a comparably thin buried oxide layer which can cause substrate leakage when its width gets too small (Fig. 4.5). The oxide layer itself needs to have a minimal thickness to avoid optical leakage. In principle, a thinner BOX would allow for higher bending radii of a microtoroid by not affecting its intrinsic quality-factor. Therefore, a thinner BOX from the perspective of the microtoroid, regarding space consumption, would be desirable. Also, by relaxing the limit for the BOX thickness other commercially available SOI wafers might be used for the fabrication, which can increase the integratability with other optical device systems.

As an undercut-etch in the silicon substrate needs to be done in any case, an attempt to relax the BOX thickness requirements would be to define small circles placed in parallel to the waveguides, used as opening holes in the BOX. These opening holes will cause the waveguide to be undercut, which would allow for thinner BOX thickness as the substrate leakage is reduced (Fig. 7.2).

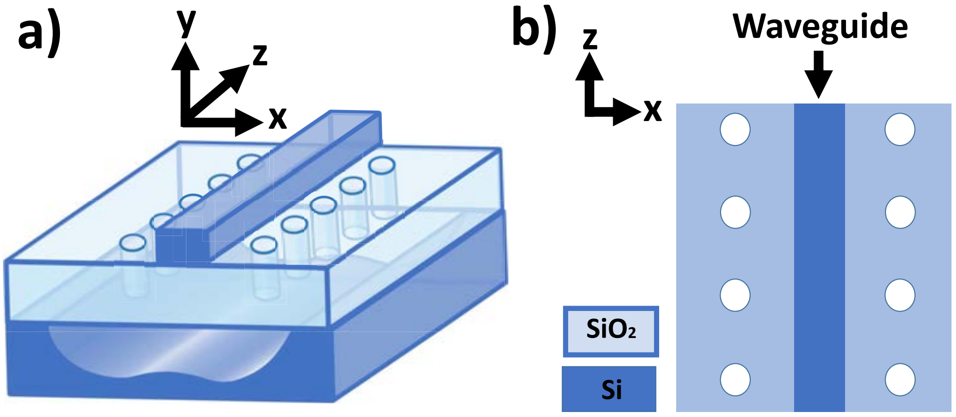

Figure 7.2: Undercut silicon transmission waveguides built on SOI platform. (**a**) Scheme of a partially undercut silicon interconnect waveguide. (**b**) Holes (in the BOX layer), placed in parallel to a silicon transmission waveguide, which are used for undercutting the latter.

Grating Coupler

Up to now, only TM-polarization has been under consideration, as this theoretically should lead to higher intrinsic quality-factors for the microtoroid. However, most devices in silicon photonics rely on TE-polarization. In principle, it would be desirable to test the inverted microtoroid device with TE-polarization as well. Grating couplers are usually more suitable for TE-polarization allowing for a denser integration of the microtoroid as no extensive routing of waveguides to the chip-edges is required.

By the combination of a grating coupler with an oxide cladding and a local undercut, the coupling efficiency could be reasonably high. In the current setup entirely etched TE grating couplers show a coupling loss per coupler in the order of 8 dB at a wavelength of $\lambda = 1590\,\text{nm}$. This high coupling loss is most likely caused by the relative thin BOX and the fact that the gratings are fully etched.

7.2.4 Intrinsic quality-factor and power level

Water contamination

The surface of a silica microtoroid is highly hygroscopic, leading to water molecules on the surface. Water absorbs light efficiently in the near-infrared ($\lambda = 1.55\,\mu\text{m}$), and even a monolayer on the resonator's surface leads to additional losses and is decreasing the quality-factor [113]. The quality-factor is altered to a steady state within about 100 s but can be partially recovered when the resonator is baked out at about 400 °C [116]. In the current state, the optical characterization of the inverted microtoroids is done under ambient conditions. Therefore, the measurement setup would need to be equipped with a nitrogen-purged box, or with another inert gas. As the handling of a chip outside the box still will be done under ambient conditions, additionally a heating system needs to be added that can heat up the chip sufficiency to recover its quality-factor before the optical measurements. Ideally, once characterized, the device is held under a nitrogen atmosphere, or even is boxed separately.

Micro-bendings

Micro-bendings of the microtoroid's resonator can degrade its intrinsic quality-factor, as a micro-bending is a defect, which is causing enhanced optical bending losses. For example, a microtoroid with a major radius of 50 µm has a bending-limited intrinsic quality-factor of 8 to 9 million (see Section 6.2.2). The radius of such a micro-bend can be even smaller, leading to a higher bending loss. Also, an adiabatic mode transition between the optical resonator mode and the mode of the micro-bend is not achieved. This mode mismatch can lead to an additional optical loss. Even though the occurrence of micro-bendings was reduced during the process development, future developments should target the reduction of micro-bendings especially in the waveguide-entrance region of the heat spreader (see Fig. 6.10).

Excess losses

Directional coupler excess losses per pass γ are parasitic losses, which are caused by scattering losses, a coupling into unwanted higher order modes, or radiation modes as the coupling gap decreases. They are limiting the maximum attainable quality-factor of a resonator [27] (see also Section 2.3.5). Especially the scattering might become a problem in the monolithically coupled microtoroid in which a silicon waveguide is coupled monolithically to a silica resonator. The microtoroids presented in Section 6.3 are highly overcoupled, and indeed the intrinsic measured quality-factors are below what simulations predict (compare Section 4.2.4 and Section 4.2.7). For reducing excess losses of the microtoroid, the coupler design was improved (compare Section 2.3.5). However, for finally achieving the desired high intrinsic quality-factor the microtoroid needs to be coupled in the critical- or under-coupled regime. Therefore, the distance between the heat spreader and the coupling junction waveguide needs to be increased. Further, additional systematic sweeping of the distance needs to be done.

Microtoroid size

The microtoroid's intrinsic quality-factor is limited by its optical bending losses. Therefore, fabricating microtoroids of an increased major radius may lead to higher intrinsic quality-factors.

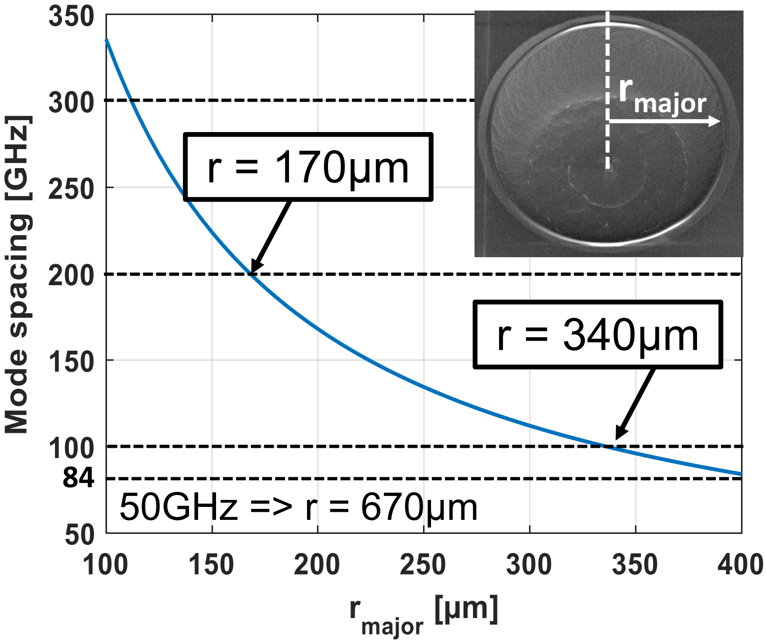

Figure 7.3: Mode spacing of microtoroid's resonances as a function of major radius. A major radius of 140 μm leads to a mode spacing of approximately 250 GHz. By further increasing the major radius, a modes spacing of 50 GHz can be targeted.

With increasing radius, higher excess losses can be tolerated, as the intrinsic total propagation losses in the resonator are higher nonetheless, due to its increased length (compare Section 2.3.5). Furthermore, a repetition rate (mode spacing) of resonances of 50 GHz ($r_{\mathrm{major}} = 670\,\mu\mathrm{m}$) can be achieved (Fig. 7.3).

Bibliography

[1] D. K. Armani, T. J. Kippenberg, S. M. Spillane, and K. J. Vahala, “Ultra-high-Q toroid microcavity on a chip,” *Nature*, vol. 421, no. 6926, pp. 925–928, 2003.

[2] T. J. Kippenberg, R. Holzwarth, and S. A. Diddams, “Microresonator-Based Optical Frequency Combs,” *Science*, vol. 332, no. 6029, pp. 555–559, 2011.

[3] J. Witzens, T. Baehr-Jones, and M. Hochberg, “Silicon photonics: On-chip OPOs,” *Nature Photonics*, vol. 4, no. 1, pp. 10–12, 2010.

[4] J. Pfeifle, V. Brasch, M. Lauermann, Y. Yu, D. Wegner, T. Herr, K. Hartinger, P. Schindler, J. Li, D. Hillerkuss, R. Schmogrow, C. Weimann, R. Holzwarth, W. Freude, J. Leuthold, T. J. Kippenberg, and C. Koos, “Coherent terabit communications with microresonator Kerr frequency combs,” *Nature Photonics*, vol. 8, no. 5, pp. 375–380, 2014.

[5] P. Marin-Palomo, J. N. Kemal, M. Karpov, A. Kordts, J. Pfeifle, M. H. P. Pfeiffer, P. Trocha, S. Wolf, V. Brasch, M. H. Anderson, R. Rosenberger, K. Vijayan, W. Freude, T. J. Kippenberg, and C. Koos, “Microresonator-based solitons for massively parallel coherent optical communications,” *Nature*, vol. 546, no. 7657, pp. 274–279, 2017.

[6] A. M. Armani and K. J. Vahala, “Heavy water detection using ultra-high-Q microcavities,” *Optics Letters*, vol. 31, no. 12, p. 1896, 2006.

[7] F. Vollmer, S. Arnold, D. Braun, I. Teraoka, and A. Libchaber, “Multiplexed DNA Quantification by Spectroscopic Shift of Two Microsphere Cavities,” *Biophysical Journal*, vol. 85, no. 3, pp. 1974–1979, 2003.

[8] S. Arnold, M. Khoshsima, I. Teraoka, S. Holler, and F. Vollmer, “Shift of whispering-gallery modes in microspheres by protein adsorption,” *Optics Letters*, vol. 28, no. 4, p. 272, 2003.

[9] F. Vollmer, S. Arnold, and D. Keng, “Single virus detection from the reactive shift of a whispering-gallery mode,” *Proceedings of the National Academy of Sciences of the United States of America*, vol. 105, no. 52, pp. 20701–20704, 2008.

[10] A. Ramachandran, S. Wang, J. Clarke, S. J. Ja, D. Goad, L. Wald, E. M. Flood, E. Knobbe, J. V. Hryniewicz, S. T. Chu, D. Gill, W. Chen, O. King, and B. E. Little, "A universal biosensing platform based on optical micro-ring resonators," *Biosensors & bioelectronics*, vol. 23, no. 7, pp. 939–944, 2008.

[11] F. Dell'Olio, T. Tatoli, C. Ciminelli, and M. N. Armenise, "Recent advances in miniaturized optical gyroscopes," *Journal of the European Optical Society: Rapid Publications*, vol. 9, 2014.

[12] M. Iqbal, M. A. Gleeson, B. Spaugh, F. Tybor, W. G. Gunn, M. Hochberg, T. Baehr-Jones, R. C. Bailey, and L. C. Gunn, "Label-Free Biosensor Arrays Based on Silicon Ring Resonators and High-Speed Optical Scanning Instrumentation," *IEEE Journal of Selected Topics in Quantum Electronics*, vol. 16, no. 3, pp. 654–661, 2010.

[13] J. Witzens and M. Hochberg, "Optical detection of target molecule induced aggregation of nanoparticles by means of high-Q resonators," *Optics express*, vol. 19, no. 8, pp. 7034–7061, 2011.

[14] Y. Zhao, Q. Wang, F. Meng, Y. Lin, S. Wang, Y. Li, B. Lin, S. Cao, J. Cao, Z. Fang, T. Li, and E. Zang, "High-finesse cavity external optical feedback DFB laser with hertz relative linewidth," *Optics Letters*, vol. 37, no. 22, p. 4729, 2012.

[15] W. Lewoczko-Adamczyk, C. Pyrlik, J. Häger, S. Schwertfeger, A. Wicht, A. Peters, G. Erbert, and G. Tränkle, "Ultra-narrow linewidth DFB-laser with optical feedback from a monolithic confocal Fabry-Perot cavity," *Optics express*, vol. 23, no. 8, pp. 9705–9709, 2015.

[16] W. Yoshiki, Y. Honda, T. Tetsumoto, K. Furusawa, N. Sekine, and T. Tanabe, "All-optical tunable buffering with coupled ultra-high Q whispering gallery mode microcavities," *Scientific reports*, vol. 7, no. 1, p. 10688, 2017.

[17] K. Wörhoff, R. G. Heideman, A. Leinse, and M. Hoekman, "TriPleX: A versatile dielectric photonic platform," *Advanced Optical Technologies*, vol. 4, no. 2, p. 103, 2015.

[18] T. J. Kippenberg, S. M. Spillane, and K. J. Vahala, "Kerr-nonlinearity optical parametric oscillation in an ultrahigh-Q toroid microcavity," *Physical Review Letters*, vol. 93, pp. –, 2004.

[19] P. Del'Haye, A. Schliesser, O. Arcizet, T. Wilken, R. Holzwarth, and T. J. Kippenberg, "Optical frequency comb generation from a monolithic microresonator," *Nature*, vol. 450, no. 7173, pp. 1214–1217, 2007.

[20] A. A. Savchenkov, A. B. Matsko, D. Strekalov, M. Mohageg, V. S. Ilchenko, and L. Maleki, "Low threshold optical oscillations in a whispering gallery mode CaF(2) resonator," *Physical review letters*, vol. 93, no. 24, p. 243905, 2004.

[21] A. A. Savchenkov, A. B. Matsko, V. S. Ilchenko, I. Solomatine, D. Seidel, and L. Maleki, "Tunable optical frequency comb with a crystalline whispering gallery mode resonator," *Physical review letters*, vol. 101, no. 9, p. 093902, 2008.

[22] B. A. Rose, A. J. Maker, and A. M. Armani, "Characterization of thermo-optic coefficient and material loss of high refractive index silica sol-gel films in the visible and near-IR," *Optical Materials Express*, vol. 2, no. 5, p. 671, 2012.

[23] M. A. Foster, J. S. Levy, O. Kuzucu, K. Saha, M. Lipson, and A. L. Gaeta, "Silicon-based monolithic optical frequency comb source," *Optics Express*, vol. 19, no. 15, p. 14233, 2011.

[24] M. Ghulinyan, F. Ramiro Manzano, R. Guider, N. Prtljaga, G. Pucker, and L. Pavesi, "Silicon-based monolithically integrated whispering-gallery mode resonators with buried waveguides," in *SPIE Photonics Europe*, SPIE Proceedings, p. 84311O, SPIE, 2012.

[25] A. G. Griffith, R. K. W. Lau, J. Cardenas, Y. Okawachi, A. Mohanty, R. Fain, Y. H. D. Lee, M. Yu, C. T. Phare, C. B. Poitras, A. L. Gaeta, and M. Lipson, "Silicon-chip mid-infrared frequency comb generation," *Nature communications*, vol. 6, p. 6299, 2015.

[26] Y. Okawachi, K. Saha, J. S. Levy, Y. H. Wen, M. Lipson, and A. L. Gaeta, "Octave-spanning frequency comb generation in a silicon nitride chip," *Optics letters*, vol. 36, no. 17, pp. 3398–3400, 2011.

[27] D. T. Spencer, J. F. Bauters, M. J. R. Heck, and J. E. Bowers, "Integrated waveguide coupled Si(3)N(4) resonators in the ultrahigh-Q regime," *Optica*, vol. 1, no. 3, p. 153, 2014.

[28] L. Wang, L. Chang, N. Volet, M. H. P. Pfeiffer, M. Zervas, H. Guo, T. J. Kippenberg, and J. E. Bowers, "Frequency comb generation in the green using silicon nitride microresonators," *Laser & Photonics Reviews*, vol. 10, no. 4, pp. 631–638, 2016.

[29] X. Zhang and A. M. Armani, "Silica microtoroid resonator sensor with monolithically integrated waveguides," *Optics express*, vol. 21, no. 20, pp. 23592–23603, 2013.

[30] J. Yao, D. Leuenberger, M.-C. M. Lee, and M. C. Wu, "Silicon Microtoroidal Resonators With Integrated MEMS Tunable Coupler," *IEEE Journal of Selected Topics in Quantum Electronics*, vol. 13, no. 2, pp. 202–208, 2007.

[31] V. S. Ilchenko, X. S. Yao, and L. Maleki, "Pigtailing the high-Q microsphere cavity: a simple fiber coupler for optical whispering-gallery modes," *Optics Letters*, vol. 24, no. 11, p. 723, 1999.

[32] J. Richter, M. P. Nezhad, and J. Witzens, “Monolithically integrated waveguide-coupled silica microtoroids,” in *2015 Opto-Electronics and Communications Conference (OECC)*, pp. 1–3.

[33] T. Miya, Y. Terunuma, T. Hosaka, and T. Miyashita, “Ultimate low-loss single-mode fibre at 1.55 um,” *Electronics Letters*, vol. 15, no. 4, p. 106, 1979.

[34] Saleh, Bahaa E. A. and M. C. Teich, *Fundamentals of photonics.* Wiley series in pure and applies optics, Hoboken, N.J.: Wiley-Interscience, 2nd ed. ed., 2007.

[35] G. T. Reed and A. P. Knights, *Silicon photonics: An introduction.* Chichester: Wiley, reprinted with corrections ed., 2005.

[36] L. Solymar and E. Shamonina, eds., *Waves in metamaterials.* Oxford: Oxford University Press, first edition ed., 2009.

[37] C. F. Bohren and D. R. Huffman, *Absorption and scattering of light by small particles.* New York: Wiley, 1983.

[38] J. Hecht, *City of light: The story of fiber optics.* The Sloan technology series, New York: Oxford University Press, rev. and expanded ed., paperback ed. ed., 1999.

[39] W. T. Silfvast, ed., *Laser fundamentals.* Cambridge: Cambridge University Press, 2nd ed. ed., 2004.

[40] M. J. Deen and P. K. Basu, *Silicon photonics: Fundamentals and devices.* Wiley series in materials for electronic and optoelectronic applications, Chichester, West Sussex, UK: Wiley, 2012.

[41] S. Romero-Garcia, B. Marzban, F. Merget, B. Shen, and J. Witzens, “Edge Couplers With Relaxed Alignment Tolerance for Pick-and-Place Hybrid Integration of III–V Lasers With SOI Waveguides,” *IEEE Journal of Selected Topics in Quantum Electronics*, vol. 20, no. 4, pp. 369–379, 2014.

[42] S. Romero-Garcia, B. Shen, F. Merget, B. Marzban, and J. Witzens, “Alignment Tolerant Couplers for Silicon Photonics,” *IEEE Journal of Selected Topics in Quantum Electronics*, vol. 21, no. 6, pp. 765–778, 2015.

[43] B. Schmid, A. Petrov, and M. Eich, “Optimized grating coupler with fully etched slots,” *Optics Express*, vol. 17, no. 13, pp. 11066–11076, 2009.

[44] M. Antelius, K. B. Gylfason, and H. Sohlström, “An apodized SOI waveguide-to-fiber surface grating coupler for single lithography silicon photonics,” *Optics express*, vol. 19, no. 4, pp. 3592–3598, 2011.

[45] A. Bozzola, L. Carroll, D. Gerace, I. Cristiani, and L. C. Andreani, “Optimising apodized grating couplers in a pure SOI platform to -0.5 dB coupling efficiency,” *Optics express*, vol. 23, no. 12, pp. 16289–16304, 2015.

[46] M. Streshinsky, R. Shi, A. Novack, Cher, Roger Tern Poh, A. E.-J. Lim, P. G.-Q. Lo, T. Baehr-Jones, and M. Hochberg, “A compact bi-wavelength polarization splitting grating coupler fabricated in a 220 nm SOI platform,” *Optics express*, vol. 21, no. 25, pp. 31019–31028, 2013.

[47] K. Yamada, “Silicon Photonic Wire Waveguides: Fundamentals and Applications,” in *Silicon Photonics II* (D. J. Lockwood and L. Pavesi, eds.), vol. 119 of *Topics in Applied Physics*, pp. 1–29, Berlin, Heidelberg: Springer Berlin Heidelberg, 2011.

[48] D. G. Rabus, *Integrated Ring Resonators: The Compendium*, vol. 127 of *Springer Series in Optical Sciences.* Berlin, Heidelberg: Springer-Verlag Berlin Heidelberg, 2007.

[49] W. Bogaerts, P. de Heyn, T. van Vaerenbergh, K. de Vos, S. Kumar Selvaraja, T. Claes, P. Dumon, P. Bienstman, D. van Thourhout, and R. Baets, “Silicon microring resonators,” *Laser & Photonics Reviews*, vol. 6, no. 1, pp. 47–73, 2012.

[50] S. S. Azadeh, F. Merget, S. Romero-García, A. Moscoso-Mártir, N. von den Driesch, J. Müller, S. Mantl, D. Buca, and J. Witzens, “Low V(pi) Silicon photonics modulators with highly linear epitaxially grown phase shifters,” *Optics express*, vol. 23, no. 18, pp. 23526–23550, 2015.

[51] S. L. Chuang, *Physics of photonic devices*, vol. 2009: 1 of *Wiley series in pure and applied optics.* Hoboken, N.J.: John Wiley, 2 ed. ed., 2009.

[52] K. Okamoto, *Fundamentals of Optical Waveguides.* Academic Press, 2nd ed., 2010.

[53] P. Rabiei, W. H. Steier, C. Zhang, and L. R. Dalton, “Polymer micro-ring filters and modulators,” *Journal of Lightwave Technology*, vol. 20, no. 11, pp. 1968–1975, 2002.

[54] Rayleigh, “CXII. The problem of the whispering gallery,” *Philosophical Magazine Series 6*, vol. 20, no. 120, pp. 1001–1004, 1910.

[55] P. R. Griffiths and De Haseth, James A., *Fourier transform infrared spectrometry*, vol. v. 171 of *Chemical analysis.* Hoboken, N.J.: Wiley-Interscience, 2nd ed ed., 2007.

[56] O. Schwelb, “Transmission, Group Delay, and Dispersion in Single-Ring Optical Resonators and Add/Drop Filters—A Tutorial Overview,” *Journal of Lightwave Technology*, vol. 22, no. 5, pp. 1380–1394, 2004.

[57] P. Del'Haye, T. Herr, E. Gavartin, M. L. Gorodetsky, R. Holzwarth, and T. J. Kippenberg, "Octave spanning tunable frequency comb from a microresonator," *Physical review letters*, vol. 107, no. 6, p. 063901, 2011.

[58] I. Coddington, W. C. Swann, and N. R. Newbury, "Coherent dual-comb spectroscopy at high signal-to-noise ratio," *Physical Review A*, vol. 82, no. 4, p. 043817, 2010.

[59] A. M. Zolot, F. R. Giorgetta, E. Baumann, J. W. Nicholson, W. C. Swann, I. Coddington, and N. R. Newbury, "Direct-comb molecular spectroscopy with accurate, resolved comb teeth over 43 THz," *Optics letters*, vol. 37, no. 4, pp. 638–640, 2012.

[60] D. W. Vernooy, V. S. Ilchenko, H. Mabuchi, E. W. Streed, and H. J. Kimble, "High-Q measurements of fused-silica microspheres in the near infrared," *Optics Letters*, vol. 23, no. 4, p. 247, 1998.

[61] S. M. Spillane, T. J. Kippenberg, O. J. Painter, and K. J. Vahala, "Ideality in a fiber-taper-coupled microresonator system for application to cavity quantum electrodynamics," *Physical review letters*, vol. 91, no. 4, p. 043902, 2003.

[62] H. Lee, T. Chen, J. Li, K. Y. Yang, S. Jeon, O. Painter, and K. J. Vahala, "Chemically etched ultrahigh-Q wedge-resonator on a silicon chip," *Nature Photonics*, vol. 6, no. 6, pp. 369–373, 2012.

[63] F. Ramiro-Manzano, N. Prtljaga, L. Pavesi, G. Pucker, and M. Ghulinyan, "Monolithic integration of high-Q wedge resonators with vertically coupled waveguides," in *SPIE Microtechnologies* (J.-M. Fédéli, L. Vivien, and M. K. Smit, eds.), SPIE Proceedings, p. 876704, SPIE, 2013.

[64] G. Li, P. Liu, X. Jiang, C. Yang, J. Ma, H. Wu, and M. Xiao, "High-Q silica microdisk optical resonators with large wedge angles on a silicon chip," *Photonics Research*, vol. 3, no. 5, p. 279, 2015.

[65] P. Del'Haye, O. Arcizet, A. Schliesser, R. Holzwarth, and T. J. Kippenberg, "Full Stabilization of a Microresonator-Based Optical Frequency Comb," *Physical Review Letters*, vol. 101, no. 5, 2008.

[66] P. Del'Haye, A. Coillet, T. Fortier, K. Beha, D. C. Cole, K. Y. Yang, H. Lee, K. J. Vahala, S. B. Papp, and S. A. Diddams, "Phase-coherent microwave-to-optical link with a self-referenced microcomb," *Nature Photonics*, vol. 10, no. 8, pp. 516–520, 2016.

[67] T. Herr, V. Brasch, J. D. Jost, C. Y. Wang, N. M. Kondratiev, M. L. Gorodetsky, and T. J. Kippenberg, "Temporal solitons in optical microresonators," *Nature Photonics*, vol. 8, no. 2, pp. 145–152, 2013.

[68] E. Lucas, H. Guo, J. D. Jost, M. Karpov, and T. J. Kippenberg, “Detuning-dependent properties and dispersion-induced instabilities of temporal dissipative Kerr solitons in optical microresonators,” *Physical Review A*, vol. 95, no. 4, 2017.

[69] C. Javerzac-Galy, K. Plekhanov, N. R. Bernier, L. D. Toth, A. K. Feofanov, and T. J. Kippenberg, “On-chip microwave-to-optical quantum coherent converter based on a superconducting resonator coupled to an electro-optic microresonator,” *Physical Review A*, vol. 94, no. 5, 2016.

[70] H. Jung, C. Xiong, K. Y. Fong, X. Zhang, and H. X. Tang, “Optical frequency comb generation from aluminum nitride microring resonator,” *Optics letters*, vol. 38, no. 15, pp. 2810–2813, 2013.

[71] H. Yoshioka, T. Ota, C. Chen, S. Ryu, K. Yasui, and Y. Oki, “Extreme ultra-low lasing threshold of full-polymeric fundamental microdisk printed with room-temperature atmospheric ink-jet technique,” *Scientific reports*, vol. 5, p. 10623, 2015.

[72] L. Yang, T. Carmon, B. Min, S. M. Spillane, and K. J. Vahala, “Erbium-doped and Raman microlasers on a silicon chip fabricated by the sol-gel process,” *Applied Physics Letters*, vol. 86, no. 9, p. 091114, 2005.

[73] D. T. Spencer, J. F. Bauters, M. J. R. Heck, and J. E. Bowers, “Integrated waveguide coupled Si(3)N(4)resonators in the ultrahigh-Q regime,” *Optica*, vol. 1, no. 3, p. 153, 2014.

[74] F. Monifi, S. K. Ozdemir, J. Friedlein, and L. Yang, “Encapsulation of a Fiber Taper Coupled Microtoroid Resonator in a Polymer Matrix,” *IEEE Photonics Technology Letters*, vol. 25, no. 15, pp. 1458–1461, 2013.

[75] C. Lecaplain, C. Javerzac-Galy, M. L. Gorodetsky, and T. J. Kippenberg, “Mid-infrared ultra-high-Q resonators based on fluoride crystalline materials,” *Nature communications*, vol. 7, p. 13383, 2016.

[76] K. J. Vahala, “Optical microcavities,” *Nature*, vol. 424, no. 6950, pp. 839–846, 2003.

[77] F. Luan, M. D. Pelusi, M. R. Lamont, D.-Y. Choi, S. Madden, B. Luther-Davies, and B. J. Eggleton, “Dispersion engineered as2s3 planar waveguides for broadband four-wave mixing based wavelength conversion of 40 gb/s signals,” *Opt. Express*, vol. 17, pp. 3514–3520, Mar 2009.

[78] L. Razzari, D. Duchesne, M. Ferrera, R. Morandotti, S. Chu, B. E. Little, and D. J. Moss, “CMOS-compatible integrated optical hyper-parametric oscillator,” *Nature Photonics*, vol. 4, no. 1, pp. 41–45, 2010.

[79] J. S. Levy, A. Gondarenko, M. A. Foster, A. C. Turner-Foster, A. L. Gaeta, and M. Lipson, “CMOS-compatible multiple-wavelength oscillator for on-chip optical interconnects,” *Nature Photonics*, vol. 4, no. 1, pp. 37–40, 2009.

[80] J. Muller, J. Hauck, A. Moscoso-Martir, N. Chimot, S. Romero-Garcia, B. Shen, F. Merget, F. Lelarge, and J. Witzens, “High speed WDM interconnect using silicon photonics ring modulators and mode-locked laser,” pp. 1–3.

[81] S. Pathak, M. Vanslembrouck, P. Dumon, D. van Thourhout, and W. Bogaerts, “Optimized Silicon AWG With Flattened Spectral Response Using an MMI Aperture,” *Journal of Lightwave Technology*, vol. 31, no. 1, pp. 87–93, 2013.

[82] F. Merget, S. S. Azadeh, J. Mueller, B. Shen, M. P. Nezhad, J. Hauck, and J. Witzens, “Silicon photonics plasma-modulators with advanced transmission line design,” *Optics express*, vol. 21, no. 17, pp. 19593–19607, 2013.

[83] B. Jalali and S. Fathpour, “Silicon Photonics,” *Journal of Lightwave Technology*, vol. 24, no. 12, pp. 4600–4615, 2006.

[84] N. C. Harris, Y. Ma, J. Mower, T. Baehr-Jones, D. Englund, M. Hochberg, and C. Galland, “Efficient, compact and low loss thermo-optic phase shifter in silicon.”

[85] G. Beninca de Farias, S. Menezo, O. Dubray, D. Marris-Morini, L. Vivien, A. Myko, and B. Blampey, “Up to 64-QAM Modulation of a Silicon-Ring-Resonator-Modulator,” in *Optical Fiber Communication Conference*, (Washington, D.C.), p. M3G.3, OSA, 2014.

[86] K. Preston, S. Manipatruni, A. Gondarenko, C. B. Poitras, and M. Lipson, “Deposited silicon high-speed integrated electro-optic modulator,” *Optics Express*, vol. 17, no. 7, p. 5118, 2009.

[87] R. Ding, T. Baehr-Jones, Y. Liu, R. Bojko, J. Witzens, S. Huang, J. Luo, S. Benight, P. Sullivan, J.-M. Fedeli, M. Fournier, L. Dalton, A. Jen, and M. Hochberg, eds., *A low VπL modulator with GHz bandwidth based on an electro-optic polymer-clad silicon slot waveguide: 1 - 3 Sept. 2010, Beijing, China*, (Piscataway, NJ), IEEE, 2010.

[88] J.-M. Brosi, C. Koos, L. C. Andreani, M. Waldow, J. Leuthold, and W. Freude, “High-speed low-voltage electro-optic modulator with a polymer-infiltrated silicon photonic crystal waveguide,” *Optics Express*, vol. 16, no. 6, p. 4177, 2008.

[89] R. S. Jacobsen, K. N. Andersen, P. I. Borel, J. Fage-Pedersen, L. H. Frandsen, O. Hansen, M. Kristensen, A. V. Lavrinenko, G. Moulin, H. Ou, C. Peucheret, B. Zsigri, and A. Bjarklev, “Strained silicon as a new electro-optic material,” *Nature*, vol. 441, no. 7090, pp. 199–202, 2006.

[90] B. Chmielak, M. Waldow, C. Matheisen, C. Ripperda, J. Bolten, T. Wahlbrink, M. Nagel, F. Merget, and H. Kurz, “Pockels effect based fully integrated, strained silicon electro-optic modulator,” *Optics express*, vol. 19, no. 18, pp. 17212–17219, 2011.

[91] J. Kalkman, A. Tchebotareva, A. Polman, T. J. Kippenberg, B. Min, and K. J. Vahala, “Fabrication and characterization of erbium-doped toroidal microcavity lasers,” *Journal of Applied Physics*, vol. 99, no. 8, p. 083103, 2006.

[92] A. Polman, B. Min, J. Kalkman, T. J. Kippenberg, and K. J. Vahala, “Ultralow-threshold erbium-implanted toroidal microlaser on silicon,” *Applied Physics Letters*, vol. 84, no. 7, pp. 1037–1039, 2004.

[93] O. Boyraz and B. Jalali, “Demonstration of a silicon Raman laser,” *Optics Express*, vol. 12, no. 21, p. 5269, 2004.

[94] T. J. Kippenberg, “Microresonators: Particle sizing by mode splitting,” *Nature Photonics*, vol. 4, no. 1, pp. 9–10, 2010.

[95] J. Zhu, S. K. Ozdemir, Y.-F. Xiao, L. Li, L. He, D.-R. Chen, and L. Yang, “On-chip single nanoparticle detection and sizing by mode splitting in an ultrahigh-Q microresonator,” *Nature Photonics*, vol. 4, no. 1, pp. 46–49, 2009.

[96] E. Gavartin, P. Verlot, and T. J. Kippenberg, “A hybrid on-chip optomechanical transducer for ultrasensitive force measurements,” *Nature Nanotechnology*, vol. 7, no. 8, pp. 509–514, 2012.

[97] G. Villares, A. Hugi, S. Blaser, and J. Faist, “Dual-comb spectroscopy based on quantum-cascade-laser frequency combs,” *Nature communications*, vol. 5, p. 5192, 2014.

[98] I. Coddington, W. Swann, and N. Newbury, “Coherent Multiheterodyne Spectroscopy Using Stabilized Optical Frequency Combs,” *Physical Review Letters*, vol. 100, no. 1, 2008.

[99] T. Ideguchi, A. Poisson, G. Guelachvili, N. Picqué, and T. W. Hänsch, “Adaptive real-time dual-comb spectroscopy,” *Nature communications*, vol. 5, p. 3375, 2014.

[100] S. A. Diddams, L. Hollberg, and V. Mbele, “Molecular fingerprinting with the resolved modes of a femtosecond laser frequency comb,” *Nature*, vol. 445, no. 7128, pp. 627–630, 2007.

[101] J. Li, M.-G. Suh, and K. Vahala, “Microresonator Brillouin gyroscope,” *Optica*, vol. 4, no. 3, p. 346, 2017.

[102] P. An, Y. Zheng, S. Yan, C. Xue, W. Wang, and J. Liu, “High- Q microsphere resonators for angular velocity sensing in gyroscopes,” *Applied Physics Letters*, vol. 106, no. 6, p. 063504, 2015.

[103] W. Liang, V. S. Ilchenko, A. A. Savchenkov, E. Dale, D. Eliyahu, A. B. Matsko, and L. Maleki, “Resonant microphotonic gyroscope,” *Optica*, vol. 4, no. 1, p. 114, 2017.

[104] I. S. Grudinin, N. Yu, and L. Maleki, “Generation of optical frequency combs with a CaF(2) resonator,” *Optics Letters*, vol. 34, no. 7, p. 878, 2009.

[105] A. Tulek, D. Akbulut, and M. Bayindir, “Ultralow threshold laser action from toroidal polymer microcavity,” *Applied Physics Letters*, vol. 94, no. 20, p. 203302, 2009.

[106] E. Ozgur, P. Toren, O. Aktas, E. Huseyinoglu, and M. Bayindir, “Label-Free Biosensing with High Selectivity in Complex Media using Microtoroidal Optical Resonators,” *Scientific reports*, vol. 5, p. 13173, 2015.

[107] H. F. Winters and J. W. Coburn, “The etching of silicon with XeF(2) vapor,” *Applied Physics Letters*, vol. 34, no. 1, p. 70, 1979.

[108] K. Sugano and O. Tabata, “Reduction of surface roughness and aperture size effect for etching of Si with XeF(2),” *Journal of Micromechanics and Microengineering*, vol. 12, no. 6, pp. 911–916, 2002.

[109] C. K. N. Patel, “Continuous-Wave Laser Action on Vibrational-Rotational Transitions of CO(2),” *Physical Review*, vol. 136, no. 5A, pp. A1187–A1193, 1964.

[110] M. Sheik-bahae and H. S. Kwok, “Controlled CO(2) laser melting of silicon,” *Journal of Applied Physics*, vol. 63, no. 2, p. 518, 1988.

[111] A. D. McLachlan and F. P. Meyer, “Temperature dependence of the extinction coefficient of fused silica for CO(2) laser wavelengths,” *Applied optics*, vol. 26, no. 9, pp. 1728–1731, 1987.

[112] T. J. Kippenberg, S. M. Spillane, D. K. Armani, and K. J. Vahala, “Fabrication and coupling to planar high-Q silica disk microcavities,” *Applied Physics Letters*, vol. 83, no. 4, pp. 797–799, 2003.

[113] A. Schließer, *Cavity optomechanics and optical frequency comb generation with silica whispering-gallery-mode microresonators.* PhD thesis, München, 2009.

[114] T. J. Kippenberg, *Nonlinear Optics in Ultra-high-Q Whispering-Gallery Optical Microcavities.* PhD thesis, California Institute of Technology, 2004.

[115] P. Del'Haye, *Optical frequency comb generation in monolithic microresonators.* München: Verl. Dr. Hut, 1. aufl. ed., 2011.

[116] M. L. Gorodetsky, A. A. Savchenkov, and V. S. Ilchenko, "Ultimate Q of optical microsphere resonators," *Optics Letters*, vol. 21, no. 7, p. 453, 1996.

[117] M. L. Gorodetsky, A. D. Pryamikov, and V. S. Ilchenko, "Rayleigh scattering in high-Q microspheres," *Journal of the Optical Society of America B*, vol. 17, no. 6, p. 1051, 2000.

[118] H. Rokhsari, S. M. Spillane, and K. J. Vahala, "Loss characterization in microcavities using the thermal bistability effect," *Applied Physics Letters*, vol. 85, no. 15, p. 3029, 2004.

[119] Ilchenko, V. S. and Gorodetsky, M. L., "Thermal Nonlinear Effects in Optical Whispering Gallery Microresonators," *Laser Physics*, vol. 2, no. 6, p. 1004, 1992.

[120] Sean Michael Spillane, *Fiber-coupled ultra-high-Q microresonators for nonlinear and quantum optics.* PhD thesis, 2004.

[121] B. Min, L. Yang, and K. Vahala, "Perturbative analytic theory of an ultrahigh-Q toroidal microcavity," *Physical Review A*, vol. 76, no. 1, 2007.

[122] M. H. P. Pfeiffer, A. Kordts, V. Brasch, M. Zervas, M. Geiselmann, J. D. Jost, and T. J. Kippenberg, "Photonic Damascene process for integrated high-Q microresonator based nonlinear photonics," *Optica*, vol. 3, no. 1, p. 20, 2016.

[123] W. D. Sacher, Y. Huang, G.-Q. Lo, and J. K. S. Poon, "Multilayer Silicon Nitride-on-Silicon Integrated Photonic Platforms and Devices," *Journal of Lightwave Technology*, vol. 33, no. 4, pp. 901–910, 2015.

[124] D. Schulz, C. Glingener, M. Bludszuweit, and E. Voge, "Mixed finite element beam propagation method," *Journal of Lightwave Technology*, vol. 16, no. 7, pp. 1336–1342, 1998.

[125] M. Koshiba, S. Maruyama, and K. Hirayama, "A vector finite element method with the high-order mixed-interpolation-type triangular elements for optical waveguiding problems," *Journal of Lightwave Technology*, vol. 12, no. 3, pp. 495–502, 1994.

[126] J. Jin, ed., *The finite element method in electromagnetics.* New York, N.Y.: Wiley-Interscience, 2. ed., [repr.] ed., 2002.

[127] R. Baets and P. E. Lagasse, "Loss calculation and design of arbitrarily curved integrated-optic waveguides," *Journal of the Optical Society of America*, vol. 73, no. 2, p. 177, 1983.

[128] D. M. Shyroki, “Exact Equivalent Straight Waveguide Model for Bent and Twisted Waveguides,” *IEEE Transactions on Microwave Theory and Techniques*, vol. 56, no. 2, pp. 414–419, 2008.

[129] A. Taflove, ed., *Computational electrodynamics: The finite-difference time-domain method.* Artech House Antenna Library, Boston and London: Artech House, op. 1995.

[130] K. Yee, “Numerical solution of initial boundary value problems involving maxwell’s equations in isotropic media,” *IEEE Transactions on Antennas and Propagation*, vol. 14, no. 3, pp. 302–307, 1966.

[131] M. Pu, L. Liu, H. Ou, K. Yvind, and J. M. Hvam, “Ultra-low-loss inverted taper coupler for silicon-on-insulator ridge waveguide,” *Optics Communications*, vol. 283, no. 19, pp. 3678–3682, 2010.

[132] C. e. a. Kopp, “Silicon Photonic Circuits: On-CMOS Integration, Fiber Optical Coupling, and Packaging,” *IEEE Journal of Selected Topics in Quantum Electronics*, vol. 17, no. 3, pp. 498–509, 2011.

[133] A. W. Snyder and J. D. Love, eds., *Optical waveguide theory.* London: Chapman and Hall, 1983.

[134] P. Dumon, W. Bogaerts, V. Wiaux, J. Wouters, S. Beckx, J. van Campenhout, D. Taillaert, B. Luyssaert, P. Bienstman, D. van Thourhout, and R. Baets, “Low-Loss SOI Photonic Wires and Ring Resonators Fabricated With Deep UV Lithography,” *IEEE Photonics Technology Letters*, vol. 16, no. 5, pp. 1328–1330, 2004.

[135] G. A. Reider, *Photonik: Eine Einführung in die Grundlagen.* SpringerLink: Springer e-Books, Vienna: Springer-Verlag/Wien, zweite, überarbeitete und erweiterte auflage ed., 2005.

[136] A. K. Paul, A. K. Dimri, and R. P. Bajpai, “Plasma etch models based on different plasma chemistry for micro-electro-mechanical-systems application,” *Vacuum*, vol. 68, no. 2, pp. 191–196, 2002.

[137] P. Rai-Choudhury, ed., *Handbook of microlithography, micromachining, and microfabrication*, vol. PM39 of *SPIE Press monograph.* Bellingham, Washington: SPIE Optical Engineering Press, 1997.

[138] R. Gunn, D. Stephens, C. Welch, “Comparison of etch processes for patterning high aspect ratio and nanoscale features in silicon,” *Bristol, UK: Oxford Instruments Plasma Technology Ltd*, 2009.

[139] K. P. Larsen, D. H. Petersen, and O. Hansen, “Study of the Roughness in a Photoresist Masked, Isotropic, SF[sub 6]-Based ICP Silicon Etch,” *Journal of The Electrochemical Society*, vol. 153, no. 12, p. G1051, 2006.

[140] K. Nojiri, ed., *Dry Etching Technology for Semiconductors.* Cham: Springer International Publishing and Imprint: Springer, 2015.

[141] J. A. Arnaud, W. M. Hubbard, G. D. Mandeville, B. de La Clavière, E. A. Franke, and J. M. Franke, “Technique for fast measurement of gaussian laser beam parameters,” *Applied Optics*, vol. 10, no. 12, pp. 2775–2776, 1971.

[142] Eric Paul Ostby, *Photonic whispering-gallery resonators in new environments.* PhD thesis, 2009.

[143] D. B. Leviton and B. J. Frey, “Temperature-dependent absolute refractive index measurements of synthetic fused silica,” p. 62732K, 2008.

[144] P. Del’Haye, O. Arcizet, A. Schliesser, R. Holzwarth, and T. J. Kippenberg, “Full Stabilization of a Microresonator-Based Optical Frequency Comb,” *Physical Review Letters*, vol. 101, no. 5, 2008.

[145] J. Richter, A. Abdou, O. A. Williams, J. Witzens, and M. P. Nezhad, “CO(2) laser micromachining of nanocrystalline diamond films grown on doped silicon substrates,” *Optical Materials Express*, vol. 6, no. 12, p. 3916, 2016.

[146] A. Abdou, P. Panduranga, J. Richter, E. L. H. Thomas, S. Mandal, O. A. Williams, J. Witzens, and M. P. Nezhad, “Air-clad suspended nanocrystalline diamond ridge waveguides,” *Optics express*, vol. 26, no. 11, pp. 13883–13890, 2018.

[147] J. Witzens, “Integrated microtoroids monolithically coupled with integrated waveguides,” US Patent 9268086B2. filed Aug. 2013.

Appendix A

CO_2 Reflow-Setup Overview

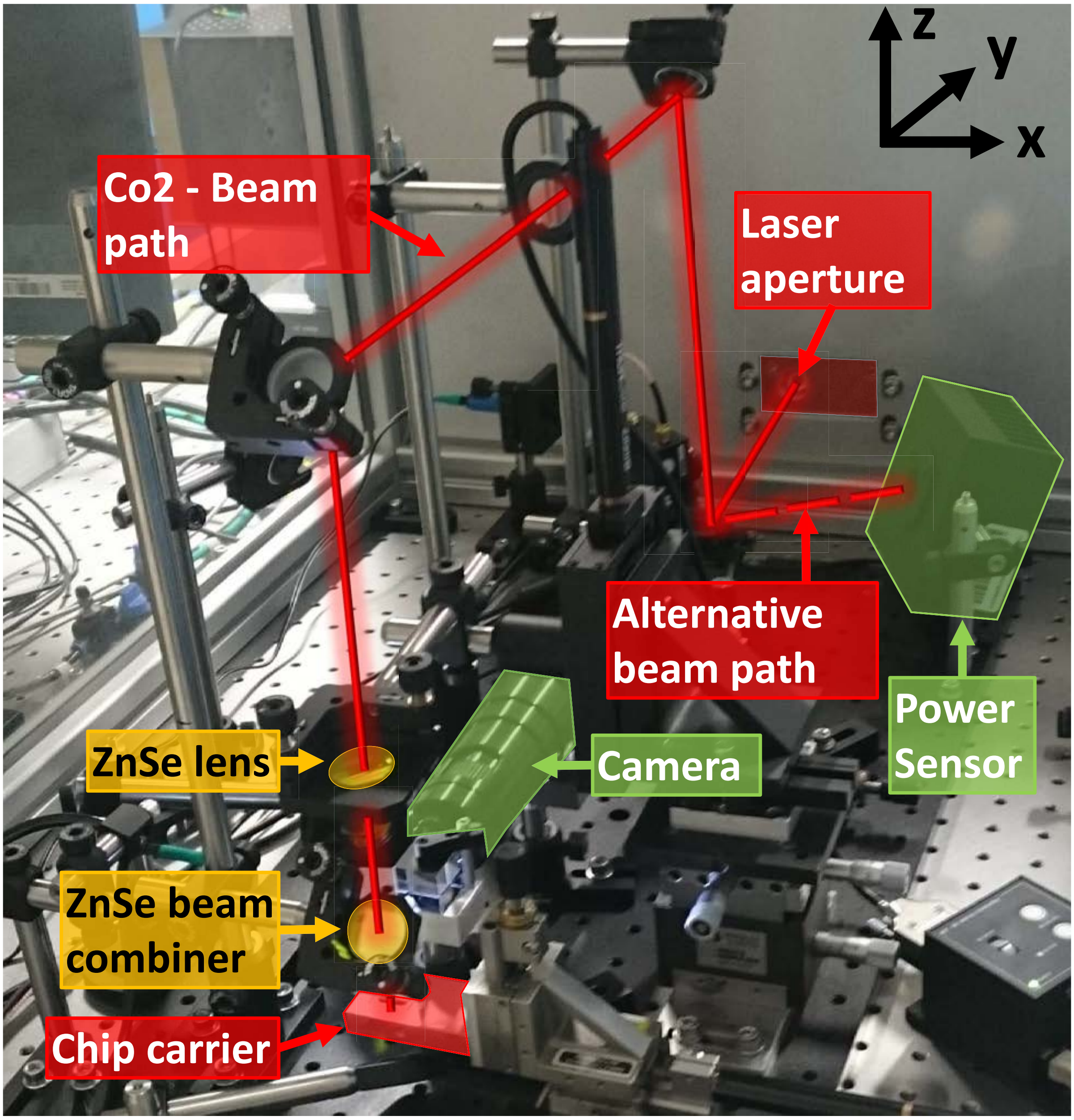

Figure A.1: Overview image of the nitrogen-purged reflow setup used to reflow inverted microtoroids. The laser beam is routed with the help of a flip mirror to hit a thermal power sensor directly or to enter the setup. When entering the setup, the beam is focused by the use of a ZnSe Bi-Convex lens with a focal length of 100 mm. Before the focused beam hits a chip to be processed located on a chip carrier, a ZnSe-beam combiner is used to overlay a camera system, which makes it possible to get a live view camera image of the melting process.

Appendix B

Standard cleaning procedure

For preparing the samples before fabrication, the following standard cleaning method was used:

1. Leave for 10 minutes in acetone → 10 minutes Isopropanol → Rinse for 5 minutes in high-purity water
2. Leave for 10 minutes in H_2O_2:H_2SO_4 (1:2) → Rinse for 5 minutes in high-purity water
3. Leave for 10 seconds in a buffered oxide etch (BOE) → Rinse for 5 minutes in high-purity water
4. Leave for 10 minutes H_2O:H_2O_2:NH_3 (4:1:1) → Rinse for 5 minutes in high-purity water
5. Leave for 10 seconds in BOE → Rinse for 5 minutes in high-purity water
6. Leave for 10 minutes H_2O:H_2O_2:HCl (4:1:1) → Rinse for 5 minutes in high-purity water
7. Leave for 10 seconds in BOE (before next processing step) → Rinse for 5 minutes in high-purity water

Appendix C

Optical resist coating, exposure, and development

Treatmend - After silicon etching and before silica etching:

1. Adhesion promotion: Coat chips with HMDS at 135 °C on a sealed hot plate.
2. Spin-coating: Spin AZ5214E resist (by MicroChemicals) for 3 seconds at 1000 rpm followed by 30 seconds at 3000 rpm to get a resist thickness of about 1.8 µm.
3. Soft-bake: Heat the resist for 2 minutes at 120 °C on a hot plate.
4. Optical lithography: Use a MA6BA6 mask aligner (in hard contact mode) and expose resist for 5 seconds at 15 mW/cm^2 at a wavelength of 405 nm.
5. Development: Develop the resist for 50 seconds in AZ726MIF (by MicroChemicals) (include paddling).
6. Cleaning: Rinse with high purity water (DI-water).

Treatment - After silicon undercut etching and before dicing:

1. Coating: Add AZ520D (by MicroChemicals) in the edge-coupler and microtoroid section of a chip by mean of a pipette (as thin as possible).
2. First short bake: Put the chip on a heating plate for 1 minute at 100 °C. The resist will start sticking to the chip.
3. (Optional) Spread resist: In case, the resist thickness is too high (the structures are not visible through the resist); carefully move the chip in a way that gravitational forces are spreading the resist.
4. Bake: Heat the chip at 110-120°C for 5 minutes.

Appendix D

List of publications

List of publications:

Journal Papers

1. Aly Abdou, Parashara Panduranga, **Jens Richter** Oliver A. Williams, Jeremy Witzens, and Maziar P. Nezhad, “Air-clad suspended nanocrystalline diamond waveguides,” Optics express, vol. 26, no. 11, pp. 13883–13890, 2018.

2. **Jens Richter**, Aly Abdou, Oliver A. Williams, Jeremy Witzens, and Maziar P. Nezhad, "CO_2 laser micromachining of nanocrystalline diamond films grown on doped silicon substrates," Optical Materials Express, vol. 6, no. 12, p. 3916, 2016.

3. Johannes Hauck, Matthias Schrammen, Sebastan Romero-García, Juliana Müller, Bin Shen, **Jens Richter**, Florian Merget, and Jeremy Witzens, "Stabilization and Frequency Control of a DFB Laser With a Tunable Optical Reflector Integrated in a Silicon Photonics PIC," J. Lightwave Technol. 34, 5467-5473

4. Jón Mattis Hoffmann, Xinghui Yin, **Jens Richter**, Andrea Hartung, Tobias W. W. Maß, and Thomas Taubner, "Low-Cost Infrared Resonant Structures for Surface-Enhanced Infrared Absorption Spectroscopy in the Fingerprint Region from 3 to 13 µm," J. Phys. Chem. C, 2013, 117 (21), pp 11311–11316

5. **Jens Richter**, Maziar P. Nezhad, Birgit Hadam, Thomas Taubner, Joachim Knoch, Florian Merget, Alvaro Moscoso-Mártir, and Jeremy Witzens, “High-Q inverted silica microtoroid resonators monolithically integrated into a Silicon Photonics platform,” Opt. Express 26, pp 27418-27440, 2018

International Conferences

1. **Jens Richter**, M. P. Nezhad and J. Witzens, "Monolithically integrated waveguide-coupled silica microtoroids," 2015 Opto-Electronics and Communications Conference (OECC), Shanghai, 2015, pp. 1-3.

Appendix E

Curriculum Vitae

Curriculum Vitae:

PERSONAL INFROMATION

Name: Jens Richter
Date of Birth: 26. Mai 1986 (Germany, Dresden)

CURRENT WORK

Since 12/2017 : DNA Evolutions

Description: Senior-Developer at DNA Evolutions.

PREVIOUS WORK AS RESEARCH ASSISTANT

11/2011 – 12/2017 : Institute of integrated photonics

Description: Research Assistant and Ph.D. student.
Doctoral thesis: “Ultra-high-Q inverted silica microtoroid resonators monolithically integrated into a silicon photonics platform.”
Further tasks: Supervising of students and working as Laser safety officer.

08/2011–11/2011 : Fraunhofer ILT/TOS (19h/ Week)

Task: Simulation of plasmonic structures with the software package Lumerical with the goal of developing devices for collimating infrared light via surface-plasmon-polaritons.

EDUCATION

04/2006 – 08/2011 : RWTH Aachen University

Major subject: Physics
Specialisation: Solid state physics
Minor subjects: Informatics, Laser physics, Nano-optics
Degree: Diploma in physics
Diploma thesis: „Surface-enhanced infrared micro-spectroscopy with resonant particles.“

WORK AS STUDENT ASSISTANT

04/2010–04/2011 :	I. Institute of Physics RWTH (10h/ Week)
Task:	Implementing a software package for controlling a microscope stage with LabVIEW with the goal of compensating thermal drift effects via pattern recognition with the help of autocorrelation.
05/2008–04/2010 :	Fraunhofer ILT (14h/ Week)
Task:	Analysing and fabricating structures created with laser build-up welding technology for industrial projects.

CIVILIAN SERVICE

04/2005–04/2006 :	St. Remigius Krankenhaus Opladen (Hospital)
Task:	Support, care, and end-of-life-care of patients in the internal medicine.